frontiers | Research Topics

Bioluminescent indicators and sensors for biomedicine and environmental analysis

Edited by
Vadim R. Viviani, Yoshihiro Ohmiya, Elisa Michelini and Aldo Roda

Published in
Frontiers in Bioengineering and Biotechnology

ISSN 1664-8714
ISBN 978-2-83250-912-8
DOI 10.3389/978-2-83250-912-8

About Frontiers

Frontiers is more than just an open access publisher of scholarly articles: it is a pioneering approach to the world of academia, radically improving the way scholarly research is managed. The grand vision of Frontiers is a world where all people have an equal opportunity to seek, share and generate knowledge. Frontiers provides immediate and permanent online open access to all its publications, but this alone is not enough to realize our grand goals.

Frontiers journal series

The Frontiers journal series is a multi-tier and interdisciplinary set of open-access, online journals, promising a paradigm shift from the current review, selection and dissemination processes in academic publishing. All Frontiers journals are driven by researchers for researchers; therefore, they constitute a service to the scholarly community. At the same time, the *Frontiers journal series* operates on a revolutionary invention, the tiered publishing system, initially addressing specific communities of scholars, and gradually climbing up to broader public understanding, thus serving the interests of the lay society, too.

Dedication to quality

Each Frontiers article is a landmark of the highest quality, thanks to genuinely collaborative interactions between authors and review editors, who include some of the world's best academicians. Research must be certified by peers before entering a stream of knowledge that may eventually reach the public - and shape society; therefore, Frontiers only applies the most rigorous and unbiased reviews. Frontiers revolutionizes research publishing by freely delivering the most outstanding research, evaluated with no bias from both the academic and social point of view. By applying the most advanced information technologies, Frontiers is catapulting scholarly publishing into a new generation.

What are Frontiers Research Topics?

Frontiers Research Topics are very popular trademarks of the *Frontiers journals series*: they are collections of at least ten articles, all centered on a particular subject. With their unique mix of varied contributions from Original Research to Review Articles, Frontiers Research Topics unify the most influential researchers, the latest key findings and historical advances in a hot research area.

Find out more on how to host your own Frontiers Research Topic or contribute to one as an author by contacting the Frontiers editorial office: frontiersin.org/about/contact

Bioluminescent indicators and sensors for biomedicine and environmental analysis

Topic editors

Vadim R. Viviani — Federal University of São Carlos, Brazil

Yoshihiro Ohmiya — National Institute of Advanced Industrial Science and Technology (AIST), Japan

Elisa Michelini — University of Bologna, Italy

Aldo Roda — University of Bologna, Italy

Citation

Viviani, V. R., Ohmiya, Y., Michelini, E., Roda, A., eds. (2022). *Bioluminescent indicators and sensors for biomedicine and environmental analysis*. Lausanne: Frontiers Media SA. doi: 10.3389/978-2-83250-912-8

Table of contents

frontiers | Frontiers in Bioengineering and Biotechnology

TYPE Editorial
PUBLISHED 17 November 2022
DOI 10.3389/fbioe.2022.1057607

OPEN ACCESS

EDITED AND REVIEWED BY
Hasan Uludag,
University of Alberta, Canada

*CORRESPONDENCE
Vadim R. Viviani,
viviani@ufscar.br

SPECIALTY SECTION
This article was submitted to Biomaterials, a section of the journal Frontiers in Bioengineering and Biotechnology

RECEIVED 29 September 2022
ACCEPTED 25 October 2022
PUBLISHED 17 November 2022

CITATION
Viviani VR (2022), Editorial: Bioluminescent indicators and sensors for biomedicine and environmental analysis.
Front. Bioeng. Biotechnol. 10:1057607.
doi: 10.3389/fbioe.2022.1057607

Editorial: Bioluminescent indicators and sensors for biomedicine and environmental analysis

Vadim R. Viviani*

Department Physics, Chemistry and Mathematics, Center for Sustainable Sciences and Technologies (CCTS), Federal University of São Carlos, Sorocaba, Brazil

KEYWORDS

bioluminescence, biosensors, bioimaging, reporter genes, smartphone CCD imaging, near-infrared bioluminescence

Editorial on the Research Topic
Bioluminescent indicators and sensors for biomedicine and environmental analysis

At times in which the biosphere and humanity are undergoing major changes, bioanalytical and bioindication techniques to monitor health, the environment and emerging threats are on high demand. Bioluminescence, the emission of visible light by living organisms for communicative purposes, has been extensively used for bioanalytical purposes to assess biological and environmental integrity, alerting humanity about biological and environmental threats, and assessing industrial products microbiological quality. In this Research Topic, some of the latest advances about the improvement of bioluminescence systems and of associated detecting technologies for biomedical, environmental and safety bioanalysis purposes are reported.

- The increase of sensitivity of smartphone cameras, for example, is allowing the development of fast biosensing devices for point of care health and environmental applications, as can be seen in the manuscript (Wienhold et al.).
- Niwa et al. introduce the application of the TES technique for ultra-sensitive and wide-band wavelength range color imaging for biological samples with application in confocal laser scanning microscopy

The construction of novel bioluminescent fusion proteins is allowing important advances biosensing and diagnostics, for example:

- the development of intracellular calcium sensing proteins based on photoproteins with FP-tagged calcium binding domains, which allows the fast and sensitive detection of calcium flows cultured mammalian cells (Yang and Johnson) and,

- the development of a fusion protein based on a brighter firefly luciferase and ZZ-protein, which is used to detect antibodies and antigens in bioluminescent immunoassays, with sensitivity matching the commercially available chemiluminescent assays (Viviani et al.).

The development of novel brighter bioluminescent systems emitting in the FR and NIR based on combinatory chemistry and genetic engineering of luciferases, are promising for mammalian tissue bioluminescence imaging of biological and pathological processes. Among them here we report:

- A novel form of infralluciferin (Jathoul et al.) which emits in the NIR, and
- the NIR bioluminescence tracking macrophages in melanomas as shown by Zambito et al.

The engineering of luciferases is also allowing their improvement for better bioanalyitical applications such as:

- The engineering of the secreted recombinant ostracod luciferase which is allowing to better understand the structure/function relationship and to improve its expression in different heterologous systems (Mitani et al.), and
- The improvement of the thermostability of firefly luciferase which is allowing to develop more robust protein–protein interaction assays "FlimPIA" based on the functional complementation of mutant firefly luciferases (Fluc) (Ohmuro-Matsuyama et al.).

Bioluminescence is also being effectively used in biosensors for safety purposes, to detect dangerous explosives such as the optimized Escherichia coli-based bioreporter for the detection of 2,4,6-trinitrotoluene (TNT) and derivatives (DNT) (Elad et al.).

Finally, an *E.coli* bioreporter based on the randomly mutagenized ribose binding protein (RbsB) associated with the GFP-based screening was constructed to bind and detect the non-natural ligand 1,3-cyclohexanediol (13CHD) (Tavares and van der Meer).

The above papers reflect some of the continuous advances and prospects of bioengineering of bioluminescent systems and its associated detecting technologies in the fields of biomedical, environmental and safety bioanalysis.

Author contributions

VRV wrote this editorial.

Conflict of interest

The author declares that the research was conducted in the absence of any commercial or financial relationships that could be construed as a potential conflict of interest.

Publisher's note

frontiers in Bioengineering and Biotechnology

ORIGINAL RESEARCH
published: 23 July 2021
doi: 10.3389/fbioe.2021.705534

Ribose-Binding Protein Mutants With Improved Interaction Towards the Non-natural Ligand 1,3-Cyclohexanediol

*Diogo Tavares and Jan Roelof van der Meer**

Department of Fundamental Microbiology, University of Lausanne, Lausanne, Switzerland

Bioreporters consist of genetically modified living organisms that respond to the presence of target chemical compounds by production of an easily measurable signal. The central element in a bioreporter is a sensory protein or aptamer, which, upon ligand binding, modifies expression of the reporter signal protein. A variety of naturally occurring or modified versions of sensory elements has been exploited, but it has proven to be challenging to generate elements that recognize non-natural ligands. Bacterial periplasmic binding proteins have been proposed as a general scaffold to design receptor proteins for non-natural ligands, but despite various efforts, with only limited success. Here, we show how combinations of randomized mutagenesis and reporter screening improved the performance of a set of mutants in the ribose binding protein (RbsB) of *Escherichia coli*, which had been designed based on computational simulations to bind the non-natural ligand 1,3-cyclohexanediol (13CHD). Randomized mutant libraries were constructed that used the initially designed mutants as scaffolds, which were cloned in an appropriate *E. coli* bioreporter system and screened for improved induction of the GFPmut2 reporter fluorescence in presence of 1,3-cyclohexanediol. Multiple rounds of library screening, sorting, renewed mutagenesis and screening resulted in 4.5-fold improvement of the response to 1,3-cyclohexanediol and a lower detection limit of 0.25 mM. All observed mutations except one were located outside the direct ligand-binding pocket, suggesting they were compensatory and helping protein folding or functional behavior other than interaction with the ligand. Our results thus demonstrate that combinations of ligand-binding-pocket redesign and randomized mutagenesis can indeed lead to the selection and recovery of periplasmic-binding protein mutants with non-natural compound recognition. However, current lack of understanding of the intermolecular movement and ligand-binding in periplasmic binding proteins such as RbsB are limiting the rational production of further and better sensory mutants.

Keywords: biosensor, periplasmic binding proteins, *Escherichia coli*, directed mutagenesis, fluorescence assisted cell sorting

OPEN ACCESS

Edited by:
Elisa Michelini,
University of Bologna, Italy

Reviewed by:
Jon Dattelbaum,
University of Richmond, United States
Pasqualina Liana Scognamiglio,
Italian Institute of Technology (IIT), Italy

***Correspondence:**
Jan Roelof van der Meer
Janroelof.vandermeer@unil.ch

Specialty section:
This article was submitted to Biomaterials, a section of the journal Frontiers in Bioengineering and Biotechnology

Received: *05 May 2021*
Accepted: *29 June 2021*
Published: *23 July 2021*

Citation:
Tavares D and van der Meer JR (2021) Ribose-Binding Protein Mutants With Improved Interaction Towards the Non-natural Ligand 1,3-Cyclohexanediol. Front. Bioeng. Biotechnol. 9:705534. doi: 10.3389/fbioe.2021.705534

INTRODUCTION

Periplasmic binding proteins (PBPs) form a family of proteins with a conserved bilobal structure (Berntsson et al., 2010; Chu Byron and Vogel, 2011). PBPs scavenge molecules (ligands) for the cell, which upon binding are presented to transport channels and/or to membrane receptors involved in chemotaxis (Binnie et al., 1992). Crystal structures and nuclear-magnetic resonance data have shown that PBPs can adapt two semi-stable conformations. In absence of the ligand most of the protein molecules adopt an open conformation, in which the binding site is exposed. In presence of the ligand, the molecule is buried in the binding pocket and the PBP adopts a closed conformation (Björkman and Mowbray, 1998; Li et al., 2013). This particular opening-and-closing and the fact that they locate in the periplasmic space make PBPs a potentially attractive protein class for biosensing purposes (Edwards, 2021). PBPs can be integrated in an *in vivo* hybrid signaling chain leading to expression of a reporter protein, which can be easily measured (Medintz and Deschamps, 2006; van der Meer and Belkin, 2010). In the context of this work, we focused on the ribose binding protein (RbsB) of *Escherichia coli*, which in presence of the natural ligand ribose changes from open to closed conformation. RbsB and its affinity for ribose have been deployed as a bioreporter system through use of a hybrid membrane receptor named Trz1 (Reimer et al., 2014). Trz1 consists of a fusion between the C-terminal part of the *E. coli* cytoplasmic EnvZ osmoregulation histidine kinase and the N-terminal periplasmic and membrane-spanning part of the *E. coli* Trg chemotaxis receptor (Baumgartner et al., 1994). Ribose-bound RbsB triggers the Trz1 autophosphorylation cascade, leading to OmpR phosphorylation and increasing its affinity for the *ompC* promoter. This yields increased transcription of reporter genes fused to P_{ompC}.

Periplasmic binding proteins have been proposed as a flexible platform to design new ligand-binding pockets based on protein engineering approaches (Dwyer and Hellinga, 2004), with, however, very limited and controversial successes. Several studies attempted to engineer PBPs based on rational design and computational approaches, but this led to poorly foldable proteins (Boas and Harbury, 2008; Scheib et al., 2014; Banda-Vazquez et al., 2018). Other studies exploited natural properties of the PBPs to reduce or increase binding specificity (Amiss et al., 2007; Ko et al., 2017) or to graft binding-pockets between closely related PBPs (Scheib et al., 2014; Banda-Vazquez et al., 2018). We previously described six novel RbsB mutants with loss of binding to ribose and moderate but significant response to 1,3-cyclohexanediol (13CHD). These mutants were obtained through a combination of computational prediction of binding pocket mutations in RbsB and screening for gain of GFPmut2 fluorescence output in an *E. coli* bioreporter system (Tavares et al., 2019). However, all mutant proteins showed signs of poor stability, mis- or unfolding and potentially translocation problems compared to wild-type RbsB, suggesting that the poor inducibility by 13CHD may partly be due to protein instability caused by the introduced binding pocket substitutions. Indeed, other studies have shown that mutations both in the ribose binding pocket and protein periphery can destabilize the protein (Antunes et al., 2011; Reimer et al., 2017). This was refined by alanine replacement mutagenesis, in order to understand individual residue importance for RbsB folding and functioning (Vercillo et al., 2007; Reimer et al., 2017).

The goal of this work was to understand whether primitive binding of 13CHD by designed RbsB mutants (Tavares et al., 2019) can be improved by both rational and directed evolution approaches. We started with six mutant *rbsB* templates that were previously obtained (Tavares et al., 2019), which were used for random or site-directed mutagenesis, cloned into the *E. coli* GFPmut2 bioreporter strain and extensively screened by fluorescence-assisted cell sorting for improved GFPmut2 induction in presence of 13CHD. Potential gain-of-function mutants were separated and used for new rounds of mutagenesis and screening. Our hypothesis was that mutations in parts of RbsB outside the direct binding pocket may compensate folding defects and could lead to better functional PBP variants. Given that computational predictions on PBP folding are not sufficiently accurate yet, this procedure might open a route to profit from *de novo* computational binding pocket predictions to create primitive binding capacity and optimize protein functioning using random mutagenesis and selection.

RESULTS

Random Mutagenesis of RbsB Protein Variants With Primitive 13CHD Affinity

We previously selected six RbsB mutants (named DT001, DT002, DT011, DT013, DT015, and DT016) that had lost the capacity to bind ribose, and instead had gained primitive affinity to 13CHD as new ligand (Tavares et al., 2019). Purified mutant proteins, however, displayed severe misfolding, poor stability and poor translocation into the periplasmic space (Tavares et al., 2019). In order to potentially improve mutant protein functionality, we used the respective *rbsB-DT* mutant genes as individual templates to produce random mutagenesis libraries (RML) using error prone PCR (ep-PCR). RMLs produced from each starting RbsB-variant were transformed into the *E. coli* bioreporter strain carrying the Trz1-*ompR-ompC'*:*gfpmut2* signaling chain (Reimer et al., 2014). Individual clones were encapsulated in alginate beads and grown to microcolonies, which were incubated with 1 mM 13CHD to induce GFP formation (Tavares et al., 2019).

Some 10 million beads, covering three times the estimated sizes of the RML002 and RML016 (derivatives of DT002 and DT016, respectively) were screened by fluorescence-activated cell sorting (FACS), separating beads with an 13CHD-induced fluorescence above the 98th percentile. 10^5 beads were recovered, from which plasmid DNA was isolated and used as template for a new round of random mutagenesis. The new libraries (with estimated sizes of 5.5×10^6 and 8.5×10^6 clones) were again encapsulated, induced and screened, but now restricting recovery to the top 0.1% of GFPmut2 fluorescence. 6×10^3 beads were collected, purified to individual clones, and screened in eight replicates in 96-well plates for 13CHD induction. This resulted in finding three mutants (named: DT020, DT021, and DT022) with consistent and up to 2.1-fold 13CHD induction, a

significant increase and/or reduction of fluorescence background when compared with parental DT002 and DT016 (**Table 1**). Sequencing revealed a single different amino acid substitution in each of the three mutants (**Table 1**). Mutant DT020 had the exact same 1.5-fold induction as its parent DT016, but showed a 30% reduced fluorescence background intensity ($p = 2.25 \times 10^{-5}$, $n = 12$ replicates, **Table 1**). Mutants DT021 and DT022 displayed a small increase in fold induction to 1.66 ± 0.09 ($n = 13$ replicates) and 2.09 ± 0.16 ($n = 14$ replicates), respectively (**Table 1**).

Separate RMLs produced from the initial variants DT001, DT011, DT013, and DT015 (named RML001, RML011, RML013, and RML015, and with library sizes of 3.4×10^6, 2.2×10^6, 1×10^6, and 4.1×10^6 clones, respectively), were similarly encapsulated, induced with 13CHD and screened on an estimated three times library coverage for higher GFPmut2 fluorescence compared to non-induced conditions. In total, 151 beads were recovered that showed GFPmut2 fluorescence higher than any bead observed in non-induced conditions, which were purified and individually tested for 13CHD inducibility. Unfortunately, all mutants also showed significant increase in fluorescence in absence of 13CHD and none had induction levels above 1.5 times. Sequencing of some of these mutants showed gene deletions resulting in truncated RbsB mutant proteins. Pooled DNA from those 151 mutants used as template for a new library (estimated size of 1.5×10^6 variants) did not yield further improvements. In contrast, almost all tested clones showed deletions of the *rbsB* variant open reading frames resulting in truncated proteins. These RMLs were therefore not further investigated.

Random Mutagenesis of 2nd Generation Mutant RbsB Proteins With 13CHD Affinity

Because of the accumulation of truncated gene variants in the libraries we decided to create three new RMLs based on the newly isolated improved DT variants (DT020, DT021, and DT022, **Table 1**). These libraries (RML020, RML021, and RML022, with estimated sizes of 1.5×10^6, 3×10^6, and 2.5×10^6 clones, respectively) were again encapsulated to individual cells, grown to microcolonies and screened both under uninduced and 13CHD-induced conditions. In this screening, only beads with a fluorescence signal higher than the maximum observed signal under non-induced conditions for the same number of screened beads, were collected. Four mutants were recovered, with consistent and significant increase of 13CHD-dependent induction of GFPmut2 fluorescence and/or reduced background in absence of 13CHD (**Table 1**, n = 8–14 replicates). Three of those mutants displayed a single amino acid substitution, and one (DT033) showed three substitutions (**Table 1**). In one case (DT035) the substitution affected an amino acid in the signal peptide. Mutants DT033 and DT035 showed a similar fold induction, around 2.6 times, in presence of 13CHD (n = 9–12 replicates, **Table 1**). Mutants DT032 and DT038 were the most promising, with fold-inductions of 2.97 ± 0.37 and 3.19 ± 0.48 times (n = 13–14 replicates, **Table 1**). This represents a 4.5-fold increase in induction compared to the parental mutant DT016 (**Table 1**). All four mutants displayed a reduction in GFPmut2 fluorescence in absence of inducer in comparison to parental DT016, except DT033. The highest reduction was observed with DT038, with a background reduction of approximately two times (**Table 1**).

GFPmut2 fluorescence in *E. coli* cells expressing DT016, DT022, DT032, and DT038 displayed a typical dose-dependency at different 13CHD concentrations (**Figure 1**). For the four mutants, the GFPmut2 fluorescence signal after 2 h induction was saturated at 0.5–0.75 mM 13CHD with 1.5–3 times fold induction (**Figure 1B**). Higher concentrations of 13CHD, up to 2.5 mM, did not lead to further increase of fluorescence (**Figure 1A**, p = 0.06–0.99, t-test equal variance, n = 8 replicates). The lowest concentrations of 13CHD that yielded significant induction compared to medium without inducer after 2 h incubation were 0.25 mM for DT022, DT032 and DT038, and 0.5 mM 13CHD for DT016 (**Figure 1B**, inset).

The four third generation (i.e., DT032, DT033, DT035, and DT038) mutants were subsequently used to create four new RMLs, which were screened as before, but this did not lead

TABLE 1 | GPFmut2 fluorescence in *Escherichia coli* expressing wild-type- and mutant-RbsB proteins under uninduced and 13CHD-induced conditions.

Wild-type or Variant	Parental Protein	GFPmut2 uninduced fluorescence[a]	Fold induction[b] 1 mM 1,3-cyclohexanediol	Additional mutation(s)[c]
RbsB	–	**25,226 ± 4,066[d]**	**0.91 ± 0.05**	–
DT016	RbsB	127,887 ± 12,650	1.51 ± 0.02 (Tavares et al., 2019)	[e]
DT020	DT016	**87,877 ± 21,152**	1.48 ± 0.07	V10I[f]
DT021	DT016	**151,009 ± 22,735**	**1.66 ± 0.09**	K206R
DT022	DT016	132,129 ± 25,700	**2.09 ± 0.16**	G89V
DT032	DT022	**95492 ± 34689**	**2.97 ± 0.37**	L170S
DT033	DT022	100,256 ± 50,431	**2.63 ± 0.59**	L201P S207P K250R
DT035	DT022	**95,073 ± 23,566**	**2.60 ± 0.50**	K5N
DT038	DT022	**49,432 ± 13,382**	**3.19 ± 0.48[g]**	L201V

[a] *Mean (±one SD) GFPmut2 fluorescence values of uninduced cultures (n = 8–14 replicates).*
[b] *Mean fold induction ± one SD, as the ratio of mean GFPmut2 fluorescence of induced cultures with 1 mM 1,3-cyclohexanediol, by that of uninduced cultures.*
[c] *Additional mutations in comparison to the parental protein.*
[d] *Values in bold indicate statistically significant fluorescence background and/or fold induction compared to DT016 (p < 0.05, t-test, equal variance).*
[e] *DT016 carries eight mutations compared to wild-type RbsB: F16S, N64V, D89V, R90S, T134A, F164W, F214A, and Q235M.*
[f] *Underlined substitutions are located on the 25 amino acids long signal peptide.*
[g] *Improvement compared to DT016 is the net gain in fold-induction, thus (3.19–1)/(1.51–1) = 4.38.*

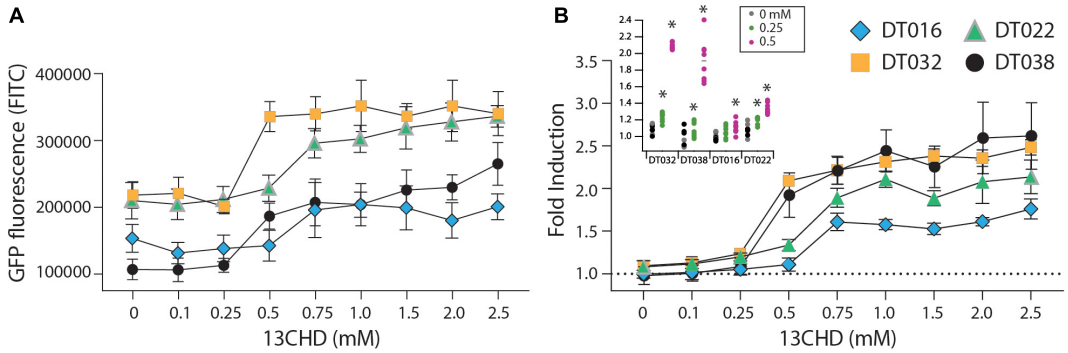

FIGURE 1 | GFPmut2 fluorescence of *Escherichia coli* BW25113 Δ*rbsB* expressing DT016 (blue diamonds), DT022 (light green triangles), DT032 (ochre squares), or DT038 (black circles) in presence of different 13CHD concentrations. **(A)** Average GFPmut2 fluorescence in flow cytometry after 2 h incubation with a range of 13CHD concentrations. **(B)** As **(A)**, but as fold induction compared to uninduced conditions. Each point shows the mean of eight biological replicates (each from a measurement of 100,000 cells). Error-bars indicate calculated *SD* (not visible when inside the symbol). Dashed line represents the non-induced level. Inset in **(B)** Asterisks point to the lowest tested 13CHD concentrations giving a statistically significantly different fluorescent signal compared to the blank control (incubated in absence of any 13CHD, $p < 0.05$, two-sided *t*-test, $n = 8$ replicates).

to isolation of mutant proteins with improved induction with 13CHD (i.e., more than three times GFPmut2 fluorescence increase upon induction compared to uninduced levels). We noted, however, that populations of several mutants displayed double fluorescence levels simultaneously, almost irrespectively of 13CHD presence (**Figure 2**). These subpopulations corresponded to completely uninduced and fully induced fluorescence levels seen from wild-type RbsB with ribose (**Figure 2A**, Low_Pop and High_pop). For example, mutant 1F6 displayed one subpopulation with a mean fluorescence value of 15,000 and a second of 220,000 (**Figure 2B**). The proportion of cells within the low and high subpopulation was approximately 36 and 62%, respectively. Upon 2 h incubation with 1 mM 13CHD the proportion of cells within either subpopulation changed to 25 and 74%, respectively (**Figure 2B**). Similar results were obtained with mutant 2C10, showing a reduction of 8% in the proportion of cells within the low fluorescence subpopulation upon 13CHD induction, and an increase of 9% in the high subpopulation (**Figure 2C**). Mutant 1F8 displayed a different behavior, with an almost equal proportion of cells distributed between the low and high subpopulations under uninduced conditions; but an increase up to 87% within the subpopulation with lowest fluorescence in presence of 13CHD (**Figure 2D**).

Across multiple tests and replicates, the proportions of cells within those subpopulations differed substantially, making it hard to judge whether this was consistent behavior one would expect from an inducible protein. This suggested, therefore, that these mutants had become hypersensitive and spontaneously switched between open (i.e., uninduced signal) and closed (i.e., induced) state at the level of an individual cell.

Positions of 2nd and 3rd Generation Mutations With Improved Induction With 13CHD

The positions of the amino acid substitutions observed in the various new mutants (**Table 1**) were threaded on the closed structure of wild-type RbsB (PDB ID: 2DRI). Six out the seven isolated mutants displayed a single amino acid substitution. Exception was DT033 that displayed three amino acid changes. Mutant DT020 displayed a conservative substitution within the signal peptide (V10I) (**Table 1**). DT021 and DT022 displayed conservative amino acid substitutions K206R and G89V, respectively (**Figure 3A** and **Table 1**). The V89 residue of DT022 is located within the binding pocket, 1.9 Å from the 13CHD molecule (**Figure 3A**). This suggests that the G89V substitution is directly responsible for the 50% increase of GFPmut2 fluorescence upon 13CHD induction, when compared to its parent DT016 (Tavares et al., 2019). Previous studies demonstrated the importance of residue 89 for ligand binding (Vercillo et al., 2007; Reimer et al., 2017; Tavares et al., 2019), suggesting that V89 improves the capacity to bind 13CHD in comparison with G89. Finally, mutation K206R found in DT021 is located in a peripheral turn of the structure (**Figure 3A**).

Two out of the four 3rd generation mutants displayed non-conservative mutations. Notably, DT032 had a leucine at position 170 instead of serine, whereas DT033 displayed a S207P substitution. DT033 showed two conservative mutations (L201P and K250R; **Figure 3A** and **Table 1**). Mutant DT035 again displayed a mutation in the signal peptide (K5N). This and the V10I substitution of DT020 in the signal peptide may have improved the translocation and/or stability of the mutant protein. Of the other five substitutions observed in this 3rd round of evolution, three (L170S, L201V, and K250R) were located outside the binding pocket in three different α-helices of the protein (**Figure 3A**). The two others (K206R and S207P) were localized in a peripheral turn of the protein structure (**Figure 3A**). All of them led to an increase of the fold–induction with 13CHD (**Table 1**). However, their peripheral position suggested they play a role in protein stability and not directly in ligand binding. Interestingly, five out the seven substitutions found in 2nd and 3rd generation mutants localized in the same region of the protein (**Figure 3A**), suggesting that changes in that area improve protein function (e.g., stability or intramolecular hinge movement). Interestingly,

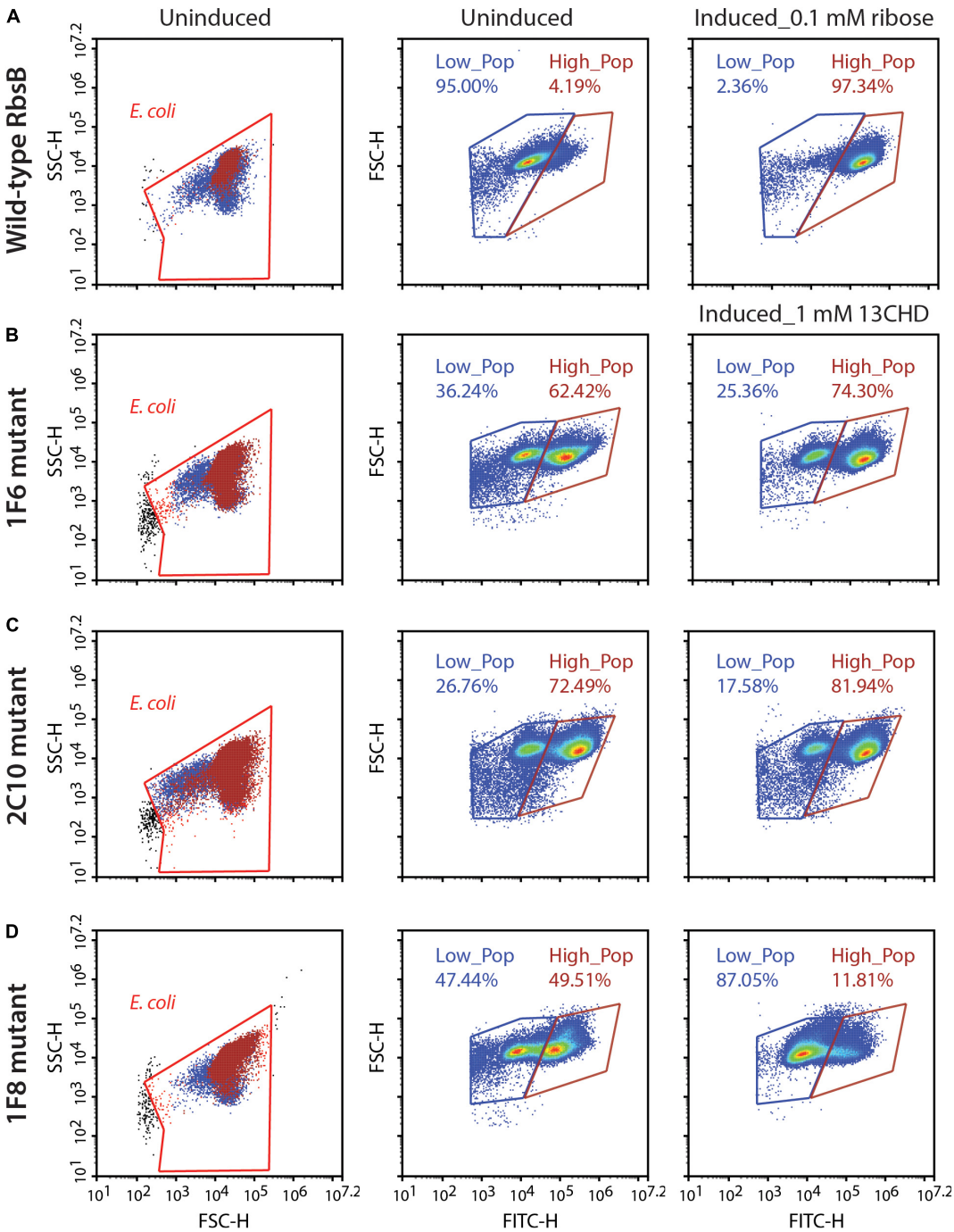

FIGURE 2 | DT038-derivative mutants displaying subpopulations with two fluorescence states. Low_Pop and High_Pop represents cells with low and high fluorescence levels, respectively. Proportions of cells within both gates are indicated. **(A)** Wild-type RbsB uninduced and induced with 0.1 mM. **(B–D)** As **(A)**, but for mutant 1F6, 2C10, and 1F8 induced with 1 mM 13CHD. Each density plot shows 100,000 cells.

leucine at position 201 was substituted twice independently by two different amino acids (i.e., proline and valine), underscoring its critical role. None of the positions recovered in these DT variants for 13CHD binding had been previously described as critical for the various roles of RbsB in a near-complete Ala-substitution scanning (Reimer et al., 2017).

To further infer potential structural changes of observed mutants in comparison to wild-type RbsB, we used Swiss-Model (Guex et al., 2009; Bertoni et al., 2017; Bienert et al., 2017; Waterhouse et al., 2018; Studer et al., 2020), Phyre2 (Kelley et al., 2015) and Missense3D (Ittisoponpisan et al., 2019). Swiss-Model, Phyre2 did not predict any structural differences of the new

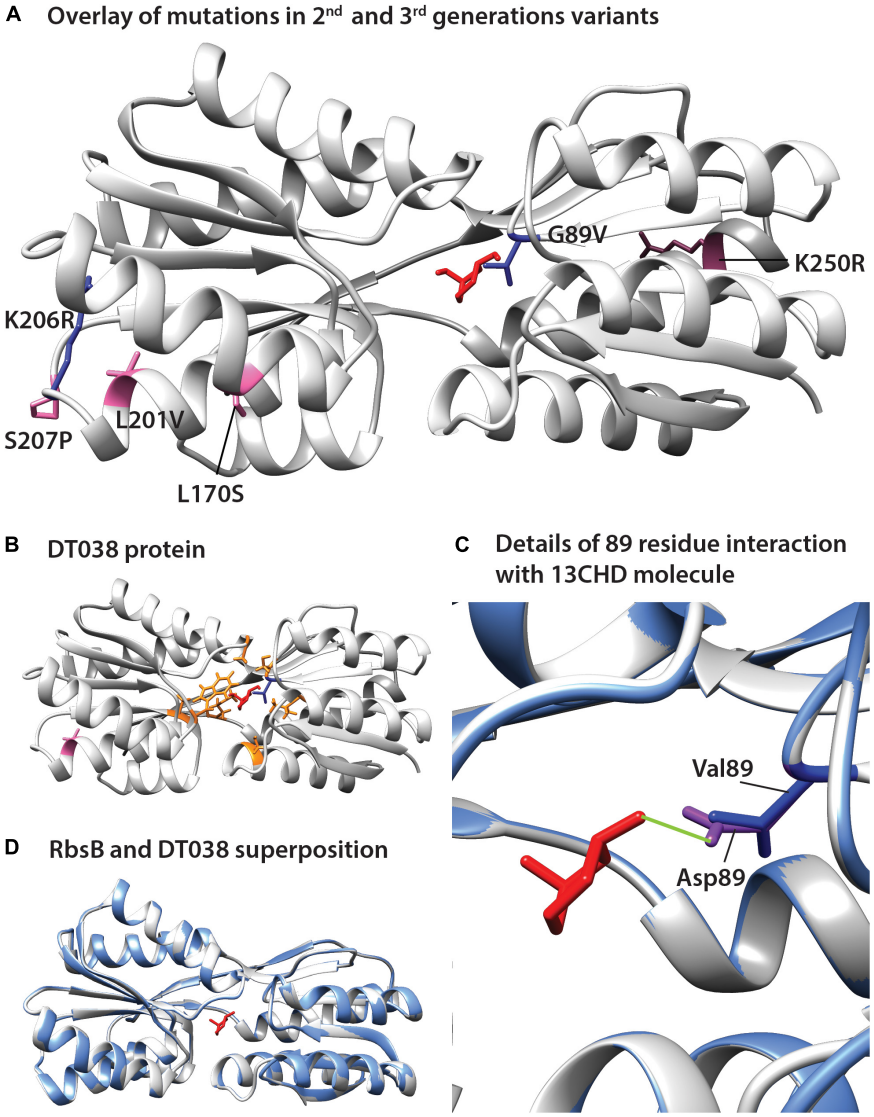

FIGURE 3 | Positions of amino acid substitutions observed in various 13CHD mutants, visualized on the closed structure of wild-type RbsB (PDB ID: 2DRI). **(A)** Mutated residues in 2nd (blue) and 3rd generation mutants (pink). **(B)** Acquired mutations in DT038, seen as a superposition of 1st (orange, in DT016; the original Rosetta designed binding pocket mutations), 2nd (blue, in DT022) and 3rd generation mutations (pink). **(C)** Superposition of wild-type RbsB (PBD ID: 2DRI, blue), and the threaded DT038 structure (light gray). **(D)** Detailed view from **(C)** panel, showing the interaction between ligand and residues located at 89 position. Asp89 of RbsB and Val89 of DT038 are colored in purple and blue, respectively. Light green line indicates a H-bond. Molecular structures of 13CHD (red) are placed in the binding pocket. Signal peptide mutations are not shown on the structure as this is cleaved off.

mutations compared to the closed structure of wild-type RbsB (**Figures 3B,C**, shown for DT038). Analysis of each of the eight amino acid substitutions in DT016 by Missense3D indicated expansion of the binding cavity by F16S and R90S, and H-bond breakage by D89V and T135A. This was expected, since these were designed and engineered ligand binding pocket mutations to accommodate 13CHD. However, none of other four mutations in DT016 were predicted by Missense3D to cause any (individual) structural difference compared to RbsB. Interestingly, the G89V mutation in DT022 compared to DT016 (or D89V compared to wild-type) was predicted to cause further expansion of the ligand binding pocket and to H-bond breakage (**Figure 3D**). This is probably the consequence of replacing a buried amino acid (Gly) by an exposed one (Val). Other individual amino acid substitutions, found in other isolated mutants, were not predicted to cause any structural difference compared to wild-type RbsB, but we acknowledge that Missense3D only tests single substitutions at a time.

DNA Shuffling and Site Saturation Mutagenesis

Rescreening of the 2nd round RML002 and RML016 libraries, led not only to the isolation of the second generation mutants

(i.e., DT020, DT021, and DT022) but to eight more variants as well (**Table 2**). Individual retesting of those eight variants showed no change in the mean fold-induction of GFPmut2 in presence of 1 mM 13CHD compared to DT016 itself (**Table 2**, p = 0.245–0.89, n = 6 replicates). On the other hand, five mutants (named here: 2H2, 7B2, 7B9, 7C5, and 7G4) displayed a lower background fluorescence in uninduced conditions, when compared to DT016 (**Table 2**, p = 0.01–0.00001, n = 6 replicates). The highest background reduction was two-fold, observed in 7G4 mutant (**Table 2**). The lower fluorescence background suggests a better equilibrium between open and closed conformation. The DNA of the eight mutants was then shuffled in the hope to create synergetic effects, but no mutant with improved induction by 13CHD was isolated from this screening.

Computational simulations had previously suggested nine amino acids as being critical for changing the specificity of RbsB protein to 13CHD (Tavares et al., 2019). Two residues were later found by ala-substitution scanning to be important for ribose binding (R141 and D215) (Reimer et al., 2017). We therefore tested whether site-saturation mutagenesis of these residues could further improve DT002 and DT016 variants for 13CHD induction (**Figure 4**). Replacement of R141 and D215 by each of the other 20 possible amino acids was confirmed by sequencing and 250 colonies of each site saturation library were tested individually by flow cytometry for gain of 13CHD induction. None of the tested mutants from the DT002_R141X, DT002_D215X, or DT016_R141X and DT016_D215X libraries showed improved 13CHD induction, compared to parental strains, whereas several were worse. *Inter alia*, this showed that R141 in mutant DT016 can be replaced by a serine without impairing inducibility by 13CHD.

TABLE 2 | List of isolated mutants from RML002 and RML016 2nd round used for DNA shuffling.

RbsB protein	GFPmut2 uninduced fluorescence[a]	Fold induction[b] 1 mM 1,3-cyclohexanediol	New mutation(s)[c]
Wild-type	**25,226 ± 4,066[d]**	**0.91 ± 0.05**	–
DT016	160,622 ± 33,495	1.87 ± 0.26	[e]
2H12	**112,793 ± 16,657**	2.01 ± 0.13	Q80R
3B11	157,805 ± 24,521	1.88 ± 0.13	V17E T58A
5H2	128,273 ± 13,989	1.97 ± 0.11	K29R A214T
6H9	132,217 ± 12,670	1.92 ± 0.1	I132T
7B2	**95,166 ± 8,064**	1.97 ± 0.11	T93M
7B9	**91,342 ± 1,4436**	1.75 ± 0.06	T10A
7C5	**85,631 ± 15,553**	1.89 ± 0.14	N175S K228Q T232D
7G4	**78,653 ± 8,090**	1.81 ± 0.16	N73S

[a] *Mean ± one SD GFPmut2 fluorescence values of uninduced cultures (n = 6–8).*
[b] *Mean fold induction ± one SD, as the ratio of the mean GFPmut2 fluorescence of induced cultures with 1 mM 13CHD and the mean fluorescence of uninduced cultures.*
[c] *Newly observed mutations in comparison to DT016.*
[d] *Values in bold are statistically significantly different from those of DT016 ($p < 0.05$, t-test, equal variance).*
[e] *DT016 carries eight mutations compared to wild-type RbsB: F16S, N64V, D89V, R90S, T134A, F164W, F214A, and Q235M.*

Mutagenesis of Neighboring Residues in DT016

Finally, we tested whether substitutions in the direct neighborhood of the previously engineered ligand binding pocket mutations would affect induction by 13CHD, through synergistic or compensatory effects on the overall protein function or behavior. For this we focused again on DT016, the most promising mutant with newly obtained specificity to 13CHD (Tavares et al., 2019). Next, we designed a strategy to mutate the two amino acids flanking (i.e., those before and after) each of the eight ligand binding pocket mutations of DT016 (**Supplementary Figure 2**). We reconstituted the *dt016* open reading frame in 12 overlapping PCR fragments (**Figure 5A**). PCR primers covered the regions of the eight introduced mutations in DT016 (**Figure 5B**), with flanking amino acids of those being replaced by all other 20 possible amino acids (**Table 3**). The disadvantage of this strategy was that stop codons could not be avoided in primer design. A library with an estimated size of 1×10^6 clones (RML-DT016AA) was screened as before by agarose encapsulation and flow cytometry. As expected, a large fraction of clones carried truncated proteins (75% from 25 randomly picked colonies from the library on plates). None of the clones displayed higher fold induction than DT016 itself. We concluded that this strategy was not worth further pursuing.

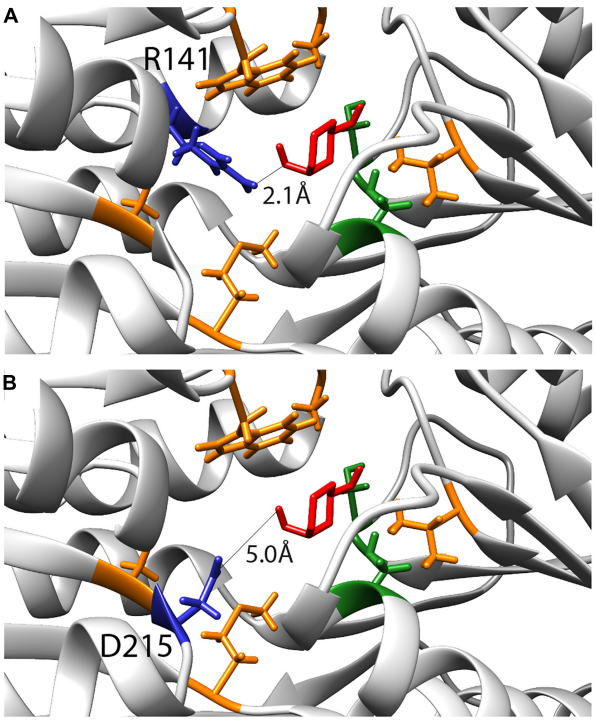

FIGURE 4 | Inferred binding pocket of DT016 in presence of 13CHD (in red) and with the substituted residues for ligand binding color-coded based on characteristics (non-polar- orange; polar- green). **(A)** Arginine at position 141, selected for site saturation mutagenesis, is highlighted in dark blue. Distance between 13CHD molecule and R141 is indicated. **(B)** As for **(A)** but for Aspartic acid at position 215.

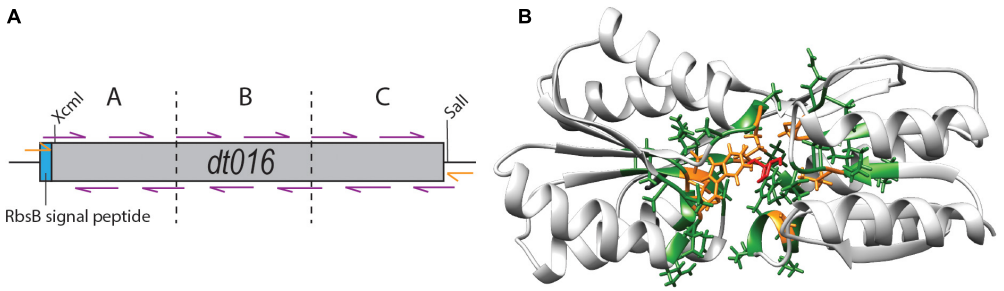

FIGURE 5 | Flanking residue mutagenesis. **(A)** Scheme of the design strategy to reconstitute *dt016* with 12 overlapping primers (purple), positioned at the sites of the previous ligand binding pocket mutations, and each covering the two neighboring codons on each side. The assembly was carried out in three steps (fragments separated by dotted lines) and followed by a final extension reaction with external primers (orange). Gene not drawn to scale. **(B)** Inferred structure of DT016 based on RbsB structure (PDB ID: 2DRI). Molecular structure with 13CHD (red) bound in its pocket. The eight designed substitutions in DT016 are highlighted in orange and flanking residues mutated with this strategy are highlighted in green.

TABLE 3 | Strains used in this study.

Strain	*E. coli* host	Plasmids	Relevant characteristics	References or sources
3044	DH5αλPir		Host for plasmid propagation	Platt et al. (2000)
3671	DH5α	pSTVPAA_mcs	pSTVPAA to clone rbsB and its derivatives	Reimer et al. (2014)
4172	BW25113 ΔrbsB	pSYK1	Host strain containing the Ptac- trzI, PompC- gfpmut2 bioreporter system	Reimer et al. (2014)
4175	BW25113 ΔrbsB	pSTVPAA_rbsB, pSYK1	RbsB expression with signal peptide for periplasmic translocation	Reimer et al. (2014)
5913	BW25113 ΔrbsB	pSTVPAA_DT001, pSYK1	As 4175, but for DT001 mutant protein of RbsB	Tavares et al. (2019)
5903	BW25113 Δ*rbsB*	pSTVPAA_DT002, pSYK1	As 4175, but for DT002 mutant protein of RbsB	Tavares et al. (2019)
5904	BW25113 Δ*rbsB*	pSTVPAA_DT011, pSYK1	As 4175, but for DT011 mutant protein of RbsB	Tavares et al. (2019)
5905	BW25113 Δ*rbsB*	pSTVPAA_DT013, pSYK1	As 4175, but for DT013 mutant protein of RbsB	Tavares et al. (2019)
5906	BW25113 Δ*rbsB*	pSTVPAA_DT015, pSYK1	As 4175, but for DT015 mutant protein of RbsB	Tavares et al. (2019)
5907	BW25113 Δ*rbsB*	pSTVPAA_DT016, pSYK1	As 4175, but for DT016 mutant protein of RbsB	Tavares et al. (2019)
7241	BW25113 Δ*rbsB*	pSTVPAA_DT020, pSYK1	As 4175, but for DT020 mutant protein of RbsB	This work
7242	BW25113 Δ*rbsB*	pSTVPAA_DT021, pSYK1	As 4175, but for DT021 mutant protein of RbsB	This work
7243	BW25113 Δ*rbsB*	pSTVPAA_DT022, pSYK1	As 4175, but for DT022 mutant protein of RbsB	This work
7244	BW25113 Δ*rbsB*	pSTVPAA_DT032, pSYK1	As 4175, but for DT032 mutant protein of RbsB	This work
7245	BW25113 Δ*rbsB*	pSTVPAA_DT033, pSYK1	As 4175, but for DT033 mutant protein of RbsB	This work
7246	BW25113 Δ*rbsB*	pSTVPAA_DT035, pSYK1	As 4175, but for DT035 mutant protein of RbsB	This work
7247	BW25113 Δ*rbsB*	pSTVPAA_DT038, pSYK1	As 4175, but for DT038 mutant protein of RbsB	This work
2H12	BW25113 Δ*rbsB*	pSTVPAA_2H12, pSYK1	As 4175, but for 2H12 mutant protein of RbsB	This work
3B11	BW25113 Δ*rbsB*	pSTVPAA_3B11, pSYK1	As 4175, but for 3B11mutant protein of RbsB	This work
5H2	BW25113 Δ*rbsB*	pSTVPAA_5H2, pSYK1	As 4175, but for 5H2 mutant protein of RbsB	This work
6H9	BW25113 Δ*rbsB*	pSTVPAA_6H9, pSYK1	As 4175, but for 6H9 mutant protein of RbsB	This work
7B2	BW25113 Δ*rbsB*	pSTVPAA_7B2, pSYK1	As 4175, but for 7B2 mutant protein of RbsB	This work
7B9	BW25113 Δ*rbsB*	pSTVPAA_7B9, pSYK1	As 4175, but for 7B9 mutant protein of RbsB	This work
7C5	BW25113 Δ*rbsB*	pSTVPAA_7C5, pSYK1	As 4175, but for 7C5 mutant protein of RbsB	This work
7G4	BW25113 Δ*rbsB*	pSTVPAA_7G4, pSYK1	As 4175, but for 7G4 mutant protein of RbsB	This work

DISCUSSION

Periplasmic binding proteins have been deployed as a starting point to design new receptor proteins (Dwyer and Hellinga, 2004). Despite the vast knowledge on PBPs structures and their natural ligands (Berntsson et al., 2010), the successful design of new ligand binding domains has been very limited so far (Schreier et al., 2009; Yang and Lai, 2017). Introducing amino acid substitutions in a protein is challenging, since they can easily lead to an abnormal function or behavior of the mutated protein (Reimer et al., 2017). In a previous study nine residues were identified and substituted in the binding pocket of RbsB, with the goal to change the binding specificity from the natural ligand ribose to the non-natural compound 13CHD (Tavares et al., 2019). Despite the modest increase of induction (up to 1.5-fold with 13CHD), six mutant proteins without ribose recognition but with 13CHD binding were isolated. Relatively poor induction had been attributed to mutant protein instability, poor translocation, and/or misfolding (Tavares et al., 2019).

The goal here was to produce and select compensatory mutations by random or semi-random approaches, which might either have a stabilizing effect or further improve 13CHD

ligand binding, or both. We focused on the previously isolated mutants, which we used as scaffolds for mutagenesis. Several rounds of random mutagenesis and increasing selectivity of sorting of bead-grown microcolonies induced with 13CHD, led to recovery of a few mutants with consistently higher induction of GFPmut2 fluorescence than their parental strains (up to 3.2-fold at 1 mM 13CHD). As these mutants carried mostly substitutions outside the direct ligand binding pocket, we assume that they are compensatory mutations that improve functions other than ligand binding itself, for example, L170S in DT032 or L201V in DT038.

In order to maximize our chances to isolate an improved variant for 13CHD detection, we used different mutagenesis approaches to create genetic variability. Our semi-random approaches did not produce the expected results, since no improved variant was isolated from the created libraries. Site saturation mutagenesis of R141 and D215 residues on DT002 and DT016 resulted in decrease of the capacity for induction by 13CHD, except for a R141S substitution in DT016 that did not affect inducibility. This indicated that we could not improve the 13CHD induction by replacing R141 and D215 residues; in contrast, it showed that their presence is essential for 13CHD binding and signaling. The importance of both R141 and D215 residues in RbsB for ribose induction and signaling (Reimer et al., 2017) and for ligand binding (D215) had been previously demonstrated (Vercillo et al., 2007). Also DNA shuffling did not lead to isolation of mutants with potential synergistic improvements, although background reduction in absence of inducer was observed (**Table 2**). Random mutation of the 32 residues flanking the nine substitutions engineered for 13CHD ligand binding did not yield improved variants either, possibly because of the high percentage of variants with a truncated protein. Some variants displayed a comparable induction level to their parent DT016 (around 1.5 times). However, given the high number of substitutions in these variants (up to 32 amino acid substitutions), an interpretation of their effect was impossible. These results indicated that changing several parts of the RbsB-mutant proteins at the same time may not be the best way to find variants with improved function. Introducing multiple mutations increases the probability to find proteins with improved capacities, but at the same time increases the chances to introduce mutations that may impair the protein function. This creates an important trade-off, and has to be considered each time when designing and implementing a mutagenesis strategy.

In contrast, random mutagenesis across the complete gene variants led to the isolation of seven mutants with significantly improved 13CHD inducibility, two of which with 4–4.5-fold improvement of induction. This was accomplished by screening of relatively large libraries on microcolonies grown in beads, under different screening thresholds and several rounds of repetition. We acknowledge that FACS thresholding in such screening is a difficult point, because distinguishing between fluorescence outliers of false-positive clones and true positive inducible ones can be subjective. In less restrictive sortings, all beads above the 98th fluorescence percentile of the 13CHD induced library were collected, re-used as template for a new library, from which we recovered the top 0.1% fluorescence beads. This strategy led to isolation of three variants with improved induction with 13CHD. In the more restrictive sorting, only beads with a fluorescence higher than any bead under uninduced conditions were recovered. This resulted in isolation of four mutants with up to 3.2-fold induction by 13CHD. Since both strategies allowed us to isolate mutants with improved 13CHD detection, we conclude that the restrictive sorting is a better strategy, partly because of the time investment and downstream screening of individual clones. A disadvantage of the restrictive strategy is that mutants are missed that have low fluorescence background under uninduced conditions and intermediate fluorescence upon induction (i.e., a fluorescence signal less than the maximum observed in the uninduced library). Alternatively, one could try to "bin" mutants in different fluorescence categories in the hope of finding some with lower fluorescence backgrounds and still some induction. The difficulty is that *a priori* the evolutionary path of a variant highly inducible by 13CHD is not known and may pass through intermediates with high uninduced levels to regain background, or through those with low uninduced levels and gain specificity (Romero and Arnold, 2009; Tracewell and Arnold, 2009; Zheng et al., 2020). Multiple rounds of mutagenesis thus allowed to improve 13CHD detection in a step-by-step manner. This suggests that further rounds of random mutagenesis could eventually lead to the isolation of a variant with similar binding capacity to 13CHD as wild-type RbsB toward ribose (13 fold) (Tavares et al., 2019), although we could not achieve that here. Some studies show that multiple rounds of evolution are needed to improve a specific protein ability without impairing the protein (Brustad and Arnold, 2011).

What can we conclude from the obtained DT variants in terms of amino acid substitution effects? Two mutants (DT020 and DT035) displayed an amino acid substitution in the signal peptide (V10I and K5N). The improved 13CHD induction might have been due to higher periplasmic protein levels, being the result of a positive effect on peptide recognition by SecB chaperone, responsible for presenting RbsB to the translocation channel, and or improved stability. Only one variant (DT022) carried a substitution (G89V) in the binding pocket (**Figures 3A,D**). This residue is less than 2 Å away from the inferred position of 13CHD and previous studies demonstrated the importance of residue 89 for ligand binding (Vercillo et al., 2007; Reimer et al., 2017; Tavares et al., 2019). An exposed valine residue at this position thus might improve 13CHD binding, yielding a 50% higher fold induction when compared with parent DT016 (**Table 1**). All other mutations were found outside the binding cavity, and we assume that they must have improved other aspects of protein functionality than ligand binding itself, although we did not test this specifically by biochemical methods on purified protein. This could affect, for example, protein stability or improved hinge flexibility, or binding to the chemoreceptor Trz1. Five out the seven mutations were located in the same peripheral region of the protein (**Figure 3A**), but none concerned positions previously implicated in RbsB functioning by Ala-substitution scanning (Reimer et al., 2017). Leucine at position 201 was replaced by two other non-polar residues in two different isolated mutants and neighboring residues K206 and S207 were

replaced by arginine and proline, respectively. The concentration of observed mutations in this region suggests that previous introduced mutations may have disturbed this region of the protein and compensatory mutations were needed. This specific region of the protein, therefore, could be a promising target for future rounds of mutagenesis, aiming to find variants with better overall function. Importantly, the new variants were not only more highly induced by 13CHD, but also displayed reduced fluorescence background, especially DT032, DT035, and DT038. This is further evidence that these mutations are compensatory and improve the overall functionality of the proteins in the bioreporter signaling cascade.

Creation of new ligand-binding cavities in PBPs had been heralded more than a decade ago as one of the key areas of advance for computational protein design (Looger et al., 2003), but more recent *de novo* design of protein (and peptide) structure design have focused more on small-molecule-binding proteins (Polizzi and DeGrado, 2020), switchable/allosteric capacity (Langan et al., 2019), protein folding (Rocklin et al., 2017) and epitope-scaffolds design (Sesterhenn et al., 2020). Much of the initial claimed successes of PBP ligand pocket engineering has not held up under the scrutiny of independent repetitions (Schreier et al., 2009; Reimer et al., 2014). More recent advances have been reported that have shown grafting of existing ligand pockets in PBPs, and a single study of a *de novo* design achieving marginal 13CHD binding (Scheib et al., 2014; Banda-Vazquez et al., 2018; Tavares et al., 2019). It might thus well be that, in contrast to the original assumption of a wide protein family with known crystal structures of open and closed configurations, PBPs are actually particularly difficult to engineer. The reasons may be that PBPs need an inherent intramolecular protein movement between open and closed configuration and have manifold functional constraints, such as ligand binding, binding to the receptor, or translocation. Current ligand pocket predictions do not take the other constraints into consideration, which make complete rational computational design challenging.

For example, in the RbsB-based bioreporter configuration wild-type and mutant-RbsB proteins have to be expressed and translocated to the periplasmic space. Once in the periplasmic they recognize and bind their ligand, leading to a conformational change of the protein (Boas and Harbury, 2008; Stank et al., 2016). Subsequently, the closed form of the protein binds the hybrid Trz1 receptor, starting a phosphorylation cascade that in the end leads to induction of GFPmut2 expression (Reimer et al., 2014). It is important to understand that if an introduced mutation affects any aspect of these steps the final outcome (i.e., GFPmut2 signal) is affected. The transition between open and closed conformation is extremely important for PBPs with bilobal structure such as RbsB. It is assumed that PBPs in absence of ligand can be found in a dynamic equilibrium of open and closed state (Ravindranathan et al., 2005; Schreier et al., 2009), which is important for their function. Similar characteristics are observed in other PBPs, for example in the closely related galactose-binding protein of *E. coli* (Unione et al., 2016). In presence of the proper ligand, the closed form is stabilized (Schreier et al., 2009) and, like in case of RbsB can present the ligand molecule (ribose) to either the chemoreceptor (i.e., Trg and Trz1) or to ribose transport channels (Binnie et al., 1992; Riley, 1993; Stewart and Hermodson, 2003). We observed that introduced mutations can block RbsB variants in either of the two states, and consequently, disable its function to bind the ligand and trigger the bioreporter system, or trigger the receptor signaling cascade without binding the ligand. We also observed RbsB-DT variants that in the *E. coli* bioreporter strain caused "stable" double populations with different GFPmut2 fluorescence intensities both in absence and in presence of inducer. This is in contrast to wild-type RbsB behavior, which (despite reported open-closed form dynamics in absence of ligand) in absence of ribose results in coherent low reporter output and in the presence of ribose in coherent high fluorescence. This suggests that the time-scale of the dynamics may be affected by the introduced mutations, blocking the DT variants in either open or closed form long enough to trigger (or not) the bioreporter signaling cascade leading to GFP expression. This is supported by the fact that these subpopulations corresponded to completely uninduced and fully induced fluorescence levels seen from wild-type RbsB with ribose (**Figure 2**). A small percentage of the low fluorescence population shifts to high fluorescence upon induction, indicating that ligand-binding is still affecting the transition states, but is insufficiently discriminating between the two (**Figures 2B,C**). The implications of individual and combinations of secondary mutations for specific aspects of RbsB-DT variant functionality, e.g., translocation, stability, intermolecular movement, folding, ligand or receptor binding, however, can only be derived from more precise biochemical techniques with purified protein.

In conclusion, the results obtained in this study showed that it is possible to improve the signaling performance of previously designed RbsB mutants with *de novo* ligand binding pockets using random mutagenesis. The two most promising mutants DT032 and DT038 displayed a 4–4.5-fold improvement in induction to 13CHD, mostly as a result of background reduction in absence of inducer (**Table 1**). The variants react in a dose-dependent manner, with a lower detection limit around 0.25 mM 13CHD. This study demonstrates the principle that new PBP ligand-binding domains can be engineered using the RbsB signal transduction bioreporter platform and that more work is needed to achieve a ligand detection limit that approaches the wild-type RbsB sensor for ribose, which demonstrates a 13-fold fluorescence induction and 50 nM detection limit (Reimer et al., 2014; Tavares et al., 2019).

MATERIALS AND METHODS

Bacterial Strains and Culture Conditions

Expression of the RbsB-Trz1-*ompCp-gfpmut2* signaling chain (or the RbsB variants) was tested in *E. coli* BW25113 Δ*rbsB* as host. In this case, cells were cultured in minimal medium (MM) supplemented with 20 mM fumarate. For selection of mutants by FACS, cells were first grown within alginate beads in low phosphate minimal medium (MM LP) supplemented with 20 mM fumarate and appropriate antibiotics to produce microcolonies, as described previously (Tavares et al., 2019). The cells-in-beads were then induced with 0.1 mM ribose

or 1 mM 1,3-cyclohexanediol (13CHD) for 2 h, as described previously (Tavares et al., 2019). *Escherichia coli* DH5α cells were used for cloning and plasmid propagation. Random libraries were transformed into ElectroMAX DH10B T1 Phage-Resistant competent cells (Thermofisher).

All strains used in this study are listed in **Table 3**.

Random Mutagenesis Libraries and Plasmid Construction

Mutations in the *rbsB* gene or its *dt* variants were generated by error-prone PCR (ep-PCR). Gene variants were amplified by primers flanking the coding sequence in the plasmids pSTVPAA-DTxxx and located up- and downstream of the *Sal*I and *Nde*I sites (**Supplementary Figure 1**). Error-prone-PCR reactions were carried out with 4 ng of DNA template in presence of varying $MnCl_2$ concentrations (0.025–0.06 mM). Six reactions were prepared simultaneously to average stochastic biases. After an initial denaturation step of 10 min at 94°C, the following steps were repeated for 25 cycles: 1 min at 94°C, 1 min at 70°C, and 1.5 min at 72°C, followed by an extension of 10 min at 72°C. Amplicons were then visualized by agarose electrophoresis, and products of around 1 kb were excised, pooled and purified. Purified PCR products and pSTVPAA plasmids were digested with *Sal*I and *Nde*I at 37°C and 300 rpm for 45 min. Plasmid self-ligation was prevented by treating the digested plasmid with Shrimp Alkaline Phosphatase (rSAP, New Englang Biolabds). The digestion products were visualized by agarose electrophoresis, and the correctly sized digested bands were excised from the gel and purified.

Plasmid and amplicon fragments were ligated with T4 DNA ligase using a ratio of 1:2 vector to insert. The ligation mixture was incubated overnight at room temperature, and aliquots of 100 ng DNA were electro-transformed into ElectroMAX DH10B cells. Cells were recovered after the electroporation by addition of 1 mL of SOC medium, pooled from five separate reactions and incubated for 1 h 30 at 37°C, 225 rpm. Small proportions of these mixtures where plated on LB agar (Cm, chloramphenicol at 30 $\mu g\ ml^{-1}$) plates to estimate the number of colony forming units in the libraries. The remainder was cultured *en masse* in 200 ml LB medium (with Cm), which was used to isolate and purify a plasmid-library pool. Aliquots of 1.6 mL of the grown culture were stored in 15% *(v/v)* glycerol at −80°C. Five aliquots of each 100 ng of purified pSTVPAA-mutant plasmid pool were then transformed into the bioreporter strain *E. coli* BW25113 Δ*rbsB*, for testing of ribose- and 13CHD-dependent expression of GFPmut2. Library aliquots were again stored at −80°C. Error-prone-PCR in presence of different $MnCl_2$ concentrations (0.025–0.06 mM) resulted in between 1 and 3 mutations per 1,000 bp.

DNA Shuffling and Site Saturation Mutagenesis

As an alternative to error-prone-PCR we used DNA shuffling to create new *rbsB* variants. For this we used eight *rbsB* variants as template (**Table 2**), which were amplified by PCR using primers outside the coding regions and beyond the *Xcm*I and *Sal*I sites (**Supplementary Figure 1** and **Table 4**). PCR-amplified templates (200 ng each) were mixed and digested with 0.5 U of DNase I for 3 min at 15°C, after which the reaction was inactivated at 80°C for 10 min. Aliquots of 200 ng of fragmented DNA were then reassembled by PCR in progressive hybridization in presence of 2.5 U of GoTaq polymerase (Thermofisher) and 200 μM of each dNTP in the following temperature cycles. After an initial denaturation period of 2 min at 94°C, the following steps were repeated for 35 cycles: 40s at 94°C, 90s from 65 to 41°C in intervals of 3°C and 90s at 68°C, followed by a final 30 min period at 68°C. The PCR reassembly products were next amplified with primers located inside the previous ones (**Supplementary Figure 1** and **Table 4**), visualized by agarose electrophoresis, after which 1-kb DNA bands were isolated and purified. These products were digested with *Xcm*I and *Sal*I and ligated to pSTVPAA digested with the same enzymes. Ligation mixture aliquots of 100 ng each were then transformed into the bioreporter strain *E. coli* BW25113 Δ*rbsB*.

Positions R141 and D215 in the DT002 and DT016 were changed by site-saturation mutagenesis. For this, the entire plasmid(s) pSTVPAA-DT002 or −016 (5 ng) was amplified by Q5 High-Fidelity DNA polymerase using overlapping but reverse complementary primers with ambiguous bases at the desired positions (**Figure 4** and **Table 4**). PCR products were digested with *Dpn*I to remove template DNA and after enzyme inactivation were directly transformed into the bioreporter strain *E. coli* BW25113 Δ*rbsB*. Variant genes were confirmed by sequencing.

Mutagenesis of Neighboring Residues in DT016

In order to reconstitute the *rbsB* gene 12 overlapping primers were designed (**Table 5**). Assembly of the 12 designed primers was carried out in two steps. In the first step, primers were divided in three independent annealing groups (**Figure 5A**). PCR for every group was performed with 200 μM of dNTPs, 50 nM of each primer and 0.02 U/μL of Q5 High-Fidelity DNA polymerase. After an initial denaturation period of 30 s at 98°C, the following steps were repeated for 10 cycles: 10 s at 98°C, 15 s at 45°C, and 20 s at 72°C, followed by a final 2 min period at 72°C. In the second step, 2 μL of the three independent reactions were mixed with 200 μM of dNTPs and 0.02 U/μL of Q5 High-Fidelity DNA polymerase (same PCR conditions as in step1). PCR products were then finally extended with external primers, 1 μL of the 2nd assembly reaction was amplified by PCR and reactions were performed in triplicate to remove any bias. After an initial denaturation period of 30 s at 98°C, the following steps were repeated for 35 cycles: 10 s at 98°C, 30 s at 68°C, and 30 s at 72°C, followed by a final 5 min period at 72°C. Amplified products were visualized by agarose electrophoresis and 1 kb DNA bands were isolated and purified. Final products were digested with *Xcm*I and *Sal*I and ligated to pSTVPAA digested with same enzymes. After overnight ligation with T4 DNA ligase, D5Hα cells were transformed with 100 ng of DNA for plasmid replication. After rescue a small percentage of cells were plated and were sent for sequencing to estimate library size and variability.

TABLE 4 | List of primers used to introduce new mutations in RbsB-derivate proteins.

Mutagenesis Technique	Target	Primers	DNA sequence (5′–3′)
DNA shuffling	*rbsB* (outer primers)	190101 F	CAGCTGGCGAAAGGGGGATGTG
		130401 R	CTGAGCACATCAGCAGGAC
	rbsB (inner primers)	160401 F	CACGACGTTGTAAAACGACGGCC
		190102 R	CTGGCTACCCTGGTTTCCGCTG
Site saturation mutagenesis	pSTVPAA-DT002R141X	180901 F	GAAGCCTTCGCCNNNTTCACGGGCTGCGGACGCACC[a]
		180702 R	GCAGCCCGTGAANNNGGCGAAGGCTTCCAGCAGGCC
	pSTVPAA-DT002D215x	180705 F	ATCCGGTGTACCNNNAGCTCCGACGACCATCACATC
		180706 R	GTCGTCGGATCGNNNGGTACACCGGATGGCGAAAAA
	pSTVPAA-DT016R141X	180901 F	GAAGCCTTCGCCNNNTTCACGGGCTGCGGACGCACC
		180702 R	GCAGCCCGTGAANNNGGCGAAGGCTTCCAGCAGGCC
	pSTVPAA-DT016D215x	180901 F	ATCCGGTGTACCNNNCGCTCCGACGACCATCACATC
		180708 R	GTCGTCGGAGCGNNNGGTACACCGGATGGCGAAAAA

[a]*NNN indicates mutated positions for production of the libraries.*

TABLE 5 | List of primers used to introduce new mutations close to pre-existing mutations on DT016 protein.

Primers	Target, assembly reaction	DNA sequence (5′–3′)
190201 For	*dt016* gene, 1st assembly - reaction A	ATGGCAAAAGACACCATCGCGCTGGTGGTCTCCACGCTTAACAACNNNNNNAGCNNNNNNCTGAAA GATGGCGCGCAG[a]
190202 Rev	*dt016* gene, 1st assembly - reaction A	TCGCCGGGTTGTTCTGGGAGTCCAGCACCACCAGGTTATAGCCAAGTTTATCCGCCTCTTTCTGCGC GCCATCTTTCAGNNNNNNGCTNNNNNNGTTGTTAAGCGTGGAG
190203 For	*dt016* gene, 1st assembly - reaction A	AGAACAACCCGGCGAAAGAGCTGGCGAACGTGCAGGACTTAACCGTTCGCGGCACAAAAATTCTGN NNNNNGTGNNNNNNGACTCC
190204 Rev	*dt016* gene, 1st assembly - reaction A	ACCTTTCGTNNNNNNGCTGCCNNNNNNGATAACCGGGATGTTCGCCTGGTTAGCCATCTTCACAGCA TTACCCACTGCGTCGGAGTCNNNNNNCACNNNNNNCAGAATTTTTGT
190205 For	*dt016* gene, 1st assembly - reaction B	TCCCGGTTATCNNNNNNGGCAGCNNNNNNACGAAAGGTGAAGTGGTGAGCCACATTGCTTCTGATAA CGTACTGGGCGGCAAAATCGCTGGTGATTACATCGCG
190206 Rev	*dt016* gene, 1st assembly - reaction B	ACGTTCACGGGCNNNNNNCGCNNNNNNAATGCCTTGCAGCTCGATAACTTTGGCACCTTCACCCGC TTTCTTCGCGATGTAATCACCA
190207 For	*dt016* gene, 1st assembly - reaction B	AGGCATTNNNNNNGCGNNNNNNGCCCGTGAACGTGGCGAAGGCTTCCAGCAGGCCGTTGCTGCTC ACAAGTTTAATGTTCTTGCCAGCCAGCCANNNNNNTGGNNNNNNATTAAAGGT
190208 Rev	*dt016* gene, 1st assembly - reaction B	CCCAGCGCCATNNNNNNGTTNNNNNNGAATACAGCCTGAACATCCGGATGAGCGGTCAACAGGTTC TGCATTACGTTCAAACCTTTAATNNNNNNCCANNNNNNTGGCTGGCTGGC
190209 For	*dt016* gene, 1st assembly - reaction C	GGCTGTATTCNNNNNNAACNNNNNNATGGCGCTGGGCGCGCTGCGCGCACTGCAAACTGCCGGTA AATCGGATGTGATGGTCNNNNNNGCGNNNNNNACACCGGATGGCGA
190210 Rev	*dt016* gene, 1st assembly - reaction C	AATCTGATCNNNNNNCATNNNNNNAGTCGCTGCTAGTTTGCCATCATTCACCGCTTTTTCGCCATCCG GTGTNNNNNNCGCNNNNNNGACCATCACATC
190211 For	*dt016* gene, 1st assembly - reaction C	AGCAGCGACTNNNNNNATGNNNNNNGATCAGATTGGCGCGAAAGGCGTCGAAACCGCAGATAAAGT GCTGAAAGGCGAGAAAGTTCAGGCTAAG
190212 Rev	*dt016* gene, 1st assembly - reaction C	CAAGCTTGCATGCCTGCAGGTCGACTCAGTGGTGGTGGTGGTGGTGGAGCTGCTTAACAACCAGTTT CAGATCAACCGGATACTTAGCCTGAACTTT
190301 For	pSTVPAA before *dt016 gene*, final extension	TGCGAATGCGATGGCAAAAGACACCATCGC
190302 Rev	pSTVPAA after *dt016 gene*, final extension	ACGGCCAGTGCCAAGCTTGCATGCCTGCAGG

[a]*NNN indicates positions for introduction of random amino acids.*

RbsB-Based Bioreporters Assays

RbsB- and DT-based libraries in *E. coli,* or single purified clones were screened for GFPmut2 expression by FACS and/or flow cytometry, as described in detail previously (Tavares et al., 2019). In short, cells were encapsulated and grown to microcolonies in alginate beads, before induction. Beads (microcolonies) expressing higher GFPmut2 signal (measured in the FITC-H channel of the instrument) than the set thresholds were sorted and collected in tubes containing 1 ml LB medium supplemented with Amp and Cm. Sorted mutants were regrown and re-screened either as alginate-bead mixtures or as pure cultures in 96-well plates (in at least eight individually grown replicates). Media, incubation conditions, experiments and instruments details are explained previously (Tavares et al., 2019).

Statistical Analysis

Flow cytometry induction of GFPmut2 in *E. coli* cultures was measured in multiple independently grown biological replicates (n = 6–14). Induction is then expressed as the ratio of the mean GFPmut2 fluorescence of induced cultures by that of their uninduced (split) halves. Differences among the mean GFPmut2 uninduced fluorescence and fold induction were tested using Student's t-test.

Structure Threading and Analysis

Threaded structures of RbsB variants were determined with Swiss-Model (Guex et al., 2009; Bertoni et al., 2017; Bienert et al., 2017; Waterhouse et al., 2018; Studer et al., 2020) and Phyre2 (Kelley et al., 2015), with wild-type RbsB structure (PDB ID: 2DRI) as scaffold. Structural superpositions and distance analysis were calculated with UCSF Chimera (Pettersen et al., 2004).

DATA AVAILABILITY STATEMENT

The original contributions presented in the study are included in the article/**Supplementary Material**, further inquiries can be directed to the corresponding authors.

AUTHOR CONTRIBUTIONS

DT carried out all the experiments. DT and JM analyzed data and wrote the main text. Both authors contributed to the article and approved the submitted version.

FUNDING

This work was supported by grants 244405 (Biomonar) and OCEAN-2013-614010 (BRAAVOO) from the European Seventh Framework Program (FP7).

ACKNOWLEDGMENTS

We thank Julien Dénéréaz, Ludivine Jotterand, Thibaut Laurent, Valentina Benigno, Maxime Brunner, and Cédric Schneider for helping with library preparations, cloning and flow cytometry screening.

SUPPLEMENTARY MATERIAL

The Supplementary Material for this article can be found online at: https://www.frontiersin.org/articles/10.3389/fbioe.2021.705534/full#supplementary-material

REFERENCES

Amiss, T. J., Sherman, D. B., Nycz, C. M., Andaluz, S. A., and Pitner, J. B. (2007). Engineering and rapid selection of a low-affinity glucose/galactose-binding protein for a glucose biosensor. *Protein Sci.* 16, 2350–2359. doi: 10.1110/ps.073119507

Antunes, M. S., Morey, K. J., Smith, J. J., Albrecht, K. D., Bowen, T. A., Zdunek, J. K., et al. (2011). Programmable ligand detection system in plants through a synthetic signal transduction pathway. *PLoS One* 6:e16292. doi: 10.1371/journal.pone.0016292

Banda-Vazquez, J., Shanmugaratnam, S., Rodriguez-Sotres, R., Torres-Larios, A., Hocker, B., and Sosa-Peinado, A. (2018). Redesign of LAOBP to bind novel l-amino acid ligands. *Protein Sci.* 27, 957–968. doi: 10.1002/pro.3403

Baumgartner, J. W., Kim, C., Brissette, R. E., Inouye, M., Park, C., and Hazelbauer, G. L. (1994). Transmembrane signalling by a hybrid protein: communication from the domain of chemoreceptor Trg that recognizes sugar-binding proteins to the kinase/phosphatase domain of osmosensor EnvZ. *J. Bacteriol.* 176, 1157–1163.

Berntsson, R. P. A., Smits, S. H. J., Schmitt, L., Slotboom, D.-J., and Poolman, B. (2010). A structural classification of substrate-binding proteins. *FEBS Lett.* 584, 2606–2617. doi: 10.1016/j.febslet.2010.04.043

Bertoni, M., Kiefer, F., Biasini, M., Bordoli, L., and Schwede, T. (2017). Modeling protein quaternary structure of homo- and hetero-oligomers beyond binary interactions by homology. *Sci. Rep.* 7:10480. doi: 10.1038/s41598-017-09654-8

Bienert, S., Waterhouse, A., de Beer, T. A., Tauriello, G., Studer, G., Bordoli, L., et al. (2017). The SWISS-MODEL Repository-new features and functionality. *Nucleic Acids Res.* 45, D313–D319. doi: 10.1093/nar/gkw1132

Binnie, R. A., Zhang, H., Mowbray, S., and Hermodson, M. A. (1992). Functional mapping of the surface of *Escherichia coli* ribose-binding protein: mutations that affect chemotaxis and transport. *Protein Sci.* 1, 1642–1651. doi: 10.1002/pro.5560011212

Björkman, A. J., and Mowbray, S. L. (1998). Multiple open forms of ribose-binding protein trace the path of its conformational change. *J. Mol. Biol.* 279, 651–664. doi: 10.1006/jmbi.1998.1785

Boas, F. E., and Harbury, P. B. (2008). Design of protein-ligand binding based on the molecular- mechanics energy model. *J. Mol. Biol.* 380, 415–424.

Brustad, E. M., and Arnold, F. H. (2011). Optimizing non-natural protein function with directed evolution. *Curr. Opin. Chem. Biol.* 15, 201–210. doi: 10.1016/j.cbpa.2010.11.020

Chu Byron, C. H., and Vogel, H. J. (2011). A structural and functional analysis of type III periplasmic and substrate binding proteins: their role in bacterial siderophore and heme transport. *Biol. Chemvol.* 392, 39–52.

Dwyer, M. A., and Hellinga, H. W. (2004). Periplasmic binding proteins: a versatile superfamily for protein engineering. *Curr. Opin. Struct. Biol.* 14, 495–504. doi: 10.1016/j.sbi.2004.07.004

Edwards, K. A. (2021). Periplasmic-binding protein-based biosensors and bioanalytical assay platforms: advances, considerations, and strategies for optimal utility. *Talanta Open* 3:100038. doi: 10.1016/j.talo.2021.100038

Guex, N., Peitsch, M. C., and Schwede, T. (2009). Automated comparative protein structure modeling with SWISS-MODEL and Swiss-PdbViewer: a historical perspective. *Electrophoresis* 30(Suppl. 1), S162–S173. doi: 10.1002/elps.200900140

Ittisoponpisan, S., Islam, S. A., Khanna, T., Alhuzimi, E., David, A., and Sternberg, M. J. E. (2019). Can predicted protein 3D structures provide reliable insights into whether missense variants are disease associated? *J. Mol. Biol.* 431, 2197–2212. doi: 10.1016/j.jmb.2019.04.009

Kelley, L. A., Mezulis, S., Yates, C. M., Wass, M. N., and Sternberg, M. J. (2015). The Phyre2 web portal for protein modeling, prediction and analysis. *Nat. Protoc.* 10, 845–858. doi: 10.1038/nprot.2015.053

Ko, W., Kim, S., and Lee, H. S. (2017). Engineering a periplasmic binding protein for amino acid sensors with improved binding properties. *Org. Biomol. Chem.* 15, 8761–8769. doi: 10.1039/C7OB02165H

Langan, R. A., Boyken, S. E., Ng, A. H., Samson, J. A., Dods, G., Westbrook, A. M., et al. (2019). De novo design of bioactive protein switches. *Nature* 572, 205–210. doi: 10.1038/s41586-019-1432-8

Li, H. Y., Cao, Z. X., Zhao, L. L., and Wang, J. H. (2013). Analysis of conformational motions and residue fluctuations for *Escherichia coli* ribose-binding protein revealed with elastic network models. *Intern. J. Mol. Sci.* 14, 10552–10569. doi: 10.3390/ijms140510552

Looger, L. L., Dwyer, M. A., Smith, J. J., and Hellinga, H. W. (2003). Computational design of receptor and sensor proteins with novel functions. *Nature* 423, 185–190.

Medintz, I. L., and Deschamps, J. R. (2006). Maltose-binding protein: a versatile platform for prototyping biosensing. *Curr. Opin. Biotechnol.* 17, 17–27. doi: 10.1016/j.copbio.2006.01.002

Pettersen, E. F., Goddard, T. D., Huang, C. C., Couch, G. S., Greenblatt, D. M., Meng, E. C., et al. (2004). UCSF Chimera–a visualization system for exploratory research and analysis. *J. Comput. Chem.* 25, 1605–1612. doi: 10.1002/jcc.20084

Platt, R., Drescher, C., Park, S. K., and Phillips, G. J. (2000). Genetic system for reversible integration of DNA constructs and *lacZ* gene fusions into the *Escherichia coli* chromosome. *Plasmid* 43, 12–23. doi: 10.1006/plas.1999.1433

Polizzi, N. F., and DeGrado, W. F. (2020). A defined structural unit enables de novo design of small-molecule-binding proteins. *Science* 369, 1227–1233. doi: 10.1126/science.abb8330

Ravindranathan, K. P., Gallicchio, E., and Levy, R. M. (2005). Conformational equilibria and free energy profiles for the allosteric transition of the ribose-binding protein. *J. Mol. Biol.* 353, 196–210. doi: 10.1016/j.jmb.2005.08.009

Reimer, A., Maffenbeier, V., Dubey, M., Sentchilo, V., Tavares, D., Gil, M. H., et al. (2017). Complete alanine scanning of the *Escherichia coli* RbsB ribose binding protein reveals residues important for chemoreceptor signaling and periplasmic abundance. *Sci. Rep.* 7:8245. doi: 10.1038/s41598-017-08035-5

Reimer, A., Yagur-Kroll, S., Belkin, S., Roy, S., and van der Meer, J. R. (2014). *Escherchia coli* ribose binding protein based bioreporters revisited. *Sci. Rep.* 4:5626. doi: 10.1038/srep05626

Riley, M. (1993). Functions of the gene products of *Escherichia coli*. *Microbiol. Rev.* 57, 862–952.:

Rocklin, G. J., Chidyausiku, T. M., Goreshnik, I., Ford, A., Houliston, S., Lemak, A., et al. (2017). Global analysis of protein folding using massively parallel design, synthesis, and testing. *Science* 357, 168–175. doi: 10.1126/science.aan0693

Romero, P. A., and Arnold, F. H. (2009). Exploring protein fitness landscapes by directed evolution. *Nat. Rev. Mol. Cell Biol.* 10, 866–876. doi: 10.1038/nrm2805

Scheib, U., Shanmugaratnam, S., Farias-Rico, J. A., and Hocker, B. (2014). Change in protein-ligand specificity through binding pocket grafting. *J. Struct. Biol.* 185, 186–192. doi: 10.1016/j.jsb.2013.06.002

Schreier, B., Stumpp, C., Wiesner, S., and Höcker, B. (2009). Computational design of ligand binding is not a solved problem. *Proc. Natl. Acad. Sci. U.S.A.* 106, 18491–18496. doi: 10.1073/pnas.0907950106

Sesterhenn, F., Yang, C., Bonet, J., Cramer, J. T., Wen, X., Wang, Y., et al. (2020). De novo protein design enables the precise induction of RSV-neutralizing antibodies. *Science* 368:eaay5051. doi: 10.1126/science.aay5051

Stank, A., Kokh, D. B., Fuller, J. C., and Wade, R. C. (2016). Protein binding pocket dynamics. *Acc. Chem. Res.* 49, 809–815. doi: 10.1021/acs.accounts.5b00516

Stewart, J. B., and Hermodson, M. A. (2003). Topology of RbsC, the membrane component of the *Escherichia coli* ribose transporter. *J. Bacteriol.* 185, 5234–5239. doi: 10.1128/jb.185.17.5234-5239.2003

Studer, G., Rempfer, C., Waterhouse, A. M., Gumienny, R., Haas, J., and Schwede, T. (2020). QMEANDisCo-distance constraints applied on model quality estimation. *Bioinformatics* 36, 1765–1771. doi: 10.1093/bioinformatics/btz828

Tavares, D., Reimer, A., Roy, S., Joublin, A., Sentchilo, V., and van der Meer, J. R. (2019). Computational redesign of the *Escherichia coli* ribose-binding protein ligand binding pocket for 1,3-cyclohexanediol and cyclohexanol. *Sci. Rep.* 9:16940. doi: 10.1038/s41598-019-53507-5

Tracewell, C. A., and Arnold, F. H. (2009). Directed enzyme evolution: climbing fitness peaks one amino acid at a time. *Curr. Opin. Chem. Biol.* 13, 3–9. doi: 10.1016/j.cbpa.2009.01.017

Unione, L., Ortega, G., Mallagaray, A., Corzana, F., Perez-Castells, J., Canales, A., et al. (2016). Unraveling the conformational landscape of ligand binding to glucose/galactose-binding protein by paramagnetic NMR and MD simulations. *ACS Chem. Biol.* 11, 2149–2157. doi: 10.1021/acschembio.6b00148

van der Meer, J. R., and Belkin, S. (2010). Where microbiology meets microengineering: design and applications of reporter bacteria. *Nat. Rev. Microbiol.* 8, 511–522.

Vercillo, N. C., Herald, K. J., Fox, J. M., Der, B. S., and Dattelbaum, J. D. (2007). Analysis of ligand binding to a ribose biosensor using site-directed mutagenesis and fluorescence spectroscopy. *Protein Sci.* 16, 362–368. doi: 10.1110/ps.062595707

Waterhouse, A., Bertoni, M., Bienert, S., Studer, G., Tauriello, G., Gumienny, R., et al. (2018). SWISS-MODEL: homology modelling of protein structures and complexes. *Nucleic Acids Res.* 46, W296–W303. doi: 10.1093/nar/gky427

Yang, W., and Lai, L. (2017). Computational design of ligand-binding proteins. *Curr. Opin. Struct. Biol.* 45, 67–73. doi: 10.1016/j.sbi.2016.11.021

Zheng, J., Guo, N., and Wagner, A. (2020). Selection enhances protein evolvability by increasing mutational robustness and foldability. *Science* 370:eabb5962. doi: 10.1126/science.abb5962

Conflict of Interest: The authors declare that the research was conducted in the absence of any commercial or financial relationships that could be construed as a potential conflict of interest.

Publisher's Note: All claims expressed in this article are solely those of the authors and do not necessarily represent those of their affiliated organizations, or those of the publisher, the editors and the reviewers. Any product that may be evaluated in this article, or claim that may be made by its manufacturer, is not guaranteed or endorsed by the publisher.

frontiers in Bioengineering and Biotechnology

ORIGINAL RESEARCH
published: 18 October 2021
doi: 10.3389/fbioe.2021.755045

A Novel Brighter Bioluminescent Fusion Protein Based on ZZ Domain and *Amydetes vivianii* Firefly Luciferase for Immunoassays

Vadim R. Viviani[1,2]*, *Jaqueline Rodrigues Silva*[1,2] *and Paulo Lee Ho*[3]

[1]Department of Physics, Chemistry and Mathematics, Federal University of São Carlos (UFSCar), Sorocaba, Brazil, [2]Graduate Program of Biotechnology and Environmental Monitoring, Federal University of São Carlos (UFSCar), Sorocaba, Brazil, [3]Núcleo de Produção de Vacinas Bacterianas, Centro BioIndustrial, Instituto Butantan, São Paulo, Brazil

Immunoassays are widely used for detection of antibodies against specific antigens in diagnosis, as well as in electrophoretic techniques such as Western Blotting. They usually rely on colorimetric, fluorescent or chemiluminescent methods for detection. Whereas the chemiluminescence methods are more sensitive and widely used, they usually suffer of fast luminescence decay. Here we constructed a novel bioluminescent fusion protein based on the N-terminal ZZ portion of protein A and the brighter green-blue emitting *Amydetes vivianii* firefly luciferase. In the presence of D-luciferin/ATP assay solution, the new fusion protein, displays higher bioluminescence activity, is very thermostable and produces a sustained emission ($t_{1/2}$ > 30 min). In dot blots, we could successfully detect rabbit IgG against firefly luciferases, Limpet Haemocyanin, and SARS-CoV-2 Nucleoprotein (1–250 ng), as well as the antigen bound antibodies using either CCD imaging, and even photography using smartphones. Using CCD imaging, we could detect up to 100 pg of SARS-CoV-2 Nucleoprotein. Using this system, we could also successfully detect firefly luciferase and SARS-CoV-2 nucleoprotein in Western Blots (5–250 ng). Comparatively, the new fusion protein displays slightly higher and more sustained luminescent signal when compared to commercial HRP-labeled secondary antibodies, constituting a novel promising alternative for Western Blotting and immunoassays.

Keywords: luciferase, immunoassays, Amydetes vivianii, SARS-CoV-2, western blot, ZZ-domain

OPEN ACCESS

Edited by:
Masoud Mozafari,
University of Toronto, Canada

Reviewed by:
Joaquim C. G. Esteves Da Silva,
University of Porto, Portugal
Alexey Kotlobay,
Institute of Bioorganic Chemistry (RAS), Russia
Luís Pinto Da Silva,
University of Porto, Portugal

***Correspondence:**
Vadim R. Viviani
viviani@ufscar.br

Specialty section:
This article was submitted to Biomaterials, a section of the journal Frontiers in Bioengineering and Biotechnology

Received: *07 August 2021*
Accepted: *30 September 2021*
Published: *18 October 2021*

Citation:
Viviani VR, Silva JR and Ho PL (2021) A Novel Brighter Bioluminescent Fusion Protein Based on ZZ Domain and Amydetes vivianii *Firefly Luciferase for Immunoassays. Front. Bioeng. Biotechnol. 9:755045. doi: 10.3389/fbioe.2021.755045*

INTRODUCTION

Bioluminescence, the emission of visible light by living organisms has been extensively used for bioanalytical purposes during the past decades, including their use as reagents for ATP and enzymatic assays, and reporter genes for bioimaging biological and pathological processes and biosensors (Viviani and Ohmiya 2006; Roda et al., 2009). In times of pandemics, sensitive and fast detection and diagnostic methods such as immunoassays are especially demanded.

Immunoassays are widely used for detection of antibodies against specific antigens in diagnosis, as well as in electrophoretic techniques such as Western Blotting. In the past, radioactive methods involving I^{125} labelled Protein A to detect antigenic proteins have been used for Western Blots and Immunoassays (Kessler, 1975, 1981; McConahey and Dixon, 1980). Later, the radioactive methods were replaced by safer colorimetric, fluorescent or chemiluminescent methods.

The chemiluminescence methods are in general more sensitive and specific. They usually rely on the conjugation of HRP to a secondary antibody which recognizes IgG, which upon mixing with the chemiluminescent substrate solution, consisting of luminol or a derivative and H_2O_2, emits a blue chemiluminescence (Nesbitt and Horton, 1992).

The need of novel sensitive chemiluminescence immunoassays is especially important in times of emerging viruses and pandemics of SARS-CoV-2. As an example of the wide use of chemiluminescence immunoassays for SARS-CoV-2, a recent report shows that among the current 54 commercially available antibody-based assays for SARS-CoV-2, 13 of them are luminescent and 10 are chemiluminescent. The chemiluminescent tests display between 66 and 75% sensitivity for IgM, and 75–100% for IgG (Kojouri, 2020). Methods and reagents for automated chemiluminescence enzyme immunoassays for SARS-CoV-2 nucleocapsid protein and spike proteins are also being developed.

Bioluminescence based immunoassays consisting on the fusion of luciferases or photoproteins to antigen or an antibodies were also proposed, but in general, they were not so popular like the chemiluminescent ones. Luciferase from bacteria (*Vibrio harveyi*) was fused to protein A showing its applicability in bioluminescent immunoassays (Lindbladh et al., 1991). The photoprotein obelin from *Obelia longissima* (Cnidaria) was attached to ZZ-domain of protein A demonstrating the possibility of its application in immunoassays (Frank et al., 1995). Obelin was also conjugated to anti-thyroid hormones (human thyrotropin and thyroxine), and the sensitivity of these bioluminescent immunoassays were similar to those using radioisotopes (Frank et al., 2004). Kobatake et al. (1993) produced a fusion protein based on the protein A fused to N-terminal deleted *Photinus pyralis* firefly luciferase. However, despite being antigenically active, this construct displayed weaker luminescent activity than wild-type firefly luciferase. Later, the authors fused protein A to the full-length firefly luciferase, obtaining a more active construct, with high affinity for IgG, detecting up to 5 pg of tumor marker a-fetoprotein (AFP) (Zhang et al., 2000).

More recently, the nanoluciferase from *Oplophorus gracilirostris* (deep-sea shrimp) was fused to a nanobody against aflatoxin B_1, a potentially carcinogenic mycotoxin produced by fungi in cereals, resulting in an attractive, simple, and rapid analytical tool for quantification of the pollutants in commercial foods (Ren et al., 2019). An immunoassay for antibodies against SARS-CoV-2 proteins based on the fusion of viral S e N protein fragments with NanoLuc luciferase was also developed. This method was specific to quantify the levels of SARS-CoV-2 antibodies in patients (Haljasmägi et al., 2020).

A quantitative bioluminescence immunoassay for immunohistochemistry based on *Cypridina* luciferase conjugated secondary antibody and its luciferin, was also developed and successfully used to detect the tumor marker carcinoembryonic antigen (Wang et al., 2020). Bioluminescent sensors to detect multiple antibodies based on microfluidics and BRET were also proposed (Kosuke et al., 2020).

Although nowadays most immunoassays use IgG based secondary antibodies, protein A still remains a useful and cheaper alternative, especially for affinity purification of antibodies (Huang et al., 2006). Protein A was first isolated from *Staphylococcus aureus*, and due to its high affinity for the portion Fc of immunoglobulins, has been extensively used in immunoassays. Furthermore, the small ZZ portion of protein A, can be used to construct smaller fusion proteins which are highly expressed in bacteria (Drevet et al., 1997).

In order to develop efficient bioluminescence based immunoassays, here we report the construction and uses of a novel bioluminescent fusion protein based on the ZZ portion of protein A and a brighter luciferase arising from *Amydetes vivianii* firefly, which emits a more blue-shifted emission than other firefly luciferases (Viviani et al., 2011; Pelentir et al., 2019). The new fusion protein can be successfully used for CCD imaging and photographical detection of several primary antibodies in immunoassays and Western Blots, including the detection of Anti-SARS-CoV-2 nucleoprotein.

MATERIAL AND METHODS

Reagents. SARS-CoV-2 Nucleoprotein and Anti-SARS-CoV-2-Nucleoprotein were obtained from CusaBio (Houston, United States); Anti-goat firefly luciferase, firefly D-luciferin potassium salt was obtained from Promega (Madison, United States); Anti-rabbit Hemocyanin and CoA were obtained from Sigma (St Louis, United States). Western Blotting chemiluminescent detection kit was obtained from GE Healthcare (Chicago, United States).

cDNAs and constructions. The chimeric protein DNA was constructed by ligating protein A ZZ fragment with the N-terminal of *Amydetes vivianii* firefly luciferase cDNA inside the pCold vector (Takara, Japan). For this purpose, ZZ DNA fragment was amplified from the plasmid pCP (Drevet et al., 1997), using primers containing *Nde*I restriction sites (ZZ-For) GAT ATA CAT ATG GCG CAA CAC and (ZZ-Rev) GCC GCA TAT GGA TCC ATG GAC TAG TGA TC. The amplification product was digested with *Nde*I, purified, and then ligated to the *Nde* I-digested and dephosporylated pCold vector containing the *Amydetes* luciferase cDNA (pC-Amy), using Takara Ligation kit. The ligation was used to transform *E. coli* XL1Blue, the recombinant colonies were induced with IPTG O/N, sprayed with D-luciferin and screened by photodetection using CCD camera (ATTO, Japan). The construction was confirmed by digestion with *Nde I*, by PCR using ZZ and pCold-F primers, and finally by DNA sequencing.

Protein expression and purification. The vectors containing the wild-type *Amydetes vivianii* (pC-AmyLuc) and chimeric protein (pC-ZZ-AmyLuc) were used to transform *E. coli* BL21 cells. For ZZ-AmyLuc and wild-type luciferase expression, transformed *E. coli* BL21 (DE3) cells were grown in 100–1,000 ml of LB medium at 37°C up to OD_{600} = 0.4, and then induced at 18°C with 0.4 mM IPTG during 18 h. Cells were harvested by centrifugation at 2,500 g for 15 min and resuspended in extraction buffer consisting of 0.10 M sodium

TABLE 1 | Luminescence properties of ZZ-AmyLuc fusion protein, wild-type *Amydetes vivianii* luciferase and HRP-conjugated secondary antibody from GE Healthcare.

luciferase	Specific Activity (10^{12}cps/mg)	Half-life at 37°C (h)	k_{cat} (10^{-6}cps)	$t_{1/2}$ (min)	λmax (nm)
Amydetes vivianii luciferase	6.0	12	109	12 ± 0.325	550
ZZ-AmyLuc	5.1 ± 0.8	18	150	18.7 ± 2.5/28 ± 2.8[a]	550
HRP- secondary antibody-	2.5 ± 0.54	—	—	10.3 ± 0.76	460

[a]*Half-life of the luminescence kinetics obtained in the presence of CoA.*

phosphate buffer, 1 mM EDTA, and 1% Triton X-100, 10% glycerol and protease inhibitor cocktail (Roche, Switzerland), pH 8.0, lysed by ultrasonication and centrifuged at 15,000 g for 15 min at 4°C. The N-terminal histidine-tagged fusion protein and wild-type *Amydetes* firefly luciferase were purified by agarose-Nickel affinity chromatography (Wash buffer: 50 mM Phosphate pH 7.0; 300 mM NaCl, 20 mM imidazole and Elution buffer 50 mM Phosphate pH 7.0; 300 mM NaCl, 250 mM imidazole) followed by dialysis (25 mM TRIS-HCl pH 8.0, 10 mM NaCl, 1 mM EDTA, 2 mM DTT, and 15% glycerol), as described (Pelentir et al., 2019). The concentrations of purified luciferases were between 0.5 and 1 mg/ml, and the estimated purity, according to SDS-PAGE gels were about 90%.

Luminometric assays for bioluminescence and chemiluminescence. Luciferase bioluminescence and HRP chemiluminescence activities were measured using an AB2200 (ATTO; Tokyo, Japan) luminometer. The assays for luciferase activity were performed by mixing 5 µl of 40 mM ATP/80 mM $MgSO_4$ solution with a solution consisting of 5 µl of luciferase or chimeric protein and 90 µl of 10 mM luciferin in 0.10 M Tris-HCl pH 8.0 at 22 C. For commercial rabbit horseradish peroxidase (HRP) conjugated antibody chemiluminescence activity, 5 µl of diluted HRP-conjugated antibody were mixed with 50 µl of substrate solution 1 and 50 µl of substrate solution 2. All measurements were done in triplicate for at least three independent luciferase preparations, and averages and the standard deviations were reported in **Table 1**.

Kinetics. The kinetics of luminescence reactions were measured using a TD-III luminometer (Japan). The half-life of luminescence ($t_{1/2}$) was the time necessary to reach half intensity from the peak of intensity, and was calculated form the average of three assays. In the standard assay, 5 µl of 80 mM MgSO4 and 40 mM ATP solution were mixed to a solution consisting of 5 µl of luciferase and 90 µl of 10 mM D-luciferin in 0.10 M Tris-HCl buffer pH 8.0.

CCD Imaging. Dot blot and Western blotting chemiluminescence detection was done using a LightCapture II CCD camera (ATTO, Japan) at different exposure times.

Smartphone and photographic imaging. For photographical imaging of immunoassays, we used a Canon Ti5, and for smartphone imaging we used a dark-adapted box for smartphones cameras, and a Samsung Galaxy S10 *Plus* cell phone.

Immuno-dot. For dot blotting using distinct antibodies, 1 µl of the antibodies at concentrations ranging from 1 to 500 ng/µl were spotted over nitrocellulose (NC) membrane. Then the membrane was incubated with blocking solution (5% dry milk in PBS-Tween) for 1 h, followed by 2 fast washes and 1 wash for 10 min in PBS-Tween (0.5 mM Na_2HPO_4; 0.5 mM NaH_2PO_4; 10 mM NaCl; 0.1% Tween pH 7.4), incubation with the ZZ-AmyLuc (1/400–1/1,000 dilutions) or rabbit HRP-labelled secondary antibody (1/1,000) during 1 h, and then washed again. Finally, 0.5–1 ml of luciferase assay solution (0.5 mM D-luciferin, 2 mM ATP, 4 mM $MgSO_4$, 5 mM DTT, 0.25 mM CoA in 0.10 M Tris-HCl buffer pH 8.0) or HRP substrate solution mix, were pipetted over the NC membrane, the membrane was left standing during 1 min, and finally exposed to CCD camera LightCapture II (ATTO, Japan) or photographic detection.

Western Blotting. For Western Blotting, SDS-PAGE electrophoresis of different protein samples was performed, and then the proteins were electro-transferred from the SDS-PAGE gel to NC membranes. The NC membranes were then threated as described for Dot Blotting, first by incubation with blocking solution, followed by incubation with the primary antibodies, secondary HRP-labeled antibody or ZZ-AmyLuc fusion protein, and finally the luminescence revealed upon addition of luciferase assay solution for ZZ-AmyLuc chimeric protein, or substrate solution 1 and 2 mix for commercial HRP-labelled secondary antibody.

RESULTS AND DISCUSSION

ZZ-AmyLuc Molecular Properties

We constructed a fusion protein using the cDNA of the ZZ portion of protein A at the N-terminus of a brighter luciferase (**Figure 1**), originally cloned from *Amydetes vivianii* firefly from campus of Sorocaba of Federal Univ. of São Carlos, which emits one of the most blue-shifted emissions among firefly luciferases (Viviani et al., 2011). The chimeric protein ZZ-AmyLuc DNA consists of 423 bp of the ZZ portion of protein A and the full-length cDNA of *Amydetes vivianii* luciferase inside the pCold vector (pC-ZZ-AmyLuc). The coded chimeric protein has therefore 699 amino-acid residues, consisting of a 11 amino-acid residues N-terminal fragment containing a 6 His-tag conferred by the pCold vector, followed by the 141 amino-acid residues of the ZZ portion of protein A, and finally the 547 residues of *Amydetes vivianii* firefly luciferase. The protein has a calculated MW of 77.879 Da and pI = 6.24.

Expression and Purification

The ZZ-AmyLuc fusion protein, as well as the wild-type luciferase, were expressed in bacteria and purified by nickel-agarose affinity chromatography according to published procedures (Pelentir et al., 2019). In the SDS-PAGE, the polypeptide displayed a MW of ~75 kDa, and the final purification yield was ~10 mg/L of bacterial culture (**Figure 2**).

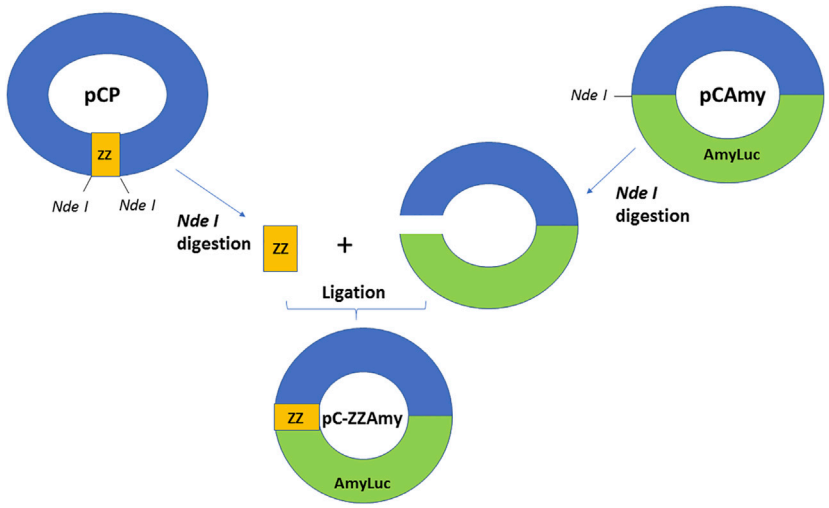

FIGURE 1 | Chimeric ZZ-Amy protein DNA construction scheme.

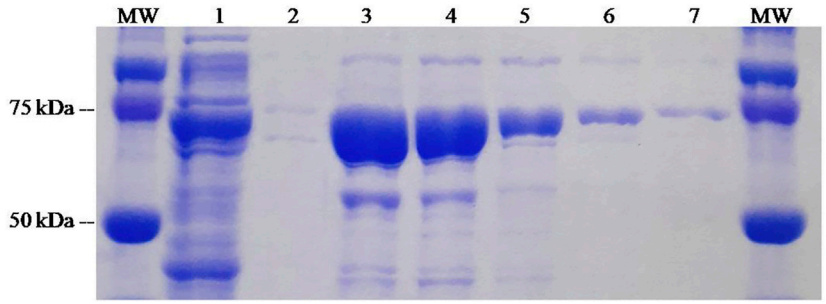

FIGURE 2 | SDS-PAGE of the purification process of ZZ-Amy fusion-protein: (MW) molecular weight standard; (1) crude extract of *E. coli* expressing ZZ-Amy; (2) void volume; (3) elution 1; (4) elution 2; (5) elution 3; (6) elution 4; (7) elution 5.

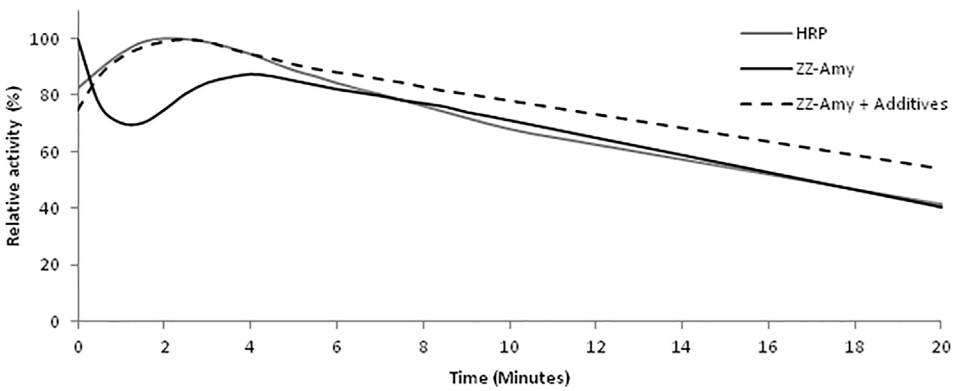

FIGURE 3 | Comparison of the luminescence kinetics of the commercial chemiluminescent HRP/luminol assay and with the bioluminescent fusion protein ZZ-AmyLuc assay. The HRP/luminol chemiluminescent assay was performed by mixing 5 µl of HRP-conjugated secondary antibody with 50 µl of Solution 1 and 50 µl of Solution 2. The standard bioluminescent assay with ZZ-AmyLuc was performed by mixing 5 µl of fusion protein with 95 µl of a solution consisting of 0.5 mM D-luciferin, 2 mM ATP and 4 mM MgSO4 in 0.1 M Tris-HCl pH 8,0. The assay with additives was performed in the additional presence of 0.25 mM CoA and 5 mM DTT.

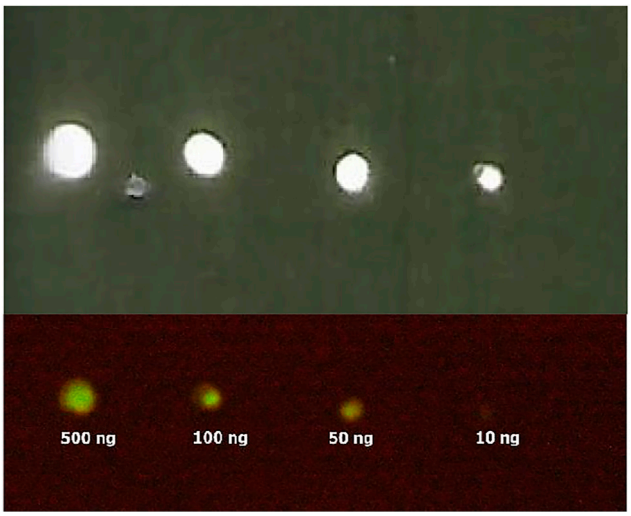

FIGURE 4 | Bioluminescence immunodot showing different amounts of immobilized Anti-SARS-CoV-2 nucleoprotein using ZZ-AmyLuc fusion protein: (upper image) CCD imaging, and (lower image) photographic detection. Using CCD imaging, it is possible to detect up to 1 ng of primary antibody, whereas using photographic detection it is possible to detect up to 10 ng.

Bioluminescent Properties of the Fusion Protein

Table 1 summarizes the bioluminescence properties of ZZ-AmyLuc fusion protein, and compares its luminescence properties with those of wild-type luciferase and commercial GE-Helathcare chemiluminescent kit using HRP/Luminol system. The specific luminescent activity of ZZ-AmyLuc (5.10^{12} cps/mg) was similar to that of the wild-type *Amydetes vivianii* firefly luciferase (6. 10^{12} cps/mg). The catalytic constant was slightly higher for the fusion protein in relation to the wild-type luciferase.

The luminescence reaction kinetics in the presence of luciferin, ATP and magnesium at pH 8.0 displays a flash with fast decay, followed by a slight increase and a very slow decay which is sustained for several minutes (**Figure 3**), with a half-life of ~20 min. In the presence of CoA and DTT, however, the kinetics became slower, lasting hours, with a half-life of ~30 min at room temperature. CoA has been shown to be a substrate of firefly luciferase, reacting by thioesterification with the potent inhibitor dehydroluciferyl-adenylate, which is responsible for the fast inhibition of the luminescence reaction and flash-like luminescence kinetics (Fraga et al., 2005). Addition of CoA causes removal of this inhibitor from the active site, resulting in a more sustained luminescence. This sustained luminescence kinetics displayed by the fusion protein allows detecting even weaker signals upon integration for longer times.

The fusion protein was also quite stable, keeping 38% of activity when incubated at 37°C during 24 h, 60% activity when incubated at 4°C during 37 days, and 84% activity when incubated at 4°C during 65 days in the presence of glycerol 15%.

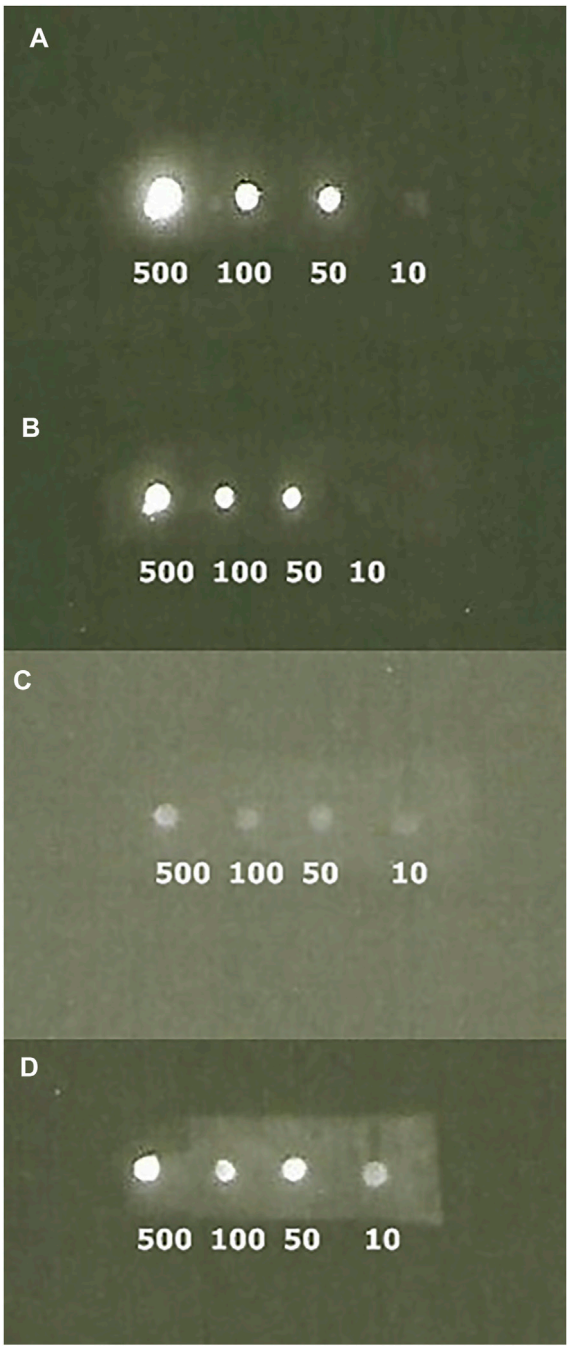

FIGURE 5 | CCD imaging of Dot blots comparing the luminescent signal of primary polyclonal antibodies raised against limpet hemocyanin revealed with ZZ-AmyLuc fusion protein (A and B) and commercial HRP-labeled secondary antibody (C and D): **(A)** revealed with ZZ-AmyLuc fusion protein and its assay solution after 1 min exposure; **(B)** same experiment of A after 2 h incubation at room temperature and 1 min exposure; **(C)** revealed with commercial HRP-labeled secondary antibody and its assay solution from GE HealthCare after 1 min exposure and **(D)** same experiment of C after 5 min exposure.

Finally, the bioluminescence spectrum overlapped with that of the wild-type *Amydetes vivianii* luciferase, with an emission peak at 550 nm, and also displaying pH-sensitivity (results not shown).

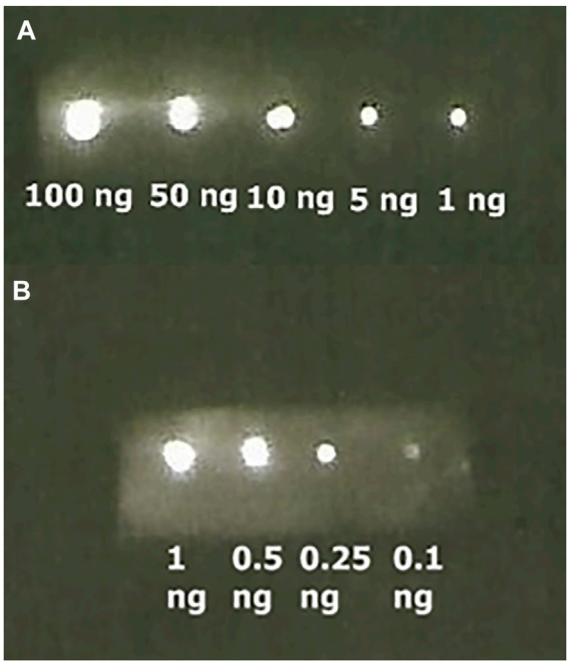

FIGURE 6 | Bioluminescence immunoassay of SARS-CoV-2 Nucleoprotein bound to its respective antibody and revealed with ZZ-AmyLuc fusion protein: **(A)** from 100 ng to 1 ng exposed during 1 min, and **(B)** from 1 to 0.10 ng exposed 5 min.

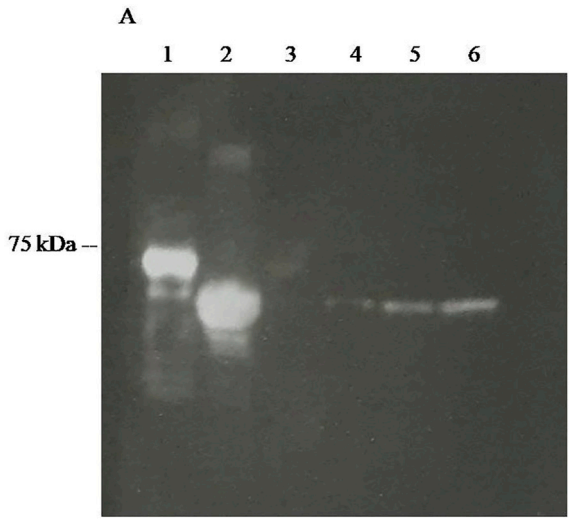

FIGURE 7 | CCD imaging of Western blots firefly luciferases using polyclonal antibodies raised against *Photinus pyralis* firefly luciferase revealed using ZZ-AmyLuc fusion protein as a secondary antibody and its assay solution: (1) ZZ-AmyLuc; (2) purified WT *Amydetes vivianii* firefly luciferase; (3) 10 ng of purified *Amydetes vivianii* luciferase; (4) 50 ng of purified *Amydetes vivianii* luciferase; (5) 100 of purified *Amydetes vivianii* luciferase; (6) 200 ng of purified *Amydetes vivianii* luciferase.

IgG BINDING PROPERTIES

IgG binding activity of ZZ-AmyLuc. The binding activity of ZZ-AmyLuc fusion protein was first analyzed by spotting primary antibodies on nitrocellulose membranes, followed by incubation with ZZ-AmyLuc or with HRP-labelled secondary antibody, and revealed by bio- and chemiluminescence using the respective assay solutions. Distinct IgGs, especially those raised from rabbits, including Anti-SARS-CoV-2 nucleoprotein and anti-hemocyanin were detected by CCD imaging (**Figure 4** and **Figure 5**). The luminescent signal was easily detected by conventional CCD camera system (LightCapture 2 ATTO, Japan) after 1 min exposure, and was also intense enough to be photographically detected (**Figure 4**). Considering **Figure 4**, less than 1 ng of rabbit antibodies against SARS-CoV-2 nucleoprotein could be detected using CCD camera, and less than 10 ng by photographic detection.

Then, we performed immunoblotting by spotting SARS-CoV-2 nucleoprotein over the NC membrane, followed by incubation with its primary antibody, the ZZ-AmyLuc protein and revealed with its assay solution. Using this procedure, we could detect up to 100 pg of antigen by conventional CCD imaging (**Figure 6**).

Western Blots. In Western Blots, the fusion protein could also be effectively used to reveal commercial and home expressed firefly luciferases (**Figure 7**) and SARS-CoV-2 Nucleoprotein (**Figure 8**). The luminescent signals were intense and comparable with Western blots revealed using commercial HRP-labeled secondary antibodies.

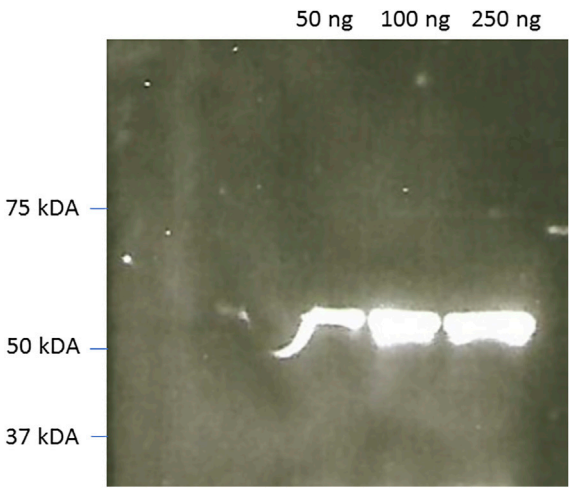

FIGURE 8 | CCD imaging of Western blots of commercial SARS-Covid-2 nucleoproteín using rabbit Anti-SARS-covid and reveled using ZZ-AmyLuc fusion protein as a secondary antibody and its assay solution. Exposure time: 1 min.

Comparison of ZZ-AmyLuc bioluminescent assay with commercial HRP/luminol. As shown above, the bioluminescent immunoassays using ZZ-AmyLuc fusion protein and its assay solution with luciferin and MgATP, were brighter than the commercial chemiluminescent assay of GE HealthCare based on the HRP conjugated secondary antibody and luminol.

Whereas the relative *in vitro* luminescent activity of the HRP-based chemiluminescent assay of GE Healthcare was higher than that of the fusion protein ZZ-AmyLuc, when using the same volumes of enzyme and respective assays solutions (5 µl enzyme and 95 µl of respective assay solution), the specific activity of the ZZ-AmyLuc fusion protein was higher than that of the commercial HRP conjugated secondary antibody (**Table 1**). Furthermore, considering the higher sensitivity of the luminometer photomultiplier in the blue region, where the HRP/luminol reaction emits (460 nm), in relation to ZZ-AmyLuc/luciferin system which emits in the green region (550 nm), it is expected that ZZ-AmyLuc may display even higher luminescence activity than the HRP-luminol system.

The duration of the luminescent signal of ZZ-Amy fusion protein bioluminescent assay, as measured from the half-life from the peak of luminescence activity, was longer than the signal of the HRP/luminol chemiluminescent assay, with a half-life of ~20 min in the classic assay with luciferin and ATP, and ~30 min for the assay solution with additives, whereas the commercial HRP/luminol-based assay had a half-life of only ~10 min. These properties indicate that the luminescence signal of Western Blots and immunoassays could be detected later than 30 min after the addition of the reagent, whereas HRP assay can be used not much longer than 10 min. In practice, the intensity of the luminescence signal emitted by the immobilized complex of ZZ-AmyLuc-primary antibody-antigen complex in dot blots, was still very high after 2 h from the beginning of the assay. Finally, the reagent Amy-Luc also showed very good stability in buffered solution at 4°C, keeping the full activity for more than 2 months.

We could not directly compare the bioluminescence activity and properties of this ZZ-AmyLuc fusion protein with those of the construct of *Photinus pyralis* firefly luciferase/protein-A described by Kobatake et al. (1993). However, considering that: 1) the reported bioluminescence activity of *P. pyralis* firefly luciferase construct is nearly the same of the respective wild-type luciferase; 2) that *A. vivianii* wild-type luciferase has similar catalytic constant than *P. pyralis* luciferase (Pelentir eta l., 2020), and 3) that the construct ZZ-AmyLuc described here has slightly higher catalytic constant than the respective wild-type luciferase, we assume that ZZ-Amy-Luc also has higher bioluminescence activity than *P. pyralis* firefly luciferase-Protein A construct.

Altogether, these properties make the ZZ-AmyLuc fusion protein an attractive brighter and a stable competitive luminescent reagent for immunoassays. One drawback of this system is the differential recognition of immunoglobulins by protein A. It is known that protein A may usually binds effectively to distinct IgGs from distinct biological sources (rabbit, goat, mouse, human), but not to IgM, restricting its applicability to IgGs. However, the construction and properties of the fusion-protein reported here, besides being useful to detect IgGs, demonstrates the potential of *Amydetes* luciferase for construction of novel bioluminescent fusion protein with high affinity for antibodies. Another issue to be considered for the potential commercial use of this fusion protein in immunoassays, is the elevated cost of the substrate D-luciferin and assay solutions. However, although the luminol and H_2O_2 solutions are cheaper than D-luciferin, an estimate made by comparing the number of assays performable with GE-Healthcare Western Blotting kit and with the D-luciferin assay solution prepared here, in the absence of the very expensive CoA, showed that the price for assay is cheaper for the luciferin solution than that of luminol solution 1 and 2.

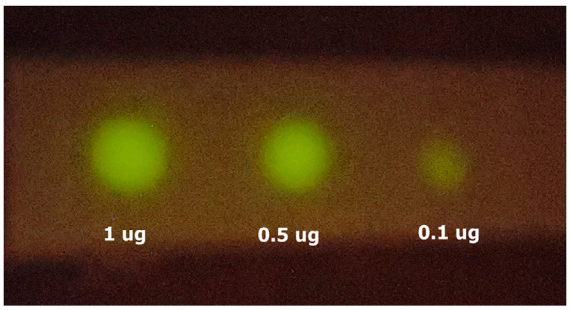

FIGURE 9 | Smartphone imaging of spotted antibodies against SARS-CoV-2 nucleoprotein, revealed with ZZ-AmyLuc and its assay solution. The image was obtained with a Galaxy S10 Plus smartphone.

Smartphone detection. The use of smartphones for clinical diagnosis using bioluminescence is an increasing trend for point-of-care medicine and biosensors (Roda et al., 2014; Tomimuro et al., 2020). We have imaged the bioluminescent signal emitted by dot blots with spotted SARS-CoV-2 nucleoprotein and haemocyanin primary antibodies, and revealed with ZZ-AmyLuc fusion protein and its assay solution, using a Galaxy S-10 *plus* cell phone CCD camera. Using this procedure, we could detect up to 100 ng of antibodies (**Figure 9**). Considering that the CCD camera of this smartphone displays an average sensitivity to light among the smartphones CCD cameras found in the market, the experiment shown here also attests the feasibility of using smartphone technology for bioluminescent immunoassays using ZZ-AmyLuc fusion protein.

CONCLUDING REMARKS

We constructed a novel bioluminescent fusion protein based on ZZ portion of protein A and the brighter *Amydetes vivianii* firefly luciferase for immunoassays and Western Blots. The new fusion protein displayed superior luminescence properties, effectively recognizing rabbit primary antibodies in immunoassays and Western Blots. The fusion protein could be successfully used to detect less than 1 ng of primary antibody against SARS-CoV-2 nucleoprotein by CCD imaging, 10 ng by photography, and up to 100 pg of immobilized SARS-CoV-2 nucleoprotein using its respective antibody. The luminescence signal emitted by the fusion protein in dot blots is very bright and lasts enough time to be detected until to 2 h after the beginning of the assay. The methodology is also sensitive enough to allow detection of up to 100 ng of antibodies using an average smartphone camera. Altogether, these properties make ZZ-AmyLuc a novel promising bioluminescent secondary antibody for immunoassays and Western Blots.

DATA AVAILABILITY STATEMENT

The original contributions presented in the study are included in the article/supplementary material, further inquiries can be directed to the corresponding author.

AUTHOR CONTRIBUTIONS

VV idealized the work, performed the fusion protein construction, its characterization and wrote the manuscript; JRS performed protein analysis and Western Blot characterization and manuscript preparation and PLH contributed with the idea, provided the plasmid pCP, helped in the construction and manuscript preparation.

ACKNOWLEDGMENTS

Thanks to Fundação de Amparo à Pesquisa do Estado de São Paulo, Brazil (FAPESP Grant number: 2010/05426-8 to VRV), National Research Council (CNPq 401.867/2016-1 to VRV and 305430/2019-0 to PLH), Fundação Butantan (to PLH) for financial support, and Daniel R. de Souza (UFSCar) for DNA sequencing and Gabriel F. Pelentir (UFSCar) for preparing figures.

REFERENCES

Drevet, P., Lemaire, C., Gasparini, S., Zinn-Justin, S., Lajeunesse, E., Ducancel, F., et al. (1997). High-Level Production and Isotope Labeling of Snake Neurotoxins, Disulfide-Rich Proteins. *Protein Expr. Purif.* 10, 293–300. doi:10.1006/prep.1997.0740

Fraga, H., Fernandes, D., Fontes, R., and Esteves da Silva, J. C. G. (2005). Coenzyme A Affects Firefly Luciferase Luminescence Because it Acts as a Substrate and Not as an Allosteric Effector. *FEBS J.* 272, 5206–5216. doi:10.1111/j.1742-4658.2005.04895.x

Frank, L. A., Illarionova, V. A., and Vysotski, E. S. (1996). Use of proZZ-Obelin Fusion Protein in Bioluminescent Immunoassay. *Biochem. Biophysical Res. Commun.* 219, 475–479. doi:10.1006/bbrc.1996.0258

Frank, L. A., Petunin, A. I., and Vysotski, E. S. (2004). Bioluminescent Immunoassay of Thyrotropin and Thyroxine Using Obelin as a Label. *Anal. Biochem.* 325, 240–246. doi:10.1016/j.ab.2003.11.003

Haljasmägi, L., Remm, A., Rumm, A. P., Krassohhina, E., Sein, H., Tamm, A., et al. (2020). LIPS Method for the Detection of SARS-CoV-2 Antibodies to Spike and Nucleocapsid Proteins. *Eur. J. Immunol.* 50, 1234–1236. doi:10.1002/eji.202048715

Huang, Q.-L., Chen, C., Jiang, S.-H., Pan, X., and Hua, Z.-C. (2006). Immobilized Protein ZZ, an Affinity Tool for Immunoglobulin Isolation and Immunological Experimentation. *Biotechnol. Appl. Biochem.* 45, 87–92. doi:10.1042/BA20060055

Kessler, S. W. (1981). [31] Use of Protein A-Bearing Staphylococci for the Immunoprecipitation and Isolation of Antigens from Cells. *Methods Enzymol.* 73, 442–459. doi:10.1016/0076-6879(81)73084-2

Kessler, S. W. (1975). Rapid Isolation of Antigens from Cells with Staphylococcal Protein_A Antibody Absorbent: Parameters for Interaction of Antibody-Antigen Complexes with Protein. *A. J. Immunol.* 115, 1617–1624.

Kobatake, E., Iwai, T., Ikariyama, Y., and Aizawa, M. (1993). Bioluminescent Immunoassay with a Protein A-Luciferase Fusion Protein. *Anal. Biochem.* 208, 300–305. doi:10.1006/abio.1993.1050

Kojouri, M. (2020). Performance of Commercially Antibody-Based Assays for Covid-19 Detection. *AJBSR* 9, 461–471. doi:10.34297/AJBSR.2020.09.001453

Lindbladh, C., Mosbach, K., and Bülow, L. (1991). Preparation of a Genetically Fused Protein A/luciferase Conjugate for Use in Bioluminescent Immunoassays. *J. Immunological Methods* 137, 199–207. doi:10.1016/0022-1759(91)90025-b

McConahey, P. J., and Dixon, F. J. (1980). [11] Radioiodination of Proteins by the Use of the Chloramine-T Method. *Methods Enzymol.* 70, 210–213. doi:10.1016/s0076-6879(80)70050-2

Nesbitt, S. A., and Horton, M. A. (1992). A Nonradioactive Biochemical Characterization of Membrane Proteins Using Enhanced Chemiluminescence. *Anal. Biochem.* 206, 267–272. doi:10.1016/0003-2697(92)90365-e

Pelentir, G. F., Bevilaqua, V. R., and Viviani, V. R. (2019). A Highly Efficient, Thermostable and Cadmium Selective Firefly Luciferase Suitable for Ratiometric Metal and pH Biosensing and for Sensitive ATP Assays. *Photochem. Photobiol. Sci.* 18, 2061–2070. doi:10.1039/c9pp00174c

Ren, W., Li, Z., Xu, Y., Wan, D., Barnych, B., Li, Y., et al. (2019). One-Step Ultrasensitive Bioluminescent Enzyme Immunoassay Based on Nanobody/Nanoluciferase Fusion for Detection of Aflatoxin B1 in Cereal. *J. Agric. Food Chem.* 67, 5221–5229. doi:10.1021/acs.jafc.9b00688

Roda, A., Guardigli, M., Michelini, E., and Mirasoli, M. (2009). Bioluminescence in Analytical Chemistry and *In Vivo* Imaging. *Trac Trends Anal. Chem.* 28, 307–322. doi:10.1016/j.trac.2008.11.015

Roda, A., Michelini, E., Cevenini, L., CalabriaSimoni, D. P., Calabretta, M. M., and Simoni, P. (2014). Integrating Biochemiluminescence Detection on Smartphones: Mobile Chemistry Platform for Point-of-Need Analysis. *Anal. Chem.* 86, 7299–7304. doi:10.1021/ac502137s

Tomimuro, k., Tenda, K., Ni, Y., Hiruta, Y., Merkx, M., and Citterio, D. (2020). Thread-based Bioluminescent Sensor for Detecting Multiple Antibodies in a Single Drop of Whole Blood. *ACS Sens.* 5, 1786–1794. doi:10.1021/acssensors.0c00564

Viviani, V. R., Amaral, D., Prado, R., and Arnoldi, F. G. C. (2011). A New Blue-Shifted Luciferase from the Brazilian *Amydetes Fanestratus* (Coleoptera: Lampyridae) Firefly: Molecular Evolution and Structural/functional Properties. *Photochem. Photobiol. Sci.* 10, 1879–1886. doi:10.1039/c1pp05210a

Viviani, V. R., and Ohmiya, Y. (2006). *Beetle Luciferases: Colorful Lights on Biological Processes and Diseases*. Darmstadt: Photoprot. Bioanal.Wiley-VCH, 49–63. doi:10.1002/3527609148.ch3

Wang, K. Y., Wu, C., Shimajiri, S., Enomoto, T., Kubota, H., Akiyama, H., et al. (2020). Quantitative Immunohistochemistry Using an Antibody-Fused Bioluminescent Protein. *BioTechniques* 69, 302–306. doi:10.2144/btn-2020-0006

Zhang, X.-m., Kobatake, E., Kobayashi, K., Yanagida, Y., and Aizawa, M. (2000). Genetically Fused Protein A-Luciferase for Immunological Blotting Analyses. *Anal. Biochem.* 282, 65–69. doi:10.1006/abio.2000.4584

Conflict of Interest: The authors declare that the research was conducted in the absence of any commercial or financial relationships that could be construed as a potential conflict of interest.

Publisher's Note: All claims expressed in this article are solely those of the authors and do not necessarily represent those of their affiliated organizations, or those of the publisher, the editors and the reviewers. Any product that may be evaluated in this article, or claim that may be made by its manufacturer, is not guaranteed or endorsed by the publisher.

frontiers in Bioengineering and Biotechnology

ORIGINAL RESEARCH
published: 27 October 2021
doi: 10.3389/fbioe.2021.773353

Bioluminescent Sensors for Ca^{++} Flux Imaging and the Introduction of a New Intensity-Based Ca^{++} Sensor

Jie Yang[1] *and Carl Hirschie Johnson*[2]*

[1]Britton Chance Center for Biomedical Photonics, Wuhan National Laboratory for Optoelectronics-Huazhong University of Science and Technology, Wuhan, China, [2]Department of Biological Sciences, Vanderbilt University, Nashville, TN, United States

Sensitive detection of biological events is a goal for the design and characterization of sensors that can be used *in vitro* and *in vivo*. One important second messenger is Ca^{++} which has been a focus of using genetically encoded Ca^{++} indicators (GECIs) within living cells or intact organisms *in vivo*. An ideal GECI would exhibit high signal intensity, excellent signal-to-noise ratio (SNR), rapid kinetics, a large dynamic range within relevant physiological conditions, and red-shifted emission. Most available GECIs are based on fluorescence, but bioluminescent GECIs have potential advantages in terms of avoiding tissue autofluorescence, phototoxicity, photobleaching, and spectral overlap, as well as enhancing SNR. Here, we summarize current progress in the development of bioluminescent GECIs and introduce a new and previously unpublished biosensor. Because these biosensors require a substrate, we also describe the pros and cons of various substrates used with these sensors. The novel GECI that is introduced here is called CalBiT, and it is a Ca^{++} indicator based on the functional complementation of NanoBiT which shows a high dynamic change in response to Ca^{++} fluxes. Here, we use CalBiT for the detection of Ca^{++} fluctuations in cultured cells, including its ability for real-time imaging in living cells.

Keywords: GECIs, bioluminescent imaging, nanoluc, luciferin, real-time imaging

OPEN ACCESS

Edited by:
Vadim R. Viviani,
Federal University of São Carlos, Brazil

Reviewed by:
Yoshihiro Ohmiya,
National Institute of Advanced Industrial Science and Technology (AIST), Japan
Anderson Garbuglio Oliveira,
University of São Paulo, Brazil

***Correspondence:**
Carl Hirschie Johnson
carl.h.johnson@vanderbilt.edu

Specialty section:
This article was submitted to Biomaterials, a section of the journal Frontiers in Bioengineering and Biotechnology

Received: *09 September 2021*
Accepted: *13 October 2021*
Published: *27 October 2021*

Citation:
Yang J and Johnson CH (2021) Bioluminescent Sensors for Ca^{++} Flux Imaging and the Introduction of a New Intensity-Based Ca^{++} Sensor. Front. Bioeng. Biotechnol. 9:773353. doi: 10.3389/fbioe.2021.773353

INTRODUCTION

Free calcium ions (Ca^{++}) are an important secondary messenger in cells. Key physiological processes such as cellular differentiation (Machaca, 2007), proliferation (Capiod, 2011), signal transmission (Zurgil et al., 1986), and muscle contraction (Kuo and Ehrlich, 2015) require Ca^{++} signaling. In the past decades, various versions of genetically encoded Ca^{++} indicators (GECIs) have been developed for the detection of Ca^{++} fluxes in cells (Greenwald et al., 2018). A GECI is an artificially designed molecule that converts chemical signals in the form of Ca^{++} concentration into optical signals and allows the detection or visualization of Ca^{++} fluctuations in a real-time, dynamic, and noninvasive manner in living cells and tissues.

Two types of GECIs involve changes in fluorescence or bioluminescence properties in response to changes in Ca^{++} levels (Greenwald et al., 2018). Fluorescent GECIs are excited by light, after which time they emit photons. On the other hand, bioluminescent GECIs do not require excitation by light, but instead require a substrate for chemical conversion and subsequent release of photons. The substrates are called "luciferins" and the enzymes that accomplish this bioluminescence reaction are called "luciferases;" most luciferases require the presence of oxygen to allow the bioluminescence reaction (Wilson and Hastings, 2013). Compared with bioluminescent GECIs, fluorescent GECIs can

often be made to produce relatively stronger signals because the intensity of the excitation can be increased [with concomitant deleterious consequences of the strong irradiation (Robertson et al., 2013)]. However, because bioluminescent GECIs do not require excitation light, they have advantages, including no tissue autofluorescence, phototoxicity, photobleaching, or spectral overlap between sensor and optogenetic actuators. Regarding the latter point, bioluminescent GECI sensors can couple optimally with optogenetic probes as they do not require light excitation, and therefore light excitation can be used exclusively to active the optogenetic actuator without spectral crosstalk to the sensor (Yang et al., 2016). In contrast, because continuous excitation is required for the stimulation of fluorescent GECIs, combining these fluorescent sensors with optogenetic probes requires very careful separation of spectral overlaps, which can never be completely eliminated. Finally, owing to the low background, bioluminescent GECIs also have a very high signal-to-noise ratio (SNR) and are suitable for less-invasive deep tissue *in-vivo* imaging in live animals.

Herein we discuss the currently available bioluminescent GECIs, as well as introducing a novel bioluminescent GECI that is based upon functional complementation of a luciferase that is mediated by changes in Ca^{++} levels.

MATERIALS AND METHODS

Protein Purification and *in vitro* Experiments

To purify CalBiT fusion proteins, we expressed each CalBiT in a modified bacterial expression vector pRSETb. The cDNA sequences were inserted between the *Eco*RI and *Hind*III restriction enzyme sites of pRSETb. The plasmid was transformed into BL21(DE3) *Escherichia coli* cells for the expression and purification of the fusion protein. The His6-tagged CalBiT proteins were purified using TALON Metal Affinity Co^{++} Resin. The signal intensity of each purified protein in response to varying [Ca^{++}] was measured using Ca^{++} buffers (Molecular Probes, Life Technologies) and a fluorescence spectrophotometer (QuantaMaster, Photon Technology International Inc). The free Ca^{++} buffers of varying concentrations were prepared according to the manufacturer's protocol. Briefly, buffer 1 (10 mM EGTA, 100 mM KCl, and 30 mM MOPS, pH 7.2) and buffer 2 (10 mM CaEGTA, 100 mM KCl, and 30 mM MOPS, pH 7.2) were mixed in different proportions to prepare varying free Ca^{++} concentrations. For all *in vitro* experiments, 10 μM final concentration of the NLuc substrate furimazine was added.

Cellular Expression and Characterization

To construct the CalBiT1.0-3.0 family, we used the 11S (residues 1–156) and 114 (residues 157–169) versions of LgBiT and SmBiT, respectively (Dixon et al., 2016). The CalBiT2.0 sequence was constructed using a plasmid with the CAG promoter (pCAG) (Niwa et al., 1991), and CalBiT2.0 was expressed under the control of pCAG when transfected via Lipofectamine 2000 (ThermoFisher Scientific Inc.) into either HEK293 or HeLa cells grown in Dulbecco's Modified Eagle Medium (Gibco). Two days later, signal responses were recorded using an inverted Olympus IX-71 epi-fluorescence microscope inside a temperature-controlled, light-tight box with a cooled Electron Multiplying-CCD (EM-CCD) camera. During real-time imaging, changes in cytosolic Ca^{++} were elicited by the addition of 10 μM histamine to HeLa cells (**Figures 4A,B**) or thapsigargin to HEK cells (**Figure 4C**), and the intensity of CalBiT2.0 luminescence was assayed. Expression of CalBiT2.0 was coupled with expression of the optogenetic melanopsion (*Opn4*) by constructing a bi-cistronic expression plasmid with a T2A coding sequence using CalBiT2.0 plus mouse melanopsin (*Opn4*) under the control of pCAG. The cells were transfected with the CalBiT2.0–2A-Opn4 construct and stimulated with a blue light pulse (470 ± 30 nm) for 1 s and later with 1 μM thapsigargin (**Figure 4D**).

Data Analyses

The average light intensity in the regions of interest within cells was analyzed using ImageJ software (NIH). The Hill coefficient and Kd values (**Figure 1C**) were determined using the OriginLab 6 software (OriginLab).

REVIEW OF CURRENTLY AVAILABLE BIOLUMINESCENT GECIS

Sensitive Imaging Using Bioluminescent GECIs

A sensitive GECI requires high signal intensity, a large dynamic range, and rapid kinetics. However, bioluminescent sensors as a general observation generate relatively weaker signal intensity and therefore imaging usually requires a sensitive charge-coupled device (CCD) camera with a relatively longer exposure time so as to capture more photons, thereby attaining sufficient resolution. Some physiological reactions are involved in fast kinetic events of Ca^{++} flux in cells, for example, the action potentials of excitatory neurons with millisecond-level responses (Müller et al., 2007). For imaging such rapid events, brief exposures are necessary. In such cases, bright sensors are required to obtain enough photons within brief exposures for acquiring sufficient spatial and temporal resolution for the resulting images. To improve the signal intensity of bioluminescent molecules, the following two strategies are usually adopted: 1) development and use of brighter bioluminescent systems based on brighter luciferases and/or luciferins. For instance, bioluminescent systems have been developed from the first generation aequorin to the brighter third-generation engineered luciferase called NanoLuc (NLuc) (Hall et al., 2012); 2) to increase the intensity by intramolecular bioluminescence resonance energy transfer (BRET) between a luciferase and a fluorophore (Takai et al., 2015) (see discussion below in part 3). The following two reasons may explain why the signal intensity can sometimes be enhanced by BRET: 1) luciferase enzyme sometimes forms a relatively more stable molecular conformation when fused with a fluorescent protein (Baubet et al., 2000), and/or 2) when a fluorescent protein with high extinction coefficient and quantum yield acts as a BRET

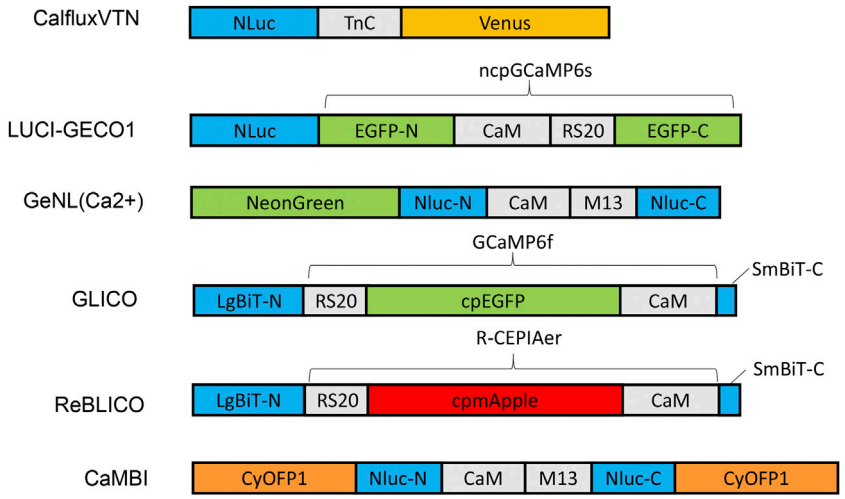

FIGURE 1 | Schematic diagram of various designs and constructs of bioluminescent GECIs based on NLuc or NanoBiT. Abbreviations: LgBiT-N, N-terminal large NanoBiT; SmBiT-C, C-terminal small NanoBiT; CaM, calmodulin; RS20 and M13, calmodulin-binding peptide; NLuc-N and NLuc-C, N-terminal and C-terminal of NanoLuc, respectively.

acceptor, more efficient emission can be produced via non-radiative energy transfer (Saito et al., 2012).

Apart from signal intensity, affinity and dynamic range are two key factors for sensitive imaging using bioluminescent GECIs (Chiu and Haynes, 1977; Pérez Koldenkova and Nagai, 2013). The dissociation constant (Kd) stands for the binding capacity between the indicating sensor and Ca^{++}, and it can be determined using buffers prepared with ethylene glycol tetraacetic acid (EGTA) and Ca^{++}-EGTA to achieve specific concentrations of free calcium ions (Pérez Koldenkova and Nagai, 2013; Yang et al., 2016). These data are normalized to the maximal (defined as 1.0 under Ca^{++} saturation conditions) and to the minimal (defined as 0 under Ca^{++} depletion conditions) signal intensity or BRET ratio value. The dynamic range is defined as the maximal intensity or BRET ratio (in a saturated Ca^{++}-bound state) divided by the minimal intensity or BRET ratio (determined in the presence of zero-added calcium plus EGTA). In living cells, when resting Ca^{++} concentration lies within the detectable range of the indicator/sensor, high baseline signals can be generated using a high affinity (low Kd value) indicator. Similarly to the measurement of different lengths where a micrometer is optimal for micrometers to a centimeter while a meter-stick is best for lengths between a centimeter and a meter, measuring intracellular Ca^{++} levels requires the selection of the most appropriate measuring sensor. As different cell organelles contain different Ca^{++} concentrations, it is necessary to develop GECIs with appropriate Kd values (e.g., higher Kd for high Ca^{++} regions, etc.). To address this need, Hossain and co-workers developed a family of multicolor bioluminescent GECIs with different Kd values for simultaneous imaging in the endoplasmic reticulum (ER), nucleus, and mitochondria (Hossain et al., 2018).

The detection methods of GECIs include intensiometric and ratiometric imaging (Greenwald et al., 2018). Intensiometric imaging assesses in the change of signal intensity in response to changes in Ca^{++} levels and is effectively using a single wavelength channel. On the other hand, ratiometric imaging requires the calculation of the ratio between the intensities at two (or more) different wavelengths and the data are therefore collected from two (or more) channels. The intensiometric method is relatively easier to perform, but as its results are obtained by a single channel, they can be disturbed by movement artifacts, out-of-focus, changes in the level of expression of the sensor, and decay of the active substrate concentration during a long imaging interval. Any of those effects can cause serious artifacts and therefore incorrect conclusions. In contrast, ratiometric imaging corrects the influences of those adverse factors, but requires dual-view dichroic equipment to split the image into light of different contributing wavelengths, such as W-VIEW GEMINI 2C Image Splitting Optics (https://www.micromecanique.fr/product/view/fc0ff0d4–87d2–4a2f-b302–17dfb890f2fa). Consequently, while ratiometric imaging has many advantages, its need for an image splitting system increases the experimental cost of the imaging system. Alternatively, some of the adverse factors can be minimized for short-term recording session if an intensiometric indicator with a high enough dynamic range is used because the change from out-of-focus and decay of the substrate artifacts can be neglected when genuine signal changes from the GECI is large and the recording interval is short.

Development of Bioluminescent GECIs

Three generations of bioluminescent GECIs based on different luciferases have been developed as of the present time (**Table 1**). Aequorin, the first generation bioluminescent GECI, was identified and isolated from jellyfish along with the green fluorescent protein (GFP) by Shimomura and colleagues (Shimomura et al., 1962). In native jellyfish, aequorin interacts

TABLE 1 | Summary of properties of bioluminescent GECIs.

GECI names	Luciferase	Substrate	Readout	Kd (μM)	References
Aequorin	Aequorin	Coelenterazine	Intensity	2.6	Tricoire et al. (2006)
GFP-Aequorin	Aequorin	Coelenterazine	Intensity	Not determined	Baubet et al. (2000)
BRAC	Rluc8	Coelenterazine	Ratio	1.9	Saito et al. (2010)
Nano-lantern (Ca2+)	Split Rluc8	Coelenterazine	Intensity	0.62	Saito et al. (2012)
CalfluxVTN	NLuc	Furimazine	Ratio	0.48	Yang et al. (2016)
LUCI-GECO1	NLuc	Furimazine	Ratio	0.285	Qian et al. (2019)
GeNL (Ca2+)	Split NLuc	Furimazine	Intensity	Four versions: 0.060; 0.25; 0.48; 0.52	Suzuki et al. (2016)
GLICO	NanoBiT	Furimazine	Intensity	0.23	Farhana et al. (2019)
ReBLICO	NanoBiT	Furimazine	Intensity	1,526	Farhana et al. (2019)
Orange CaMBI	Split NLuc	Furimazine; Hydrofurimazine	Intensity	Four versions: 0.11; 0.2; 0.27; 0.3	Oh et al. (2019)

closely with GFP to form a BRET molecular complex so that the intrinsically blue luminescence of aequorin is converted to green luminescence by virtue of Förster resonance energy transfer (Morin and Hastings, 1971). Aequorin contains three EF-hand domains of Ca^{++}-binding sites, and exists at low Ca^{++} concentrations bound to the substrate/luciferin (coelenterazine) in an enzymatically locked intermediate form. The binding of Ca^{++} induces a conformational change that allows the completion of the enzymatic reaction, converting coelenterazine to coelenteramide and releasing a photon of blue light. Unlike Firefly luciferase (FLuc), the final step of the aequorin reaction is not dependent upon ATP, and therefore its reaction is allowed in ATP-deficient domains, e.g., extracellular spaces (Montero et al., 2000).

Aequorin is useful for monitoring Ca^{++} concentration in cells or tissues, and it responds to increases in Ca^{++} with flashes that discharge the aequorin; the inactive apo-aequorin can be recharged to active aequorin, but the recharging process can require hours. Moreover, the bioluminescent flashes of aequorin are relatively dim. To enhance the intensity of the aequorin signal, Baubet and co-workers fused GFP onto apo-aequorin to form an intramolecular BRET indicator, known as GFP-Aequorin, which increased the signal intensity by 16-fold to 65-fold (Baubet et al., 2000). It is not clear whether this enhancement is due to an increase in the intensity of each flash, or if the turnover of GFP-Aequorin is slower than that of aequorin, and therefore larger amounts of GFP-Aequorin accumulate in cells as a result of expression of the transgene. GFP-Aequorin has been used to monitor Ca^{++} concentration in different subcellular locations such as nucleus (Brini et al., 1993), mitochondria (Filippin et al., 2005), ER (Kendall et al., 1992), and the Golgi apparatus (Rodriguez-Garcia et al., 2014). To monitor neuronal activity in freely-behaving zebrafish, Naumann and co-workers used GFP-Aequorin to label ~20 neurons of the hypocretin-positive hypothalamus in freely behaving zebrafish using a non-imaging approach and found that the neurons were associated with increased locomotor activity and identified two classes of neural activity corresponding to distinct swimming behaviors (Naumann et al., 2010).

GFP-Aequorin allows monitoring of Ca^{++} fluxes in cultured cells or living animals, but it still underperforms because of low brightness and slow recharge. Saito et al. developed two second-generation Ca^{++} sensors based on the continuously turning-over luciferase from *Renilla* (RLuc), e.g., BRAC (Saito et al., 2010) and Nano-Lantern(Ca^{++}) (Saito et al., 2012); the particular version of RLuc was "RLuc8," a bright mutant RLuc derived from consensus-guided mutagenesis (Loening et al., 2006). The ratiometric sensor BRAC is a fusion of Venus-CaM-M13-RLuc8 and it responds to binding of Ca^{++} to the calmodulin (CaM) moiety by intramolecular BRET between the RLuc8 and Venus; however, this ratiometric change has only a 0.6-fold dynamic range (Saito et al., 2010). Later, the same research group developed a non-ratiometric Ca^{++} sensor GECI based on Nano-Lantern (Saito et al., 2012). Nano-Lantern is a direct fusion of RLuc8 to Venus, and it showed a 10× higher luminescence intensity than that of RLuc8 alone. The Ca^{++} sensor Nano-Lantern(Ca^{++}) was constructed by insertion of the Ca^{++}-sensing domain CaM-M13 into the RLuc8 portion of Nano-lantern. Binding of Ca^{++} to CaM induces a conformational change that allows the inactive split RLuc8 to recombine and reconstitute its activity. Nano-lantern(Ca^{++}) showed a great improvement in signal intensity compared with that of aequorin and enabled visualization of biological phenomena that could not be visualized with aequorin. Moreover, both BRAC and Nano-lantern(Ca^{++}) rely on continuously turning-over luciferase that does not entail the slow recharging phenomenon that aequorin requires. However, these second-generation sensors still have weaker signal intensity than competing fluorescent sensors. For instance, Nano-Lantern(Ca^{++}) luminescence still requires long (100 ms) exposure times, and is kinetically too slow for imaging fast events such as neuronal spikes (Saito et al., 2012).

The recent development and directed evolution of NLuc initiated a third generation of sensors that made the first two generations of sensors obsolete. The NanoLuc "system" was derived from bio-engineering to optimize both a luciferase and its luciferin to achieve more efficient light emission (Hall et al., 2012). Using a small but active fragment (19 kDa) of the much larger luciferase of the deep-sea shrimp *Oplophorus gracilirostris* (106 kDa), Hall and co-workers optimized the protein structure of the luciferase as well as testing analogs of the original luciferin (coelenterazine) to discover a novel imidazopyrazinone substrate (furimazine); the end result being a luciferase/luciferin combination with a specific activity 150-fold greater than that of either FLuc or RLuc systems similarly configured for glow-type assays. The final size of Nluc (19 kD) is approximately one-half

the size of Rluc8 (36 kD) (Hall et al., 2012); small size is a useful characteristic when fusing a sensor to other proteins. Moreover, NLuc has a fast turnover rate of 6.6 reactions per second per molecule, which is 1.7-fold and 8,700-fold higher than that of RLuc8 and aequorin, respectively (Oh et al., 2019). Similarly to aequorin and Rluc, the NLuc reaction is not ATP-dependent.

Various GECI constructs based on NLuc have been developed. Ratiometric indicators such as CalfluxVTN (Yang et al., 2016) and LUCI-GECO1 (Qian et al., 2019) have been developed to detect Ca^{++} fluxes, e.g., in neurons and in conjuction with optogenetics. The ratiometric indicator, CalfluxVTN, is a fusion of three separate moieties: Venus, Troponin, and NLuc (**Figure 1**). CalfluxVTN exhibits strong Förster resonance energy transfer from NLuc to Venus under high Ca^{++} conditions (due to a conformational change mediated by binding of Ca^{++} to the Ca^{++}-sensitive Troponin moiety), whereas the energy transfer almost disappears under low Ca^{++} conditions. The ratio of Venus to NLuc exhibits a large dynamic range (~11 fold *in vitro* and 4~6-fold dynamic change in cells) (Yang et al., 2016). The design of LUCI-GECO1 is different from that of CalfluxVTN, and is constructed by the fusion of NLuc with ncpGCaMP6s, a topological variant of GCaMP6s, to form an intramolecular BRET pair (**Figure 1**). Both CalfluxVTN and LUCI-GECO1 have fluorescent domains that can be helpful for tracking their localization or abundance independently of luminescence (the Venus moiety for CalfluxVTN, the ncpGCaMP acceptor domain for LUCI-GECO1) (Qian et al., 2019). Both CalfluxVTN and LUCI-GECO1 enable sensitive imaging of Ca^{++} fluxes under the stimulation of optogenetically induced Ca^{++} concentration changes in cultured neurons.

Intensiometric GECIs based on NLuc include GeNL (Ca^{++}) (Suzuki et al., 2016), GLICO & ReBLICO (Farhana et al., 2019), and CaMBI (Oh et al., 2019) (**Figure 1**). Suzuki and co-workers developed GeNL(Ca^{++}) based on GeNL, which is a BRET molecule formed by the fusion of NLuc and mNeonGreen, the brightest green fluorescent protein, resulting in ~2-fold improvement of the emission signal intensity. The Ca^{++}-sensitive CaM-M13 domain was inserted between Gly66 and Leu67 of the NLuc moiety. The GeNL-based Ca^{++} indicator exhibited ~5-fold *in-vitro* and 1~2-fold dynamic change in response to Ca^{++} changes in cultured cells (Suzuki et al., 2016). Nagai and co-workers developed GLICO and ReBLICO (**Figure 1**) (Farhana et al., 2019), which utilizes a binary complementation reporter NanoBiT system derived from Nluc (Dixon et al., 2016). GLICO is constructed by the fusion of two fragment components of NanoBiT, large BiT (LgBiT, 18 kDa) and small BiT (SmBiT, 1.3 kDa), with GCaMP6f. Similarly, ReBLICO is constructed by the fusion of LgBiT/R-CEPIA1er/SmBiT. Both GLICO and ReBLICO possess the advantages of fluorescent and bioluminescent GECIs with a wide range of applications (Farhana et al., 2019).

For *in-vivo* imaging deeper into a tissue than just the surface, high penetration of photons is required (Men and Yuan, 2019). Moreover, bioluminescence has a theoretical advantage over fluorescence for imaging tissues because only the emission light needs to penetrate the tissues, whereas for fluorescence it is a "two-way street" and penetration of the excitatory irradiation is also critical. Furthermore, red-shifted light, including near-infrared light, has better penetration power in tissue than blue-shifted light. However, the emission spectra of most GECIs range between blue and yellow, and therefore there is strong absorption of the light by the tissues–hence, poor penetration. Chu et al. developed a BRET reporter designated as Antares by the fusion of CyOFP1-NLuc-CyOFP1, in which CyOFP1 is a fluorescent protein with a large Stokes shift (in this case, an excitation {EX} peak at 470 nm and an emission {EM} peak at 570 nm) that emits orange-red light (Chu et al., 2016). Based on Antares, Oh and co-workers developed an orange GECI known as Orange CAMBI by the insertion of the CaM-M13 sequence into the Leu133 site of Antares NLuc (**Figure 1**) (Oh et al., 2019). Orange CaMBI was used to monitor Ca^{++} fluctuations in living mouse liver, wherein the liver lobes showed regionally differing phases of Ca^{++} oscillations (Oh et al., 2019). The 580–600 nm EM peak of Orange CaMBI is still far from the ideal optical window (750–1,000 nm). In future studies, the development of brighter and more red-shifted GECIs will be helpful for sensitive detection of Ca^{++} fluctuations within deep tissues *in vivo*.

Current Commercially Available Substrates

Bioluminescence is an enzyme-catalyzed chemiluminescence reaction with a substrate in which the energy released is used to produce an intermediate in an electronically excited state, P*, which then emits a photon. The emission does not come from or depend on light absorbed, as in fluorescence, but the excited state produced is indistinguishable from that produced in fluorescence after the fluorophore has absorbed a photon. As such, the luciferin substrate is an essential partner with the luciferase in determining the characteristics of the overall luminescent system. The bioluminescence substrates D-luciferin and coelenterazine are naturally synthesized via biosynthetic pathways. D-luciferin is the most commonly used substrate of FLuc. The FLuc/D-luciferin system and its derivative series, including Fluc/CycLuc1 (Evans et al., 2014) and AKaLuc/AkaLumine-HCl (Kuchimaru et al., 2016; Iwano et al., 2018), require ATP and Mg^{++}, which can fluctuate in a circadian manner (Feeney et al., 2016). So far, a few GECIs have been constructed on the basis of FLuc luminescence with D-luciferin or its analogs. However, most bioluminescent GECIs have been constructed using luciferases that catalyze reactions involving coelenterazine or its analogs such as native coelenterazine, coelenterazine-h coelenterazine-400a, bis-coelenterazine, Furimazine (Inouye et al., 2013), and 8pyDTZ (Yeh et al., 2019). Although D-luciferin is a more stable substrate than coelenterazine, most GECIs are based on coelenterazine-catalyzing luciferases because of other advantageous characteristics (e.g., brightness, wavelength of emission, insensitivity of the emission wavelength to pH, size of the luciferases, etc.).

An ideal luminescent substrate would be non-toxic, cell permeable, and stable (long half-life). Native coelenterazine and most of its analogs are hydrophobic and consequently freely permeable through the cell membrane. Also, native coelenterazine is not toxic, but on the other hand in the presence of oxygen, it auto-oxidizes and decays relatively quickly. Promeage Corporation developed two coelenterazine

analogs, EnduRen™ and ViviRen™, that are two chemically modified substrates designed for the protection of oxidation sites in coelenterazine by esters or oxymethyl ethers (Otto-Duessel et al., 2006). Their protecting groups increase the half-life of these live-cell substrates in culture medium as compared with the unprotected coelenterazine substrates (including native coelenterazine). Because of the protecting groups, EnduRen™ and ViviRen™ cannot be oxidized by luciferases, but once they pass across plasma membranes and enter into viable cells, intracellular esterases and lipases cleave the protecting groups from the modified substrates, thus generating enzymatically activatable substrates (e.g., coelenterazine-h) that can be catalyzed by intracellular luciferases to emit light. Another benefit of using these protected substrates is that they enable a low background of auto-luminescence/oxidation in the extracellular medium because of the low concentration of active esterases and lipases in the culture medium; thus, the background signal can be decreased by 10- to 100-fold, thereby further improving the SNR (Otto-Duessel et al., 2006).

Furimazine, a highly specific substrate for NLuc, is an artificially synthesized coelenterazine analog which allows the NLuc/furimazine system that is 150× brighter than that of the Fluc/D-luciferin system (Hall et al., 2012). As mentioned earlier, third generation bioluminescent GECIs were developed based on NLuc/furimazine. However, the NLuc/furimazine system typically emits blue photons that are not optimal for *in vivo* applications that require tissue penetration. Yeh and co-workers optimized teLuc (NanoLuc-D19S/D85N/C164H)/diphenylterazine from NLuc and fused it to CyOFP1 (Yeh et al., 2017). Together with another coelenterazine analog (DTZ), the CyOFP1-teLuc-CyOFP1 combination enabled a new bioluminescence system in which the EM has two prominent peaks, one at 502 nm and the other at 580 nm, which is dramatically red-shifted from the standard NLuc/furimazine system (Yeh et al., 2017). Besides the emission of blue light, another characteristic of the NLuc/furimazine system that can be problematic in some applications is that furimazine is so hydrophobic that it exhibits poor solubility in some media (it is a tradeoff: this characteristic is good for membrane permeability, but can be troublesome for substrate application). To improve the solubility and bioavailability of the NLuc substrate in media, Su and co-workers developed a new substrate, hydrofurimazine (Su et al., 2020), that has enhanced aqueous solubility, thereby facilitating higher dose delivery to mice. In the mouse liver, hydrofurimazine with Antares (the fusion of CyOFP1-NLuc-CyOFP1) exhibited similar brightness as exhibited by the AkaLuc/AkaLumine system, thus allowing two-population imaging with these two luciferase systems.

RESULTS

A New Functional Complementation/Intensity Sensor: CalBit

In addition to the foregoing summary of bioluminescent GECIs, we also introduce here a novel bioluminescent GECI based on the functional complementation of NanoBiT. Two NanoBiT subunits, LgBiT (large fragment) and SmBiT (small fragment), have been previously optimized to interact with low affinity and reversibly to reconstitute luminescence activity (Dixon et al., 2016). We used the NanoBiT concept to construct a novel GECI by sandwiching CaM-M13 between the LgBiT (18 kDa) and SmBiT (1.3 kDa) subunits of NLuc (we used the 11S {residues 1–156} and 114 {residues 157–169} versions of LgBiT and SmBiT, respectively). The conformational changes of CaM-M13 lead to reversible changes in the distance between the LgBit and SmBit subunits in response to Ca^{++} concentration, thereby leading to Ca^{++}-dependent changes in luminescent intensity. We call these constructs that are based on NanoBiT "CalBiT", and the schematic diagram of different versions of CalBiT is shown in **Figure 2A**. The CaM-M13 sequences are from the D3cpv plasmid, in which the CaM-M13 sequence has been altered into a version with low binding ability with native CaM but high affinity to the CaM sequence within the CaM-M13 cassette

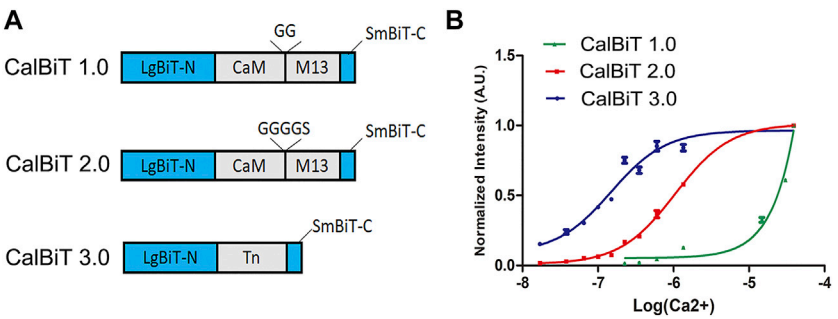

FIGURE 2 | Characteristics of CalBiTs *in vitro*. **(A)** The CaM-M13 or troponin C domain (TnC) was inserted between LgBit-N and SmBiT-C, two functional complementation fragments of NanoBiT (Dixon et al., 2016). Three versions of CalBiT were developed using different linkers and Ca^{++}-binding domains. In CalBiT1.0, two Gly residues were used as linkers between CaM and M13 and GGGGS was used as a linker between CaM and M13 in CalBiT2.0, whereas TnC was the Ca^{++}-binding domain inserted between LgBit-N and SmBiT-C in CalBiT3.0. **(B)** Comparison of [Ca^{++}] dependency *in vitro* for CalBiT1.0 (green line), CalBiT2.0 (red line), and CalBiT3.0 (blue line). The intensities of the three CalBiTs were measured by a QuantaMaster spectrofluorimeter (not using fluorescence excitation). The plotted values were normalized to the maximal signal intensity achieved at 39 mM Ca^{++}. Values for the Hill coefficient and Kd of Calflux VTN are shown in **Table 2**, mean ± standard deviations. n = 3.

TABLE 2 | Properties of three versions of CalBiT reported here.

	ΔI/I (%)	Kd (μM)	Hill coefficient
CalBiT 1.0	67	25	2.22
CalBiT 2.0	56	1.11	1.49
CalBit 3.0	5.5	0.14	1.22

(Palmer et al., 2006). Therefore, the CaM-M13 of D3cpv will be minimally responsive to the Calmodulin protein that is endogenously present in cells.

To develop GECIs with appropriate affinity for Ca^{++}, we used different linkers for the fusion of CaM and M13 (the linkers between CaM and M13 can modify the Ca^{++} binding affinity (Saito et al., 2012). We used combinations of different linkers such as GG (two Gly residues) and GGGGS (four Gly residues and one Ser residue) to construct two CaM-M13 versions of CalBiT, CalBiT1.0 and CalBiT2.0, which exhibit different Ca^{++} affinities, with 25 and 1.11 μM Kd values, respectively. We also created a version of CalBiT that is based on the Ca^{++}-binding domain (TnC) domain of troponin C from *Opsanus tau*. This is the same Ca^{++}-binding domain as that used in Twitch-3 and CalfluxVTN (Thestrup et al., 2014; Yang et al., 2016). We designated this TnC-based CalBiT as CalBiT3.0, and it showed a high Ca^{++} affinity with a Kd value of 0.14 μM.

CalBiT1.0 and CalBiT2.0 exhibited dynamic ranges of 67-fold and 56-fold, respectively (**Figure 2B** and **Table 2**). As per our knowledge, there are no reported GECIs that can exceed CalBiT1.0 and CalBiT2.0 in terms of dynamic range. The higher Kd of CalBiT1.0 may be useful for measuring Ca^{++} levels in subcompartments of cells that have higher resting Ca^{++} levels, such as the ER or mitochondria. CalBiT2.0 has a Kd value of 1.11 μM, and therefore of these three CalBiTs, it is the most suitable for the detection of Ca^{++} fluxes in the cytosolic compartment. The intensity of the CalBiT family is not sensitive to the changes in Mg^{++}, K^{+}, and Na^{+} concentrations or pH that might be expected to occur within the physiological ranges in cells; the properties for CalBiT2.0 are shown in **Figure 3**.

Histamine can stimulate Ca^{++} oscillations in HeLa cells (Sauvé et al., 1991). We expressed CalBiT2.0 in HeLa cells under the control of the CAG promoter, and used 10 μM histamine to stimulate the cells (**Figure 4A**). The CalBiT2.0 intensity signal reported robust histamine-induced Ca^{++} oscillations in the HeLa cells within a large amplitude (~10-fold) following the addition of furimazine (substrate for CalBiT) and 10 μM histamine into the culture medium. Also, different cells oscillated independently, as indicated by the out-of-phase rhythms of the CalBiT signal (**Figure 4B**, also see **Supplementary Movie S1**).

Next, we investigated whether CalBiT2.0 can be coupled with an optogenetic probe. Since melanopsin triggers the release of internal calcium stores in response to blue light (Kumbalasiri, et al., 2007; Qiu et al., 2005), we further constructed a pCAG-CalBiT2.0–2A-Opn4 plasmid having a self-cleaving T2A sequence for the fusion of CalBiT2.0 with melanopsin (gene name is *Opn4*) and formation of a co-expression sequence. We transfected CalBiT2.0 into HEK293 cells with and without *Opn4* co-expression. Ca^{++} levels in HEK293 cells transfected with

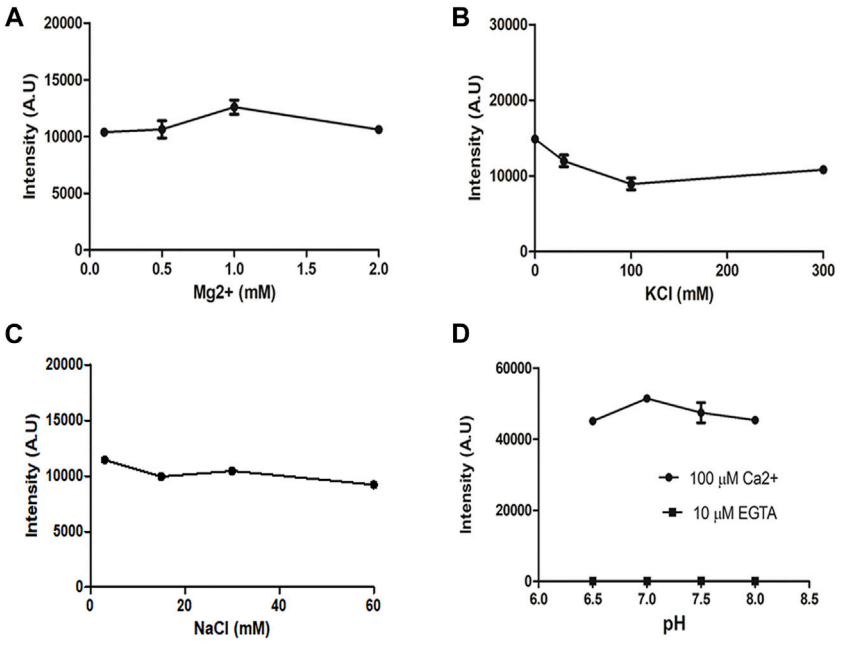

FIGURE 3 | Insensitivity of CalBiT2.0 to Mg, K^{+}, Na^{+}, and H^{+} ions *in vitro*. CalBiT2.0 was purified using a 6-His tag and the intensity was recorded in solutions with increasing concentrations of the ions as shown. The data are plotted as intensity in response to increasing [Mg^{++}] **(A)**; [K^{+}] **(B)**; [Na^{+}] **(C)**; H^{+} as pH **(D)** (mean ± standard deviations. n = 3).$^{++}$.

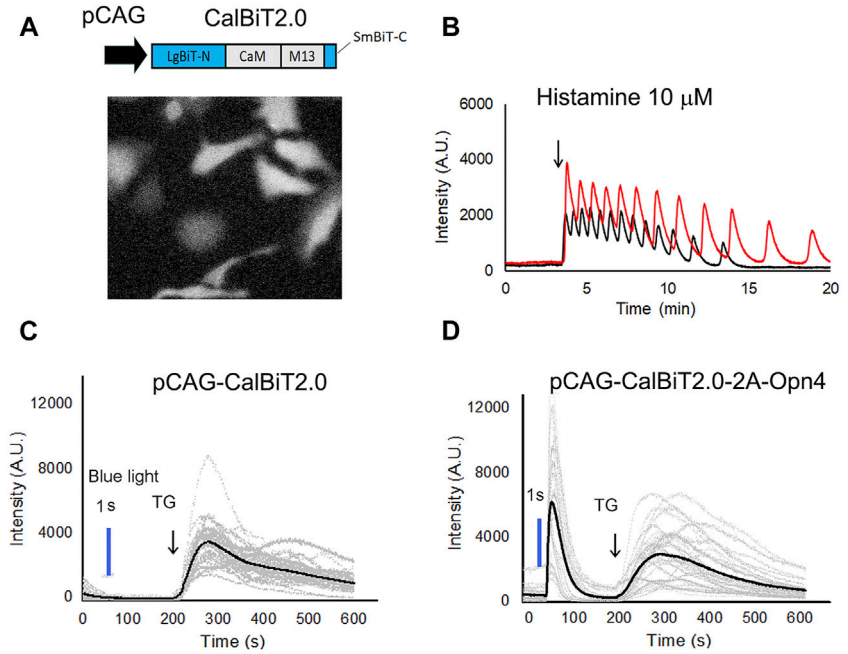

FIGURE 4 | CalBiT2.0 as a Ca^{++} sensor in mammalian cells. **(A)** CalBiT2.0 construct driven by the CAG promoter (pCAG) for mammalian cell expression (upper), and snap-shot photomicrographs of HeLa cells expressing CalBiT2.0 during the addition of furimazine substrate and 10 μM histamine into media (below). **(B)** Two HeLa cells (red and black traces, respectively) transfected with the pCAG-CalBiT2.0 plasmid. The signal intensity of the two cells showed out-of-phase oscillations in response to 10 μM histamine. The arrow shows when histamine was added. See also **Supplementary Movie S1**. **(C)** and **(D)** Monitoring Ca^{++} fluxes with CalBiT2.0 in response to an optogenetic actuator (melanopsin encoded by *Opn4*) and/or an agent that releases store-operated Ca^{++} (thapsigargin, TG). HEK293 cells transfected with pCAG-driven construct encoding CalBiT2.0 alone **(C)** or transfected with bicistronic pCAG-driven construct encoding CalBiT2.0 and melanopsin (*Opn4*, **(D)**. Both groups of cells in **(C and D)** were exposed to blue light (blue line) for 1 s, followed by the addition of 1 μM thapsigargin (at the time indicated by the arrow and "TG"). The gray lines represent the signal intensity for each cell as a function of time, and the black line represents the average signal intensity of all cells. HEK293 cells that do not express melanopsin (panel **C**) did not exhibit a Ca^{++} flux in response to the blue light pulse, but HEK293 cells that additionally express melanopsin (panel **D**) showed large Ca^{++} changes in response to optogenetic actuation. Both the groups of the HEK293 cells exhibit large and persisting changes in signal intensity in response to stimulation of store-operated Ca^{++} release by thapsigargin.

the pCAG-CalBiT2.0 plasmid increased in response to thapsigargin (TG) but not in response to blue light (**Figure 4C**). The cells with co-expression of CalBiT2.0 and melanopsin exhibited an increase in Ca^{++} levels in response to both thapsigargin and blue light (**Figure 4D**).

DISCUSSION

We summarize here the bioluminescent GECIs that are available for measuring Ca^{++} fluxes in cells. Primarily, we focus on the design and application of the third generation of bioluminescent GECIs based on NLuc which, because of their brightness, generally have an advantage for assaying rapid Ca^{++} response events with high signal-to-noise ratio (SNR) in cells, which is especially important for neurons. Although fluorescent GECIs are currently the most commonly used Ca^{++} sensors for neuron imaging in brains of living animals, however, the optic fibers that are required for those measurements (for both EX and EM) will inevitably damage the brain tissues and perturb authentic Ca^{++} responses. We believe that there is great promise toward the realization of non-invasive Ca^{++} imaging of neuronal activity without the use of the fiber optics as bioluminescent GECI technology continues to develop in the future. In particular, with genetic tools to express and target the sensor, and substrates that can cross the blood-brain barrier–in conjunction with a red-shifted EM, a completely non-invasive measurement of Ca^{++} fluxes in freely behaving animals can be accomplished. However, there are still some problems to be solved when using bioluminescent GECIs for non-invasive Ca^{++} imaging *in vivo*. For instance, the substrates need to be more compatible with tissues, especially we need to develop substrates that are permeable across the blood-brain barrier for neural imaging. A more water-soluble furimazine called hydrofurimazine has been reported to be feasible for liver tissue imaging after injection into the tail vein (Su et al., 2020), but whether it can effectively permeate across the blood brain barrier has not yet been verified. Furthermore, for deep tissue Ca^{++} imaging, the red-shifted Orange CaMBI has been developed to monitor Ca^{++} fluctuations in living animals (Oh et al., 2019). However, the 580–600 nm EM peak of Orange CaMBI is still far from the ideal far-red/infrared optical window (750–1,000 nm). We envisage the development of brighter and more red-shifted GECIs that will be optimal for sensitive detection of Ca^{++} fluxes within deep tissues *in vivo*.

We also introduce here a family of novel bioluminescent intensitometric GECIs. The calcium response range of CalBiT2.0 looks promising for monitoring physiological Ca^{++} changes in the cytosol. CalBiT2.0 exhibited large dynamic ranges *in vitro* (56-fold) and in living cells (~10-fold) (**Figures 2**, **4**). CalBiT2.0 effectively reported Ca^{++} fluxes resulting from Ca^{++} oscillations and optogenetic stimulation of melanopsin (**Figure 4**). Although the maximum signal intensity of CalBiT2.0 is weaker than that of CalfluxVTN (Yang et al., 2016), further optimization of CalBiT2.0 is warranted to create a next-generation sensor with the large dynamic range of CalBiT2.0 and a brighter signal.

DATA AVAILABILITY STATEMENT

The original contributions presented in the study are included in the article/**Supplementary Material**, further inquiries can be directed to the corresponding author.

AUTHOR CONTRIBUTIONS

JY performed experiments and analysed data; CJ designed and supervised the study; JY and CJ wrote the manuscript.

FUNDING

Research on developing new radiometric and intensitometric luminescence sensors in our lab was supported by R21MH116150 from the NIH/National Institute of Mental Health (to CHJ).

SUPPLEMENTARY MATERIAL

The Supplementary Material for this article can be found online at: https://www.frontiersin.org/articles/10.3389/fbioe.2021.773353/full#supplementary-material

REFERENCES

Baubet, V., Le Mouellic, H., Campbell, A. K., Lucas-Meunier, E., Fossier, P., and Brúlet, P. (2000). Chimeric green Fluorescent Protein-Aequorin as Bioluminescent Ca2+ Reporters at the Single-Cell Level. *Proc. Natl. Acad. Sci.* 97, 7260–7265. doi:10.1073/pnas.97.13.7260

Brini, M., Murgia, M., Pasti, L., Picard, D., Pozzan, T., and Rizzuto, R. (1993). Nuclear Ca2+ Concentration Measured with Specifically Targeted Recombinant Aequorin. *EMBO J.* 12, 4813–4819. doi:10.1002/j.1460-2075.1993.tb06170.x

Capiod, T. (2011). Cell Proliferation, Calcium Influx and Calcium Channels. *Biochimie* 93, 2075–2079. doi:10.1016/j.biochi.2011.07.015

Chiu, V. C., and Haynes, D. H. (1977). High and Low Affinity Ca2+ Binding to the Sarcoplasmic Reticulum: Use of a High-Affinity Fluorescent Calcium Indicator. *Biophysical J.* 18, 3–22. doi:10.1016/S0006-3495(77)85592-6

Chu, J., Oh, Y., Sens, A., Ataie, N., Dana, H., Macklin, J. J., et al. (2016). A Bright Cyan-Excitable orange Fluorescent Protein Facilitates Dual-Emission Microscopy and Enhances Bioluminescence Imaging *In Vivo*. *Nat. Biotechnol.* 34, 760–767. doi:10.1038/nbt.3550

Dixon, A. S., Schwinn, M. K., Hall, M. P., Zimmerman, K., Otto, P., Lubben, T. H., et al. (2016). NanoLuc Complementation Reporter Optimized for Accurate Measurement of Protein Interactions in Cells. *ACS Chem. Biol.* 11, 400–408. doi:10.1021/acschembio.5b00753

Evans, M. S., Chaurette, J. P., Adams, S. T., Jr, Reddy, G. R., Paley, M. A., Aronin, N., et al. (2014). A Synthetic Luciferin Improves Bioluminescence Imaging in Live Mice. *Nat. Methods* 11, 393–395. doi:10.1038/nmeth.2839

Farhana, I., Hossain, M. N., Suzuki, K., Matsuda, T., and Nagai, T. (2019). Genetically Encoded Fluorescence/Bioluminescence Bimodal Indicators for Ca2+ Imaging. *ACS Sens.* 4, 1825–1834. doi:10.1021/acssensors.9b00531

Feeney, K. A., Putker, M., Brancaccio, M., and O'Neill, J. S. (2016). In-Depth Characterization of Firefly Luciferase as a Reporter of Circadian Gene Expression in Mammalian Cells. *J. Biol. Rhythms* 31, 540–550. doi:10.1177/0748730416668898

Filippin, L., Abad, M. C., Gastaldello, S., Magalhães, P. J., Sandonà, D., and Pozzan, T. (2005). Improved Strategies for the Delivery of GFP-Based Ca2+ Sensors into the Mitochondrial Matrix. *Cell Calcium* 37, 129–136. doi:10.1016/j.ceca.2004.08.002

Greenwald, E. C., Mehta, S., and Zhang, J. (2018). Genetically Encoded Fluorescent Biosensors Illuminate the Spatiotemporal Regulation of Signaling Networks. *Chem. Rev.* 118, 11707–11794. doi:10.1021/acs.chemrev.8b00333

Hall, M. P., Unch, J., Binkowski, B. F., Valley, M. P., Butler, B. L., Wood, M. G., et al. (2012). Engineered Luciferase Reporter from a Deep Sea Shrimp Utilizing a Novel Imidazopyrazinone Substrate. *ACS Chem. Biol.* 7, 1848–1857. doi:10.1021/cb3002478

Hossain, M. N., Suzuki, K., Iwano, M., Matsuda, T., and Nagai, T. (2018). Bioluminescent Low-Affinity Ca2+ Indicator for ER with Multicolor Calcium Imaging in Single Living Cells. *ACS Chem. Biol.* 13, 1862–1871. doi:10.1021/acschembio.7b0101413

Inouye, S., Sato, J.-i., Sahara-Miura, Y., Yoshida, S., Kurakata, H., and Hosoya, T. (2013). C6-Deoxy Coelenterazine Analogues as an Efficient Substrate for Glow Luminescence Reaction of nanoKAZ: The Mutated Catalytic 19kDa Component of Oplophorus Luciferase. *Biochem. Biophys. Res. Commun.* 437, 23–28. doi:10.1016/j.bbrc.2013.06.026

Iwano, S., Sugiyama, M., Hama, H., Watakabe, A., Hasegawa, N., Kuchimaru, T., et al. (2018). Single-cell Bioluminescence Imaging of Deep Tissue in Freely Moving Animals. *Science* 359, 935–939. doi:10.1126/science.aaq1067

Kendall, J. M., Dormer, R. L., and Campbell, A. K. (1992). Targeting Aequorin to the Endoplasmic Reticulum of Living Cells. *Biochem. Biophys. Res. Commun.* 189, 1008–1016. doi:10.1016/0006-291x(92)92304-g

Kuchimaru, T., Iwano, S., Kiyama, M., Mitsumata, S., Kadonosono, T., Niwa, H., et al. (2016). A Luciferin Analogue Generating Near-Infrared Bioluminescence Achieves Highly Sensitive Deep-Tissue Imaging. *Nat. Commun.* 7, 11856. doi:10.1038/ncomms11856

Kumbalasiri, T., Rollag, M. D., Isoldi, M. C., Castrucci, A. M. d. L., and Provencio, I. (2007). Melanopsin Triggers the Release of Internal Calcium Stores in Response to Light†. *Photochem. Photobiol.* 83, 273–280. doi:10.1562/2006-07-11-RA-964

Kuo, I. Y., and Ehrlich, B. E. (2015). Signaling in Muscle Contraction. *Cold Spring Harb Perspect. Biol.* 7, a006023. doi:10.1101/cshperspect.a006023

Loening, A. M., Fenn, T. D., Wu, A. M., and Gambhir, S. S. (2006). Consensus Guided Mutagenesis of Renilla Luciferase Yields Enhanced Stability and Light Output. *Protein Eng. Des. Sel.* 19, 391–400. doi:10.1093/protein/gzl023

Machaca, K. (2007). Ca2+ Signaling Differentiation during Oocyte Maturation. *J. Cel. Physiol.* 213, 331–340. doi:10.1002/jcp.21194

Men, X., and Yuan, Z. (2019). Multifunctional Conjugated Polymer Nanoparticles for Photoacoustic-Based Multimodal Imaging and Cancer Photothermal Therapy. *J. Innov. Opt. Health Sci.* 12, 1930001. doi:10.1142/S1793545819300015

Montero, M., Alonso, M. T., Carnicero, E., Cuchillo-Ibáñez, I., Albillos, A., García, A. G., et al. (2000). Chromaffin-cell Stimulation Triggers Fast Millimolar Mitochondrial Ca2+ Transients that Modulate Secretion. *Nat. Cel Biol.* 2, 57–61. doi:10.1038/35000001

Morin, J. G., and Hastings, J. W. (1971). Energy Transfer in a Bioluminescent System. *J. Cel. Physiol.* 77, 313–318. doi:10.1002/jcp.1040770305

Müller, A., Kukley, M., Uebachs, M., Beck, H., and Dietrich, D. (2007). Nanodomains of Single Ca2+ Channels Contribute to Action Potential

Repolarization in Cortical Neurons. *J. Neurosci.* 27, 483–495. doi:10.1523/JNEUROSCI.3816-06.2007

Naumann, E. A., Kampff, A. R., Prober, D. A., Schier, A. F., and Engert, F. (2010). Monitoring Neural Activity with Bioluminescence during Natural Behavior. *Nat. Neurosci.* 13, 513–520. doi:10.1038/nn.2518

Niwa, H., Yamamura, K., and Miyazaki, J. (1991). Efficient Selection for High-Expression Transfectants with a Novel Eukaryotic Vector. *Gene* 108, 193–199. doi:10.1016/0378-1119(91)90434-d

Oh, Y., Park, Y., Cho, J. H., Wu, H., Paulk, N. K., Liu, L. X., et al. (2019). An orange Calcium-Modulated Bioluminescent Indicator for Non-invasive Activity Imaging. *Nat. Chem. Biol.* 15, 433–436. doi:10.1038/s41589-019-0256-z

Otto-Duessel, M., Khankaldyyan, V., Gonzalez-Gomez, I., Jensen, M. C., Laug, W. E., and Rosol, M. (2006). *In Vivo* testing of Renilla Luciferase Substrate Analogs in an Orthotopic Murine Model of Human Glioblastoma. *Mol. Imaging* 5, 57–64. doi:10.2310/7290.2006.00006

Palmer, A. E., Giacomello, M., Kortemme, T., Hires, S. A., Lev-Ram, V., Baker, D., et al. (2006). Ca2+ Indicators Based on Computationally Redesigned Calmodulin-Peptide Pairs. *Chem. Biol.* 13, 521–530. doi:10.1016/j.chembiol.2006.03.007

Pérez Koldenkova, V., and Nagai, T. (2013). Genetically Encoded Ca2+ Indicators: Properties and Evaluation. *Biochim. Biophys. Acta (Bba) - Mol. Cel Res.* 1833, 1787–1797. doi:10.1016/j.bbamcr.2013.01.011

Qian, Y., Rancic, V., Wu, J., Ballanyi, K., and Campbell, R. E. (2019). A Bioluminescent Ca 2+ Indicator Based on a Topological Variant of GCaMP6s. *Chembiochem* 20, 516–520. doi:10.1002/cbic.201800255

Qiu, X., Kumbalasiri, T., Carlson, S. M., Wong, K. Y., Krishna, V., Provencio, I., et al. (2005). Induction of Photosensitivity by Heterologous Expression of Melanopsin. *Nature* 433, 745–749. doi:10.1038/nature03345

Robertson, J. B., Davis, C. R., and Johnson, C. H. (2013). Visible Light Alters Yeast Metabolic Rhythms by Inhibiting Respiration. *Proc. Natl. Acad. Sci.* 110, 21130–21135. doi:10.1073/pnas.1313369110

Rodriguez-Garcia, A., Rojo-Ruiz, J., Navas-Navarro, P., Aulestia, F. J., Gallego-Sandin, S., Garcia-Sancho, J., et al. (2014). GAP, an Aequorin-Based Fluorescent Indicator for Imaging Ca2+ in Organelles. *Proc. Natl. Acad. Sci.* 111, 2584–2589. doi:10.1073/pnas.1316539111

Saito, K., Hatsugai, N., Horikawa, K., Kobayashi, K., Matsu-Ura, T., Mikoshiba, K., et al. (2010). Auto-luminescent Genetically-Encoded Ratiometric Indicator for Real-Time Ca2+ Imaging at the Single Cell Level. *PLoS One* 5, e9935. doi:10.1371/journal.pone.0009935

Saito, K., Chang, Y.-F., Horikawa, K., Hatsugai, N., Higuchi, Y., Hashida, M., et al. (2012). Luminescent Proteins for High-Speed Single-Cell and Whole-Body Imaging. *Nat. Commun.* 3, 1262. doi:10.1038/ncomms2248

Sauvé, R., Diarra, A., Chahine, M., Simoneau, C., Morier, N., and Roy, G. (1991). Ca2+ Oscillations Induced by Histamine H1 Receptor Stimulation in HeLa Cells: Fura-2 and Patch Clamp Analysis. *Cell Calcium* 12, 165–176. doi:10.1016/0143-4160(91)90018-a

Shimomura, O., Johnson, F. H., and Saiga, Y. (1962). Extraction, Purification and Properties of Aequorin, a Bioluminescent Protein from the Luminous Hydromedusan,Aequorea. *J. Cel. Comp. Physiol.* 59, 223–239. doi:10.1002/jcp.1030590302

Su, Y., Walker, J. R., Park, Y., Smith, T. P., Liu, L. X., Hall, M. P., et al. (2020). Novel NanoLuc Substrates Enable Bright Two-Population Bioluminescence Imaging in Animals. *Nat. Methods* 17, 852–860. doi:10.1038/s41592-020-0889-6

Suzuki, K., Kimura, T., Shinoda, H., Bai, G., Daniels, M. J., Arai, Y., et al. (2016). Five Colour Variants of Bright Luminescent Protein for Real-Time Multicolour Bioimaging. *Nat. Commun.* 7, 13718. doi:10.1038/ncomms13718

Takai, A., Nakano, M., Saito, K., Haruno, R., Watanabe, T. M., Ohyanagi, T., et al. (2015). Expanded Palette of Nano-Lanterns for Real-Time Multicolor Luminescence Imaging. *Proc. Natl. Acad. Sci. USA* 112, 4352–4356. doi:10.1073/pnas.1418468112

Thestrup, T., Litzlbauer, J., Bartholomäus, I., Mues, M., Russo, L., Dana, H., et al. (2014). Optimized Ratiometric Calcium Sensors for Functional *In Vivo* Imaging of Neurons and T Lymphocytes. *Nat. Methods* 11, 175–182. doi:10.1038/nmeth.2773

Tricoire, L., Tsuzuki, K., Courjean, O., Gibelin, N., Bourout, G., Rossier, J., et al. (2006). Calcium Dependence of Aequorin Bioluminescence Dissected by Random Mutagenesis. *Proc. Natl. Acad. Sci.* 103, 9500–9505. doi:10.1073/pnas.0603176103

Wilson, T., and Hastings, J. W. (2013). *Bioluminescence: Living Lights, Lights for Living*. Cambridge, MA: Harvard University Press, 176.

Yang, J., Cumberbatch, D., Centanni, S., Shi, S.-q., Winder, D., Webb, D., et al. (2016). Coupling Optogenetic Stimulation with NanoLuc-Based Luminescence (BRET) Ca++ Sensing. *Nat. Commun.* 7, 13268. doi:10.1038/ncomms13268

Yeh, H.-W., Karmach, O., Ji, A., Carter, D., Martins-Green, M. M., and Ai, H.-w. (2017). Red-shifted Luciferase-Luciferin Pairs for Enhanced Bioluminescence Imaging. *Nat. Methods* 14, 971–974. doi:10.1038/nmeth.4400

Yeh, H.-W., Xiong, Y., Wu, T., Chen, M., Ji, A., Li, X., et al. (2019). ATP-independent Bioluminescent Reporter Variants to Improve *In Vivo* Imaging. *ACS Chem. Biol.* 14, 959–965. doi:10.1021/acschembio.9b00150

Zurgil, N., Yarom, M., and Zisapel, N. (1986). Concerted Enhancement of Calcium Influx. Neurotransmitter Release and Protein Phosphorylation by a Phorbol Ester in Cultured Brain Neurons. *Neuroscience* 19, 1255–1264. doi:10.1016/0306-4522(86)90140-5

Conflict of Interest: The authors declare that the research was conducted in the absence of any commercial or financial relationships that could be construed as a potential conflict of interest.

The handling editor VRV declared a past co-authorship with one of the authors CHJ.

Publisher's Note: All claims expressed in this article are solely those of the authors and do not necessarily represent those of their affiliated organizations, or those of the publisher, the editors and the reviewers. Any product that may be evaluated in this article, or claim that may be made by its manufacturer, is not guaranteed or endorsed by the publisher.

frontiers in Bioengineering and Biotechnology

BRIEF RESEARCH REPORT
published: 11 November 2021
doi: 10.3389/fbioe.2021.778120

Improving the Stability of Protein–Protein Interaction Assay FlimPIA Using a Thermostabilized Firefly Luciferase

Yuki Ohmuro-Matsuyama[1,2,3], *Keiko Gomi*[4], *Takuya Shimoda*[2], *Hideki Yamaji*[2] *and Hiroshi Ueda*[1]*

[1]Laboratory of Chemistry and Life Science, Institute of Innovative Research, Tokyo Institute of Technology, Yokohama, Japan, [2]Department of Chemical Science and Engineering, Graduate School of Engineering, Kobe University, Kobe, Japan, [3]Technology Research Laboratory, Shimadzu Corporation, Kyoto, Japan, [4]Kikkoman Co., Ltd., Noda, Japan

The protein–protein interaction assay is a key technology in various fields, being applicable in drug screening as well as in diagnosis and inspection, wherein the stability of assays is important. In a previous study, we developed a unique protein–protein interaction assay "FlimPIA" based on the functional complementation of mutant firefly luciferases (Fluc). The catalytic step of Fluc was divided into two half steps: D-luciferin was adenylated in the first step, while adenylated luciferin was oxidized in the second step. We constructed two mutants of Fluc from *Photinus pyralis* (Ppy); one mutant named Donor is defective in the second half reaction, while the other mutant named Acceptor exhibited low activity in the first half reaction. To date, Ppy has been used in the system; however, its thermostability is low. In this study, to improve the stability of the system, we applied Fluc from thermostabilized *Luciola lateralis* to FlimPIA. We screened suitable mutants as probes for FlimPIA and obtained Acceptor and Donor candidates. We detected the interaction of FKBP12-FRB with FlimPIA using these candidates. Furthermore, after the incubation of the probes at 37°C for 1 h, the luminescence signal of the new system was 2.4-fold higher than that of the previous system, showing significant improvement in the stability of the assay.

Keywords: protein-protein interaction (PPI), firefly luciferase (Fluc), bioluminescence, adenylation, oxidative reaction, thermostability, assay stability

OPEN ACCESS

Edited by:
Vadim R. Viviani,
Federal University of São Carlos, Brazil

Reviewed by:
Shiburaj Sugathan,
University of Kerala, India
Wen-Chao Yang,
Central China Normal University, China

***Correspondence:**
Hiroshi Ueda
ueda@res.titech.ac.jp

Specialty section:
This article was submitted to Biomaterials, a section of the journal Frontiers in Bioengineering and Biotechnology

Received: *16 September 2021*
Accepted: *27 October 2021*
Published: *11 November 2021*

Citation:
Ohmuro-Matsuyama Y, Gomi K, Shimoda T, Yamaji H and Ueda H (2021) Improving the Stability of Protein–Protein Interaction Assay FlimPIA Using a Thermostabilized Firefly Luciferase. Front. Bioeng. Biotechnol. 9:778120. doi: 10.3389/fbioe.2021.778120

1 INTRODUCTION

The protein–protein interaction (PPI) assay is a key technology, not only in basic biology but also for practical purposes in drug screening (Gul and Hadian, 2014; Xu et al., 2016; Ashkenazi et al., 2017), diagnosis (Yuan et al., 2017; Atan et al., 2018), and food inspection (Rasooly, 2001; Katam et al., 2016). We previously developed a PPI assay based on the two divided catalytic reactions of firefly luciferase (Fluc); the first catalytic half-reaction involves the adenylation of D-luciferin (LH_2), which produces the reaction intermediate, luciferyl adenylate (LH_2-AMP), while the second half-reaction involves the oxidation of LH_2-AMP, which produces oxyluciferin (OxL). Subsequently, the excited OxL emits light (**Figure 1A**) (Branchini et al., 2011; Sundlov et al., 2012). Two Fluc mutants named Donor and Acceptor were made of Fluc from *Photinus pyralis* (Ppy). The Donor maintains the activity in the first half-reaction but is defective in the second half-reaction, while the Acceptor has a low activity in the first half-reaction but mostly retains the activity in the second-half reaction.

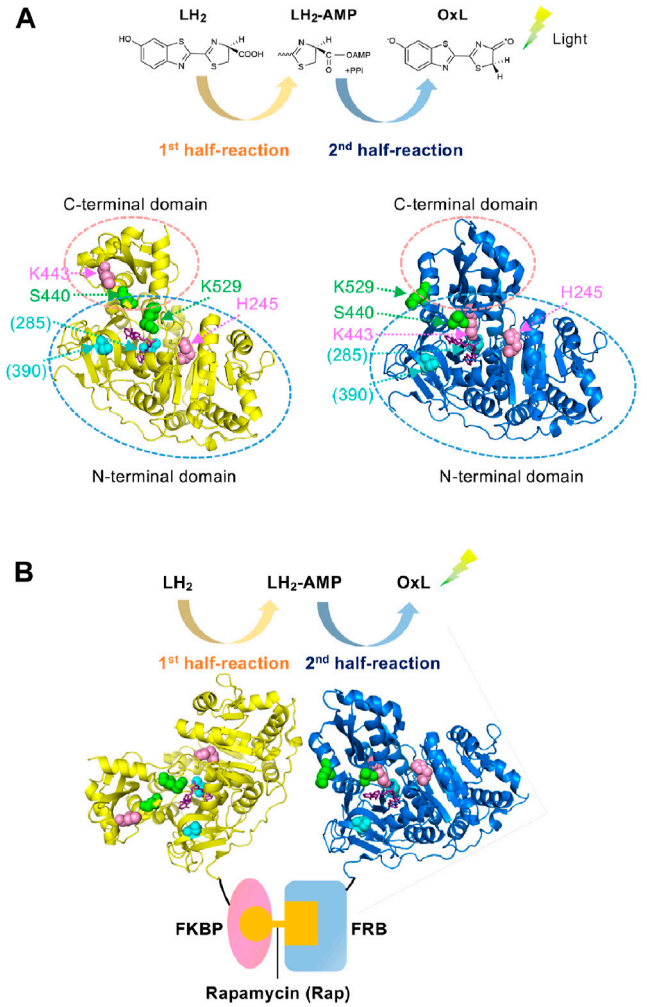

FIGURE 1 | Working principle of FlimPIA **(A)** Chemical reaction catalyzed by Fluc. Each of the two half-reactions is catalyzed by the different conformation. Ppy enzyme at the adenylation conformation (pdb 4G36) is shown in yellow, while that for the oxidative light-emitting reactions (pdb 4G37) is shown in blue. Magenta: the mutated residues in the Donor; green: those in the Acceptor; cyan: sites mutated for improved stability in LlL (in parentheses); purple; substrate analogue DLSA. The residue numbers are shown as those in Ppy throughout. **(B)** The scheme of FlimPIA in this paper. When the Donor is far from the Acceptor, LH_2-AMP produced by the Donor does not reach the Acceptor. When the PPI between FKBP and FRB is induced by rapamycin, the Donor and Acceptor are in close proximity and the Acceptor catalyzes LH_2-AMP produced by the Donor more efficiently.

Therefore, the Donor can produce the reaction intermediate, LH_2-AMP, while producing almost no OxL. However, the Acceptor cannot produce LH_2-AMP but can retain the catalytic activity for the oxidation of the intermediate. When the Donor and Acceptor are each fused to an interacting protein, the interaction of the proteins induces the approximation of the two mutant enzymes. Based on this principle, previously, we succeeded to detect 1) the interaction between FK506-binding protein 12 (FKBP12) and FKBP-rapamycin-associated protein (FRB), which interact depending on an immunosuppressant rapamycin, and 2) that between p53 and its inhibitor Mdm2, which controls apoptosis, senescence, DNA repair and cell growth. Each PPI results in a higher rate of LH_2-AMP catalysis into OxL by the Acceptor, leading to the higher light emission (**Figure 1B**). This PPI assay was named Firefly luminescent intermediate Protein-protein Interaction Assay or FlimPIA (Ohmuro-Matsuyama et al., 2013b; Ohmuro-Matsuyama et al., 2014; Kurihara et al., 2016; Ohmuro-Matsuyama and Ueda, 2016, 2017; Ohmuro-Matsuyama et al., 2018a; Ohmuro-Matsuyama et al., 2018b).

FlimPIA has several advantages. The signal/background ratio and sensitivity are higher, and the detectable size of the interacting protein is larger than that of fluorescent protein-based Förster/fluorescence resonance energy transfer assay and Fluc-based protein-fragment complementation assay. Furthermore, the thermostability of the probe is 4-fold higher than that of Fluc PCA probes because of the unstable split forms of PCA probes and the structural integrity of FlimPIA probes employing the full-length Fluc (Ohmuro-Matsuyama et al., 2013a).

However, the thermostability of FlimPIA remains insufficient owing to the low stability of Ppy. Although Fluc is applied to a hygiene monitoring system (Corbitt et al., 2000; Bakke and Suzuki, 2018), incubation of the enzyme for 1 h at 37°C resulted in an 83% decrease in signal intensity. To overcome this problem, many researchers have attempted to enhance the stability of Fluc (White et al., 1996; Koksharov and Ugarova, 2011a; Koksharov and Ugarova, 2011b; Rasouli et al., 2011; Lohrasbi-Nejad et al., 2016; Solgi et al., 2016; Branchini and Southworth, 2017; Jazayeri et al., 2017; Rahban et al., 2017; Pozzo et al., 2018; Branchini et al., 2019). In this study, we applied *Luciola lateralis* (Heike-botaru) Fluc (LlL) with mutations for thermostability and organic solvent tolerance (Kodama and Nasu, 2011) to FlimPIA for improving the stability at physiological reaction condition. LlL was obtained by random mutagenesis and screening of a high activity mutant L344A, encoding two mutations V287A and V392I.

2 MATERIALS AND METHODS

2.1 Materials

Firefly luciferin (LH_2) was obtained from Biosynth AG (Staad, Switzerland). Rapamycin was purchased from LKT Laboratories (St. Paul, MN, United States), and 3-(N-morpholino) propanesulfonic acid (MOPS) was purchased from Dojindo (Kumamoto, Japan). Oligonucleotides were synthesized by Eurofins (Tokyo, Japan). A QuikChange Site-Directed Mutagenesis Kit was obtained from Agilent (Santa Clara, CA, United States). An In-Fusion HD Cloning Kit was purchased from Takara-Bio (Shiga, Japan). Restriction enzymes and *E. coli* SHuffle T7 express lysY were obtained from New England Biolabs (Ipswich, MA, United States). *E. coli* JM109 competent cells were from SciTrove (Tokyo, Japan). Overnight Express Autoinduction System and BugBuster Master Mix were obtained from MERCK (Kenilworth, NJ, United States). Other reagents of the highest grade available were purchased from Kanto Chemicals (Tokyo,

Japan), Fujifilm-Wako Pure Chemical Industries (Osaka, Japan), or Nacalai-Tesque (Kyoto, Japan), unless otherwise indicated.

2.2 Construction of Plasmids and Their Libraries

The primers used in this study are listed in **Supplementary Table S1**. To yield pET26-LlL (H245D), QuikChange Site-Directed Mutagenesis Kit was used according to the manufacturer's protocol using pET26-LlL (Kodama and Nasu, 2011) as a template and the primer set of LlLH245S_BspHI+ and LlLH245D_BspHI+-r. To yield pET26-LlL(K443A), the same procedure was used with the primers of LlLK443A_AseI+ and LlLK443A_AseI+-r. To yield pET-LlL (K529A; the lysine was at 529 in Ppy and 530 in LlL), the primers of LlLK530A_MfeI+ and LlLK530A_MfiI+-r were used, whereas primers of LlL K530Q_AgeI+ and LlLK530Q_AgeI+-r were used to yield pET26-LlL(K529Q).

To yield FK506-binding protein 12 (FKBP12)-fused LlL(K443A), LlL(K443A) was amplified by polymerase chain reaction (PCR) using pET26-LlL(K443A) as a template and the primers LlLNotG4S-for and LlLXho-rev. The amplified fragment was digested with *Not*I and *Xho*I and inserted between the *Not*I and *Xho*I sites of pET32-FKBP-Donor, which was constructed previously (Ohmuro-Matsuyama et al., 2013b). To yield FKBP12-rapamycin complex-associated protein (FRB)-fused LlL (K529Q), LlL (K529Q) was amplified by PCR using pET26-LlL(K529Q) as a template and the primers LlLNotG4S-for and LlLXho-rev. The amplified fragment was digested with *Not*I and *Xho*I and inserted between the same sites of pET32-FRB-Donor.

To acquire the FRB-LlL(S440X/K529Q) library, QuikChange site-directed mutagenesis was performed using pET32-FRB-LlL(K529Q) as a template and LlL447_KpnI and LlLS440X-KpnI-r as primers. Because bulky amino acids such as leucine and phenylalanine at the position of 440 were suitable as the Ppy Acceptor, the primer LlLS440X-KpnI-r was designed to selectively encode these residues at this position. To yield the FRB-LlL(S440M/K529X) library, the full-length pET32-FRB-LlL (S440M/K529Q) was amplified and site-directly mutated via PCR using the primer set of LlL530X-for and LlLS530X-rev. As the primers encoded 15 nt each of homologous sequences at the ends, both ends of the amplified fragment were recombined by In-Fusion cloning. To yield the FKBP-LlL(H245X/K443A) library, the full-length pET32-FKBP-LlL(K443A) was amplified and site-directly mutated via PCR with the primer set of LlLH245X-for and LlLH245X-rev. Both ends of the amplified fragment were recombined using In-Fusion cloning. To obtain the FKBP-LlLH245E/K443A library, pET32-FKBP-LlL(H245E/K443A) was amplified and site-directly mutated via PCR using the primer set of LlLK443X-for and LlLK443X-rev. Both ends of the amplified fragment were recombined using In-Fusion cloning, according to the manufacturer's protocol. To confirm that each resultant library contained sufficient variation of the mutants, the DNA sequences of several clones were analyzed.

To obtain FRB-LlL(S440F/K529Q) and FRB-LlL(S440W/K529Q), pET32-FRB-LlL (S440M/K529M) was amplified and site-directly mutated by PCR using the primers LlLS440FW-KpnI and LlL447-KpnI-r, and both ends of the amplified fragment were fused by In-Fusion cloning. pET32-FKBP-LlL(H245E/K443A/I530R) and pET32-FKBP-LlL(H245E/K443A/I530K) were obtained similarly using pET32-FKBP-LlL(H245E/K443A) as a template and LlLI530X-for and LlLI530X-rev as primers.

2.3 Expression and Characterization of the Probe Proteins

The probes for FlimPIA were expressed in *E. coli* SHuffle T7 Express lysY and purified using the TALON metal affinity resin, as described previously (Ohmuro-Matsuyama et al., 2013b). The purification profile of each protein was confirmed by SDS-PAGE (**Supplementary Figure S1**). The kinetic constants K_m and V_{max} for LH_2-AMP were determined using chemically synthesized LH_2-AMP, as described previously (Kurihara et al., 2016). To estimate the adenylation activity, the amount of enzymatically formed LH_2-AMP was measured using the N-domain of Ppy Fluc, as described previously (Ayabe et al., 2005).

2.4 Detection of PPI by FlimPIA

An equimolar mixture of the Donor and Acceptor candidates with or without rapamycin in the reaction buffer (50 µl of 100 mM MOPS and 10 mM $MgSO_4$; pH 7.3), wherein the concentration of $MgSO_4$ and pH were previously optimized for FlimPIA (Ohmuro-Matsuyama et al., 2013b), was added to a well of a 96-well half-area white plate (3693, Corning, Tokyo, Japan). The measurement was performed using a microplate-based luminometer AB2350 at 0.1-s intervals (ATTO, Tokyo, Japan) immediately after injecting 50 µl of the reaction buffer containing the substrates (LH_2 and ATP). Rapamycin was dissolved in dimethyl sulfoxide (DMSO), and the same amount of DMSO (0.1%) was added as a vehicle to the negative sample. In the optimized buffer conditions, 1 mM of coenzyme A was added to reduce the amount of spontaneously produced dehydroluciferyl-AMP (L-AMP), which acts as a competitor of LH_2-AMP and inhibits light emission. The addition of coenzyme A results in the conversion of L-AMP to dehydroluciferyl-coenzyme A, which does not act as a competitor (Fontes et al., 1997; Fraga et al., 2005; Kurihara et al., 2016).

2.5 Screening

E. coli SHuffle T7 Express lys Y was transformed with the mutant plasmids and cultured on LBA agar plates (10 g/L tryptone, 5 g/L yeast extract, 5 g/L sodium chloride, 100 µg/ml ampicillin, and 15 g/L agar). The colonies were selected and cultured using the Overnight Express Autoinduction System in a 96-well culture plate at 30°C overnight. The pellet of each clone was lysed in 50 µl of BugBuster Master Mix, according to the manufacturer's protocol. The lysates were centrifuged, and the supernatants were collected. To estimate the adenylation activity, each supernatant (10 µl) was added to 90 µl of reaction buffer containing 150 µM of LH_2 and 2 mM ATP. To estimate the oxidative luminescent activity, 90 µl of the reaction buffer containing 200 nM LH_2-AMP was added to each supernatant (10 µl).

3 RESULTS AND DISCUSSION

3.1 Testing Ppy Mutations in LlL-Based FlimPIA

Previously, two mutant Ppy enzymes were used to perform FlimPIA. Fluc consists of N- and C-terminal domains, and the C-terminal domain rotates ~140° according to the reaction proceeds from the first to the second half-reaction (Branchini et al., 2011; Sundlov et al., 2012). Based on this knowledge, the H245D/K443A/I530R mutant of Ppy has been used as the Donor that produces luciferyl adenylate (Ohmuro-Matsuyama et al., 2013b). Among the three mutations, two mutations, H245D near the active site (Ayabe et al., 2005) and K443A in the C-terminal domain (Branchini et al., 2005), suppress the oxidative reaction steps, thereby playing a central role as the Donor. In contrast, being K529 as an essential residue for the adenylation reaction (Branchini et al., 2000), Ppy enzymes with the mutations K529A, K529Q, K529Q/S440F, or K529Q/S440W were used as the Acceptors. While the mutations at K529 are most important for the Acceptor that suppress the adenylation reaction, those for S440 located in the hinge region between the N- and C-terminal domains augment the steric hindrance to suppress the adenylation conformation (Ohmuro-Matsuyama et al., 2018b) (**Figure 1**). Based on these previous observations, we first obtained the LlL mutants of H245D, K443A, K529A, and K529Q and then analyzed their kinetic constants for LH_2-AMP (**Supplementary Table S2**). As a result, suppression of the oxidative reaction steps by H245D and K443A mutations was observed. In contrast, the reaction rate was relatively maintained by the K529A and K529Q mutant LlLs. Next, the relative amounts of LH_2-AMP produced by the same mutant LlLs were compared to analyze the adenylation activity. The amount of adenylate produced by K443A was higher than that produced by H245D, K529A, and K529Q (**Supplementary Figure S2**). These results indicate that K443A might act as a Donor because of its high adenylation activity and low oxidative activity, suggesting the importance of K443 in the oxidative steps in LlL. However, the adenylation activity of H245D was too low to act as a Donor. Next, FlimPIA using heterogeneous pairs of LlL-based and Ppy-based mutants was performed using 1) the pair of FKBP-fused LlL (K443A) as a Donor and FRB-fused Ppy Acceptor and 2) the pair of FKBP-fused Ppy Donor and FRB-fused LlL(K529Q) as a possible Acceptor (**Supplementary Figure S3**). Since the interaction between FKBP and FRB is rapamycin (Rap) dependent (Brown et al., 1994; Chiu et al., 1994; Chen et al., 1995), the luminescence intensity was expected to increase with the addition of Rap. As a result, when rapamycin was added to the first pair of LlL(K443A) and Ppy Acceptor, a higher luminescent intensity was observed in the presence of Rap. However, the second pair of LlL K529Q and Ppy Donor did not show a Rap-dependent signal.

3.2 Strategy for Screening LlL Mutants

Because the mutations of H245D and K529Q were not functional for LlL-based FlimPIA, we decided to perform screening for more suitable mutants by the following procedure. 1) The saturation mutagenesis libraries, K529X, S440X, H245X, and K443X were screened. *E. coli* was transformed using the library, and several clones were expressed in the cultured *E. coli* using an autoinduction system. 2) To analyze the first half reaction, ATP and LH_2 were added to the lysates of *E. coli*. 3) To assess the second half reaction, LH_2-AMP was added to the lysates. 4) The ratios of the luminescence intensity of 2) and that of 3) were calculated. When the ratio was high, the clone was suitable as a Donor, whereas when the ratio was low, the clone was suitable as an Acceptor.

3.3 Screening for LlL Acceptor

As the interacting proteins, FKBP and FRB were used, and the rapamycin dependent interaction was detected (**Figure 1B**). To obtain an LlL-based Acceptor, an FRB/S440X/K529Q library was created, and 96 colonies were selected for screening. Among them, five clones, namely, FRB/S440N/K529Q (two clones), FRB/S440K/K529Q (two clones), and FRB/S440M/K529Q, were selected. The proteins of FRB/S440S/K529Q, FRB/S440N/K529Q, FRB/S440K/K529Q, and FRB/S440M/K529Q were expressed in *E. coli* and purified. Using each protein as the Acceptor and FKBP/Ppy Donor, FlimPIA was performed (**Figure 2A**). The luminescence intensities of all Acceptor candidates were increased by the addition of Rap. The maximum signal/background (S/B) ratios were in the order of S440M>S440K>S440N>S440S.

In our previous study (Ohmuro-Matsuyama and Ueda, 2017), Ppy (S440F/K529Q) and Ppy (S440W/K529Q) were found to be suitable as the Acceptors. To validate the results of the screening in this study, FRB/LlL(S440F/K529Q) and FRB/LlL(S440W/K529Q) were also prepared and tested. FlimPIA was performed using each FRB/LlL Acceptor candidate and FKBP/Ppy Donor. When Rap was added, the maximum S/B ratios of S440F/K529Q and S440W/K529Q were lower than those of S440S/K529Q (**Supplementary Figure S4**). Previously, we showed that the optimization of ATP concentration was important for the suppression of the background luminescence intensity and the enhancement of the S/B ratio. Although different concentrations of ATP (20, 5, and 1.25 mM) were examined, the maximum S/B ratios remained low. Therefore, we concluded that the screening method was suitable for the selection of mutants for FlimPIA.

To obtain a better mutant Acceptor, the FRB/LlL S440M/K529X library was constructed. In addition, 6 out of 192 clones were selected. The truncated Flucs were observed in two clones, and the remaining clones were FRB/S440M/K529R (two clones), FRB/S440M/K529M, and FRB/S440M/K529N. FlimPIA was performed using each FRB/LlL Acceptor candidate and FKBP/Ppy Donor. As a result, all candidates acted as the Acceptors, and the maximum S/B ratio of K529M was remarkably higher than that of the other candidates (**Figure 2B**).

3.4 Screening for LlL Donor

To obtain an LlL-based Donor, screening was performed using the FKBP/LlL H245X/K443A library. As a result, 9 out of 288 clones were selected. These included FKBP/H245N/K443A (three clones), FKBP/H245E/K443A (three clones), FKBP/H245A/K443A, FKBP/H245S/K443A, and FKBP/H245P/K443A.

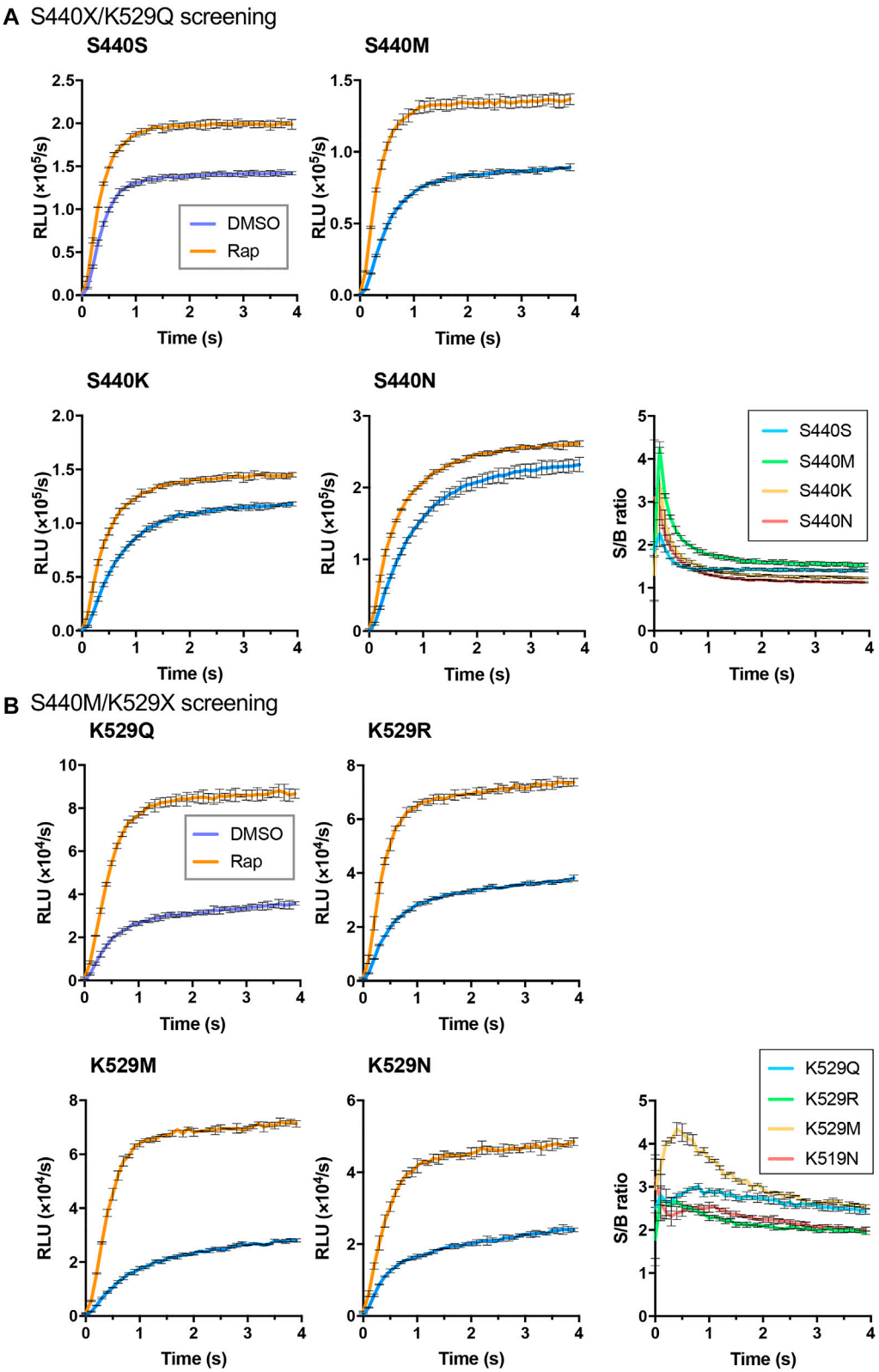

FIGURE 2 | Screening of LIL Acceptors. **(A)** S440X/K529Q screening. **(B)** S440M/K529X screening. Error bar: ±1 × SD (n = 3). Ppy Donor (50 nM) and each candidate of LIL Acceptor (50 nM) were reacted with ATP (10 mM) and LH_2 (37.5 μM) with/without rapamycin (Rap) (50 nM).

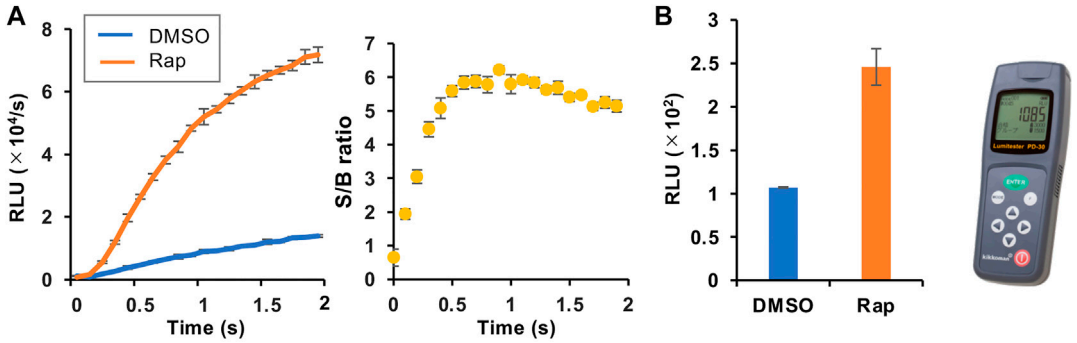

FIGURE 3 | Optimization of the assay condition. **(A)** FlimPIA under the optimized condition. **(B)** Measurement using the Lumitester PD-30. Error bar: ±1 × SD (*n* = 3). Ppy Donor (50 nM) and LIL Acceptor (50 nM) were reacted with LH_2 (33 μM) and ATP (1.25 mM) with/without rapamycin (Rap, 50 nM) in the presence of 1 mM of coenzyme A.

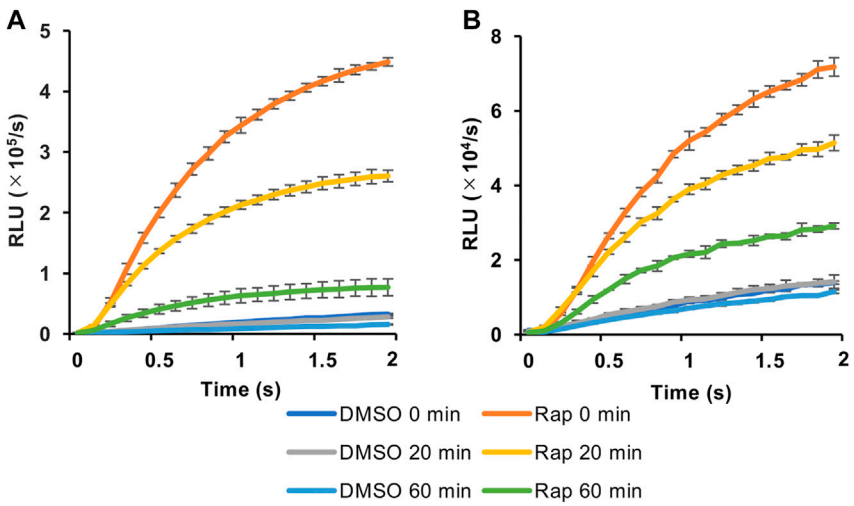

FIGURE 4 | Effect of preincubation in FlimPIA. **(A)** The pair of FKBP-Ppy Donor and FRB-Ppy Acceptor. **(B)** The pair of FKBP-Ppy Donor and FRB-LIL Acceptor. After the incubation at 37°C FlimPIA was performed. Error bar: ±1 × SD (*n* = 3). Donor (50 nM) and Acceptor (50 nM) were reacted with LH_2 (33 μM) and ATP (1.25 mM) with/without rapamycin (Rap, 50 nM). The reaction buffer was added with 1 mM of coenzyme A.

FlimPIA was performed using each candidate and FRB/LIL(S440M/K529M). Among these candidates, only H245E/K443A showed increased luminescence intensity upon Rap addition (**Supplementary Figure S5**). However, the S/B ratio and luminescence intensity were significantly lower than those obtained with the FKBP/Ppy Donor and FRB/LIL(S440M/K529M).

To improve the LIL Donor, another screening was performed using the FKBP/LIL (H245E/K443X) library. Among 288 clones, H245E/K443R (three clones), H245E/K443G (two clones), H245E/K443V, H245E/K443P, and H245E/K443A were selected. FlimPIA was performed using each candidate and the FRB/Ppy Acceptor (K529Q/S440F) (**Supplementary Figure S6A**). However, the results using these candidates were almost the same for several ATP concentrations. In addition, FRB/LIL (H245E/K443A/I530R) and FRB/LIL (H245E/K443A/I530K) were expressed in *E. coli* and purified. Because I530R is effective for the stabilization of ATP in Ppy (Fujii et al., 2007), we hypothesized that the positively charged amino acids at this position (I530R, I530K) might enhance the adenylation activity. However, in FlimPIA, these mutations decreased the luminescence intensities and could not increase the S/B ratios under several ATP concentrations (**Supplementary Figure S6B**).

3.5 FlimPIA Using Selected Enzymes

Because of the low intensity and S/B ratio of the FKBP/LIL Donor (H245E/K443A) and FRB/LIL Acceptor (S440M/K529M), the stability of the heterologous pair of the Ppy Donor and LIL Acceptor was compared with that of the LIL Donor and LIL Acceptor pair (**Supplementary Figure S7**). FlimPIA was performed after two overnight incubations at 25°C. Unexpectedly, the S/B ratio and luminescence intensity of the

heterologous pair were as high as those of the homologous pair. Ppy Donor might have produced an excess amount of LH_2-AMP for FlimPIA; therefore, the lower production of LH_2-AMP after the incubation might not remarkably change the result of FlimPIA.

We then selected the heterologous pair of FKBP/Ppy Donor and FRB/LlL Acceptor and optimized the assay conditions. Under the conditions of 1.25 mM ATP, 33 μM LH_2, and 1 mM coenzyme A, the maximum S/B ratio reached more than 6 (**Figure 3A**). In addition, when a portable luminometer (Lumitester PD-30, Kikkoman, Chiba, Japan) was used, an S/B ratio of more than 2 was attained (**Figure 3B**). Finally, we compared the thermostabilities of the Ppy pair of FKBP/Ppy Donor and FRB/Ppy Acceptor and the heterologous pair of FKBP/Ppy Donor and FRB/LlL Acceptor at 37°C (**Figure 4**). After incubation for 20 and 60 min, the signal intensity of the Ppy pair was 58 and 17%, while the intensity of the heterologous pair was still 72 and 41%, respectively.

In conclusion, we succeeded in improving the thermostability of FlimPIA, enhancing its applicability for clinical diagnoses and inspections in such as food factories. In this study, it was revealed that both Ppy Fluc and LlL Fluc could be applied to FlimPIA. In the future, other similar enzymes such as Eluc (enhanced green-emitting luciferase) (Nakajima et al., 2010), which produces a brighter light in mammalian cells, may further expand the scope of this assay in practical applications.

DATA AVAILABILITY STATEMENT

The original contributions presented in the study are included in the article/**Supplementary Material**, further inquiries can be directed to the corresponding author.

AUTHOR CONTRIBUTIONS

YO-M designed and carried out the experiments and wrote the manuscript draft. TS performed the experiments under the guidance of YO-M and HY. HU conceived the study and wrote the manuscript with the inputs from all authors. KG supplied the LlL gene and supported the experiments. HY provided research facility and funding. All authors have given approval to the final version of the manuscript.

FUNDING

This work was supported in part by JSPS KAKENHI Grant Numbers JP18H03851 (to HU), and JP17K06920 (to YO-M) from the Japan Society for the Promotion of Science, Japan.

ACKNOWLEDGMENTS

We thank Chiaki Toyama for experimental help, the Biomaterials Analysis Division, Open Facility Center, Tokyo Institute of Technology for DNA sequence analysis, and the support by Dynamic Alliance for Open Innovation Bridging Human, Environment and Materials from MEXT, Japan.

SUPPLEMENTARY MATERIAL

The Supplementary Material for this article can be found online at: https://www.frontiersin.org/articles/10.3389/fbioe.2021.778120/full#supplementary-material

REFERENCES

Amiri Dash Atan, N., Koushki, M., Rezaei Tavirani, M., and Ahmadi, N. A. (2018). Protein-Protein Interaction Network Analysis of Salivary Proteomic Data in Oral Cancer Cases. *Asian Pac. J. Cancer Prev.* 19 (6), 1639–1645. doi:10.22034/APJCP.2018.19.6.1639

Ashkenazi, S., Plotnikov, A., Bahat, A., and Dikstein, R. (2017). Effective Cell-free Drug Screening Protocol for Protein-Protein Interaction. *Anal. Biochem.* 532, 53–59. doi:10.1016/j.ab.2017.05.030

Ayabe, K., Zako, T., and Ueda, H. (2005). The Role of Firefly Luciferase C-Terminal Domain in Efficient Coupling of Adenylation and Oxidative Steps. *FEBS Lett.* 579 (20), 4389–4394. doi:10.1016/j.febslet.2005.07.004

Bakke, M., and Suzuki, S. (2018). Development of a Novel Hygiene Monitoring System Based on the Detection of Total Adenylate (ATP+ADP+AMP). *J. Food Prot.* 81 (5), 729–737. doi:10.4315/0362-028X.JFP-17-432

Branchini, B. R., Fontaine, D. M., Southworth, T. L., Huta, B. P., Racela, A., Patel, K. D., et al. (2019). Mutagenesis and Structural Studies Reveal the Basis for the Activity and Stability Properties that Distinguish the Photinus Luciferases Scintillans and Pyralis. *Biochemistry* 58 (42), 4293–4303. doi:10.1021/acs.biochem.9b00719

Branchini, B. R., Murtiashaw, M. H., Magyar, R. A., and Anderson, S. M. (2000). The Role of Lysine 529, a Conserved Residue of the Acyl-Adenylate-Forming Enzyme Superfamily, in Firefly Luciferase. *Biochemistry* 39 (18), 5433–5440. doi:10.1021/bi9928804

Branchini, B. R., Rosenberg, J. C., Fontaine, D. M., Southworth, T. L., Behney, C. E., and Uzasci, L. (2011). Bioluminescence Is Produced from a Trapped Firefly Luciferase Conformation Predicted by the Domain Alternation Mechanism. *J. Am. Chem. Soc.* 133 (29), 11088–11091. doi:10.1021/ja2041496

Branchini, B. R., and Southworth, T. L. (2017). A Highly Sensitive Biosensor for ATP Using a Chimeric Firefly Luciferase. *Methods Enzymol.* 589, 351–364. doi:10.1016/bs.mie.2017.01.004

Branchini, B. R., Southworth, T. L., Murtiashaw, M. H., Wilkinson, S. R., Khattak, N. F., Rosenberg, J. C., et al. (2005). Mutagenesis Evidence that the Partial Reactions of Firefly Bioluminescence Are Catalyzed by Different Conformations of the Luciferase C-Terminal Domain. *Biochemistry* 44 (5), 1385–1393. doi:10.1021/bi047903f

Brown, E. J., Albers, M. W., Bum Shin, T., Ichikawa, K., Keith, C. T., Lane, W. S., et al. (1994). A Mammalian Protein Targeted by G1-Arresting Rapamycin-Receptor Complex. *Nature* 369 (6483), 756–758. doi:10.1038/369756a0

Chen, J., Zheng, X. F., Brown, E. J., and Schreiber, S. L. (1995). Identification of an 11-kDa FKBP12-Rapamycin-Binding Domain within the 289-kDa FKBP12-Rapamycin-Associated Protein and Characterization of a Critical Serine Residue. *Proc. Natl. Acad. Sci.* 92 (11), 4947–4951. doi:10.1073/pnas.92.11.4947

Chiu, M. I., Katz, H., and Berlin, V. (1994). RAPT1, a Mammalian Homolog of Yeast Tor, Interacts with the FKBP12/rapamycin Complex. *Proc. Natl. Acad. Sci.* 91 (26), 12574–12578. doi:10.1073/pnas.91.26.12574

Corbitt, A. J., Bennion, N., and Forsythe, S. J. (2000). Adenylate Kinase Amplification of ATP Bioluminescence for hygiene Monitoring in the Food and Beverage Industry. *Lett. Appl. Microbiol.* 30 (6), 443–447. doi:10.1046/j.1472-765x.2000.00744.x

Fontes, R., Dukhovich, A., Sillero, A., and Sillero, M. A. G. (1997). Synthesis of Dehydroluciferin by Firefly Luciferase: Effect of Dehydroluciferin, Coenzyme A and Nucleoside Triphosphates on the Luminescent Reaction. *Biochem. Biophysical Res. Commun.* 237 (2), 445–450. doi:10.1006/bbrc.1997.7161

Fraga, H., Fernandes, D., Fontes, R., and Esteves da Silva, J. C. G. (2005). Coenzyme A Affects Firefly Luciferase Luminescence Because it Acts as a Substrate and

Not as an Allosteric Effector. *FEBS J.* 272 (20), 5206–5216. doi:10.1111/j.1742-4658.2005.04895.x

Fujii, H., Noda, K., Asami, Y., Kuroda, A., Sakata, M., and Tokida, A. (2007). Increase in Bioluminescence Intensity of Firefly Luciferase Using Genetic Modification. *Anal. Biochem.* 366 (2), 131–136. doi:10.1016/j.ab.2007.04.018

Gul, S., and Hadian, K. (2014). Protein-protein Interaction Modulator Drug Discovery: Past Efforts and Future Opportunities Using a Rich Source of Low- and High-Throughput Screening Assays. *Expert Opin. Drug Discov.* 9 (12), 1393–1404. doi:10.1517/17460441.2014.954544

Jazayeri, F. S., Amininasab, M., and Hosseinkhani, S. (2017). Structural and Dynamical Insight into Thermally Induced Functional Inactivation of Firefly Luciferase. *PLoS One* 12 (7), e0180667. doi:10.1371/journal.pone.0180667

Katam, R., Sakata, K., Suravajhala, P., Pechan, T., Kambiranda, D. M., Naik, K. S., et al. (2016). Comparative Leaf Proteomics of Drought-Tolerant and -susceptible Peanut in Response to Water Stress. *J. Proteomics* 143, 209–226. doi:10.1016/j.jprot.2016.05.031

Kodama, Y., and Nasu, E. (2011). *Firefly Luciferase and Gene Thereof, and Process for Production of Firefly Luciferase*. PCT patent application. WO 2011/058767 A1, Geneva, Switzerland: World Intellectual Property Organization.

Koksharov, M. I., and Ugarova, N. N. (2011a). Thermostabilization of Firefly Luciferase by *In Vivo* Directed Evolution. *Protein Eng. Des. Sel* 24 (11), 835–844. doi:10.1093/protein/gzr044

Koksharov, M. I., and Ugarova, N. N. (2011b). Triple Substitution G216N/A217L/S398M Leads to the Active and Thermostable Luciola Mingrelica Firefly Luciferase. *Photochem. Photobiol. Sci.* 10 (6), 931–938. doi:10.1039/c0pp00318b

Kurihara, M., Ohmuro-Matsuyama, Y., Ayabe, K., Yamashita, T., Yamaji, H., and Ueda, H. (2016). Ultra Sensitive Firefly Luciferase-based Protein-protein Interaction Assay (FlimPIA) Attained by Hinge Region Engineering and Optimized Reaction Conditions. *Biotechnol. J.* 11 (1), 91–99. doi:10.1002/biot.201500189

Lohrasbi-Nejad, A., Torkzadeh-Mahani, M., and Hosseinkhani, S. (2016). Hydrophobin-1 Promotes Thermostability of Firefly Luciferase. *FEBS J.* 283 (13), 2494–2507. doi:10.1111/febs.13757

Nakajima, Y., Yamazaki, T., Nishii, S., Noguchi, T., Hoshino, H., Niwa, K., et al. (2010). Enhanced Beetle Luciferase for High-Resolution Bioluminescence Imaging. *PLoS One* 5 (4), e10011. doi:10.1371/journal.pone.0010011

Ohmuro-Matsuyama, Y., Chung, C.-I., and Ueda, H. (2013a). Demonstration of Protein-Fragment Complementation Assay Using Purified Firefly Luciferase Fragments. *BMC Biotechnol.* 13, 31. doi:10.1186/1472-6750-13-31

Ohmuro-Matsuyama, Y., Hara, Y., and Ueda, H. (2014). Improved Protein-Protein Interaction Assay FlimPIA by the Entrapment of Luciferase Conformation. *Anal. Chem.* 86 (4), 2013–2018. doi:10.1021/ac403065v

Ohmuro-Matsuyama, Y., Nakano, K., Kimura, A., Ayabe, K., Ihara, M., Wada, T., et al. (2013b). A Protein-Protein Interaction Assay Based on the Functional Complementation of Mutant Firefly Luciferases. *Anal. Chem.* 85 (16), 7935–7940. doi:10.1021/ac4016825

Ohmuro-Matsuyama, Y., and Ueda, H. (2016). A Protein-Protein Interaction Assay FlimPIA Based on the Functional Complementation of Mutant Firefly Luciferases. *Methods Mol. Biol.* 1461, 131–142. doi:10.1007/978-1-4939-3813-1_10

Ohmuro-Matsuyama, Y., and Ueda, H. (2017). Ultrasensitive Firefly Luminescent Intermediate-Based Protein-Protein Interaction Assay (FlimPIA) Based on the Functional Complementation of Mutant Firefly Luciferases. *Methods Mol. Biol.* 1596, 119–130. doi:10.1007/978-1-4939-6940-1_8

Ohmuro-Matsuyama, Y., Yamashita, T., Gomi, K., Yamaji, H., and Ueda, H. (2018a). Evaluation of Protein-Ligand Interactions Using the Luminescent Interaction Assay FlimPIA with Streptavidin-Biotin Linkage. *Anal. Biochem.* 563, 61–66. doi:10.1016/j.ab.2018.10.010

Ohmuro-Matsuyama, Y., Yamashita, T., Lin, H., Yamaji, H., and Ueda, H. (2018b). Improved Sensitivity of Firefly Luminescent Intermediate-Based Protein Interaction Assay Using Ser 440 Mutant with Lower Adenylation Activity. *Luminescence* 33 (1), 125–130. doi:10.1002/bio.3381

Pozzo, T., Akter, F., Nomura, Y., Louie, A. Y., and Yokobayashi, Y. (2018). Firefly Luciferase Mutant with Enhanced Activity and Thermostability. *ACS Omega* 3 (3), 2628–2633. doi:10.1021/acsomega.7b02068

Rahban, M., Salehi, N., Saboury, A. A., Hosseinkhani, S., Karimi-Jafari, M. H., Firouzi, R., et al. (2017). Histidine Substitution in the Most Flexible Fragments of Firefly Luciferase Modifies its thermal Stability. *Arch. Biochem. Biophys.* 629, 8–18. doi:10.1016/j.abb.2017.07.003

Rasooly, A. (2001). Surface Plasmon Resonance Analysis of Staphylococcal Enterotoxin B in Food. *J. Food Prot.* 64 (1), 37–43. doi:10.4315/0362-028x-64.1.37

Rasouli, S., Hosseinkhani, S., Yaghmaei, P., and Ebrahim-Habibi, A. (2011). Effects of Sucrose and Trehalose on Stability, Kinetic Properties, and thermal Aggregation of Firefly Luciferase. *Appl. Biochem. Biotechnol.* 165 (2), 572–582. doi:10.1007/s12010-011-9276-1

Solgi, Z., Khalifeh, K., Hosseinkhani, S., and Ranjbar, B. (2016). Surface Arginine Saturation Effect on Unfolding Reaction of Firefly Luciferase: A Thermodynamic and Kinetic Perspective. *Photochem. Photobiol.* 92 (5), 688–693. doi:10.1111/php.12614

Sundlov, J. A., Fontaine, D. M., Southworth, T. L., Branchini, B. R., and Gulick, A. M. (2012). Crystal Structure of Firefly Luciferase in a Second Catalytic Conformation Supports a Domain Alternation Mechanism. *Biochemistry* 51 (33), 6493–6495. doi:10.1021/bi300934s

White, P. J., Squirrell, D. J., Arnaud, P., Lowe, C. R., and Murray, J. A. H. (1996). Improved Thermostability of the North American Firefly Luciferase: Saturation Mutagenesis at Position 354. *Biochem. J.* 319 (Pt 2), 343–350. doi:10.1042/bj3190343

Xu, M., Liu, C., Zhou, M., Li, Q., Wang, R., and Kang, J. (2016). Screening of Small-Molecule Inhibitors of Protein-Protein Interaction with Capillary Electrophoresis Frontal Analysis. *Anal. Chem.* 88 (16), 8050–8057. doi:10.1021/acs.analchem.6b01430

Yuan, X., Chen, J., Lin, Y., Li, Y., Xu, L., Chen, L., et al. (2017). Network Biomarkers Constructed from Gene Expression and Protein-Protein Interaction Data for Accurate Prediction of Leukemia. *J. Cancer* 8 (2), 278–286. doi:10.7150/jca.17302

Conflict of Interest: Authors YO-M and KG are employed by Shimadzu Corporation and Kikkoman, Co., Ltd. respectively.

The remaining authors declare that the research was conducted in the absence of any commercial or financial relationships that could be construed as a potential conflict of interest.

Publisher's Note: All claims expressed in this article are solely those of the authors and do not necessarily represent those of their affiliated organizations, or those of the publisher, the editors and the reviewers. Any product that may be evaluated in this article, or claim that may be made by its manufacturer, is not guaranteed or endorsed by the publisher.

frontiers in Bioengineering and Biotechnology

ORIGINAL RESEARCH
published: 19 November 2021
doi: 10.3389/fbioe.2021.767313

Improvements in Smartphone and Night Vision Imaging Technologies Enable Low Cost, On-Site Assays of Bioluminescent Cells

*Mark Wienhold[1], Andrew Kirkpatrick[1], Tingting Xu[2], Steven Ripp[1,2], Gary Sayler[1] and Dan Close[1]**

[1]490 BioTech, Inc., Knoxville, TN, United States, [2]Center for Environmental Biotechnology, The University of Tennessee, Knoxville, TN, United States

Technologies enabling on-site environmental detection or medical diagnostics in resource-limited settings have a strong disruptive potential compared to current analytical approaches that require trained personnel in laboratories with immobile, resource intensive instrumentation. Handheld devices, such as smartphones, are now routinely produced with CPUs, RAM, wireless data transfer capabilities, and high-resolution complementary metal oxide semiconductor (CMOS) cameras capable of supporting the capture and processing of bioluminescent signals. In theory, combining the capabilities of these devices with continuously bioluminescent human cell-based bioreporters would allow them to replicate the functionality of more expensive, more complex, and less flexible platforms while supporting human-relevant conclusions. In this work, we compare the performance of smartphone (CMOS) and night vision (image intensifier) devices with *in vivo* (CCD camera), and *in vitro* (photomultiplier tube) laboratory instrumentation for monitoring signal dynamics from continuously bioluminescent human cellular models under toxic, stable, and induced expression scenarios. All systems detected bioluminescence from cells at common plating densities. While the *in vivo* and *in vitro* systems were more sensitive and detected signal dynamics representing cellular health changes earlier, the night vision and smartphone systems also detected these changes with relatively similar coefficients of variation and linear detection capabilities. The smartphone system did not detect transcriptional induction. The night vision system did detect transcriptional activation, but was less sensitive than the *in vivo* or *in vitro* systems and required a stronger induction before the change could be resolved.

Keywords: bioluminescence, luciferase, optical imaging, remote sensing, smartphone, portable analytical device, toxicity

OPEN ACCESS

Edited by:
Elisa Michelini,
University of Bologna, Italy

Reviewed by:
Laura Mezzanotte,
Erasmus Medical Center, Netherlands
Shimshon Belkin,
Hebrew University of Jerusalem, Israel
Jan Roelof Van Der Meer,
University of Lausanne, Switzerland

****Correspondence:***
Dan Close
dan.close@490biotech.com

Specialty section:
This article was submitted to Biomaterials, a section of the journal Frontiers in Bioengineering and Biotechnology

Received: *30 August 2021*
Accepted: *02 November 2021*
Published: *19 November 2021*

Citation:
Wienhold M, Kirkpatrick A, Xu T, Ripp S, Sayler G and Close D (2021) Improvements in Smartphone and Night Vision Imaging Technologies Enable Low Cost, On-Site Assays of Bioluminescent Cells. Front. Bioeng. Biotechnol. 9:767313. doi: 10.3389/fbioe.2021.767313

INTRODUCTION

Most laboratory grade fluorescent or luminescent screening instrumentation utilizes either charge coupled device (CCD) cameras or photomultiplier tubes (PMTs) as sensors. CCD cameras consist of many light-sensitive areas that convert photons into electrons when struck, such that the number of electrons collected will be directly proportional to the photon intensity recorded within each area. This allows them to be very sensitive, but also makes them vulnerable to dark current noise if not

integrated with cooling systems to reduce thermal noise (Janesick, 2001). For laboratory use, they are often mounted atop a light-tight box where samples can be placed, but as their technology improves, they are starting to become imbedded within plate reader instrumentation to enable multimodal high-content imaging. PMTs are most commonly incorporated into plate reader-based instrumentation. Like CCD cameras they also report photon detection via the production of an electron. However, as their name suggests, that signal is then amplified using a series of electrodes to generate an output current proportional to the input flux. While this amplification procedure makes them highly sensitive, their incorporation into plate readers with integrated mechanical systems that move them from well to well, or move the plate relative to their position, results in devices that are relatively large and fragile and requires stable, higher voltage power supplies (Wright, 2017). The complexity and sensitivity of these types of sensors requires them to be integrated into instrumentation that can protect them from physical harm, supply them with the necessary power for optimal performance, and protect them from background light exposure. This often prevents their use in mobile operations, where small sizes, low power requirements, and robustness against environmental exposure is prioritized. Because of these reasons, there is an increased interest in the use of smaller, less expensive, and more easily obtainable instrumentation to perform biological assays, especially under low resource constraints.

Two optical detection devices readily available to the public and specifically designed for use under adverse conditions are night vision optics and smartphones. Originally produced for military applications, but now available to sportsman and for general use, night vision optics are often manufactured specifically to survive mobile use under harsh environmental conditions with minimal power requirements. Their sensor elements are image intensifiers that operate similar to PMTs. Within these sensors, photons strike a photocathode, are converted to electrons, and are then accelerated towards a higher voltage microchannel plate where they are amplified and retransmitted in a straight line towards a phosphor screen. Following absorption by the phosphor screen, they are reemitted as photons so they can be viewed or recorded by the observer (Haque and Muntjir, 2017). Although sparsely reported in biological research, night vision optics have previously been used to visualize luminescence, but not to quantify luminescent output.

Due to their ubiquity in modern society, smartphones are designed to meet similar usage requirements. The cameras in these devices are primarily based on complementary metal oxide semiconductor (CMOS) sensors. These sensors are similar to CCD sensors, but due to their method of manufacture can integrate a number of processing and control functions directly onto the sensor. Unlike CCDs, this allows them to operate with lower power consumption, a single master clock, and a single-voltage power supply (El Gamal and Eltoukhy, 2005). Although their performance was originally overshadowed by CCDs, due to competition in the consumer mobile electronics market and their prevalence in these devices, there has been heavy investment towards improving their performance that now makes them direct competitors with CCD sensors. CMOS sensors have broader representation in biological publications, having been used to measure chemiluminescence (Zangheri et al., 2015; Zangheri et al., 2021), and firefly (Kim et al., 2017; Michelini et al., 2019; Hattori et al., 2020) and bacterial luciferase (Ma et al., 2020) activity in animals, cultured human cells, and bacteria.

Bioluminescence has become an attractive assay modality for these applications because most study targets do not naturally produce luminescent signals, it can be easily measured using a variety of different sensor types, and host cells can modulate post-treatment signal intensity to achieve a wide detection range. One of the most common bioluminescent assay types is toxicity screening. It is well suited to this role because it can be genetically encoded into a target, such as a cell or bacterium, and the presence, absence, or change in intensity of the post-exposure bioluminescent signal provides an easily interpreted indication of the level of toxicity to the host. An example of this is the Microtox toxicity test, which is based on the use of a bioluminescent bacterium and has served as an official standard for acute toxicity screening in countries such as Germany (DIN 38412-26:1994-05) and the United States (ASTM method D5660-96). As our understanding of the complexities and dynamics of cytotoxic responses between species and within the different tissue types of a single species has improved (Slater, 2001), there has been a push to identify human-relevant toxicity using new assay procedures that can more quickly and inexpensively screen large numbers of samples, work within a variety of tissue types, and perform under a variety of conditions (Judson et al., 2013). Most of this testing relies on laboratory-based assays that require expensive, complex, and resource intensive analytical instrumentation to report the activation of specific cytotoxic pathways, the production of cytotoxic marker compounds such as released enzymes or reactive oxygen species, or the state of cellular metabolism as a representative proxy for cellular health (Fan and Wood, 2007). However, there is a growing body of work that seeks to perform these assays with lower cost, more readily available instrumentation in the hope of enabling more efficient testing or making testing available in areas without access to scientific facilities.

An additional complication for bioluminescent assays is that they are hindered by the high cost of the requisite chemical substrate addition that must be performed prior to each generation of signal, the hands-on time required to scale cultures due to obligatory sample destruction concurrent with interrogation, and the inability to provide continuously bioluminescent signals at timescales enabling detection by the less sensitive sensor technologies that are found in portable, inexpensive devices. A possible solution for overcoming these limitations is to replace their use with newer continuously bioluminescent reporter technologies that continuously produce bioluminescence and autonomously adjust signal intensity to reflect real-time changes in host viability (Xu et al., 2014; Conway et al., 2020). These reporter systems use the host's rapidly fluctuating pool of $FMNH_2$ to modulate signal

intensity similar to how luciferin-dependent reporters use total ATP availability as a limiting reagent to control signal intensity. However, unlike externally excited reporters, they genetically encode both the luciferin and luciferase production components of the bioluminescent pathway. This allows them to continuously recycle luciferin, which negates the need to externally induce signal activation, potentiates bioluminescent signal production across the full host lifetime, and allows the phenotype to be passaged to further generations (Close et al., 2010).

Their ability to encode both the luciferase and luciferin synthesis components of the bioluminescent pathway enable them to function continuously, while their ability to assemble luciferin using only metabolites endogenous to the eukaryotic cytoplasm and their dependence on reducing power, rather than ATP, as a limiting reagent allows them to self-modulate signal intensity (Close et al., 2009). Comparative testing has shown that continuously bioluminescent technologies yield similar results to their luciferin-dependent counterparts (Class et al., 2015). They are also capable of maintaining a consistent bioluminescent output intensity under steady state conditions and do not show any toxic effect on the host cell despite the reactive potential of their aldehyde-based luciferin (Close et al., 2011). Rather, unlike the short lived and dynamic bioluminescent signals observed following luciferin supplementation using externally excited systems, the consistent signal of continuously bioluminescent reporters should produce a sufficiently stable signal output to enable reliable detection using less sensitive hardware.

To evaluate the performance of the image intensifier and CMOS-based consumer sensor systems relative to traditional laboratory-based equipment, this work compares their ability to detect and quantify these bioluminescent signals from target cells. These comparisons will provide a basis for better determining if such consumer-focused tools can be used by appropriately trained scientific personnel to enable lower cost, point-of-use human cellular assays and are not to suggest that untrained individuals with access to these systems should endeavor to perform potentially hazardous work. This work compares the detection and performance capabilities of commercially available smartphone (CMOS-based, Google Pixel 4a 5G) and night vision (Image intensifier, AGM Global Vision PVS-12 NL2 night vision monocular) devices with laboratory grade *in vivo* imaging systems (CCD camera-based, IVIS Lumina), and multimode plate readers (PMT-based, BMG CLARIOstar plate reader) for the detection of bioluminescence under common assay objectives.

MATERIALS AND METHODS

Cell Culture and Processing

Continuously bioluminescent LiveLight^{TM} HEK293 cells (490 BioTech) were used for all assays except reporter induction, in which case HEK293 wild type cells (ATCC) were used. All cells were grown in Dulbecco's Modified Eagle's Medium (DMEM; Gibco) supplemented with 10% Fetal Bovine Serum (FBS; Gibco), 1× GlutaMAX (Gibco), and 1 × Penicillin/Streptomycin (Gibco). All cultures were maintained at 37°C and 5% CO_2 in a humidified incubator for routine growth. For CCD-based assays cells were grown in optically opaque black bottom plates. For PMT, image intensifier (night vision), and CMOS (smartphone)-based assays cells were grown in optically opaque white bottom plates.

Steady State Assays

Minimum signal threshold, linear detection, signal variability, and signal resolution assays were performed using serial dilutions of LiveLight^{TM} HEK293 cells ranging from 2×10^5 to two cells/well in either white or black-walled opaque bottom 96-well plates depending on the imaging method used. Cells were imaged 4 h post plating. This time point was selected because it was sufficient to allow settling and adherence to the plate, but before confluence-based declines in cellular health and growth rate were observed at the highest plating density. Ambient background light levels were measured and maintained as internally consistent for each imaging method and identical between the night vision and CMOS systems.

Dynamic Signal Assays

For toxicity assays, LiveLight^{TM} HEK293 cells were plated at 2×10^4 cells/well in 96-well plates, incubated overnight at 37°C and 5% CO_2 in a humidified incubator, and then challenged with either 0, 200, 400, or 800 µg Zeocin (Gibco)/mL. Following challenge, cells were assayed for 24 h and viability was determined relative to the untreated control. For transcriptional induction assays, wild type HEK293 cells were grown in DMEM supplemented with 10% FBS, 1 × GlutaMAX, and 1 × Penicillin/Streptomycin. All cultures were maintained at 37°C and 5% CO_2 in a humidified incubator for routine growth and transfected with the LiveReport^{TM} CRE (cyclic AMP response element) kit (490 BioTech) according to the manufacturer's instructions. Twenty-four hours after transfection, cells were challenged with 1×10^{-5} M forskolin (Cayman Chemical) and assayed for 24 h.

CCD Camera Imaging

As a representative CCD-camera-based instrument, bioluminescence was measured using an IVIS Lumina imaging system (PerkinElmer). Luminescent detection was performed across 1 min acquisition periods using medium binning and an F/Stop of 1. A stage temperature of 37°C was used for all assays and measurements were acquired at 1 h intervals.

PMT Imaging

As a representative PMT-based instrument, bioluminescence was measured using a CLARIOstar multimode plate reader (BMG Labtech). Luminescent detection was performed across 1 s acquisition periods for each well using the automatic gain control settings of the instrument's firmware. Because this instrument features an atmospherically controlled imaging chamber, cells were maintained at 37°C and 5% CO_2 throughout the duration of the assay and measurements were acquired at 1 h intervals.

Image Intensifier Imaging

As a representative image intensifier-based instrument, bioluminescence was detected using a PVS-12 NL2 night vision monocular (AGM Global Vision). Because this instrument does not have innate acquisition capabilities, images were acquired by mounting a camera to the monocular using the supplied adaptor. Assays were performed by maintaining cells at 37°C and 5% CO_2 in a humidified incubator between readings, then transferring the plate to a dark room under ambient atmospheric conditions for image acquisition at 8 h intervals before returning the cells to the incubator until the next acquisition.

CMOS Imaging

As a representative CMOS-based sensor, bioluminescence was detected using a Pixel 4a 5G smartphone (Google). The built-in camera on this device has 12.2 MP dual-pixel, 1.4 µm pixel width, and f/1.7 aperture capabilities built upon an IMX363 back-illuminated, stacked CMOS sensor (Sony). Assays were performed by maintaining cells at 37°C and 5% CO_2 in a humidified incubator until imaging, then transferring the plate to a dark room under ambient atmospheric conditions for image acquisition. To represent usage by an end user with minimal training, photos were taken using the default "Night Sight" settings recommended by the manufacturer for capturing low light images.

Image Processing Software and Statistical Analysis

Image acquisition and bioluminescence measurements made on the IVIS Lumina instrument were performed using Living Image v4.7.2 Software (PerkinElmer). Bioluminescent measurements made on the CLARIOstar plate reader were processed using MARS Data Analysis Software v3.41 (BMG Labtech). Images obtained using the PVS-12 NL2 night vision monocular and Pixel 4a 5G smartphone were processed using ImageJ v1.52 (National Institutes of Health). All statistical analyses were performed using Microsoft Excel. Average values were calculated as arithmetic means. Errors were calculated as ± the standard error of the mean (S.E.M.) for all measurements. Statistical differences between groups were identified using Student's t-tests with p-value cut offs of $p \leq 0.05$. Pearson's correlation coefficients were used to determine R^2 values showing relationships between different parameters.

RESULTS

Ambient Light Measurement and Standardization for Comparison Between Systems

Ambient light detection was measured for each of the assay systems. The plate reading chamber within the PMT-based plate reader had the lowest level of ambient light at 3.12×10^4 ($\pm 6.15 \times 10^3$) photons/sec. The imaging chamber of the CCD camera-based system was the second lowest, with a measured value of 3.04×10^5 ($\pm 7.45 \times 10^4$) photons/sec. The image intensifier and CMOS systems were both tested in the same location under low light conditions. The background for those measurements was slightly higher (2.88×10^6 ($\pm 7.13 \times 10^5$) and 2.65×10^6 ($\pm 6.63 \times 10^5$), respectively). However, these values were not statistically different from one another ($p = 0.8249$). To enable comparison between the systems that report values in arbitrary units (PMT, image intensifier, and CMOS), a standard was measured in each device and a conversion factor was determined to convert values to photons/sec. Each RLU reported by the PMT corresponded to 45.7 photons/sec. Each raw integrated density reported by the image intensifier corresponded to 64.5 photons/sec. Each raw integrated density reported by the CMOS corresponded to 277.8 photons/sec.

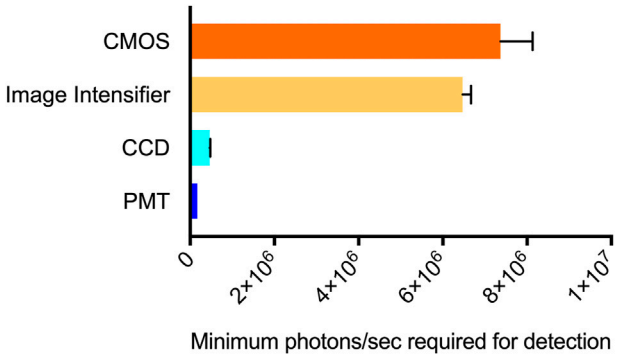

FIGURE 1 | Minimum signal detection threshold for each system. The CMOS (smartphone) system required the highest level of flux to detect bioluminescence at 7.37×10^6 photons/sec. The image intensifier (night vision) system was slightly more sensitive, requiring a minimum of 6.47×10^6 photons/sec. The CCD and PMT systems had lower minimum detection thresholds of 4.65×10^5 and 1.7×10^5 photons/sec, respectively. $n = 3$; error = S.E.M.

Minimum Signal Detection Threshold

CCD camera-based imaging detected bioluminescence down to a minimum threshold of 200 cells/well. Based on the photon counts from the CCD camera, this represents a flux requirement of 4.65×10^5 ($\pm 1.27 \times 10^4$) photons/sec. PMT-based imaging detected luminescence at a minimum threshold of 20 cells/well. This represents a minimum flux requirement of 1.7×10^5 ($\pm 2.26 \times 10^4$) photons/sec. The image intensifier and CMOS-based systems were less sensitive. Both displayed a minimum signal detection threshold of 2×10^3 cells/well. Their minimum flux requirements were measured as 6.47×10^6 ($\pm 1.98 \times 10^5$) photons/sec (image intensifier) and 7.37×10^6 ($\pm 7.63 \times 10^5$) photons/sec (CMOS) (**Figure 1**). All systems successfully detected bioluminescence at cell counts representative of common cellular plating densities for assays performed in 96-well plates (ATCC, 2021) and at flux values below what could be detected by the naked eye.

Linear Detection Capabilities

The linear detection capabilities of each imaging method were determined by serially diluting continuously bioluminescent LiveLight™ HEK293 cells (490 BioTech) from 2×10^5 to two

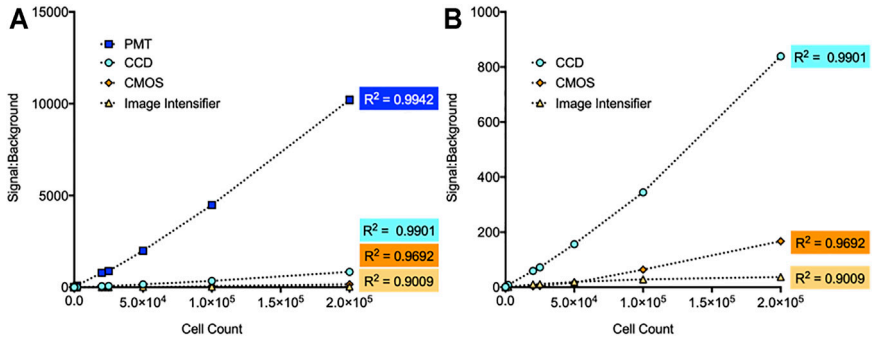

FIGURE 2 | Comparison of linear detection capabilities for different imaging systems. **(A)** Each system showed a high correlation between measured signal: background and cell count. The PMT system had the strongest correlation (R^2 = 0.9942), followed by the CCD system (R^2 = 0.9901), CMOS system (R^2 = 0.9692), and image intensifier system (R^2 = 0.9009). **(B)** Zoomed view of the CCD, CMOS, and image intensifier data points. *n* = 3; error = S.E.M.

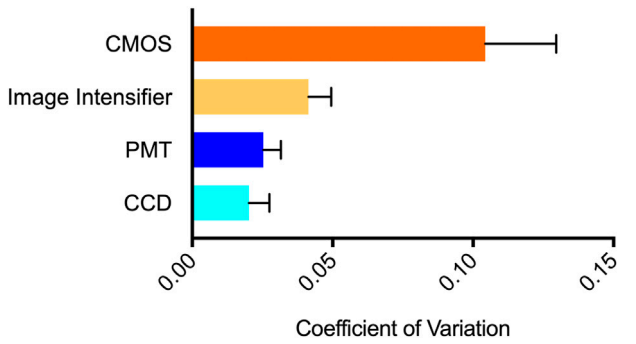

FIGURE 3 | Variability of steady state signal detection visualized using coefficient of variation. The CMOS system showed the highest variability (CV = 0.1043), followed by the image intensifier system (0.0414), PMT system (0.0252), and CCD system (0.0202). *n* = 6; error = S.E.M.

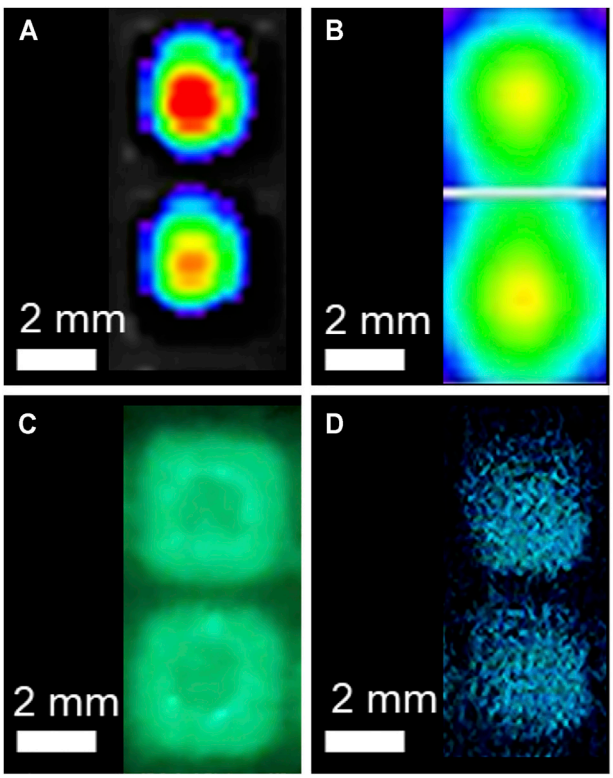

FIGURE 4 | Signal resolution testing of the CCD, PMT, image intensifier, and CMOS detection systems. The **(A)** CCD, **(C)** image intensifier, and **(D)** CMOS systems all successfully resolved individual signals separated by 0.87 mm following plating of continuously bioluminescent cells in the 384-well plate format. The **(A)** CCD and **(B)** PMT images are pseudocolor images with warmer colors representing relatively increased signal intensity. The **(B)** PMT-based plate reader was not able to acquire signal from multiple wells simultaneously, so each pixel in this image represents a 1.1 μm^2 area within the well to demonstrate the resolution of signal discrimination within the well.

cells/well to ensure measurement across the full spectrum of detectable cell numbers for each system as determined above. The minimum detection threshold of each system observed during this experiment remained consistent with the previous values. Both the CCD and PMT-based imaging systems showed strong linear correlations between the plated cell number and measured bioluminescent signal (R^2 = 0.9901 and 0.9942, respectively). CMOS-based imaging also had a strong linear correlation (R^2 = 0.9692). The image intensifier-based system was highly correlated (R^2 = 0.9009), but less capable of identifying a linear correlation compared to other imaging methods (**Figure 2**). This may be indicative of a lower signal: background ratio resulting from performance of the measurement outside of a light tight imaging chamber, or it may be due to higher detection variability. The latter possibility is further explored below.

Variability of Steady State Signal Detection

The coefficient of variation (CV) was calculated for each system to determine its variability during steady state signal acquisition (**Figure 3**). Individual CV values were obtained from replicate measurements made using six different concentrations of cells to determine if signal intensity affected variability. However, no intensity-based effects were observed. The CCD, PMT, and image intensifier devices had statistically similar (p = 0.1477) CV values of 0.0202, 0.0252, and 0.0414, respectively. The CMOS device had

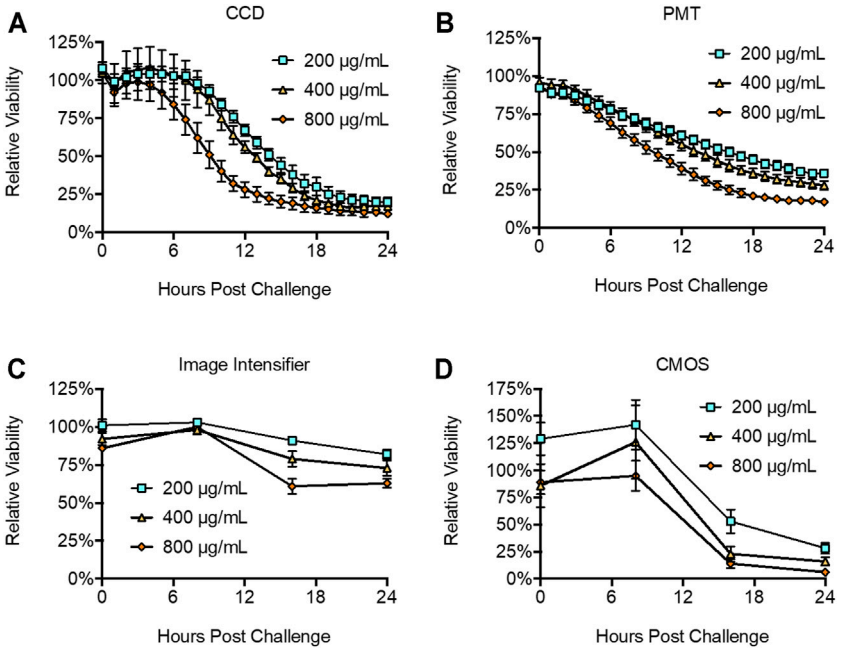

FIGURE 5 | Detection of toxicity following Zeocin challenge. The **(A)** CDD, **(B)**, PMT, **(C)** image intensifier, and **(D)** CMOS systems all successfully reported declines in cellular health following Zeocin challenge. The **(B)** PMT system was the most sensitive, reporting significant differences at 1 h post challenge. The **(A)** CCD system did not discriminate a statistically significant change until 8 h post challenge, while the **(C)** image intensifier and **(D)** CMOS systems both required 16 h to identify a statistically significant change. Untreated control is defined as 100% viability. n = 3; error = S.E.M.

a CV of 0.1043, which was statistically different than the other three imaging methods (p = 0.0394).

Signal Resolution Limitation

To determine each systems ability to discriminate spatially constrained independent signals, LiveLight™ HEK293 cells were plated in the 384-well format. This created a 0.87 mm non-luminescent separation between wells. The CCD, image intensifier, and CMOS systems all successfully resolved individual wells at this distance (**Figure 4**). The PMT-based image, which was obtained in a plate reader and therefore not capable of observing multiple wells simultaneously, was tested by performing a 30 × 30 matrix well scan to generate a pseudocolor image representative of bioluminescence intensity within the well at a resolution of 1.1 μm^2/pixel. Both the CCD and PMT produced pseudocolor images based on luminescent intensity. The image intensifier and CMOS images could be directly observed.

Detection of Toxicity

Continuously bioluminescent LiveLight™ HEK293 cells were plated at 2×10^4 cells/well in a 96-well plate and challenged with increasing concentrations of the cytotoxic chemical Zeocin to monitor toxicity. Zeocin induces toxicity by intercalating into DNA and inducing double strand breaks that ultimately compromise genomic integrity and result in cell death (Ehrenfeld et al., 1987). CCD imaging identified a significant (p = 0.0468) decrease in cellular health at 8 h post treatment from the 800 µg/ml challenge, with toxicity decreasing in a dose dependent pattern for lower challenges (**Figure 5A**). PMT-based imaging identified a statistically significant (p = 0.0268) decrease in cellular health within 1 h post treatment at the 800 µg/ml challenge. It also showed toxicity decreasing in a dose dependent manner and detected statistically significant decreases from all challenge levels after the 3 h time point (200 µg/ml, p = 0.0104; 400 µg/ml, p = 0.0095; 800 µg/ml, p = 0.0028) (**Figure 5B**). The image intensifier and CMOS-based systems identified statistically significant changes in cellular health at the 800 µg/ml (p = 0.0003 and 0.0023), 400 µg/ml (p = 0.0063 and 0.0041), and 200 µg/ml (p = 0.0062 and 0.0075) dosage levels in a dose dependent manner (**Figures 5C,D**). However, this detection was not observed until 16 h post challenge.

Detection of Reporter Induction

The LiveReport™ CRE Assay Kit (490 BioTech) was used to compare each systems' ability to detect bioluminescent reporter induction. The LiveReport™ CRE assay kit was transfected into wild-type HEK293 cells according to the manufacturer's instructions. Transfected cells were treated with forskolin to activate cyclic AMP response element (CRE) expression and assayed over a 24 h period. CCD imaging detected significant (p = 0.0074) induction beginning at 2 h post treatment, with peak induction ranging from 6 to 12 h post treatment and maximum induction reaching 53-fold over control (**Figure 6**). PMT imaging detected significant (p = 0.0005) induction starting 2 h post treatment, with peak induction ranging from 5 to 10 h post treatment and a maximum induction of 76-fold over control.

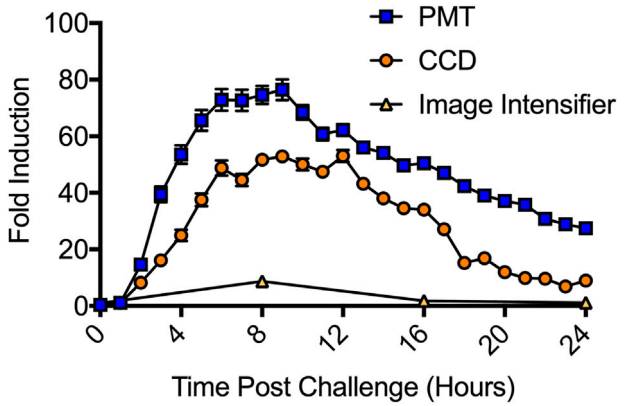

FIGURE 6 | Detection of CRE induction following forskolin treatment. The PMT system was the most sensitive system tested. It detected significant induction at 2 h post treatment and recorded a maximum induction of 76-fold. The CCD system was the second most sensitive. It also detected significant induction at 2 h post treatment, but only recorded a 53-fold maximum induction. The image intensifier system required 8 h to report a significant induction and only observed a 9-fold maximum induction. The CMOS system (not shown) did not detect significant induction at any surveyed time point. n = 3; error = S.E.M.

For both CCD and PMT imaging, induction was still significant (p = 0.0001 for both) 24 h post treatment. The image intensifier identified peak induction at 8 h post treatment, with a 9-fold increase over control. Induction was still statistically significant (p = 0.0001) at 16 h post treatment, but was no longer significant (p = 0.0893) at 24 h post treatment. CMOS imaging did not detect induction.

DISCUSSION

This study compares how specialized, laboratory-focused bioluminescent imaging systems (CCD camera-based *in vivo* imaging system and PMT-based multi-mode plate reader) perform relative to less expensive, more mobile, consumer-focused alternatives (image intensifier-based night vision and CMOS-based smartphone camera). However, it is important to note there is a wide range of CCD, PMT, image intensifier, and CMOS-based systems available, and this study only explores one example of each. Each imaging method is also dependent on the software used for image processing. In this regard, the laboratory focused IVIS Lumina and BMG CLARIOstar both use proprietary software that is provided with the instruments at the time of purchase. These software packages are responsible for both data processing and machine management. It is therefore likely the results obtained in these tests would be different if alternative software was used to control machine functionality and collect raw data from the instrument sensors. Because they are not designed primarily for laboratory usage, the AGM PVS-12 NL2 monocular and Google Pixel 4a 5G do not come with software specifically for this task. Therefore, we obtained image files from these instruments and analyzed them with the open source ImageJ software, which is commonly utilized for such applications and widely available. Just as with the laboratory-focused instruments, it is likely that use of an alternative image processing software could provide varied results. Furthermore, especially in the consumer-focused smartphone market, functionality improvements are occurring at a rapid pace and improved hardware will likely become available at similar price points in the near future. Therefore, the use of alternative equipment may have a significant impact on the results presented here.

Using the continuously bioluminescent signal of LiveLight™ HEK293 cells, both the night vision and smartphone systems could detect bioluminescence from as few as 2,000 cells/well. CCD imaging could detect bioluminescence from 200 cells/well, and PMT imaging could detect down to 20 cells/well (**Figure 1**). As expected, these data show that the CCD and PMT systems, which are designed for laboratory use, are more sensitive and have improved signal:background ratios compared to the consumer-grade alternatives. However, both night vision and smartphone-based imaging could detect bioluminescence from well below the range of common densities used for assays run in the 96-well plate format (ATCC, 2021). The CCD and PMT-based systems both showed very strong linear correlations between bioluminescence and cell number, with each achieving R^2 values ≥0.99. However, the night vision and smartphone systems were only slightly less correlated, with both achieving R^2 values ≥0.9 (**Figure 2**).

All surveyed systems showed CV values ≤0.1 (**Figure 3**), with the night vision system performing relatively similar to the CCD and PMT systems despite necessitating use outside of a light tight environment. The practical effect of the measured CV values was reflected when measuring viability. The CCD (**Figure 5A**) and PMT-based (**Figure 5B**) systems, which had the lowest CV values (**Figure 3**), show clear downward trends in viability after compound challenge. In contrast, the CMOS-based system (**Figure 5D**) appears to indicate an unexpected increase in viability between chemical challenge and the 8 h time point, followed by a significant decrease towards the 16 h time point. It is likely this reported increase, which was not statistically significant (p = 0.52), is an artifact of the higher CV associated with this modality and the minor difference between the time zero and 8 h points (86 and 126%, respectively) are due to chance. A similar effect was observed in the night vision system (**Figure 5C**), which appears to show slight increases in viability between time zero and the 8 h time point for the 400 and 800 µg Zeocin/mL treatments. Just as this modality displayed a CV between the lower variability CCD and PMT-based systems and the more variable CMOS-based system (**Figure 3**), it also showed a less pronounced difference between the suspect data points and relatively lower p values (0.0468 and 0.0007) for the two treatments than was observed for the CMOS-based system at that same time point. For all systems, variation remained consistent across a large range of bioluminescent intensities.

The sensitivity of these systems was highlighted by their performance in the toxicity and reporter induction assays. PMT-based imaging detected cellular health dynamics as early as 1 h post treatment, while CCD-based imaging required 8 h.

The night vision and smartphone-based systems both required 16 h to observe a significant change (**Figure 5**). This can be attributed at least partially to the logistical constraints of these systems. While the CCD and PMT systems could be programmed to continuously collect data every hour, the night vision and smartphone systems were limited by their requirements for manual operation and inability to maintain the cells under sterile, atmospherically favorable conditions during imaging. As such, they were only assayed at 8 h intervals with the cells housed in an incubator between readings, instead of every 1 h like the CCD and PMT systems. Therefore, although the first detectable difference was recorded at 16 h post treatment, it is likely they could achieve detection earlier if an alternative imaging schedule was used. Overall, the PMT-based system displayed the highest sensitivity and signal:background ratio, with the CCD-based system only slightly less sensitive. Interestingly, the night vision and smartphone-based systems performed roughly similarly, despite their very different photon detection methodologies. All systems could detect Zeocin-based toxicity within the manufacturer's suggested range of 50–1,000 μg/ml. However, only the more sensitive CCD and PMT systems showed the two treatments within the average selective range of 200–400 μg/ml as being similar to one another while remaining distinct from the higher 800 μg/ml dosage that is more concentrated and therefore more likely to show toxic effects earlier during the selection process (ThermoFisher, 2021).

The reporter induction assay (**Figure 6**) was a more difficult challenge because it yielded lower overall signal intensities than the toxicity assay. Both the CCD and PMT systems detected significant induction ($p < 0.01$) at the 2 h time point and reported maximal induction values of 53-fold and 76-fold, respectively. The night vision system also successfully identified induction and reported a maximal induction of 9-fold. However, it was again limited by a requirement for manual operation and inability to maintain the cells under sterile, atmospherically favorable conditions during imaging. While it detected significant ($p = 0.0001$) induction at the first possible time point (8 h), and while both the CCD and PMT systems still showed induction at this time, it suffered from a significant reduction in data resolution compared to these other assays. Although the CCD, PMT, and night vision systems all showed roughly the same timing for the start (2 h) and peak (8 h) of induction, they produced disparate maximal induction values. These values correlated with the measured background levels, sensitivities (**Figure 1**) and linear detection capabilities (**Figure 2**) of each system. It is therefore likely the discrepancies in reported maximal induction are due to the ability of each system to discriminate signal from background. Those with improved signal:background discrimination abilities, resulting from both their improved signal detection capabilities and improved ambient light exclusion properties (PMT and CDD), report higher maximal induction values. The image intensifier system, which displayed a relatively decreased discrimination ability and greater ambient light exposure, reported a lower maximal induction because it could not as easily distinguish induction from background.

Smartphone-based imaging did not detect reporter induction. However, the results of the minimum signal threshold testing (**Figure 1**) suggest the LiveReport™ CRE induction signal was only slightly below the luminescent threshold required. The Pixel 4a 5G CMOS sensor used in these experiments has a 1.4 μm pixel size. This was sufficient for resolving the spatial location of disparate signals down to the 384-well format. However, using a sensor with a larger pixel size could potentially increase photon detection capabilities by allowing more light to be captured by each pixel and increasing minimum signal detection capabilities. Since most assays are run in 96-well formats that have greater spacing between wells, this approach would tolerate the decreased resolution of larger pixels while increasing sensitivity, which was determined to be the most limiting factor for this sensor type. Although smartphone photography often emphasizes increased resolution, and therefore future versions of these devices are likely to incorporate CMOS sensors with decreased rather than increased pixel size, technical improvements in the CMOS space have focused on improving dark count rates and photon detection probabilities (Charbon et al., 2018). Given the performance of modern back-illuminated, stacked CMOS sensors, and the focus smartphone manufactures have placed on photographic quality improvement across a range of metrics, it is therefore likely an alternative camera system, or a near-future smartphone camera would be successful in this assay.

CCD and PMT-based instruments are the primary tools for bioluminescent assays in laboratories around the world because of their high sensitivity and the decision to use one over the other is typically application dependent (de la Zerda et al., 2010; Kim et al., 2020). However, while their relatively large footprint, high price, immobility, and resource requirements limit their use outside of the laboratory environment, ongoing miniaturization of PMTs is improving their ability for portable usage. The rapid improvement in night vision and especially CMOS-based smartphone imaging, along with complementary improvements in bioluminescent technologies that allow for continuous signal generation and autonomous signal control without external activation, has opened new possibilities for performing assays without these specialized instruments. When paired with autonomously bioluminescent cells, night vision and smartphone imaging can now provide an inexpensive, compact, and highly mobile alternative for bioluminescent imaging if working with applications capable of producing signal above their higher minimum detection thresholds. As these devices improve they could be used to enable a wide range of novel applications that span from performing point-of-care toxicity assays in remote locations to providing educational experiments in classrooms at all ages.

However, it is unlikely that night vision or smartphones will replace CCD and PMT-based systems in scientific laboratories anytime soon. Aside from their improved performance as showcased in this work, these systems are typically integrated with temperature control, atmospheric control, wavelength filtering, continuous integration, and a host of other accessories that allow them to perform myriad functions currently inaccessible to consumer-focused products. As retailed, night vision and smartphone systems lack these abilities. However, it is encouraging that with only minor modifications (i.e., addition of an external filter to reduce background and improve signal: background ratio) they can be employed to perform similar assays in situations inaccessible to laboratory-based systems.

DATA AVAILABILITY STATEMENT

The raw data supporting the conclusions of this article will be made available by the authors, without undue reservation.

AUTHOR CONTRIBUTIONS

MW, AK, and TX performed experiments and analysed data. SR, GS, and DC analyzed and organized data. MW, SR, and DC wrote and edited the manuscript.

FUNDING

Funding for this work was provided by the US National Institutes of Health (NIH) under award numbers NIMH-R43MH118186, NIGMS-R44GM112241, NIGMS-R42GM116622, NIEHS-R44ES022567, and NIEHS-R44ES026269 and the US National Science Foundation under award number CBET-1530953. The content is solely the responsibilities of the authors and does not necessarily represent the official views of the NIH or the NSF.

REFERENCES

ATCC (2021). HEK-293 Product Information [Online]. American Type Culture Collection Available at: https://www.atcc.org/products/crl-1573#detailed-product-information [Accessed August 27, 2021].

Charbon, E., Bruschini, C., and Lee, M.-J. (2018). "3D-stacked CMOS SPAD Image Sensors: Technology and Applications," in 2018 25th IEEE International Conference on Electronics, Circuits and Systems (ICECS) (IEEE), 1–4.

Class, B., Thorne, N., Aguisanda, F., Southall, N., Mckew, J. C., and Zheng, W. (2015). High-Throughput Viability Assay Using an Autonomously Bioluminescent Cell Line with a BacterialLuxReporter. *J. Lab. Autom.* 20(2), 164–174. doi:10.1177/2211068214560608

Close, D. M., Hahn, R. E., Patterson, S. S., Baek, S. J., Ripp, S. A., and Sayler, G. S. 2011). Comparison of Human Optimized Bacterial Luciferase, Firefly Luciferase, and green Fluorescent Protein for Continuous Imaging of Cell Culture and Animal Models. *J. Biomed. Opt.* 16(4), 047003. doi:10.1117/1.3564910

Close, D. M., Patterson, S. S., Ripp, S., Baek, S. J., Sanseverino, J., and Sayler, G. S. (2010). Autonomous Bioluminescent Expression of the Bacterial Luciferase Gene Cassette (*Lux*) in a Mammalian Cell Line. *PLoS ONE* 5 (8), e12441. doi:10.1371/journal.pone.0012441

Close, D., Ripp, S., and Sayler, G. (2009). Reporter Proteins in Whole-Cell Optical Bioreporter Detection Systems, Biosensor Integrations, and Biosensing Applications. *Sensors* 9 (11), 9147–9174. doi:10.3390/s91109147

Conway, M., Xu, T., Kirkpatrick, A., Ripp, S., Sayler, G., and Close, D. (2020). Real-time Tracking of Stem Cell Viability, Proliferation, and Differentiation with Autonomous Bioluminescence Imaging. *BMC Biol.* 18 (1), 79–14. doi:10.1186/s12915-020-00815-2

de la Zerda, A., Bodapati, S., Teed, R., Schipper, M. L., Keren, S., Smith, B. R., et al. (2010). A Comparison between Time Domain and Spectral Imaging Systems for Imaging Quantum Dots in Small Living Animals. *Mol. Imaging Biol.* 12 (5), 500–508. doi:10.1007/s11307-009-0290-4

Ehrenfeld, G. M., Shipley, J. B., Heimbrook, D. C., Sugiyama, H., Long, E. C., Van Boom, J. H., et al. (1987). Copper-dependent Cleavage of DNA by Bleomycin. *Biochemistry* 26 (3), 931–942. doi:10.1021/bi00377a038

El Gamal, A., and Eltoukhy, H. (2005). CMOS Image Sensors. *IEEE Circuits Devices Mag.* 21 (3), 6–20. doi:10.1109/mcd.2005.1438751

Fan, F., and Wood, K. V. (2007). Bioluminescent Assays for High-Throughput Screening. *Assay Drug Dev. Tech.* 5 (1), 127–136. doi:10.1089/adt.2006.053

Haque, M. J., and Muntjir, M. (2017). Night Vision Technology: An Overview. *Int. J. Comp. Appl.* 975, 8887.

Hattori, M., Shirane, S., Matsuda, T., Nagayama, K., and Nagai, T. (2020). Smartphone-based Portable Bioluminescence Imaging System Enabling Observation at Various Scales from Whole Mouse Body to Organelle. *Sensors* 20 (24), 7166. doi:10.3390/s20247166

Janesick, J. R. (2001). *Scientific Charge-Coupled Devices*. Bellingham, Washington: SPIE press.

Judson, R., Kavlock, R., Martin, M., Reif, D., Houck, K., Knudsen, T., et al. (2013). Perspectives on Validation of High-Throughput Assays Supporting 21st century Toxicity Testing. *ALTEX* 30 (1), 51–66. doi:10.14573/altex.2013.1.051

Kim, H., Jung, Y., Doh, I. J., Lozano-Mahecha, R. A., Applegate, B., and Bae, E. (2017). Smartphone-based Low Light Detection for Bioluminescence Application. *Sci. Rep.* 7 (1), 40203–40211. doi:10.1038/srep40203

Kim, S. B., Hori, S. S., Sadeghipour, N., Sukumar, U. K., Fujii, R., Massoud, T. F., et al. (2020). Highly Sensitive Eight-Channel Light Sensing System for Biomedical Applications. *Photochem. Photobiol. Sci.* 19 (4), 524–529. doi:10.1039/d0pp00017e

Ma, J., Harpaz, D., Liu, Y., and Eltzov, E. (2020). Smartphone-based Whole-Cell Biosensor Platform Utilizing an Immobilization Approach on a Filter Membrane Disk for the Monitoring of Water Toxicants. *Sensors* 20 (19), 5486. doi:10.3390/s20195486

Michelini, E., Calabretta, M. M., Cevenini, L., Lopreside, A., Southworth, T., Fontaine, D. M., et al. (2019). Smartphone-based Multicolor Bioluminescent 3D Spheroid Biosensors for Monitoring Inflammatory Activity. *Biosens. Bioelectron.* 123, 269–277. doi:10.1016/j.bios.2018.09.012

Slater, K. (2001). Cytotoxicity Tests for High-Throughput Drug Discovery. *Curr. Opin. Biotechnol.* 12 (1), 70–74. doi:10.1016/s0958-1669(00)00177-4

ThermoFisher (2021). Zeocin [Online]. ThermoFisher Scientific. Available at: https://www.thermofisher.com/us/en/home/references/protocols/cell-culture/transfection-protocol/zeocin.html [Accessed 10-19 2021].

Wright, A. (2017). *The Photomultiplier Handbook*. New York, New York: Oxford University Press.

Xu, T., Ripp, S., Sayler, G. S., and Close, D. M. (2014). Expression of a Humanized Viral 2A-Mediated *Lux* Operon Efficiently Generates Autonomous Bioluminescence in Human Cells. *PLoS ONE* 9 (5), e96347. doi:10.1371/journal.pone.0096347

Zangheri, M., Cevenini, L., Anfossi, L., Baggiani, C., Simoni, P., Di Nardo, F., et al. (2015). A Simple and Compact Smartphone Accessory for Quantitative Chemiluminescence-Based Lateral Flow Immunoassay for Salivary Cortisol Detection. *Biosens. Bioelectron.* 64, 63–68. doi:10.1016/j.bios.2014.08.048

Zangheri, M., Di Nardo, F., Calabria, D., Marchegiani, E., Anfossi, L., Guardigli, M., et al. (2021). Smartphone Biosensor for point-of-need Chemiluminescence Detection of Ochratoxin A in Wine and Coffee. *Analytica Chim. Acta* 1163, 338515. doi:10.1016/j.aca.2021.338515

Conflict of Interest: Authors MW, AK, SR, GS, and DC were employed by the company 490 BioTech, Inc.

The remaining authors declare that the research was conducted in the absence of any commercial or financial relationships that could be construed as a potential conflict of interest.

Publisher's Note: All claims expressed in this article are solely those of the authors and do not necessarily represent those of their affiliated organizations, or those of the publisher, the editors and the reviewers. Any product that may be evaluated in this article, or claim that may be made by its manufacturer, is not guaranteed or endorsed by the publisher.

frontiers in Bioengineering and Biotechnology

BRIEF RESEARCH REPORT
published: 15 December 2021
doi: 10.3389/fbioe.2021.789709

Few-Photon Spectral Confocal Microscopy for Cell Imaging Using Superconducting Transition Edge Sensor

Kazuki Niwa[1]*, *Kaori Hattori*[1,2] *and Daiji Fukuda*[1,2]

[1]Research Institute for Physical Measurement, National Metrology Institute of Japan, National Institute of Advanced Industrial Science and Technology (AIST), Tokyo, Japan, [2]AIST-UTokyo Advanced Operando-Measurement Technology Open Innovation Laboratory, Kashiwa, Japan

A superconducting transition edge sensor (TES) is an energy-dispersive single-photon detector that distinguishes the wavelength of each incident photon from visible to near-infrared (NIR) without using spectral dispersive elements. Here, we introduce an application of the TES technique for confocal laser scanning microscopy (CLSM) as proof of our concept of ultra-sensitive and wide-band wavelength range color imaging for biological samples. As a reference sample for wide-band observation, a fixed fluorescence-labeled cell sample stained with three different color dyes was observed using our TES-based CLSM method. The three different dyes were simultaneously excited by irradiating 405 and 488 nm lasers, which were coupled using an optical fiber combiner. Even when irradiated at low powers of 80 and 120 nW with the 405 and 488 nm lasers respectively, emission signals were spectrally detected by the TES and categorized into four wavelength bands: up to 500 nm (blue), from 500 to 600 nm (green), from 600 to 800 nm (red), and from 800 to 1,200 nm (NIR). Using a single scan, an RGB color image and an NIR image of the fluorescent cell sample were successfully captured with tens of photon signals in a 40 ms exposure time for each pixel. This result demonstrates that TES is a useful wide-band spectral photon detector in the field of life sciences.

Keywords: fluorescence cell imaging, superconducting transition edge sensor, confocal microscope, spectral imaging, photon counting

OPEN ACCESS

Edited by:
Elisa Michelini,
University of Bologna, Italy

Reviewed by:
Stefan Schramm,
Merck, Germany
Masataka Kinjo,
Hokkaido University, Japan

***Correspondence:**
Kazuki Niwa
niwa-k@aist.go.jp

Specialty section:
This article was submitted to Biomaterials, a section of the journal Frontiers in Bioengineering and Biotechnology

Received: *05 October 2021*
Accepted: *25 November 2021*
Published: *15 December 2021*

Citation:
Niwa K, Hattori K and Fukuda D (2021) Few-Photon Spectral Confocal Microscopy for Cell Imaging Using Superconducting Transition Edge Sensor. Front. Bioeng. Biotechnol. 9:789709. doi: 10.3389/fbioe.2021.789709

INTRODUCTION

Spectral imaging provides information about the distribution of multiple molecules and other entities via spectral analysis. In the field of life sciences, spectral confocal laser scanning microscopy (CLSM) provides substantial information on the cellular dynamics associated with various biomolecules.

In CLSM cell-imaging applications, samples are labeled with fluorescent dyes and irradiated by excitation light to obtain fluorescence signals. However, in living cells, excitation light irradiation deteriorates cells from their native state and causes photobleaching of fluorescent dyes (Icha et al., 2017). Therefore, it is ideal to minimize excitation light irradiation. However, a decrease in the excitation light results in a decrease in the fluorescence signal. In the case of auto-fluorescence, which is emitted from endogenous fluorescent molecules in living organisms, signals are weak even when the molecules are irradiated with high-power excitation light.

Moreover, there is an increasing demand for a highly sensitive photodetector, which has a smaller background noise and higher detection efficiency, to observe fluorescence signals from cellular samples at the few-photon signal level.

Consequently, numerous efforts have been made to develop more sensitive photodetectors. A transition-edge sensor (TES) is a superconducting film that acts as a thermometer and can measure weak energy at the level of a single photon (Irwin and Hilton, 2005). As the energy of a single photon is related to its wavelength by the following equation, the TES directly distinguishes the energy of an absorbed photon without using any spectral element, after which the wavelength of the photon is distinguished.

$$E = \frac{hc}{\lambda}$$

Thus, a TES can be used as an ultrasensitive spectral photodetector. The spectral efficiency of a TES is determined by its absorption/reflection properties. We designed and constructed a TES to absorb a wide range of wavelengths of photons from the visible to near infrared (NIR) range using an optical cavity structure (Fukuda et al., 2011).

Previously, we reported a concept proof of the TES technique for ultra-sensitive and wide-band spectral imaging (Niwa et al., 2017). Using a three-color ink printing test pattern (a photograph), RGB color images and NIR images were successfully captured under epi- and side-illuminated conditions. Using a TES in a 50 ms exposure time for each pixel, tens or fewer photon signals were detected to provide a color image in a single scan. Although a few photon signals for each pixel were sufficient to provide RGB color images, more signals were required to generate the wavelength spectral data. Therefore, spectral data at a single pixel were obtained by increasing the exposure time to 200 s. These results suggest the high potential of TES for use as a spectral photon-counting detector in CLSM for biological microscopy applications.

For cell imaging applications, we constructed CLSM optics using TES as a photodetector (Fukuda et al., 2017). Using microscopy optics, preliminary observation of fluorescent-labeled cell samples was performed using a single excitation laser (488 nm) to excite two fluorescent dyes (Alexa 488 and MitoTracker). Although two dyes were detected, the cells were labeled with three dyes, and full-color imaging was needed to obtain signals from all three fluorescent dyes. Because a TES is sensitive to a wide wavelength range of photons, more fluorescent dyes are detected simultaneously, which provides RGB full-color images. In this report, we introduce an improvement in CLSM optics to excite a wider range of fluorescent dyes and present the results of an extended investigation of cell samples. The excitation laser irradiation and photon counting signals were investigated to consider full-color image caption sensitivity at the photon-counting level by the TES.

MATERIALS AND METHODS

Microscope Optics

The design and construction of a scanning microscope system using a TES as a photodetector with an optical fiber has been reported (Niwa et al., 2017), and confocal optics with a single excitation laser at 488 nm have been employed for CLSM (Fukuda et al., 2018). Additionally, for full-color cell imaging, previously developed microscope optics were modified here (**Figure 1**). To irradiate with two distinct lasers for simultaneous excitation of three fluorescent dyes, 405 and 488 nm pig-tailed optical fiber diode lasers (LP405-SF15 and LP488-SF20, Thorlabs, USA) were combined using a wavelength combiner/splitter (GB29F1, Thorlabs, USA). For fluorescent signal detection, a dichroic mirror of 425 nm (DMPL425, Thorlabs, United States), a long pass filter (FELH450, Thorlabs, USA), and a notch filter (NF488-15, Thorlabs, USA) were employed. The magnitude and numerical aperture (NA) of the objective (UPLXAPO × 40, Olympus, Japan) were 40 and 0.95, respectively. A prepared microscope slide (FluoCells Prepared Slide #1, Tremo Fisher Scientific, USA) was used as a test sample for cell imaging. The test sample was mechanically scanned using a motorized XY stage (BIOS-105S, Optosigma, Japan) under a microscope. Stage control, data accumulation, and image processing were performed using LabVIEW software (National Instruments, USA).

To adjust and focus the optics, a He–Ne laser (Melles Griot, United States), epi-illumination optics (omitted in **Figure 1**, Olympus, Japan), and a CMOS camera (Infinity 1–2C, Lumenera Corp, Canada) were used. To compare the detection efficiency of the proposed TES with that of the conventional method, a photomultiplier tube (PMT; H18010 Hamamatsu Photonics, Japan) was used instead of a TES, where a 532 nm laser diode (DJ532-10, Thorlabs, USA) were added to the optics (**Supplementary Figure S1**). The irradiated excitation laser power (W) at the focal plane was measured using a microscope slide-type power meter (S170C, Thorlabs, USA), which was calibrated for each wavelength.

TES Single-Photon Spectral Detector

The TES used as the photodetector in confocal microscopy is a fiber-coupled TiAu-based optical TES (Fukuda et al., 2011). The energy of a single photon absorbed by the TES was converted into the increase in electric resistance, followed by measurement of the voltage change using a superconducting quantum interference device (SQUID) amplifier associated with the TES. The TES and SQUID amplifiers were placed on a cold stage in an adiabatic demagnetization refrigerator, where the temperature was stabilized at 100 mK. To obtain the wavelength value from the measured energy of the incident photons, the pulse signal height of the SQUID voltage was calibrated using a 1524-nm pulse laser (PLP-10-155, Hamamatsu, Japan) to irradiate with multiplexed photons with energies of 762 nm (n = 2), 506 nm (n = 3), and 381 nm (n = 4).

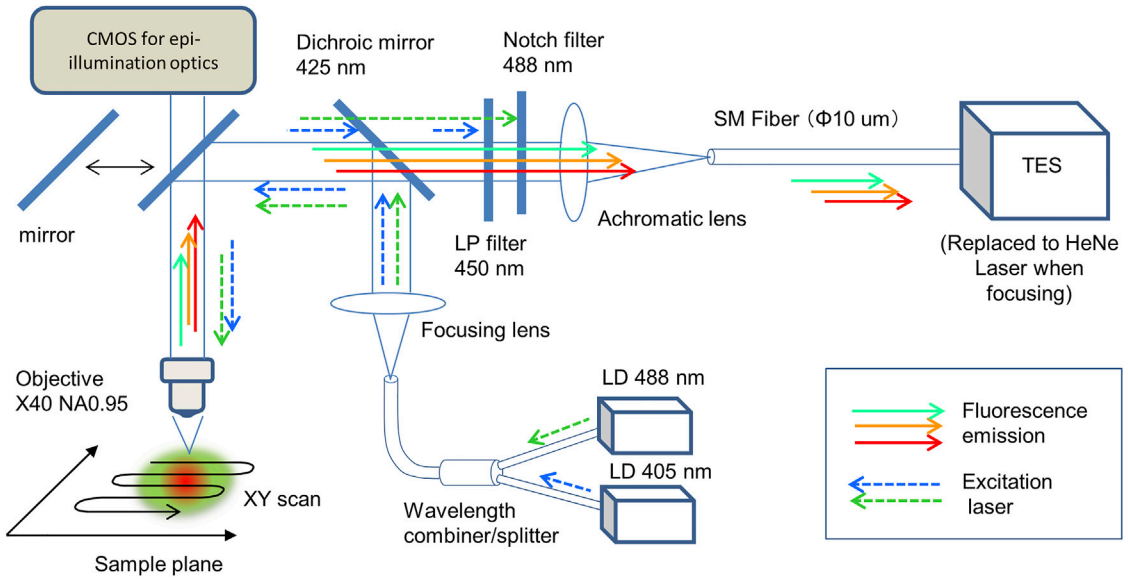

FIGURE 1 | Confocal laser microscope optics with a fiber-coupled TES. Two excitation lasers at 405 and 488 nm were combined using a fiber combiner and focused on the sample plane under the objective (×40 NA0.95). Collimated fluorescence photons were focused on the core (10 μm diameter) at the end of the optical fiber, then introduced into the TES. The sample on the focal plane was scanned to accumulate an imaging data.

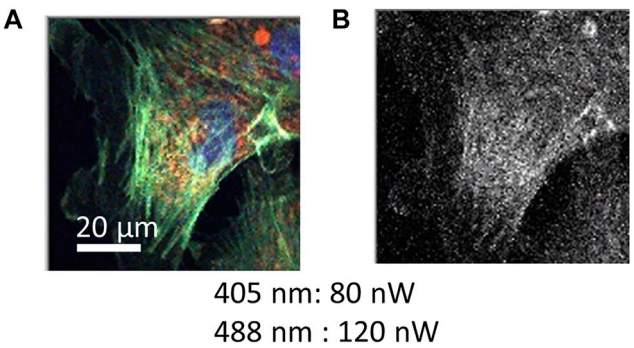

FIGURE 2 | Color image obtained by a confocal scanning microscope using a TES. A fixed cell sample stained with MitoTracker (red fluorescence for mitochondria), Alexa 488 (green fluorescence for F-actin), and DAPI (blue fluorescence for nuclei). Scanning data of 200 × 200 pixels (0.4 μm for each pixel step) is depicted as **(A)** RGB color and as **(B)** NIR images, which were obtained simultaneously. Irradiation power of excitation lasers is indicated. Exposure time of one pixel was 40 ms, and the total duration was 66 min.

To depict a color image, the photon signals detected by using the TES were distinguished by their wavelength as follows: photons shorter than 500 nm were blue, while those of from 500 to 600 nm were green, from 600 to 800 nm were red, and from 800 to 1,200 nm were in the NIR range. Additional details concerning optical photon detection via TES have been described elsewhere (Hattori et al., 2018).

RESULTS

Fluorescent Cell Imaging Using a TES

Because TES is an energy-dispersive photodetector, a wide wavelength range of photons from visible to NIR was simultaneously detected with the wavelength information. Each photon signal was distinguished into blue, green, red, and NIR in accordance with the wavelength. As a test target, a prepared microscope slide containing bovine pulmonary artery endothelial cells (BPAECs) was observed using a TES. The BPAECs in the slides were stained with MitoTracker Red (MitoTracker) for mitochondria, Alexa Fluor 488 (Alexa 488) for F-actin, and 4′,6-diamidino-2-phenylindole (DAPI) for nuclei. The excitation laser power at the focal plane measured using a power meter were 80 and 120 nW for the 405 and 488 nm lasers, respectively. Color images of the BPAEC were successfully constructed from the datasets of red for mitochondria, green for F-acting, and blue for nuclei (**Figure 2A**). Simultaneously, photon signals categorized as NIR provided an NIR image (**Figure 2B**). It took 66 min to scan 200 × 200 pixels with 40 ms exposure time for each pixel. The scanning step of each pixel was 0.4 μm. Photon counting signal intensities in the presence and absence of a cell in the images were analyzed (**Supplementary Figure S2**).

Fluorescent Cell Imaging Using a PMT

For comparison, CLSM was constructed using a PMT. Cell images of the test slide of the BPAEC were captured by irradiating the cells with excitation lasers one by one (**Figures 3A–C**). To excite DAPI for nuclei imaging, the cells were irradiated with 500 nW of a 405 nm laser (**Figure 3A**), Alexa 488 for F-actin was irradiated with 400 nW of a 488 nm laser

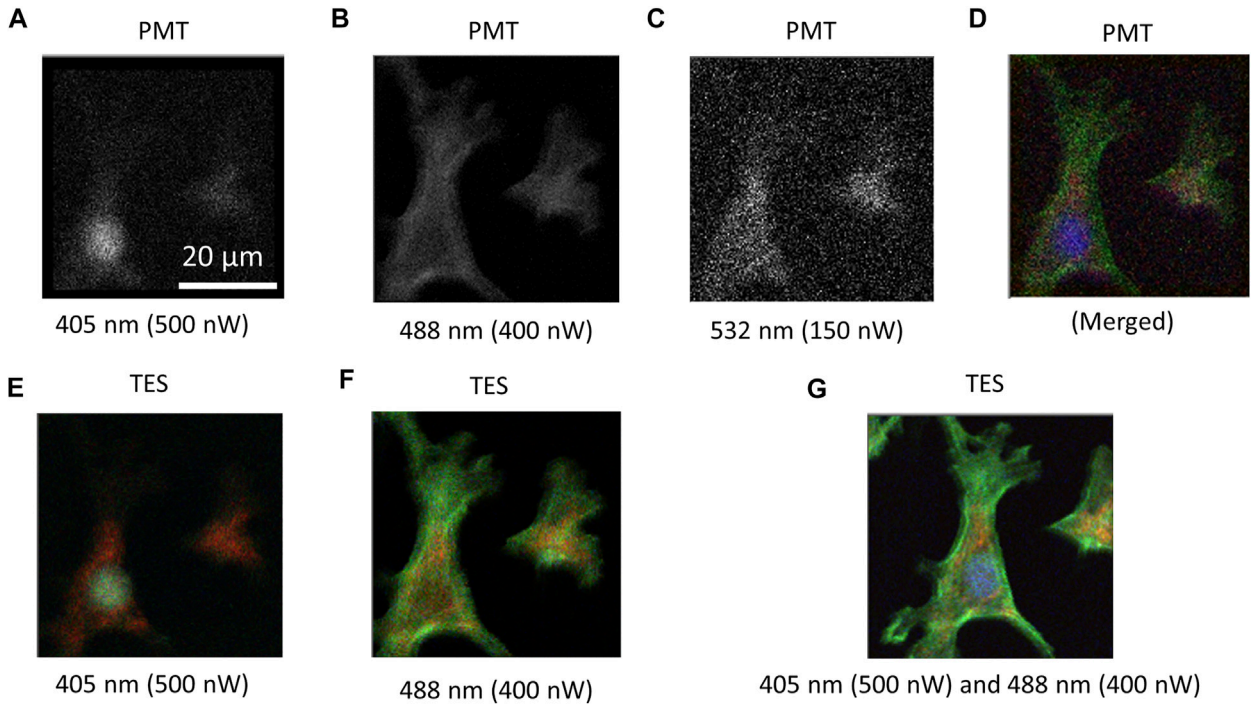

FIGURE 3 | Images obtained by confocal scanning microscopy using PMT and TES. When using PMT, scanning data were collected to provide a grayscale image individually for each fluorescent dye. Grayscale images captured using PMT for **(A)** DAPI excited by 500 nW of 405 nm laser, **(B)** Alexa488 by 400 nW of 488 nm laser, **(C)** MitoTracker by 150 nW of 532 nm laser. **(D)** Pseudo-color image developed by digitally merging the three grayscale images. **(E)** RGB color image captured using a TES under the same irradiation and scanning condition as **(A)**, where mitochondria were detected in red color and distinguished from nuclei. **(F)** RGB color image captured using a TES in the same condition as **(B)**, where mitochondria were also detected and distinguished from F-actin. **(G)** RGB color image captured using a TES by irradiating the cell with excitation lasers of 405 and 488 nm at the same power as using PMT. A single scan was sufficient to create an RGB image of all dyes by 405 nm laser and 488 nm laser. Here, a 532 nm laser could be omitted. Scanning conditions were 200 × 200 pixels, 0.25 µm scanning step, and 20 ms exposure time for all images. The total duration was 48 min.

(**Figure 3B**), and MitoTracker for mitochondria was irradiated with 150 nW of the 532 nm laser (**Figure 3C**). A pseudo-color image was obtained by merging the three independent images (**Figure 3D**). Using the TES, RGB color images were captured by a single scan at the same irradiation power, as shown in **Figure 3A** (**Figure 3E**) and **Figure 3B** (**Figure 3F**). Although a 532 nm laser was not irradiated to excite MitoTracker, a red-colored signal was observed. Hence, by combining 405 and 488 nm lasers, RGB color images were obtained at once. In all cases using both PMT and TES, it took 48 min to obtain a single image by scanning 200 × 200 pixels with 20 ms exposure time for each pixel. The scanning step of each pixel was 0.25 µm. Photon counting signal intensities from the presence and absence of a cell in the images were analyzed from the cell images obtained using TES and PMT under the same irradiation and scanning conditions (**Figure 4**).

DISCUSSION

Cell Imaging *Via* CLSM Using TES

The step size for each pixel in **Figure 2** was 0.4 µm. Under these conditions, internal cellular structures of actin filaments (green) and mitochondria (red) were successfully imaged, indicating that the optical system of the confocal microscope was constructed correctly (**Figure 2A**). Because the background signals from the empty area in the images were as small as 0–2 counts (**Supplementary Figure S2A**), a clear image was obtained. Using scanning data recorded as NIR photon signals, a grayscale image was constructed (**Figure 2B**). However, only a faint cell image could be obtained because the fluorescence spectra of dyes used to stain the cell sample were shorter than 800 nm. The photon number detected as NIR was as small as four photons (as median) for each pixel (**Supplementary Figure S2B**), although a TES is sensitive to the detection of NIR photons (Niwa et al., 2017). It has been reported that there are NIR fluorescence signals from cellular samples without labeling with any fluorescent dye, which is recognized as NIR auto-fluorescence (Paras et al., 2011). To confirm the potential of TES as a detector for NIR microscopy, further efforts should be made to observe much clearer NIR images associated with auto-fluorescence. By applying NIR fluorescent dyes, it is also possible to increase the labeling of dyes for cell imaging. Further progress of CLSM with TES is desired for NIR cell imaging.

In this report, photon energy information was transferred into four color-channel-distinguished signals to provide RGB and NIR images. Because the energy resolution ΔE of the TES used in this study was 0.1 eV, the wavelength resolution was

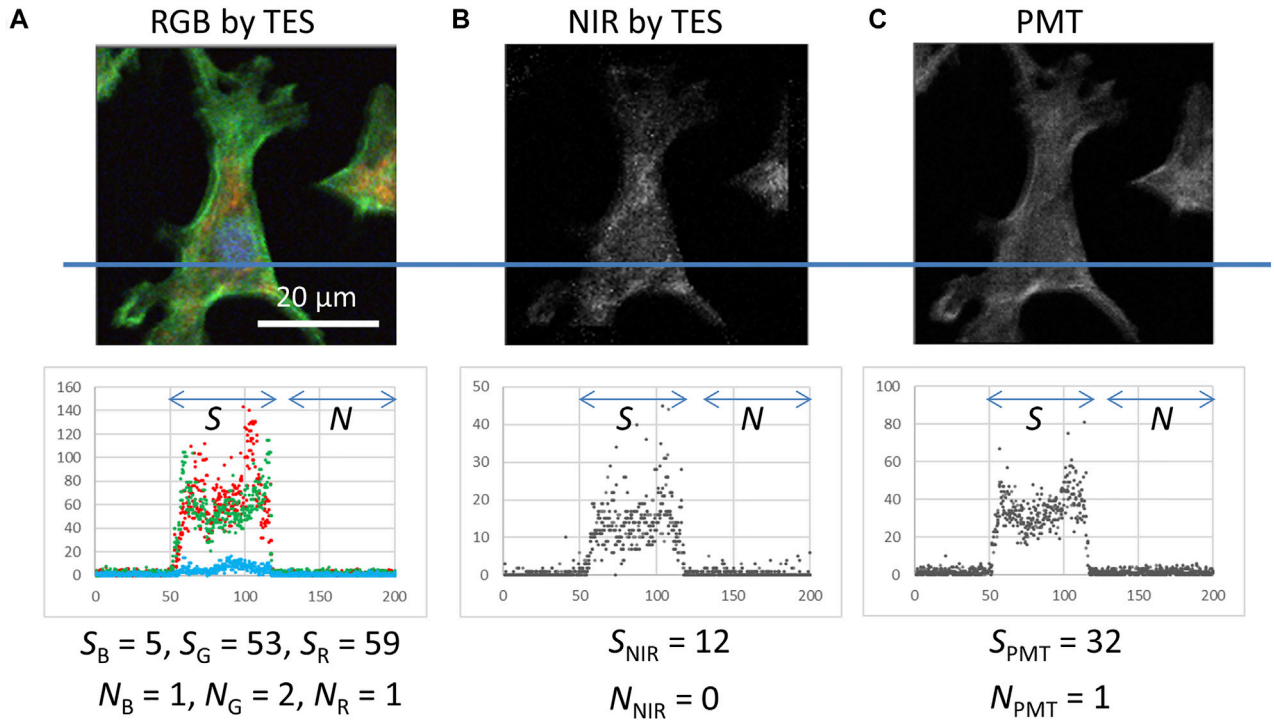

FIGURE 4 | Histograms of photon counting signals detected using the TES and PMT at the transection lines (including five pixels width) on the images and signal (*S*) and background noise (*N*) intensity as medians of the area indicated by arrows. **(A)** RGB image obtained using the TES, which is identical to the data in **Figure 3G**. **(B)** NIR image obtained using the TES, which was simultaneously captured beside **(A,C)** Grayscale image obtained using the PMT. These data were captured under the same excitation laser irradiation (500 and 400 nW for 405 and 488 nm lasers, respectively) and scanning (200 × 200 pixels, 0.25 µm step, and 20 ms exposure time) conditions.

approximately from 50 to 150 nm in the visible range. Thus, the detected fluorescence emission of the dyes partially overlapped each other, which could cause incorrect photon discrimination to the neighboring color channels. As shown in **Figure 2A**, however, three fluorescent dyes could be distinguished from each other in different colors, and the spatial distribution of each dye could be observed. If the spectra of fluorescent dyes are much closer and overlapped each other more, the overlap might deteriorate the RGB color quality. Even in this case, spectral overlapping can be statistically determined and compensated by increasing the number of color channels for TES detection (Nakajima et al., 2005). Here, the spectral information of each fluorescent dye is necessary, which can be obtained, for example, using the samples stained with each single fluorescent dye.

In **Figure 2**, the total duration time was 66 min, where the detection by TES took 26 min because the exposure time was 40 ms for each 200 × 200 pixel, and the resulting 40 min was associated with 0.4 µm scanning steps. This scanning condition differs slightly from that in **Figure 3**, in which the exposure time is 20 ms and the scanning step of 0.25 µm. In this condition for **Figure 3**, the total duration was 48 min, where detection via both TES or PMT took 13 min, and the remaining time was 35 min. Although the scanning steps were reduced from 0.4 to 0.25 µm, the scanning duration only reduced from 40 to 35 min, because the scanning duration mainly comprises data processing time behind stage movement. Therefore, the scanning duration can be significantly reduced by optimizing computer programs for data processing, resulting in a reduction in the total duration for capturing an image. Reducing the exposure time and scanning step numbers can also contribute to reducing the total duration of image capture. To reduce the exposure time, the photodetector must be more efficient for detection, which can be achieved by improving the optical absorption of the TES coatings. To reduce the number of scanning steps, the use of multiple photodetector elements contributes to reduction of scanning area. Thus, constructing an array-type TES device with a high detection efficiency will increase the demand.

Simultaneous Detection of Blue, Green, and Red Fluorescent Dyes

As this report aims to prove the concept of wide-band spectral photon counting imaging using a TES to provide a full-color image in a single scan, the sample should emit fluorescence signals as wide as from blue to red. Test slides of cells were stained with three fluorescent dyes (DAPI, Alexa 488, MitoTracker). Most photodetectors cannot distinguish the incident photon energy; they only provide grayscale images. For example, CLSM using a PMT requires three individual scans for each fluorescent dye (**Figures 3A–C**). A pseudo-color image was developed by merging the three images digitally (**Figure 3D**). Controversially, using TES, RGB color

images could be obtained even with single-laser irradiation (**Figures 3E,F**). It is notable that, without irradiating the 532 nm laser to excite MitoTracker, a remarkable fluorescent signal from MitoTracker was emitted by irradiating with the 405 nm laser (**Figures 3A,E**) and 488 nm laser (**Figures 3B,F**), because these wavelengths could be partially absorbed by and excite MitoTracker. Using TES, fluorescence emission from MitoTracker was detected as a red color and distinguished from DAPI (**Figure 3E**) and Alexa 488 (**Figure 3F**). When using PMT, however, MitoTracker was identically detected with, and could not be distinguished from, DAPI (**Figure 3A**) or Alexa 488 (**Figure 3B**). Therefore, by combining two color lasers of 405 and 488 nm and irradiating the cells simultaneously, all three fluorescent dyes could be excited to obtain an RGB color image in only a single scan (**Figure 3G**).

Because conventional optics based on dichroic mirrors are designed to separate shorter wavelengths of excitation light and longer wavelengths of fluorescence emission light, the excitation wavelength must be shorter than the fluorescence emission wavelengths. Therefore, a 405 nm laser was used to excite DAPI, whereas it could not excite Alexa 488 and MitoTracker efficiently. Therefore, an additional 488 nm laser was employed to excite longer-wavelength fluorescent dyes. Generally, a long-pass dichroic mirror at 425 nm is not appropriate for the 488 nm excitation laser to be removed. To solve this problem, we applied an imperfection of the dichroic mirror that retained 2.36% reflectance at 488 nm. Consequently, the 488 nm excitation laser was slightly reflected toward the objective and irradiated to the sample plane. Before detection of fluorescence emission, excitation lasers of 405 and 488 nm were removed using a long-pass filter (cut off 450 nm) and notch filter (at 488 nm), respectively. Thus, fluorescence signals from all three fluorescent dyes (DAPI, Alexa 488, MitoTracker) were successfully detected to provide a full-color image using two excitation lasers at 405 and 488 nm.

Few-Photon Wide-band Imaging

To compare the detection efficiency between a TES and PMT, photon-counting signals were investigated from images in which the same sample was captured under the same irradiation and scanning conditions (**Figure 4**). The photon counting signals as medians by the TES for blue (S_B), green (S_G), red (S_R), and NIR (S_{NIR}) were 5, 53, 59, and 12, respectively, obtained from the area of cell presence in the images (**Figures 4A,B**). The photon-counting signal by the PMT was 32 (S_{PMT}) (**Figure 4C**). These signal values for the TES and PMT were comparable, but it is notable that S_{PMT} is the sum of all fluorescence color signals. Nevertheless, $S_{PMT} = 32$ is remarkably less than the individual $S_G = 53$ and $S_R = 59$. Background signals from the empty area in the images were as small as 0–2 counts by both, the TES and PMT. These results indicate that TES can act as a spectral photon-counting detector for fluorescence cell imaging.

The photon counting numbers detected were in the order of 10^{-17} J. Because the exposure time for each pixel was 20 m, the energy levels were in the order of 10^{-16} W. Although the TES was less efficient in detecting shorter wavelength range photons (Niwa et al., 2017), the efficiency can be improved by optimizing the optical absorption in TES coatings. Furthermore, as the microscope optics reported were our original setup and quite primitive, there remain places for optimization. Commercially available high-end CLSM is also appropriate for employing a TES as a photodetector.

Although the detection efficiency of the PMT is high in the shorter wavelength region, the TES we used was not (Niwa et al., 2017). Nevertheless, sufficiently strong signals could be detected by the TES to depict cellular images. By optimizing the detection efficiency of the TES for a shorter wavelength region, the potential of CLSM using a TES could be improved.

Overall, the excitation irradiation power could be reduced to 100 nW to capture cell imaging, even using our primitive confocal optics with the TES. The excitation laser can be further reduced by improving the optics as well as the TES fabrication, suggesting the potential of the TES for use in cell-imaging applications as ultra-sensitive and wide-band wavelength spectral photodetectors.

CONCLUSION

CLSM optics were constructed and tested for proof of concept using TES as a photodetector for few-photon spectral confocal microscopy imaging of cell samples. Using this microscope, observations of fluorescent-labeled cell samples were used to obtain a full-color image, as well as an IR image, by a single scan. Despite the preliminary observation, excitation laser irradiation at 100 nW was effective in providing cell image data. Thus, it was proved that TES is a potent photodetector for few-photon spectral confocal cell imaging.

DATA AVAILABILITY STATEMENT

The original contributions presented in the study are included in the article/**Supplementary Material**, further inquiries can be directed to the corresponding author.

AUTHOR CONTRIBUTIONS

KN was the principal investigator for this study, and conceived the study and supervised its design. DF and KH prepared and operated the TES devices. The manuscript was drafted by KN and critically reviewed and approved by all the authors.

FUNDING

Part of this work was supported by JST CREST Grant Number JPMJCR17N4, Japan. The devices were fabricated in the clean room for analog-digital superconductivity (CRAVITY) at the National Institute of Advanced Industrial Science and Technology (AIST).

ACKNOWLEDGMENTS

We thank all the staffs of the Quantum Photonics Metrology Group in NMIJ/AIST. We would like to thank Editage (www.editage.com) for English language editing.

REFERENCES

Fukuda, D., Fujii, G., Numata, T., Amemiya, K., Yoshizawa, A., Tsuchida, H., et al. (2011). Titanium-Based Transition-Edge Photon Number Resolving Detector with 98% Detection Efficiency with Index-Matched Small-Gap Fiber Coupling. *Opt. Express* 19, 870–875. doi:10.1364/OE.19.000870

Fukuda, D., Niwa, K., Hattori, K., Inoue, S., Kobayashi, R., and Numata, T. (2018). Confocal Microscopy Imaging with an Optical Transition Edge Sensor. *J. Low Temp Phys.* 193 (5-6), 1228–1235. doi:10.1007/s10909-018-1938-8

Hattori, K., Kobayashi, R., Numata, T., Inoue, S., and Fukuda, D. (2018). Complex Impedance of Fast Optical Transition Edge Sensors up to 30 MHz. *J. Low Temp Phys.* 193 (3-4), 217–224. doi:10.1007/s10909-018-1883-6

Icha, J., Weber, M., Waters, J. C., and Norden, C. (2017). Phototoxicity in Live Fluorescence Microscopy, and How to Avoid it. *BioEssays* 39, 81700003. doi:10.1002/bies.201700003

Irwin, K. D., and Hilton, G. C. (2005). Transition-Edge Sensors. *Top. Appl. Phys.* 99, 63–150. doi:10.1007/10933596_3

Nakajima, Y., Kimura, T., Sugata, K., Enomoto, T., Asakawa, A., Kubota, H., et al. (2005). Multicolor Luciferase Assay System: One-Step Monitoring of Multiple Gene Expressions with a Single Substrate. *BioTechniques* 38 (6), 891–894. doi:10.2144/05386ST03

SUPPLEMENTARY MATERIAL

The Supplementary Material for this article can be found online at: https://www.frontiersin.org/articles/10.3389/fbioe.2021.789709/full#supplementary-material

Niwa, K., Numata, T., Hattori, K., and Fukuda, D. (2017). Few-Photon Color Imaging Using Energy-Dispersive Superconducting Transition-Edge Sensor Spectrometry. *Sci. Rep.* 7, 45660. doi:10.1038/srep45660

Paras, C., Keller, M., White, L., Phay, J., and Mahadevan-Jansen, A. (2011). Near-Infrared Autofluorescence for the Detection of Parathyroid Glands. *J. Biomed. Opt.* 16, 067012. doi:10.1117/1.3583571

Conflict of Interest: The authors declare that the research was conducted in the absence of any commercial or financial relationships that could be construed as a potential conflict of interest.

Publisher's Note: All claims expressed in this article are solely those of the authors and do not necessarily represent those of their affiliated organizations, or those of the publisher, the editors and the reviewers. Any product that may be evaluated in this article, or claim that may be made by its manufacturer, is not guaranteed or endorsed by the publisher.

frontiers in Bioengineering and Biotechnology

ORIGINAL RESEARCH
published: 07 February 2022
doi: 10.3389/fbioe.2022.774786

Host-Dependent Producibility of Recombinant *Cypridina noctiluca* Luciferase With Glycosylation Defects

Yasuo Mitani[1], Rie Yasuno[2], Kiyohito Kihira[3], KwiMi Chung[4], Nobutaka Mitsuda[4], Shusei Kanie[1], Azusa Tomioka[2], Hiroyuki Kaji[2] and Yoshihiro Ohmiya[5,6]*

[1]Bioproduction Research Institute, National Institute of Advanced Industrial Science and Technology (AIST), Sapporo, Japan, [2]Cellular and Molecular Biotechnology Research Institute, AIST, Tsukuba, Japan, [3]Japan Aerospace Exploration Agency (JAXA), Tsukuba, Japan, [4]Bioproduction Research Institute, AIST, Tsukuba, Japan, [5]Biomedical Research Institute, AIST, Ikeda, Japan, [6]Osaka Institute of Technology (OIT), Osaka, Japan

Cypridina noctiluca luciferase (CLuc) is a secreted luminescent protein that reacts with its substrate (Cypridina luciferin) to emit light. CLuc is known to be a thermostable protein and has been used for various research applications, including *in vivo* imaging and high-throughput reporter assays. Previously, we produced a large amount of recombinant CLuc for crystallographic analysis. However, this recombinant protein did not crystallize, probably due to heterogeneous N-glycan modifications. In this study, we produced recombinant CLuc without glycan modifications by introducing mutations at the N-glycan modification residues using mammalian Expi293F cells, silkworms, and tobacco Bright Yellow-2 cells. Interestingly, recombinant CLuc production depended heavily on the expression hosts. Among these selected hosts, we found that Expi293F cells efficiently produced the recombinant mutant CLuc without significant effects on its luciferase activity. We confirmed the lack of N-glycan modifications for this mutant protein by mass spectrometry analysis but found slight O-glycan modifications that we estimated were about 2% of the ion chromatogram peak area for the detected peptide fragments. Moreover, by using CLuc deletion mutants during the investigation of O-glycan modifications, we identified amino acid residues important to the luciferase activity of CLuc. Our results provide invaluable information related to CLuc function and pave the way for its crystallographic analysis.

Keywords: luciferase, *Cypridina noctiluca*, glycosylation, recombinant protein expression, mass spectrometry

OPEN ACCESS

Edited by:
May Griffith,
Université de Montréal, Canada

Reviewed by:
Xianglong Hu,
South China Normal University, China
Gaya Prasad Yadav,
University of Florida, United States

****Correspondence:***
Yasuo Mitani
mitani-y@aist.go.jp

Specialty section:
This article was submitted to Biomaterials, a section of the journal Frontiers in Bioengineering and Biotechnology

Received: *13 September 2021*
Accepted: *17 January 2022*
Published: *07 February 2022*

Citation:
Mitani Y, Yasuno R, Kihira K, Chung K, Mitsuda N, Kanie S, Tomioka A, Kaji H and Ohmiya Y (2022) Host-Dependent Producibility of Recombinant Cypridina noctiluca Luciferase With Glycosylation Defects. Front. Bioeng. Biotechnol. 10:774786. doi: 10.3389/fbioe.2022.774786

INTRODUCTION

Luciferase is an enzyme that oxidizes the substrate luciferin; some are cellular proteins, while others are secreted. Secreted luciferases have been reported in a wide range of phyla including Arthropoda, Mollusca, and Annelida (Shimomura 2012). Among them, luciferase genes have been cloned from Copepoda *Gaussia princeps* (Bryan and Szent-Gyorgyi 2001) and *Metridia longa* (Markova et al., 2004); from Ostracoda *Vargula hilgendorfii* (Thompson et al., 1989), *Cypridina noctiluca* (Nakajima et al., 2004), and Caribbean species (Hensley et al., 2021); from the deep-sea shrimp *Oplophorus gracilirostris* (Inouye et al., 2000); and from syllid worms like *Odontosyllis undecimdonta* (Mitani et al., 2018; Schultz et al., 2018) and related species (Mitani et al., 2019). Secreted luciferases are useful for high-throughput analysis because the assay is made less difficult by using culture supernatants.

Thus far, luciferases from the genera *Oplophorus* and *Gaussia* have been widely used in application research (Hall et al., 2012; Suzuki and Inouye 2014; Markova et al., 2019). *Oplophorus* luciferase (OLuc) has some advantages, such as its catalytic domain with low molecular weight, excellent heat stability, and relatively easy expression in both prokaryotic and eukaryotic cells when some amino acid mutations are incorporated (Hall et al., 2012; Inouye et al., 2013). In the case of *Gaussia* luciferase (GLuc), a production method for low-temperature expression in the presence of chaperones has been established in an *Escherichia coli* expression system (Inouye and Sahara 2008). The three-dimensional (3D) structures of these luciferases have been elucidated by crystallization and X-ray diffraction of the partial domain exhibiting the catalytic function in OLuc (Tomabechi et al., 2016) and by heteronuclear NMR for GLuc (Wu et al., 2020).

C. noctiluca luciferase (CLuc) has been developed for applied research by modifying its surface with fluorescent molecules to emit infrared light (Wu et al., 2009) and by optimizing it for a high-throughput reporter assay (Tochigi et al., 2010). CLuc is also a stable protein with high thermal stability and has high potential for further applications. However, CLuc has a higher molecular weight (62–68 kDa) than OLuc and GLuc, and may have up to 17 potential disulfide bonds between the 34 cysteine residues in its 553 amino acids, while GLuc has only 5 disulfide bonds (Wu et al., 2020), thus making protein production and applied research with CLuc difficult (Inouye and Sahara 2008). There are no reports on the prokaryotic expression of full-length CLuc. Although CLuc does not show homology to other luciferases, its first- and second-half regions display weak homology to the von Willebrand factor type D (VWD) domain (Oakley 2005). These two VWD-like domains show approximately 20% homology to each other. The first half, containing 302 amino acids, has been expressed using an *E. coli* system, resulting in 45% activity of the intact protein (Hunt et al., 2017). However, there are no biochemical reports on the residues directly involved in CLuc activity, and there is no information on its 3D structure. The establishment of a system that can stably and massively produce CLuc is expected to lead to further progress in crystallographic analysis and future applications. Structural information will also help to modify CLuc using a simple approach to bioconjugation (Hu et al., 2018).

Secreted proteins in addition to luciferases need to undergo appropriate folding, including disulfide bond formation during the secretory process, and most secreted proteins undergo post-translational modification such as glycosylation (Helenius and Aebi 2001). Although glycosylation is generally considered to contribute to protein stability by increasing folding efficiency (Helenius and Aebi 2001; Wang et al., 2018), its effects on protein function itself are inconsistent. For example, it was reported that some hormones maintain their ability to bind to receptors when glycosylation is removed by hydrogen fluoride (HF) treatment, but the downstream signals are not transduced (Lapthorn et al., 1994). In another case, human follicle-stimulating hormone (hFSH) remains fully active even after glycan chains are removed *via* point mutation (Fox et al., 2001); the folding of these glycosylation-deficit mutants is unaffected (Wilbers et al., 2016). Since glycosylation can prevent crystallization due to its heterogeneity (Lapthorn et al., 1994; Columbus 2015), glycans can be removed by deglycosylation enzyme treatment or mutagenesis to the modification site (Woods 2018). CLuc is the only secreted luciferase whose glycan structure has been analyzed and reported to remain fully active even after enzymatic removal of the glycan from wild-type (Wt) recombinant protein produced in suspension-cultured tobacco Bright Yellow-2 (BY-2) cells (Mitani et al., 2017). In the case of mutant CLuc lacking glycan modification sites expressed in COS1 cells, its specific activity has been reported to be reduced to approximately 20% when compared to the Wt recombinant protein produced in COS1 cells. However, due to the low productivity, quantitative analysis using purified CLuc proteins remains to be conducted (Yasuno et al., 2018).

In this study, we tried to produce mutant recombinant CLuc lacking N-glycan modification in available hosts in our laboratory, including Expi293F cells, silkworms, and BY-2 cells. CLuc has two conserved N-glycan modification motifs, NIT and NTS, in its amino acid sequence, starting at residues N182 and N404, respectively. These two motifs were mutated to produce a double mutant recombinant protein (Dmt CLuc) containing T184A + N404D substitutions. In comparing the specific activities of the obtained recombinant CLuc by measuring the protein amount using highly purified CLuc or anti-CLuc antibody, we found that the mutant CLuc produced by Expi293F cells showed almost the same specific activity as the Wt. We also found important amino acid residues involved in the luciferase activity by expressing amino-terminal serial deletion mutants of Dmt CLuc.

MATERIALS AND METHODS

Recombinant Proteins Used in This Study

In this study, we produced Wt and Dmt CLuc using Expi293F cells, silkworms, and BY-2 cells, designating the recombinant proteins $CLuc_{EX}$, $CLuc_{SW}$, and $CLuc_{BY}$, respectively. For clarity, we designated Dmt CLuc previously expressed using COS1 cells (Yasuno et al., 2018) as Dmt $CLuc_{CO}$ in this study.

Cypridina noctiluca Luciferase Expression Using Expi293 Expression System

Expression vectors for recombinant Wt $CLuc_{EX}$ and Dmt $CLuc_{EX}$, pcDNA-CL (Nakajima et al., 2004), and pcDNA-CL (T184A + N404D) (Yasuno et al., 2018) were prepared as previously described. The pcDNA-CL (T184A + N404D) was modified by the insertion of the sequence for His-tag and TEV protease (HHHHHHENLYFQG) following the predicted signal sequence (1–18 a.a.). Expression vectors for deletion mutants were designed with deleted amino-terminal or carboxyl-terminal residues of the mature region by modification of the His-TEV-pcDNA-CL (T184A + N404D) plasmid. These insertion and deletion modifications were outsourced to Genscript Japan. Each expression vector was transfected into Expi293F mammalian cells (Thermo Fisher Scientific, MA,

United States) according to the manufacturer's instructions. On day 5 post-transfection, the culture medium was centrifuged at 350 × g for 10 min, and the resulting supernatant was used for the following analysis, hereafter called the medium fraction. Precipitated cells were lysed with 10 mM Tris-HCl (pH 7.4) by sonication, the cell lysate was centrifuged at 20,000 × g for 5 min, and the resulting supernatant was used as the cell extract fraction. Immunoblot analysis for CLuc proteins was conducted as described previously (Yasuno et al., 2018), except that 10 µL of each medium fraction sample was prepared under reducing conditions with dithiothreitol before electrophoresis and that the anti-CLuc antibody was raised using purified recombinant CLuc in rabbit. The activities of the recombinant CLuc proteins were measured as described previously (Yasuno et al., 2018), and the intensities were obtained as relative light units (RLUs).

LC-MS/MS Analyses of *Cypridina noctiluca* Luciferase Mutated at N-Glycosylation Sites

Dmt $CLuc_{EX}$ was S-reduced and alkylated as described previously (Mitani et al., 2017). The protein was digested with a mixture of trypsin and Lys-C endopeptidase and/or chymotrypsin (TL/C/CTL). An aliquot of each digest was heated at 80°C for 2 h in 0.1% TFA to remove sialic acid and to increase the detection sensitivity of glycopeptides. Each digest was analyzed by an LC-MS system using a nanoflow LC (Ultimate 3000, Thermo Fisher Scientific) and Orbitrap Fusion Tribrid mass spectrometer (Thermo Fisher Scientific). MS and MS/MS spectra were obtained by the Orbitrap analyzer with a resolution of 120,000 at 200 m/z. Data dependently selected precursor ions were fragmented by high-energy collision-induced dissociation (HCD) and HCD-fragment-triggered EThcD. Glycan peptide cluster analysis was performed by glycan-heterogeneity-based relational identification of glycopeptide signals on elution profile (Glyco-RIDGE; Togayachi et al., 2018). MS/MS spectra were searched using Mascot (ver. 2.5.1, Matrix Science, MA, United States) with the UniProt protein sequence database for *Homo sapiens* including sequences of CLuc (gi|41152712) with mutations (T184A + N404D). Search parameters were set as described previously (Mitani et al., 2017) with slight modifications; Hex(1) HexNAc(1)_Nli(ST) or Hex(1) HexNAc(1) NeuAc(2)_Nli(ST); Nli: neutral loss and ignore mass were set, enzyme; semi for each enzyme, and maximum missed cleavage for chymotrypsin; 6.

Cypridina noctiluca Luciferase Expression in Silkworm and Initial Purification

Recombinant $CLuc_{SW}$ proteins were produced using the silkworm expression system as described previously (Maeda et al., 1985). CLuc ORF was amplified by PCR and inserted into the pHS02 vector under the control of a polyhedron promoter. The recombinant $CLuc_{SW}$ was designed to be produced with FLAG-tag at its carboxyl terminus. Silkworm body fluid was collected from 20 individuals and subjected to ion exchange chromatography using the HiTrap Q HP column (GE Healthcare, IL, United States). The activities of elusion fractions using up to 500 mM NaCl were monitored by light emission activity using synthetic cypridinid luciferin as described previously (Yasuno et al., 2018). The active fractions were pooled and concentrated using a centrifuge filter unit (Amicon Ultra-15, Millipore, MA, United States), followed by desalting using a PD-10 column (GE Healthcare) according to the manufacturer's protocol. The desalted sample was then further purified using anti-FLAG affinity gel (Merck, Germany).

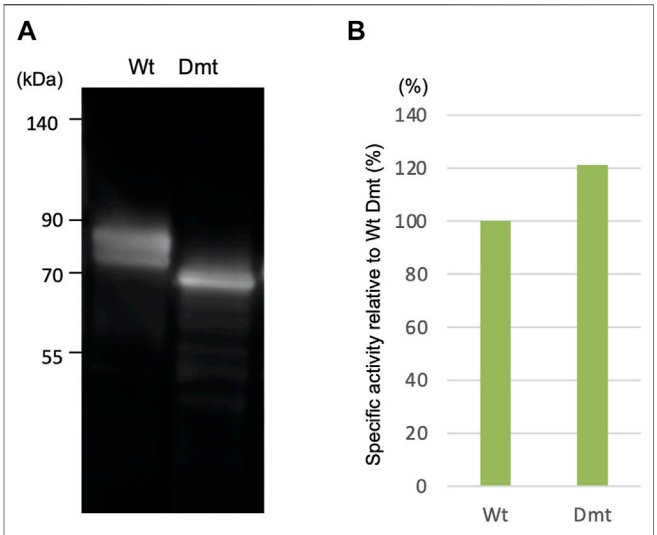

FIGURE 1 | Expression of recombinant wild-type (Wt) and double mutant (Dmt) $CLuc_{EX}$. **(A)** Immunoblot analysis of recombinant proteins using anti-CLuc antibody. **(B)** Relative specific $CLuc_{EX}$ activities in the medium. $CLuc_{EX}$-specific activities were determined by dividing the luminescence intensities by the amount of each protein estimated from immunoblot band intensities. The activity of Wt $CLuc_{EX}$ corresponds to 100%. Note that the immunoblot band looks broad due to glycosylation modification.

Purification of Double Mutant Recombinant $Protein_{SW}$

Dmt $CLuc_{SW}$ was purified by anion exchange chromatography using a MonoQ column (Cytiva, MA, United States). The purification was performed under the conditions of 20 mM HEPES-NaOH pH 7.5, 100–600 mM NaCl in a linear gradient. Finally, gel filtration chromatography using a Superdex 200 Increase column (Cytiva) was carried out under the conditions of 150 mM NaCl and 20 mM HEPES-NaOH pH 7.5 to make the final purified sample. The sample at this stage showed a single band in SDS-PAGE.

Plasmid Construction for BY-2 Cells and Protein Expression

The Dmt $CLuc_{BY}$ coding sequence was amplified by PCR from chemically synthesized cDNA with a Sma1_cLUC_ F (5′-gggccc gggATGAAGACTTTAATACTCGCT-3′) and Sal1_cLUC_R (5′-CCCGTCGACTCACTTGCACTCATCTGGCA-3′) primer pair and cloned into a p35SHSPG vector (Oshima et al., 2011). Then, CaMV35Spro::Dmt CLUC::HSPter was

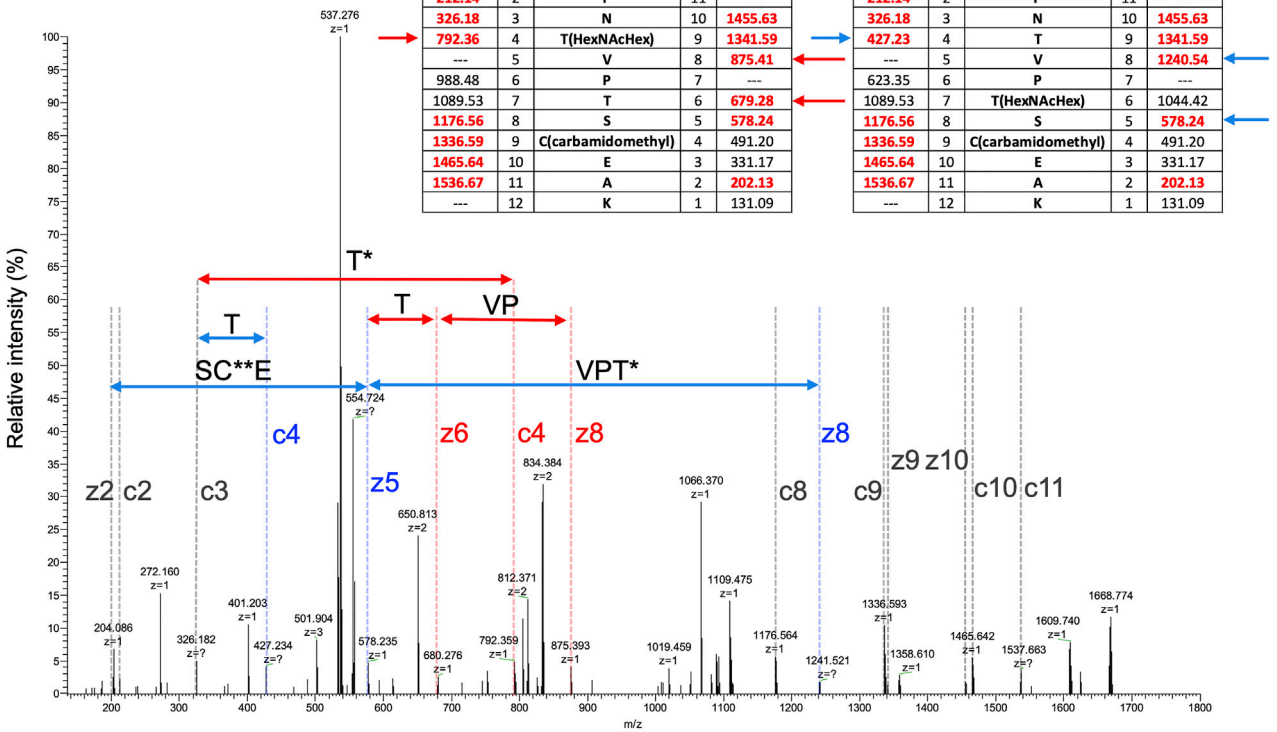

FIGURE 2 | EThcD MS/MS spectrum of a peptide (PPNTVPTSCEAK) having Hex(1) HexNAc(1). MS/MS acquired at the time of (3) in **Supplementary Figure S3**. Masses of predicted fragment ions are listed in the inset tables. Fragment ion characteristics of glycosylation at Thr-30 are indicated in red, those at Thr-33 are in blue, and common ones are in gray. HexNAcHex and carbamidomethyl modifications are indicated by single and double asterisks, respectively.

transferred to a pBCKK T-DNA vector (Mitsuda et al., 2006) and transformed into *Rhizobium radiobacter* GV3101.

RESULTS AND DISCUSSION

Recombinant *Cypridina noctiluca* Luciferase Expression Using Expi293 Expression System

In a previous work, we reported the expression of recombinant CLuc deficient in N-glycosylation binding sites (Dmt $CLuc_{CO}$) in a mammalian adherent cell, COS1. In the present study, we first focused on Expi293F cells, which have been adapted to grow in high density and to give higher recombinant protein yields, and tried a suspension culture of the Expi293 expression system, with the expectation of high expression of CLuc. Each expression vector for Wt or Dmt $CLuc_{EX}$ was transfected into Expi293F cells. After 5 days of incubation, the accumulation of $CLuc_{EX}$ in the medium was confirmed by immunoblot analysis using an anti-CLuc antibody (**Figure 1A**). Mobility shift differences between Wt and Dmt $CLuc_{EX}$ were presumably due to deficiencies in N-glycans. Over 90% of the luciferase activities were observed in the medium in both Wt and Dmt $CLuc_{EX}$, indicating that the majority of CLuc produced in Expi293F cells was secreted into the medium efficiently. The activity of $CLuc_{EX}$ was determined by measuring the luminescence intensity using synthetic cypridinid luciferin. The specific activities of Wt and Dmt $CLuc_{EX}$ in the medium were calculated by dividing the luminescence intensities by the estimated intensities of their immunoblot $CLuc_{EX}$ bands (**Figure 1B**). The visibility of the immunoblot band differed among multiple experiments, and the estimation range was broad. Thus, we performed 3 independent experiments and calculated the average of the specific activity ratio for Dmt $CLuc_{EX}$ relative to that for Wt $CLuc_{EX}$. A typical result is shown in **Figure 1B**, where the ratio was approximately 120%, but the average ratio was 90.7 ± 21.8%. These data showed that the specific activities of Wt and Dmt $CLuc_{EX}$ were almost the same, unlike the previous result of approximately 20% for Dmt $CLuc_{CO}$ expressed in COS1 cells.

Confirmation of N-glycosylation site mutations and search for O-glycosylation site(s) of Dmt $CLuc_{EX}$ expressed in Expi293F cells by LC-MS.

Dmt $CLuc_{EX}$ protein samples digested with chymotrypsin and/or a mixture of trypsin and Lys-C endopeptidase were analyzed by LC-MS/MS, and the obtained MS/MS spectra (HCD) were searched using Mascot to identify Dmt $CLuc_{EX}$-derived peptides (**Supplementary Tables S1–S6**). For the trypsin + Lys-C (TL) digest, 81% of peptides were identified, and a peptide containing mutation T184A was included. In addition,

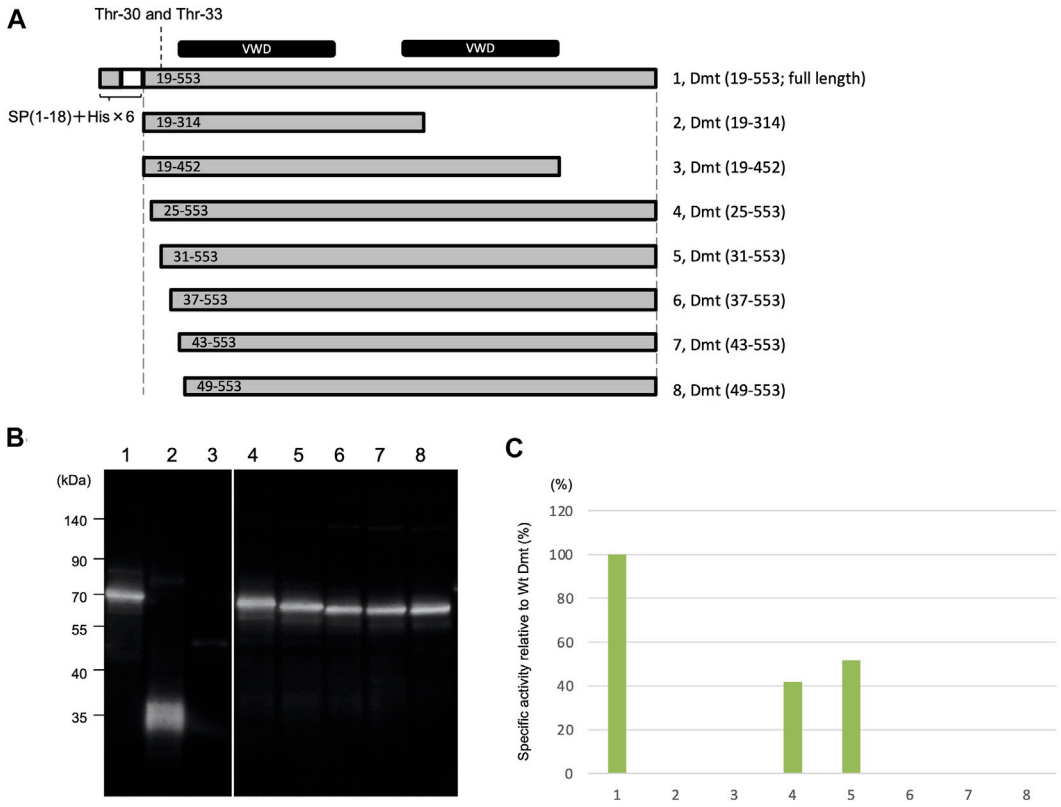

FIGURE 3 | Luminescence activities of Dmt $CLuc_{EX}$ deletion mutants. **(A)** Schematic representation of full-length Dmt $CLuc_{EX}$ and its deletion mutants. Each construct was designed to have a natural signal peptide (SP 1–18) and His tag (His × 6)–TEV sequence at the amino terminus. The O-glycosylation sites are at 30 and 33. VWD-like domains are indicated by black bars at the top of the panel. **(B)** Immunoblot analysis of Dmt $CLuc_{EX}$ deletion mutants. Expi293F cells were transfected with the indicated constructs, and the produced protein secreted into the medium was analyzed by Western blotting using anti-CLuc antibody. **(C)** Relative specific activity of each Dmt $CLuc_{EX}$ deletion mutant. Specific $CLuc_{EX}$ activities were determined as shown in **Figure 1**. Note that the band in lane 3 is very faint, probably due to the low expression level of this construct.

for the chymotrypsin digest, 87% of peptides were identified, including a peptide with an N404D mutation (**Supplementary Tables S1, S3**). These results indicate that both N-glycosylation sites were mutated and lost.

To search for other glycosylated site(s), EThcD MS/MS spectra were obtained by triggering with HCD fragments of m/z = 138, 204, or 366, that is, diagnostic fragment ions of glycan corresponding to $[HexNAc\text{-}CH_6O_3]^+$, $[HexNAc]^+$, or $[HexHexNAc]^+$, respectively. Several O-glycosylated peptides, which were modified with glycan at a serine or threonine residue, were found by the Mascot search, peptide sequences were identified from HCD spectra, and glycosylated sites were assigned by EThcD spectra (**Supplementary Tables S2, S6**, **Supplementary Figures S1–S5**). In a TL digest, the HCD MS/MS spectrum of peptide sequence PPNTVPTSCEAK (residues 27–38) having a Hex(1) HexNAc(1) NeuAc(2) modification was found, presenting a series of diagnostic ions of glycan including a NeuAc-H_2O fragment (m/z = 274) and a ladder-like signal of glycopeptides suggesting a NeuAc-Hex-HexNAc-peptide (**Supplementary Figure S1**). A partial sequence of the core peptide was assigned. In an acid-treated digest with chymotrypsin + trypsin + Lys-C (CTL), glycopeptides having the same core sequence, PPNTVPTSCEAK, carrying 1 and 2 Hex(1) HexNAc(1) modification(s), were identified. A partial peptide sequence could be assigned from their HCD spectra, but the modification sites were not identified because there are 3 potential Ser/Thr in the peptide (**Supplementary Figure S2**). Glyco-RIDGE analysis of the acid-treated TL digest revealed a cluster of the core peptide having different glycan compositions, that is, members carrying glycans of Hex:HexNAc:dHex = 0:0:0 (no glycosylation), 0:1:0, 1:1:0, 1:2:0, 2:2:0, and 3:3:0 (data not shown). Extracted ion chromatograms are shown in **Supplementary Figure S3** for the signals of 0:0:0, 0:1:0, 1:1:0, and 2:2:0. Signals of 1:2:0 and 3:3:0 were too weak to be seen in the figure. The signal of non-glycosylated peptide was highest even when the scale was reduced to 1/100, suggesting that the glycan occupancy of the peptide was quite low, about 2% of the area. The glycopeptide carrying Hex(1) HexNAc(1) showed twin broad peaks. The EThcD spectra of glycopeptide ions at 3 different retention times were compared (**Supplementary Figure S4**), revealing multiple O-glycosylated sites in the peptide sequence: Thr-30 and Thr-33 or Ser-34. MS/MS acquired at time (2) in **Supplementary Figure S3** suggested that both Thr-30 and Thr-33 were glycosylated (**Figure 2**). The EThcD spectrum of the

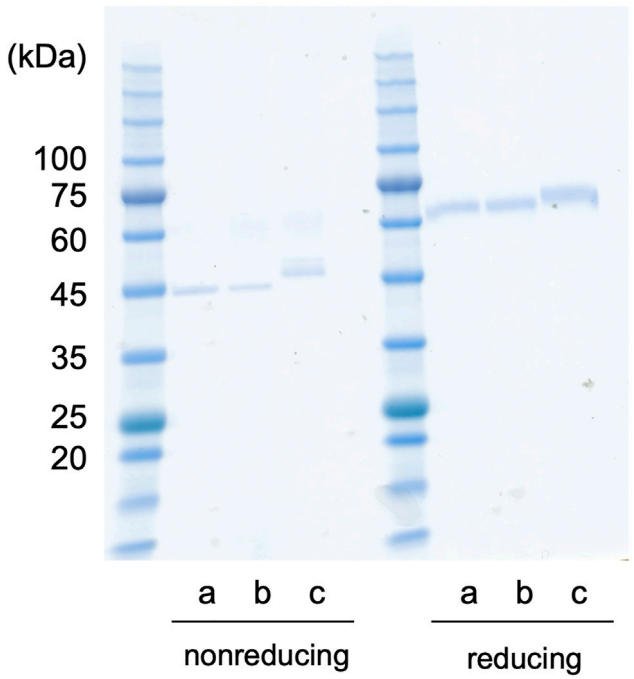

FIGURE 4 | CLuc expression in silkworm. $CLuc_{SW}$ recombinant proteins (200 ng for each lane) were analyzed by SDS-PAGE. The gel mobility was different under reducing or non-reducing conditions. The apparent molecular weight was higher under reducing conditions than under non-reducing ones, showing relative compact folding of the recombinant proteins under non-reducing condition probably due to disulfide bonding. In both cases, the recombinant Wt $CLuc_{SW}$ band looks larger than the Dmt $CLuc_{SW}$ band. (a) Dmt $CLuc_{SW}$. (b) N182D + N404D mutant $CLuc_{SW}$. (c) Wt $CLuc_{SW}$.

peptide having 2 Hex(1) HexNAc(1) was found, and Thr-30 had the Hex(2) HexNAc(2) modification (**Supplementary Figure S5**). In addition, another sequence EGECIDSSCGTCTR (residues 39–52) was found to have Hex(1) HexNAc(1); however, the site could not be assigned. The rate of O-glycosylation of the peptide was found to be quite low (<1/10^4) from the area of the extracted ion chromatogram (data not shown).

Deletion Mutants of O-Glycosylation Residues

Deletion mutants were constructed to remove the region around O-glycosylation residues at Thr-30 and Thr-33 (**Figure 3A**). Protein expression using the Expi293 expression system was confirmed by immunoblot analysis (**Figure 3B**), and specific activities were determined based on the immunoblot band intensity (**Figure 3C**). Specific activities were halved in mutants with deletions at residues 19–24 and 19–30 when compared to the full length of Dmt $CLuc_{EX}$. However, no activities were exhibited by the mutants with further deletions at residues 19–36, 19–42, or 19–48, even when the protein amounts were almost equal to those of the full-length protein. These results suggested that the amino acid residues at 31–36 (VPTSCE) were important for CLuc function. This region was highly conserved with the luciferase of the related cypridinid species, including cysteine residues (**Supplementary Figure S6**).

Moreover, the removal effects of carboxyl-terminal regions of Dmt $CLuc_{EX}$ were investigated. A deletion mutant (19–314) designed to remove the second VWD-like domain exhibited no luciferase activity even though protein production was confirmed at the predicted size of 36 kDa (**Figure 3B**), suggesting that the residues at 315–553 were indispensable regions for CLuc function. Deletion of the residues at 453–553, which was designed to remove the carboxyl region behind the second VWD-like domain, resulted in a significant reduction of protein production, observed as a slight band around 50 kDa (**Figure 3B**). Deletion of the region at 453–553 might lead to the instability of the protein or to a reduction of secretion efficiency in this expression system.

Recombinant *Cypridina noctiluca* Luciferase Expression Using Silkworm

The recombinant proteins of Dmt and Wt $CLuc_{SW}$ were produced using the silkworm expression system. First, each recombinant protein was simply purified using anti-FLAG affinity gel, and a single band was observed for each case in the SDS-PAGE analysis (**Figure 4**). Depending on the protein, treatment with a reducing agent differently affected the mobility in the gel, as shown previously (Mitani et al., 2017). The Wt $CLuc_{SW}$ band looked larger than the Dmt $CLuc_{SW}$ band, and this difference was more obvious under the non-reducing conditions (**Figure 4**). This size difference would be due to the glycan modification, suggesting that an N-glycan chain would be added to CLuc when produced in silkworm, similar to the case with COS1 and BY-2 cell expressions, as previously reported (Mitani et al., 2017; Yasuno et al., 2018). The luciferase activities of Dmt and Wt $CLuc_{SW}$ were 4.24×10^7 and 1.67×10^8 RLU ng^{-1}, respectively. These data indicated that almost 25% activity was retained in the Dmt $CLuc_{SW}$ even without glycan modification. These data were similar to those obtained using a mammalian expression system, which resulted in approximately 20% activity for Wt $CLuc_{CO}$ (Yasuno et al., 2018). We also produced another mutant, N182D + N404D, and expected an improvement in its specific activity. This mutant recombinant protein was successfully produced (**Figure 4**), but its activity was almost the same as that of Dmt $CLuc_{SW}$ (4.18×10^8 RLU ng^{-1}). Thus, we decided to use Dmt $CLuc_{SW}$ for further analysis.

Next, to improve the recombinant protein purity, each sample was successively purified by FLAG-tag affinity chromatography and anion exchange chromatography. The results showed that Dmt $CLuc_{SW}$ was separated into two major peaks (**Supplementary Figure S7A**). Considering the peak area ratio of the chromatograph, the existence ratio of these fractions was estimated to be about 1:3. The two separated peaks of Dmt $CLuc_{SW}$ were collected, and each sample was subjected to gel filtration chromatography. The higher molecular weight fraction was eluted in the void volume, and the lower one was eluted in the volume corresponding to the molecular weight of the $CLuc_{SW}$ monomer. Next, electrophoresis under native conditions was performed on each of these fractions. As shown in **Supplementary Figure S7B**, the Wt $CLuc_{SW}$ and the Dmt $CLuc_{SW}$, which were derived from the lower molecular weight fraction in the

gel filtration chromatography, showed a single band near the calculated molecular weight in each case, while the Dmt $CLuc_{SW}$, which was obtained as the void fraction in the gel filtration, showed a much higher molecular weight than the monomer. This aggregation is probably due to misfolding, since glycosylation is known to be involved in the correct folding of secreted proteins during translation (Wang et al., 2018). These aggregated Dmt $CLuc_{SW}$ did not show any luciferase activity. These data seemed reasonable because only 25% of Dmt $CLuc_{SW}$ was produced as a monomer, probably with normal activity, while the remaining 75% was aggregated during protein production, resulting in no luciferase activity. Thus, our first estimates of the specific activity of the Dmt $CLuc_{SW}$ when purified only with anti-FLAG affinity were artificially low due to the presence of a high percentage of aggregated, non-functional luciferase. In the case of Dmt $CLuc_{CO}$ expressed using COS1 cells, the specific activity was 20% of that of the Wt $CLuc_{CO}$ (Yasuno et al., 2018). Although we did not perform further purification for this protein due to the limited amount of protein produced, 80% of the recombinant protein may have aggregated during protein production, as in the case of the silkworm expression system.

Recombinant *Cypridina noctiluca* Luciferase Expression Using Suspension-Cultured Tobacco BY-2 Cells

Wt $CLuc_{BY}$ was efficiently expressed using cultured tobacco BY-2 cells (Mitani et al., 2017), and thus, we tried to produce Dmt $CLuc_{BY}$. However, none of the clones produced recombinant Dmt $CLuc_{BY}$ even though we tested 4 independent BY-2 callus clones. This result suggested that the N-glycosylation of $CLuc_{BY}$ was essential for its recombinant protein production in BY-2 cells.

CONCLUSION

In this study, we produced recombinant mutant CLuc lacking N-glycosylation motifs using Expi293F cells, silkworms, and tobacco BY-2 cells. The relative activity of the produced Dmt $CLuc_{EX}$ was almost the same as that of the Wt $CLuc_{EX}$, whereas Dmt $CLuc_{CO}$ was approximately 20% of that of Wt $CLuc_{CO}$ in the previous study (Yasuno et al., 2018). In the case of the silkworm system, the relative activity of mutant CLuc purified using only anti-FLAG affinity gel was 25% of that of Wt $CLuc_{SW}$. However, further purification revealed that approximately 75% of the FLAG-purified recombinant protein was aggregated and its enzyme activity was lost. In the BY-2 cells, our attempt to express Dmt $CLuc_{BY}$ resulted in no recombinant protein production despite the use of 4 independent transgenic callus clones. Taken together, our results suggested that the productivity of CLuc mutated in the N-glycosylation sites differed depending on the expression host. Therefore, we should choose the recombinant protein expression system carefully in order to minimize the effect of glycosylation, especially for cases such as protein crystallization, which requires the removal of glycan. In our case, the Expi293 expression system was the best choice for Dmt CLuc production. To understand the reason for these differences in protein production efficiency, we need to study the protein production pathway in detail and to investigate which point is critical for the efficient production of recombinant protein. Finally, we identified important residues involved in CLuc activity. Crystallographic analysis will be necessary to clarify the functions of these residues in the oxidation process of cypridinid luciferin.

DATA AVAILABILITY STATEMENT

The datasets presented in this study can be found in online repositories. The names of the repository/repositories and accession number(s) can be found below: https://repository.jpostdb.org/ and JPST001397, PXD029916.

AUTHOR CONTRIBUTIONS

YM, RY, KK, and YO designed the research. RY and KK performed mammalian cell expression, purification, and activity analysis. KC and NM performed Dmt CLuc construction and transformation, and supervised BY-2 transfection. SK performed BY-2 transfection, purification of recombinant protein, and activity assay. AT and HK performed glycan modification analysis. All authors read and approved the final manuscript.

FUNDING

This work was partially supported by JSPS KAKENHI (grant number JP18KK0199) (to YM).

ACKNOWLEDGMENTS

We are grateful to Mami Komatsu (AIST) for her assistance in experiments using BY-2. We thank Hensley M. Nicholai (Cornell University) for his useful comments to the manuscript.

SUPPLEMENTARY MATERIAL

The Supplementary Material for this article can be found online at: https://www.frontiersin.org/articles/10.3389/fbioe.2022.774786/full#supplementary-material

REFERENCES

Bryan, B. J., and Szent-Gyorgyi, C. (2001). *Luciferases, Fluorescent Proteins, Nucleic Acids Encoding the Luciferases and Fluorescent Proteins and the Use Thereof in Diagnostics, High Throughput Screening and novelty Items*. U.S. Patent No 6,232,107 (Pittsburgh, PA: Prolume, LTD).

Columbus, L. (2015). Post-expression Strategies for Structural Investigations of Membrane Proteins. *Curr. Opin. Struct. Biol.* 32, 131–138. doi:10.1016/j.sbi.2015.04.005

Fox, K. M., Dias, J. A., and Van Roey, P. (2001). Three-dimensional Structure of Human Follicle-Stimulating Hormone. *Mol. Endocrinol.* 15, 378–389. doi:10.1210/mend.15.3.0603

Hall, M. P., Unch, J., Binkowski, B. F., Valley, M. P., Butler, B. L., Wood, M. G., et al. (2012). Engineered Luciferase Reporter from a Deep Sea Shrimp Utilizing a Novel Imidazopyrazinone Substrate. *ACS Chem. Biol.* 7, 1848–1857. doi:10.1021/cb3002478

Helenius, A., and Aebi, a. M. (2001). Intracellular Functions of N-Linked Glycans. *Science* 291, 2364–2369. doi:10.1126/science.291.5512.2364

Hensley, N. M., Ellis, E. A., Leung, N. Y., Coupart, J., Mikhailovsky, A., Taketa, D. A., et al. (2021). Selection, Drift, and Constraint in Cypridinid Luciferases and the Diversification of Bioluminescent Signals in Sea Fireflies. *Mol. Ecol.* 30, 1864–1879. doi:10.1111/mec.15673

Hu, X., Zhao, X., He, B., Zhao, Z., Zheng, Z., Zhang, P., et al. (2018). A Simple Approach to Bioconjugation at Diverse Levels: Metal-free Click Reactions of Activated Alkynes with Native Groups of Biotargets without Prefunctionalization. *Research* 2018, 3152870. doi:10.1155/2018/3152870

Hunt, E. A., Moutsiopoulou, A., Broyles, D., Head, T., Dikici, E., Daunert, S., et al. (2017). Expression of a Soluble Truncated Vargula Luciferase in *Escherichia coli*. *Protein Expr. Purif.* 132, 68–74. doi:10.1016/j.pep.2017.01.007

Inouye, S., and Sahara, Y. (2008). Soluble Protein Expression in *E. coli* Cells Using IgG-Binding Domain of Protein A as a Solubilizing Partner in the Cold Induced System. *Biochem. Biophysical Res. Commun.* 376, 448–453. doi:10.1016/j.bbrc.2008.08.149

Inouye, S., Sato, J.-i., Sahara-Miura, Y., Yoshida, S., Kurakata, H., and Hosoya, T. (2013). C6-Deoxy Coelenterazine Analogues as an Efficient Substrate for Glow Luminescence Reaction of nanoKAZ: The Mutated Catalytic 19kDa Component of Oplophorus Luciferase. *Biochem. Biophysical Res. Commun.* 437, 23–28. doi:10.1016/j.bbrc.2013.06.026

Inouye, S., Watanabe, K., Nakamura, H., and Shimomura, O. (2000). Secretional Luciferase of the Luminous Shrimp Oplophorus Gracilirostris : cDNA Cloning of a Novel Imidazopyrazinone Luciferase. *FEBS Lett.* 481, 19–25. doi:10.1016/s0014-5793(00)01963-3

Lapthorn, A. J., Harris, D. C., Littlejohn, A., Lustbader, J. W., Canfield, R. E., Machin, K. J., et al. (1994). Crystal Structure of Human Chorionic Gonadotropin. *Nature* 369, 455–461. doi:10.1038/369455a0

Maeda, S., Kawai, T., Obinata, M., Fujiwara, H., Horiuchi, T., Saeki, Y., et al. (1985). Production of Human α-interferon in Silkworm Using a Baculovirus Vector. *Nature* 315, 592–594. doi:10.1038/315592a0

Markova, S. V., Golz, S., Frank, L. A., Kalthof, B., and Vysotski, E. S. (2004). Cloning and Expression of cDNA for a Luciferase from the Marine Copepod Metridia Longa. *J. Biol. Chem.* 279, 3212–3217. doi:10.1074/jbc.M309639200

Markova, S. V., Larionova, M. D., and Vysotski, E. S. (2019). Shining Light on the Secreted Luciferases of marine Copepods: Current Knowledge and Applications. *Photochem. Photobiol.* 95, 705–721. doi:10.1111/php.13077

Mitani, Y., Oshima, Y., Mitsuda, N., Tomioka, A., Sukegawa, M., Fujita, M., et al. (2017). Efficient Production of Glycosylated *Cypridina* Luciferase Using Plant Cells. *Protein Expr. Purif.* 133, 102–109. doi:10.1016/j.pep.2017.03.008

Mitani, Y., Yasuno, R., Futahashi, R., Oakley, T. H., and Ohmiya, Y. (2019). Luciferase Gene of a Caribbean Fireworm (Syllidae) from Puerto Rico. *Sci. Rep.* 9, 13015. doi:10.1038/s41598-019-49538-7

Mitani, Y., Yasuno, R., Isaka, M., Mitsuda, N., Futahashi, R., Kamagata, Y., et al. (2018). Novel Gene Encoding a Unique Luciferase from the Fireworm Odontsyllis Undecimdonta. *Sci. Rep.* 8, 12789. doi:10.1038/s41598-018-31086-1

Mitsuda, N., Hiratsu, K., Todaka, D., Nakashima, K., Yamaguchi-Shinozaki, K., and Ohme-Takagi, M. (2006). Efficient Production of Male and Female Sterile Plants by Expression of a Chimeric Repressor in *Arabidopsis* and rice. *Plant Biotechnol. J.* 4, 325–332. doi:10.1111/j.1467-7652.2006.00184.x

Nakajima, Y., Kobayashi, K., Yamagishi, K., Enomoto, T., and Ohmiya, Y. (2004). cDNA Cloning and Characterization of a Secreted Luciferase from the Luminous Japanese Ostracod,Cypridina Noctiluca. *Biosci. Biotechnol. Biochem.* 68, 565–570. doi:10.1271/bbb.68.565

Oakley, T. H. (2005) Myodocopa (Crustacea: Ostracoda) as Models for Evolutionary Studies of Light and Vision: Multiple Origins of Bioluminescence and Extreme Sexual Dimorphism. *Hydrobiologia* 538, 179–192. doi.org/doi:10.1007/s10750-004-4961-5

Oshima, Y., Mitsuda, N., Nakata, M., Nakagawa, T., Nagaya, S., Kato, K., et al. (2011). Novel Vector Systems to Accelerate Functional Analysis of Transcription Factors Using Chimeric Repressor Gene-Silencing Technology (CRES-T). *Plant Biotechnol.* 28, 201–210. doi:10.5511/plantbiotechnology.11.0124a

Schultz, D. T., Kotlobay, A. A., Ziganshin, R., Bannikov, A., Markina, N. M., Chepurnyh, T. V., et al. (2018). Luciferase of the Japanese Syllid Polychaete Odontosyllis Umdecimdonta. *Biochem. Biophysical Res. Commun.* 502, 318–323. doi:10.1016/j.bbrc.2018.05.135

Shimomura, O. (2012). *Bioluminescence: Chemical Principals and Methods*. Singapore, Singapore: World Scientific. doi:10.1142/8239

Suzuki, T., and Inouye, S. (2014). Video-rate Bioluminescence Imaging of Protein Secretion from a Living Cell. *Methods Mol. Biol.* 1098, 71–83. doi:10.1007/978-1-62703-718-1_6

Thompson, E. M., Nagata, S., and Tsuji, F. I. (1989). Cloning and Expression of cDNA for the Luciferase from the marine Ostracod *Vargula Hilgendorfii*. *Pnas* 86, 6567–6571. doi:10.1073/pnas.86.17.6567

Tochigi, Y., Sato, N., Sahara, T., Wu, C., Saito, S., Irie, T., et al. (2010). Sensitive and Convenient Yeast Reporter Assay for High-Throughput Analysis by Using a Secretory Luciferase from *Cypridina Noctiluca*. *Anal. Chem.* 82, 5768–5776. doi:10.1021/ac100832b

Togayachi, A., Tomioka, A., Fujita, M., Sukegawa, M., Noro, E., Takakura, D., et al. (2018). Identification of Poly-N-Acetyllactosamine-Carrying Glycoproteins from HL-60 Human Promyelocytic Leukemia Cells Using a Site-specific Glycome Analysis Method, Glyco-RIDGE. *J. Am. Soc. Mass. Spectrom.* 29, 1138–1152. doi:10.1007/s13361-018-1938-6

Tomabechi, Y., Hosoya, T., Ehara, H., Sekine, S.-i., Shirouzu, M., and Inouye, S. (2016). Crystal Structure of nanoKAZ: The Mutated 19 kDa Component of *Oplophorus* Luciferase Catalyzing the Bioluminescent Reaction with Coelenterazine. *Biochem. Biophysical Res. Commun.* 470, 88–93. doi:10.1016/j.bbrc.2015.12.123

Wang, Z., Guo, C., Liu, L., and Huang, H. (2018). Effects of N-Glycosylation on the Biochemical Properties of Recombinant bEKL Expressed in Pichia pastoris. *Enzyme Microb. Technology* 114, 40–47. doi:10.1016/j.enzmictec.2018.03.004

Wilbers, R. H. P., Westerhof, L. B., Reuter, L. J., Castilho, A., van Raaij, D. R., Nguyen, D.-L., et al. (2016). The N-Glycan on Asn54 Affects the Atypical N-Glycan Composition of Plant-Produced Interleukin-22, but Does Not Influence its Activity. *Plant Biotechnol. J.* 14, 670–681. doi:10.1111/pbi.12414

Woods, R. J. (2018). Predicting the structures of glycans, glycoproteins, and their complexes. *Chem. Rev.* 118, 8005–8024. doi:10.1021/acs.chemrev.8b00032

Wu, C., Mino, K., Akimoto, H., Kawabata, M., Nakamura, K., Ozaki, M., and Ohmiya, Y. (2009). *In vivo* far-red luminescence imaging of a Biomarker Based on BRET fromCypridinabioluminescence to an Organic Dye. *Pnas* 106, 15599–15603. doi:10.1073/pnas.0908594106

Wu, N., Kobayashi, N., Tsuda, K., Unzai, S., Saotome, T., Kuroda, Y., et al. (2020). Solution Structure of *Gaussia* Luciferase with Five Disulfide Bonds and Identification of a Putative Coelenterazine Binding Cavity by Heteronuclear NMR. *Sci. Rep.* 10, 20069. doi:10.1038/s41598-020-76486-4

Yasuno, R., Mitani, Y., and Ohmiya, Y. (2018). Effects of N -Glycosylation Deletions on Cypridina Luciferase Activity. *Photochem. Photobiol.* 94, 338–342. doi:10.1111/php.12847

Conflict of Interest: The authors declare that the research was conducted in the absence of any commercial or financial relationships that could be construed as a potential conflict of interest.

Publisher's Note: All claims expressed in this article are solely those of the authors and do not necessarily represent those of their affiliated organizations, or those of the publisher, the editors, and the reviewers. Any product that may be evaluated in this article, or claim that may be made by its manufacturer, is not guaranteed or endorsed by the publisher.

frontiers in Bioengineering and Biotechnology

ORIGINAL RESEARCH
published: 14 February 2022
doi: 10.3389/fbioe.2022.821835

Enhancing DNT Detection by a Bacterial Bioreporter: Directed Evolution of the Transcriptional Activator YhaJ

*Tal Elad[1†], Benjamin Shemer[1†], Shilat Simanowitz[1], Yossef Kabessa[2], Yosef Mizrachi[2], Azriel Gold[2], Etai Shpigel[1], Aharon J. Agranat[2] and Shimshon Belkin[1]**

[1]Department of Plant and Environmental Sciences, Institute of Life Sciences, The Hebrew University of Jerusalem, Jerusalem, Israel, [2]Department of Applied Physics and the Brojde Center for Innovative Engineering and Computer Science, The Hebrew University of Jerusalem, Jerusalem, Israel

OPEN ACCESS

Edited by:
Aldo Roda,
University of Bologna, Italy

Reviewed by:
C. French,
University of Edinburgh, United Kingdom
Baojun Wang,
University of Edinburgh, United Kingdom

***Correspondence:**
Shimshon Belkin
sb@mail.huji.ac.il

[†]These authors have contributed equally to this work and share first authorship

Specialty section:
This article was submitted to Biosafety and Biosecurity, a section of the journal Frontiers in Bioengineering and Biotechnology

Received: 25 November 2021
Accepted: 17 January 2022
Published: 14 February 2022

Citation:
Elad T, Shemer B, Simanowitz S, Kabessa Y, Mizrachi Y, Gold A, Shpigel E, Agranat AJ and Belkin S (2022) Enhancing DNT Detection by a Bacterial Bioreporter: Directed Evolution of the Transcriptional Activator YhaJ. Front. Bioeng. Biotechnol. 10:821835. doi: 10.3389/fbioe.2022.821835

Detection of buried landmines is a dangerous and complicated task that consumes large financial resources and poses significant risks to the personnel involved. A potential alternative to conventional detection methodologies is the use of microbial bioreporters, capable of emitting an optical signal upon exposure to explosives, thus revealing to a remote detector the location of buried explosive devices. We have previously reported the design, construction, and optimization of an *Escherichia coli*-based bioreporter for the detection of 2,4,6-trinitrotoluene (TNT) and its accompanying impurity 2,4-dinitrotoluene (DNT). Here we describe the further enhancement of this bioreporter by the directed evolution of YhaJ, the transcriptional activator of the *yqjF* gene promoter, the sensing element of the bioreporter's molecular circuit. This process resulted in a 37-fold reduction of the detection threshold, as well as significant enhancements to signal intensity and response time, rendering this sensor strain more suitable for detecting the minute concentrations of DNT in the soil above buried landmines. The capability of this enhanced bioreporter to detect DNT buried in sand is demonstrated.

Keywords: bioreporter, biosensor, directed evolution, explosives, landmines, LysR family, 2,4-dinitrotoluene

INTRODUCTION

The high risks involved in most prevalent methodologies for buried landmine detection, which require the on-site presence of personnel, have created an acute need for a standoff detection technology. To date, no commercially available technology meets this need.

The primary explosive found in most landmines is 2,4,6-trinitrotoluene (TNT), which is often accompanied by a 2,4-dinitrotoluene (DNT) manufacturing impurity. Vapors of both TNT and DNT have been reported to exist in soils above buried landmines (Sylvia et al., 2000; Jenkins et al., 2001). These vapors migrate to the surface through plastic components or from cracks in the casing, and their identification has served as a basis for diverse approaches for

Abbreviations: CDS, coding sequence; DNT, 2,4-dinitrotoluene; LTTR, LysR type transcription regulator; TNT, 2,4,6-trinitrotoluene.

landmine bio-detection (Habib, 2007; Smith et al., 2008). The relatively volatile and stable DNT is considered an excellent signature chemical for the presence of TNT-based explosive devices (Jenkins et al., 2001).

Microbial bioreporters are genetically engineered microbial strains, "tailored" to report the presence of chemical targets (Van der Meer and Belkin, 2010; Elad and Belkin, 2016). The recombinant constructs harbor a fusion of a gene promoter, involved in the cellular response to the target, and a reporter gene(s), the expression of which yields a quantifiable output. The most commonly used reporter elements are the *lacZ*, *gfp*, or *lux* genes, yielding chromatic, fluorescent, or bioluminescent signals.

The use of microbial bioreporters for sensing TNT or DNT vapors in soil, indicating the location of buried explosive devices, has been proposed already in 1999. A number of bacterial bioreporters for the detection of traces of explosives have since been described (Burlage et al., 1999; Altamirano et al., 2004; Radhika et al., 2007; Garmendia et al., 2008; Kim et al., 2008; de las Heras and de Lorenzo, 2011; Davidson et al., 2012; Lönneborg et al., 2012; Yagur-Kroll et al., 2014; Yagur-Kroll et al., 2015; Tan et al., 2015; Belkin et al., 2017; see Shemer et al. (2015, 2017) for reviews). Prominent among these reports is a description of *E. coli*-based DNT/TNT bioreporters harboring a genetic fusion between *E. coli*'s endogenous *yqjF* gene promoter to either the green fluorescent protein gene *GFPmut2* or to *Photorhabdus luminescens* bioluminescence *luxCDABE* genes (Yagur-Kroll et al., 2014, 2015). While the fluorescent variant has been instrumental in demonstrating the standoff detection of real antipersonnel landmines (Belkin et al., 2017), recent efforts have concentrated on molecularly enhancing the performance of the bioluminescent variants (Shemer et al., 2020; 2021; Shpigel et al., 2021), in parallel to unravelling the DNT degradation pathway (Shemer et al., 2018) and the *yqjF* regulatory mechanism in *E. coli* (Palevsky et al., 2016). The latter study has pointed at YhaJ, a member of the LysR type family of transcriptional regulators, as a positive regulator of *yqjF* activation, linked to aromatic compounds degradation.

A close look at the published characteristics of previously described bacterial explosives' sensor strains reveals that their performance may need to be significantly enhanced before their use can be considered for landmine detection under actual field conditions (Shemer et al., 2015, 2017). For example, equilibrium headspace concentrations of DNT and TNT vapors above TNT based landmines can be as low as 0.28 pg/ml and 0.077 pg/ml, respectively (Jenkins et al., 2001). Not all reported detection thresholds are sufficiently low to detect such low concentrations.

The aim of the present study was to improve the performance of the *yqjF*-based bacterial bioreporter by manipulating its regulatory protein YhaJ. This was achieved by a directed evolution of both the *yhaJ* gene and its promoter, carried out by three sequential random mutagenesis cycles. The selected final construct displayed superior DNT detection capabilities both in aqueous media and over a sand target.

MATERIALS AND METHODS

Chemicals

Analytical grade DNT was purchased from Sigma-Aldrich. An ethanol stock solution (27 g/L) was kept at 4°C and diluted according to need. Sodium alginate (CAS 9005-38-3) and polyacrylic acid (PAA, CAS 9003-01-4, M_w ~250,000, 35 wt% in H_2O) were purchased from Sigma-Aldrich (Israel).

Plasmids

To monitor the effects of sequence manipulations of the *yhaJ* gene and promoter, two separate plasmids were initially employed in the same *E. coli* host (referred to hereafter as the two-plasmid system). Plasmid pACYC-*yhaJ* (**Figure 1A**), a derivative of plasmid pACYC184 (Chang and Cohen, 1978), harbored the complete *yhaJ* gene, driven by its own original promoter. The promoter region and coding sequence of *yhaJ* were obtained by PCR amplification from the *E. coli* genome, introducing SphI and SalI restriction sites with primers yhaJ-SphI and yhaJ-SalI (**Supplementary Table S1**). The PCR products were gel-purified, digested with SphI and SalI, and ligated into the same restriction sites in pACYC184. The second plasmid, pBR-C55-luxPl (**Figure 1B**), contained a fusion between the *Photorhabdus luminescens luxCDABE* genes and C55, a mutated version of the *yqjF* promoter (Shemer et al., 2020).

A single-plasmid system (plasmid G2a, **Figure 1C**) was obtained by cloning a mutated version (G2) of the *yhaJ* gene into plasmid pBR-C55-luxPleio (Shemer et al., 2021), in which the C55 promoter is fused to the *luxCDABEG* genes of *Photobacterium leiognathi*. The G2 variant was PCR-amplified using primers 115_F and 116_R (**Supplementary Table S1**); NEBuilder HiFi DNA Assembly kit (New England Biolabs, United States) was used to assemble the two fragments.

The *E. coli* host strains and the plasmids employed or constructed in the course of the present study are listed **Table 1**. Full DNA sequences of the plasmids used in the course of this study are available as supplementary FASTA files (pBR-C55-luxPl.fasta, pBR-C55-luxPleio.fasta, pACYC-yhaJ.fasta, G2a.fasta).

Random Mutagenesis

The first two rounds of *yhaJ* mutagenesis were performed using the two-plasmid system. Error-prone PCR was conducted according to Kagiya and colleagues (Kagiya et al., 2005) with slight modifications. The reaction contained 1 mM dCTPs, 1 mM dTTPs, 0.2 mM dATPs, 0.2 mM dGTPs, 2.5 mM $MgCl_2$, 1 mM $MnCl_2$, 5 U/ml Taq DNA polymerase (Fermentas, #EP0402), and 50 pmol/ml of primers yhaJ-sphI and yhaJ-SalI (**Supplementary Table S1**). The error-prone PCR mixture (50 µL) was divided into five individual 10 µL aliquots to enhance the diversity of the resulting mutations. Following the error-prone PCR procedure, the reaction mixtures were pooled, purified, digested with SphI and SalI restriction enzymes, and ligated into the same restriction sites in pACYC. The

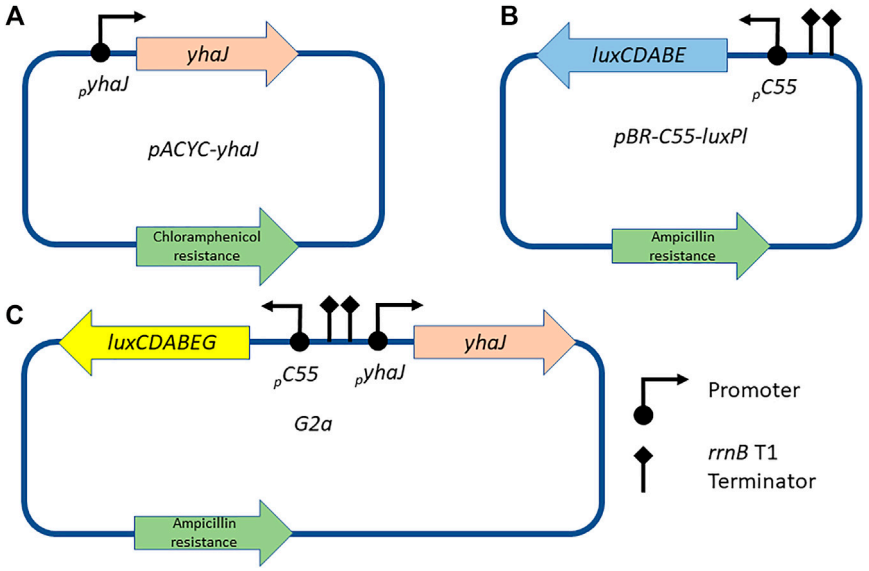

FIGURE 1 | Schematic designs of the plasmids used in this study. The *yhaJ* gene, fused to its native promoter, is mounted on a pACYC platform **(A)**; in the two-plasmid system, this plasmid is co-transformed with plasmid pBR-C55-luxPl **(B)**, which carries a fusion between the C55 promoter and the *luxCDABE* genes of *P. luminescens*. Alternatively, in the one-plasmid system, all components are mounted on a single pBR2TTS backbone, carrying a *P. leiognathi luxCDABEG* reporter gene cassette [plasmid G2a, **(C)**].

TABLE 1 | Strains and plasmids used in the course of this study.

Host strain	Description	Reference
DH5α	Standard cloning strain	
BW25113 Δ*yhaJ*	A member of the Keio collection, hosting a single gene deletion of the *yhaJ* gene	Baba et al. (2006)
Plasmid	**Description**	**Reference**
pACYC-*yhaJ* (also denoted G0)	A copy of the *yhaJ* gene and promoter, mounted on a pACYC184 (Chang and Cohen, 1978) backbone	This work
G1	1st generation of *yhaJ* random mutagenesis	This work
G2	2nd generation of *yhaJ* random mutagenesis	This work
G2a	2nd generation of *yhaJ* random mutagenesis, mounted on a pBR-C55-luxPleio backbone	This work
G3a	3rd generation of *yhaJ* random mutagenesis	This work
G3b	3rd generation of *yhaJ* random mutagenesis	This work
G11T	G2a plasmid supplemented with a G11→T mutation	This work
A51G	G2a plasmid supplemented with a A51→G mutation	This work
T133A	G2a plasmid supplemented with a T133→A mutation	This work
G11T-A51G	G2a plasmid supplemented with G11→T and A51→G mutations	This work
G11T-T133A	G2a plasmid supplemented with G11→T and T133→A mutations	This work
A51G-T133A	G2a plasmid supplemented with A51→G and T133→A mutations	This work
pBR-C55-luxPl	A sensor-reporter plasmid, carrying a fusion between the C55 promoter and the *luxCDABE* genes of *P. luminescens*	Shemer et al. (2020)
pBR-C55-luxPleio	A sensor-reporter plasmid, carrying a fusion between the C55 promoter and the *luxCDABE* genes of *P. leiognathi*	Shemer et al. (2021)

products of the ligation reaction were used to transform *E. coli* strain BW25113 *ΔyhaJ* (Baba et al., 2006), already transformed with pBR-C55-luxPl, to generate a *yhaJ* variant library. Following each round of error-prone PCR, the library was screened for improved variants as described below. A third round of the *yhaJ* promoter and gene mutagenesis was conducted with the G2a plasmid as template, using primers 117_yhaJ_RM and 118_yhaJ_RM (Table S1). For this purpose, the G2a plasmid was digested with sbfI and stuI restriction enzymes, and the amplified mutated segment was inserted via Gibson assembly technique (NEBuilder HiFi DNA Assembly kit, New England Biolabs, United States).

Site-directed mutagenesis of selected point mutations was performed by Gibson assembly using primers modified with the desired substitution, and verified by sequencing.

DNA sequences of the various *yhaJ* (promoter and gene) generations constructed in the course of this study are available as a FASTA supplementary file (yhaJ-G1-G2-G3a-G3b.fasta).

Clone Library Screening and Storage

After each round of random mutagenesis, approximately 500 colonies were screened for improved variants as follows: the colonies were picked into 96-well microtiter plates, each well containing 150 µl of lysogeny broth (LB) supplemented with kanamycin (50 mg/L), ampicillin (100 mg/L), and chloramphenicol (30 mg/L). Also picked into the same set of 96-well microtiter plates were two colonies of the best performing variant of the previous generation. The 96-well microtiter plates were incubated overnight at 37°C with shaking (200 rpm), and 10-µl aliquots were then transferred into white 96-well microtiter plates with a transparent bottom, each well of which contained 90 µl of LB with or without DNT (2 mg/L) and 2% ethanol. The plates were incubated at 37°C and luminescence intensity (in the plate reader's arbitrary relative light units, RLU) and optical density at 600 nm (OD_{600}) were measured with a microplate reader (Infinite® 200 PRO, Tecan) at 45 min intervals for several hours. Variants that displayed a higher response ratio (light intensity in the presence of DNT divided by that in its absence) and a higher (or similar) signal intensity compared to the best performing variant of the previous generation were selected for further analysis. The remaining 130 µl of each overnight culture were augmented with 130 µl of 50% glycerol solution and stored at −80°C.

Exposure of Cells to DNT, Liquid Medium

Stored bacteria were plated on LB-agar Petri dishes supplemented with ampicillin (100 µg/ml), chloramphenicol (30 mg/L), and kanamycin (50 mg/L). Fresh colonies were grown overnight in LB with the same antibiotic composition at 37°C with shaking (200 rpm). Bacteria were diluted 100-fold in fresh LB and regrown under the same conditions to the mid-exponential growth phase ($OD_{600} \approx 0.3$). Aliquots (50 µl) were pipetted into a white 96-well microplate with a transparent bottom (Greiner Bio-One) containing a twofold dilution series of DNT (double-distilled water, 4% ethanol) in the same volume. Light intensity (RLU) and absorbance (OD_{600}) were measured with a microplate reader (Infinite® 200 PRO, Tecan) at 12.5 min intervals at ambient temperature. All experiments were repeated at least three times.

Performance Evaluation

Bacterial bioreporter performance was evaluated using four main parameters: signal intensity, response ratio, detection threshold, and response time. These parameters were defined as follows: *Signal intensity*, the amount of light emitted by the culture in relative light units (RLU), divided by the culture's optical density (OD_{600}); *Response ratio*, signal intensity of the induced sample divided by that of the non-induced reference; *Detection threshold*, the DNT concentration that would promote a response ratio of 2 as estimated by interpolation (EC_{200}; Belkin et al., 1997); *Response time*, the time point at which a response ratio of two was first exceeded.

Immobilization of Microbial Biosensors in Ca-Alginate Beads

Ca-alginate, supplemented by polyacrylic acid (PAA), was used to immobilize the bacteria for the detection of DNT buried in soil as previously described (Shemer et al., 2021). A 2.5% (w/v) Na-alginate solution was prepared by dissolving 30 g of Na-alginate in 950 ml of deionized H_2O. Next, 50 ml of a 10% (w/v) PAA solution, previously neutralized to pH 7.0 with 10 M NaOH, were added and the solution was kept at room temperature overnight to ensure a clear and homogenous solution. The bacterial strains were incubated overnight (37°C, 200 rpm) in 50 ml LB supplemented with the appropriate antibiotics, and then diluted x1/50 in 50 ml LB supplemented with the same antibiotics. The culture was regrown under the same conditions to an OD_{600} of 0.8–1.0. The bacteria were then centrifuged (20 min, 6,000 rcf, 4°C, Sorval RC5C) and the pellet was weighed and resuspended in 5 ml 0.9% NaCl. An aliquot of resuspended bacteria was added to 500 ml of Na-alginate-PAA to reach a concentration of 0.1% (w/v). The bacterial suspension was dripped into 0.1 M $CaCl_2$ using a Buchi B390 Encapsulator (Buchi Labortechnik AG, Switzerland) equipped with a 1,000 µm nozzle, at a pressure of 550 mbar. The formed beads were kept in $CaCl_2$ for at least 30 min, then strained and washed with 0.9% NaCl. The washed beads [average diameter 3.97 (± 0.22 mm standard deviation), $n = 17$] were stored at 4°C until used. Cell concentration in the beads was enumerated by submerging 10 beads in 10 ml of a 2% (w/v) sodium citrate solution, until the beads were fully dissolved. Then, serial dilutions in 0.9% NaCl were plated on LB-agar plates containing the appropriate antibiotics and incubated overnight at 37°C. The average cell concentration was 1.82×10^5 [$\pm$ 1.9×10^4 standard deviation] cells/bead.

Exposure of Alginate-Immobilized Cells to DNT, Soil Surface

The bioluminescent response of the G2 and G2a bacterial bioreporters was measured on a soil surface using an imaging system comprised of a sensitive camera and an optical system for imaging the emittance of the bacteria onto the camera's sensor array. The camera employed was a cooled scientific CMOS camera (PCO.edge5.5; PCO, Germany), characterized by a very low noise, a wide dynamic range, a rapid frame rate, and a high resolution. The optical system, designed for optimal imaging of the bacterial bioluminescent signal, was based on a high precision aspherical lens (Kowa, model LM12XC), which reduces distortion and produces high-definition images. The imaging system was isolated from both optical and electronic background noise in a special chamber, in which ambient light, temperature and humidity were strictly controlled. A detailed description of this controlled chamber can be found elsewhere (Agranat et al., 2021).

A monolayer of beads was homogenously spread on triplicate 35 mm diameter targets, containing soil with different amounts of buried DNT, as well as DNT-free control targets. The target array was imaged continuously with the temperature kept at 25°C and the humidity set to 55%. The targets were imaged with varying exposure times.

To extract quantitative data out of the imaged bioluminescent response, image processing tools were applied. We first defined a region of interest in the samples' locations by applying thresholds (Otsu, 1979), detecting edges (Gao et al., 2010), and detecting shapes (Ballard, 1981). The average luminescence value was then calculated

for each sample across at least seven similar images in each batch and three similar targets. The bioluminescent response was measured in nW/cm^2, according to a previously established calibration procedure (unpublished). Light emitted by a LED light source, with an emission spectrum and an intensity range similar to bacterial bioluminescence, was simultaneously measured by the CMOS camera-based imaging system and by a calibrated power meter (model StarBright, MKS Ltd.). The response of the direct imaging system was found to be linearly correlated to the optical intensity measured by the power meter in physical units (nW/cm^2).

Further demonstration of the detection capabilities was also performed by spreading immobilized bacterial bioreporters (strain G3b) on a sand target containing DNT "hot spots". These were prepared by placing DNT crystals (100, 300 and 1,000 mg) on separate Petri dishes, covering the explosives with sand (Sigma-Aldrich, 50-70 mesh, 40 g, 12 mm depth), and integrating the plates in a large container (20 × 28 x 5 cm) filled with Mediterranean beach sand. A thin layer (ca. 1-2 mm) of beach sand covered the targets, obtaining a uniform surface. The target was left at room temperature for 5 months prior to the experiment, to allow permeation of DNT vapors to the surface. The target was lightly sprinkled with LB medium prior to applying the beads. After placing the beads, the target was incubated in a dark chamber at room temperature and photographed every 15 min using a Sony s7a ii camera (4 s exposure, ISO 400), placed 1 m above the target, for a total of 9 h. To quantify the emitted luminescence, the integrated grey value across 10 randomly selected individual beads located above each "DNT hotspot" was quantified with ImageJ analysis software (Schindelin et al., 2012).

RESULTS

We set out to improve the performance of *yqjF*-based bacterial bioreporters for landmine detection by the directed evolution of YhaJ, a transcriptional regulator of *yqjF* activation (Palevsky et al., 2016). Using error-prone PCR, two *yhaJ*-targeted sequential mutagenesis rounds were performed, in which the *yhaJ* variants were incorporated into a plasmid (**Figure 1A**) that was subsequently introduced into a *ΔyhaJ* strain. The recipient cells were already transformed with a plasmid-borne fusion of a *yqjF* promoter [variant C55, previously modified for enhanced performance (Yagur-Kroll et al., 2014, 2015; Shemer et al., 2020)] to the *P. luminescens* bioluminescence *luxCDABE* gene cassette (**Figure 1B**). The clone libraries were screened, and clones that displayed a higher response ratio and a similar or higher signal intensity compared to the previous generation were further analyzed. The strain harboring the unmodified plasmids displayed in **Figure 1A** and **Figure 1B** is referred to as G0, and the best performers of mutagenesis rounds 1 and 2 as G1 and G2, respectively. Transferring the G2 variant to a one-plasmid design has yielded clone G2a (**Figure 1C**), with which a third round of error-prone PCR was conducted. The two mutant clones selected from among the variants generated in the third mutagenesis cycle are referred to as G3a and G3b.

Effect of the Directed Evolution Process on Signal Intensity, Response Ratio, Detection Sensitivity and Response Time

The response to DNT of selected clones from the different mutagenesis cycles is displayed in **Figure 2**. The signal intensity and response ratio dynamics of all variants were characterized by a lag phase followed by a dose-dependent increase, which peaked after 4–5 h. A clear increase in luminescence intensity as a function of the progress of the evolution process was observed (**Figure 2A**), a trend that was not fully replicated in the response ratios (**Figure 2B**), a parameter which is strongly affected not only by the increase in *yqjF* induction but also by changes in the control (uninduced) luminescence. The increases in the response ratio observed in clones G1 and G2 (**Figures 2B,D**) was mostly attributed to a significant decrease in the basal luminescence level with each generation. G2's basal luminescence at time zero was similar to those of G0 and G1; however, it remained steady throughout the measurement and did not increase, as opposed to those of the two previous generations. Clones G3a and G3b, while superior to G2a in terms of signal intensity, suffered from a high background luminescence, which lowered their response ratios. The significant increase in light intensity from G2 to G2a, which harbors an identical *yhaJ* variant, is driven by the change of the *lux* reporter cassette from that of *P. luminescens* to *P. leiognathi* (Shemer et al., 2021).

Two additional performance parameters that were improved along the evolutionary progression were the detection threshold and the response time. In **Figure 3**, the light intensity at the detection threshold is plotted against the threshold DNT concentration. A clear progressive increase in sensitivity from G0 to G3 is observed; clone G3b appears to embody an optimal combination of a low detection threshold with high signal intensity. The detection threshold, calculated here as the DNT concentration promoting a response ratio of 2 (Belkin et al., 1997), decreased by 37-fold from 1.5 ± 0.6 mg/L DNT in the wild type to 0.04 ± 0.01 mg/L in the G3a and G3b variants (**Figure 3** and **Table 2**). The response time, determined as the time point at which a response ratio of two was first exceeded, was reduced from 74 to 37 min and from 127 to 66 min for 10 and 3.3 mg/L DNT, respectively. At a DNT concentration of 0.12 mg/L, detection was not observed for generations G0-G2, but was apparent after 120-160 min in the G2a, G3a and G3b variants (**Table 2**).

Mutations Introduced in the Course of the Directed Evolution Process

Variant G2 carries three point mutations in *yhaJ*'s coding sequence (CDS), as revealed by sequencing: a cytosine-to-adenine conversion in position 91 of the CDS (g.91C > A), translating into a leucine-to-methionine substitution in position 31 of the amino acid (AA) sequence (p.L31M); a thymine-to-cytosine conversion in position 461 of the CDS (g.461T > C), translating into a methionine-to-threonine substitution in position 154 of the AA sequence (p.M154T); and a C-to-T conversion in position 812 of the CDS (g.821C

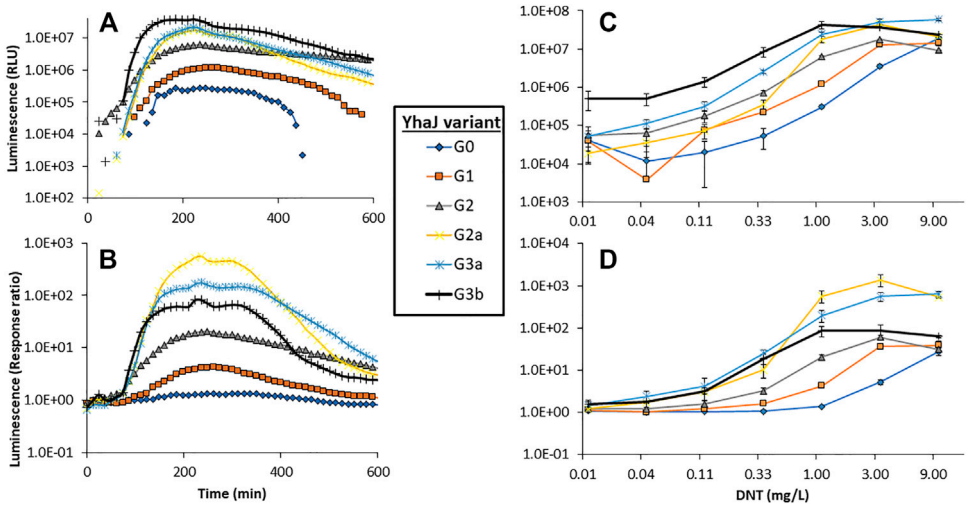

FIGURE 2 | Dynamics of the luminescent response of the various *yhaJ* generations to a single DNT concentration (1.1 mg/L), displayed as signal intensity **(A)** and response ratio **(B)**. Panels **(C)** and **(D)** depict the maximal luminescence and maximal response ratios, respectively, over a 600 min exposure, as a function of DNT concentration for all *yhaJ* variants. Error bars represent the standard deviation across three repeats.

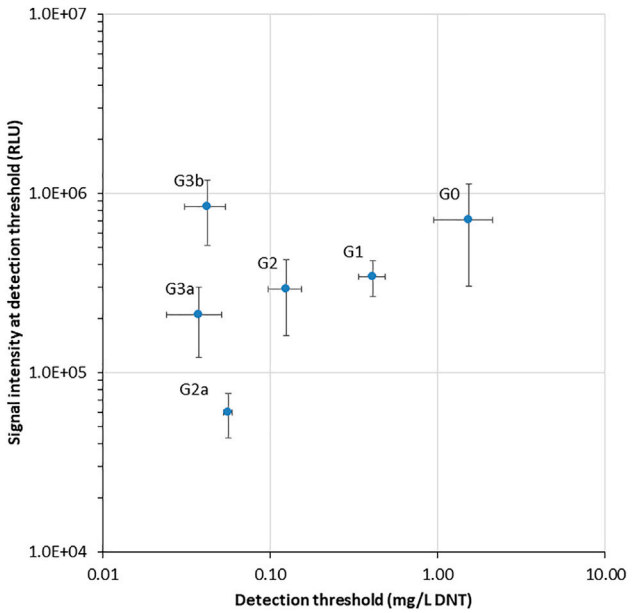

FIGURE 3 | Luminescence intensity at the detection threshold for all *yhaJ* variants, as a function of the detection threshold (EC_{200}: DNT concentration eliciting a response ratio of 2; Belkin et al., 1997). Error bars represent the standard deviation across three repeats.

> T), translating into an alanine to valine substitution in position 274 of the AA sequence (p.A274V; **Figure 4**). The first two point-mutations, p.L31M and p.M154T, were the result of the first round of random mutagenesis and are the ones carried by G1, while the third mutation, p.A274V, was introduced into *yhaJ*'s CDS in the second round.

To reduce potential instability due to plasmid imbalance, as well as to negate the need to transfect clones resulting from random mutagenesis with an additional plasmid before screening for activity, the third-generation variant (G2) of the *yhaJ* gene and promoter was mounted on the pBR-C55-*luxPleio* plasmid, yielding plasmid G2a. An additional round of mutagenesis of the *yhaJ* gene and promoter was conducted on this plasmid, and selected variants were transformed into a *yhaJ* deficient mutant. As noted above, the two mutant clones selected following this process were denoted G3a and G3b. The G3a variant has two mutations in its promoter sequence (C50 > A and A136 > G) as well as several mutations in its CDS. Three point-mutations (g.A260 > T, g.A484 > T, g.A698 > G) are reflected by AA substitutions (p.D87V, p. I162F, p. Q233 > R), while additional three codon substitutions (g.C54 > T, g.T600 > A, g.G762 > A) do not alter the AA sequence. In contrast, the G3b variant has only three point-mutations, all of which are positioned in the promoter region (G11 > T, A51 > G, T133 > A). The amino acid sequences of variants G0, G1, G2, and G3a are shown in **Figure 4**.

An estimation of the evolutionary conservation of the amino acid positions in YhaJ, based on the phylogenetic relations between homologous sequences, revealed, as expected, an agreement between the conservation level and the type of amino acid replacement. Amino acids in conserved positions were replaced with amino acids with similar properties, while other substitutions could be more radical (**Figure 4**). Querying the YhaJ AA sequence against the Protein Data Bank (PDB) (wwPDB consortium, 2019), we found a high degree of homology between YhaJ and CrgA, a LysR type transcription regulator (LTTR) from *Neisseria meningitidis*. This homology indicates that the mutations introduced here to YhaJ's amino acid sequence span all of the protein's domains, including the DNA binding domain (p.L31M), the linker helix (p.D87V), and the regulatory

TABLE 2 | Response times, signal intensity and DNT detection sensitivity for the different *yhaJ* variants.

DNT concentration	10 mg/L		3.3 mg/L		0.12 mg/L		
***yhaJ* variant**	**Response time (min)[a]**	**Max signal intensity (RLU)[b]**	**Response time (min)[a]**	**Max signal intensity[b] (RLU)**	**Response time (min)[a]**	**Max signal intensity[b] (RLU)**	**Detection threshold (mg/L)[c]**
G0	74	1.91E+07 ± 2.73E+06	127	3.54E+06 ± 3.79E+05	(–)#	2.03E+04 ± 1.79E+04	1.53 ± 0.587
G1	94	1.43E+07 ± 2.55E+06	111	1.31E+07 ± 1.34E+06	(–)	7.62E+04 ± 3.19E+04	0.41 ± 0.075
G2	49	9.18E+06 ± 2.56E+05	66	1.78E+07 ± 2.45E+05	(–)	1.82E+05 ± 6.36E+04	0.13 ± 0.028
G2a	53	2.15E+07 ± 1.84E+06	74	4.41E+07 ± 7.31E+06	156	7.36E+04 ± 6.87E+03	0.06 ± 0.003
G3a	58	5.84E+07 ± 4.10E+06	74	5.08E+07 ± 8.89E+06	123	3.23E+05 ± 8.94E+04	0.04 ± 0.014
G3b	37	2.32E+07 ± 1.62E+06	66	3.69E+07 ± 1.88E+06	152	1.40E+06 ± 3.88E+05	0.04 ± 0.012

[a]*The time at which the response ratio first exceeded 2.*
[b]*In the course of a 600 min exposure; error values are calculated as standard deviation, resulting from at least three independent duplicate repeats.*
[c]*Minimal DNT concentration at which a response ratio of two was obtained.*
#A response ratio higher than two was not obtained throughout the experiment.

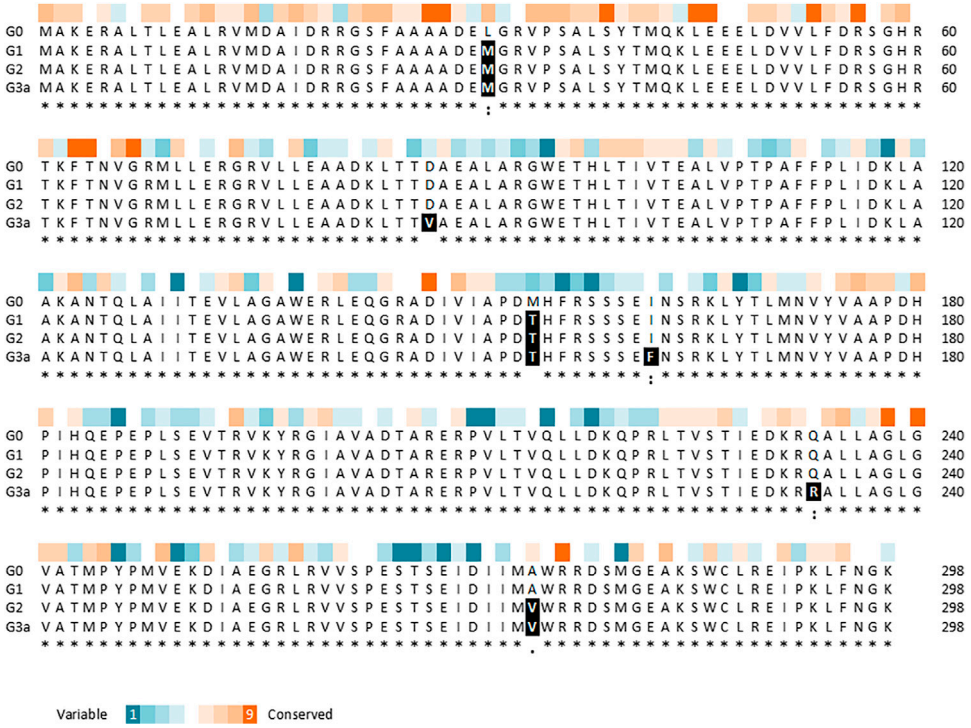

FIGURE 4 | Multiple sequence alignment of YhaJ generations G0, G1, G2, and G3a, showing the amino acid replacements, as generated using the Clustal Omega tool (Sievers et al., 2011). The residue conservation scores of YhaJ, obtained with Consurf (Ashkenazy et al., 2016) based on 150 homologues from the UniRef database, are shown above the alignment.

domains, in which substrate binding takes place (p.M154T, p. I162F, p. Q233R, and p. A274V) (Maddocks and Oyston 2008; Sainsbury et al., 2009).

In previous studies, a common motif was found in YhaJ-regulated genes (Palevsky et al., 2016; Henshke et al., 2021). Interestingly, the MEME suite algorithm (Bailey et al., 2006), has revealed a significantly enriched (E-value of 1.1×10^{-5}) sequence motif (**Figure 5A**). This motif is positioned on the (–) strand of the *yhaJ* promoter and contains a highly conserved binding site (Connolly et al., 2019; Connolly et al., 2020).

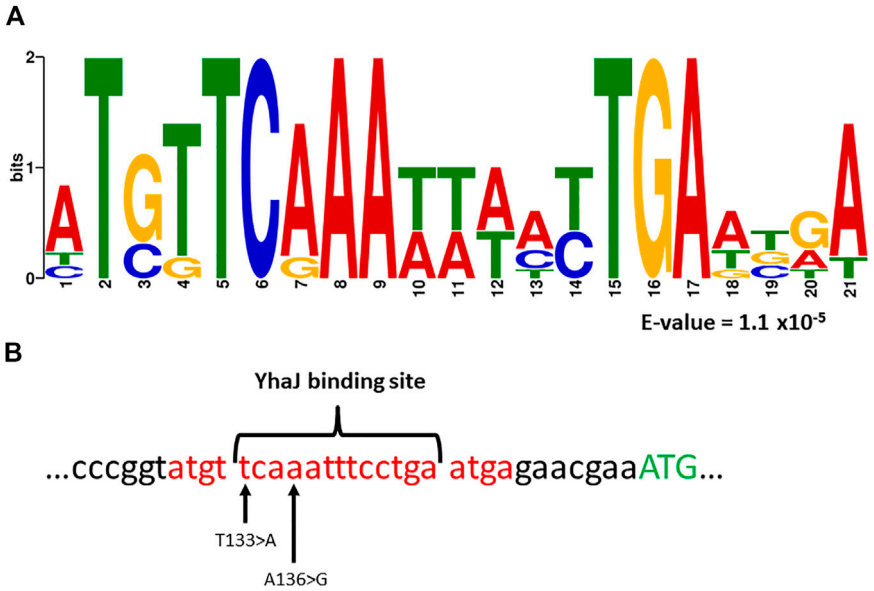

FIGURE 5 | Panel **(A)**—a common motif found in the promoter regions of *yhaJ* and genes the activation of which is YhaJ-dependent (Palevsky et al., 2016; Henshke et al., 2021). Analysis was performed with the MEME suite algorithm (Bailey et al., 2006). The E-value represents the statistical significance of the motif as calculated by the MEME algorithm. Panel **(B)**—location of the sequence motif (marked red), as well as the first methionine of YhaJ (marked green), a known YhaJ binding site (Connolly et al., 2019, 2020), and the location of two point-mutations, T133 > A and A136 > G, found to significantly enhance the response of the bioreporter to DNT.

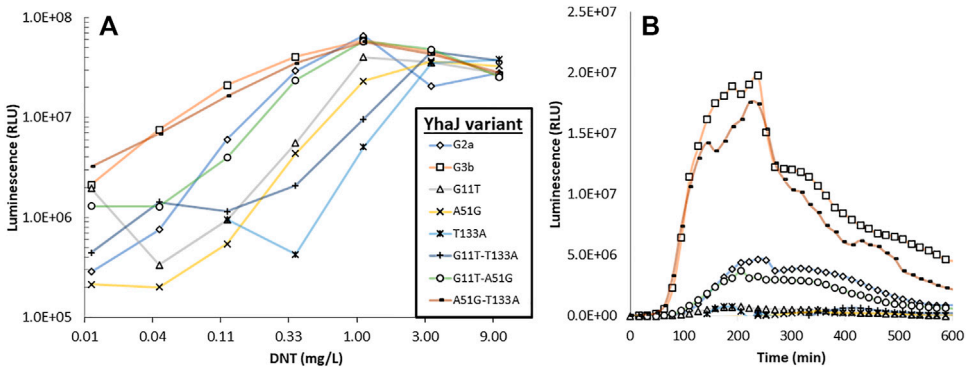

FIGURE 6 | Luminescent response to DNT of strain G2a, to which the three mutations characterizing strain G3b have been introduced singly or in pairs. Panel **(A)**—maximal signal intensity observed for each strain in the presence of different DNT concentrations; panel **(B)**—response dynamics of all strains when spiked with 0.12 mg/L DNT.

Variants G3a and G3b both host mutations located in this motif; A136 > G and T133 > A for G3a and G3b, respectively. Furthermore, in both cases the mutation is located at a highly conserved position of the YhaJ binding site (**Figure 5B**). This could hint at the importance of these two mutations in enhancing the activity of the bioreporter, as well as at the possible autoregulation of YhaJ. Autoregulation of LTTR's has been shown to be a widespread genetic phenomenon (Maddocks and Oyston, 2008), but to the best of our knowledge has not been specifically shown in YhaJ.

To characterize the contribution of each mutation originating from the last round of mutagenesis to the effect demonstrated in the G3b strain, a set of G2a plasmids was constructed, supplemented with all the possible combinations of the identified single-point mutations. As depicted in **Figure 6**, no single mutation originating from the last round of mutagenesis is accountable for the increased response in G3b. However, when modifying G2a with both A51 > G and T133 > A mutations, the response of the resulting strain is practically similar to that of G3b.

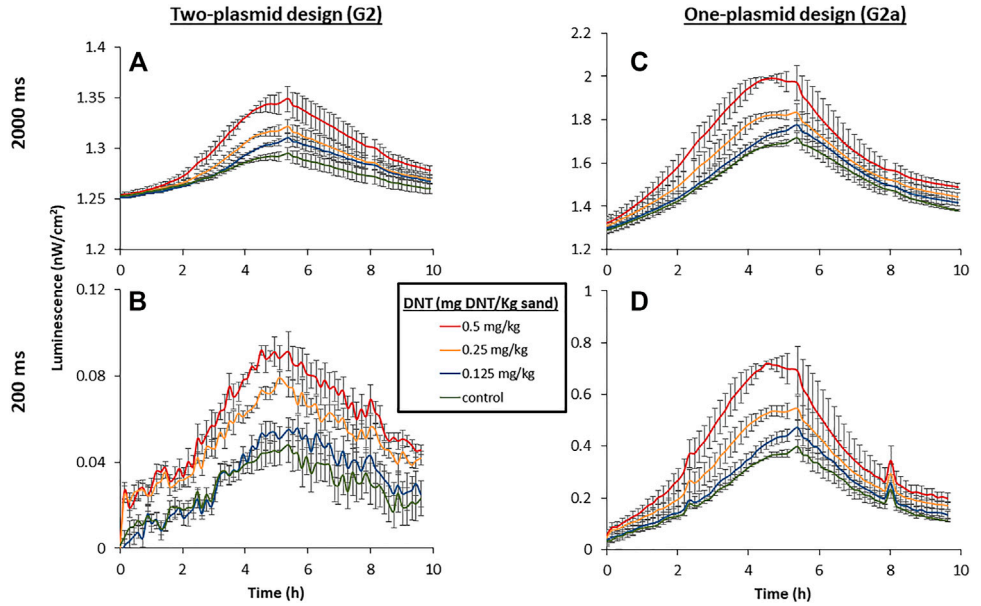

FIGURE 7 | Luminescent response of the two-plasmid design [yhaJ (G2) + pBR-C55-Pleio; **(A,B)**] and the single-plasmid design [G2a; **(C,D)**] to DNT buried in sand. The targets were incubated at 25°C, 55% relative humidity, and imaged with a PCO. edge5.5 CMOS camera at constant intervals. A calibration process was employed to convert the measured luminescent signal to physical units (nW/cm^2). Exposure times were 2000 ms **(A,C)** and 200 ms **(B,D)**.

Rapid Imaging of the G2 Variant's Luminescence: Comparing the Double-Plasmid (G2) and the Single-Plasmid (G2a) Clones

The benefit of the increased light intensity displayed by the G2a variant is further underlined when performing rapid measurements, which may be essential in actual field applications. To demonstrate this, a sensitive cooled scientific CMOS camera, installed in a temperature- and humidity-controlled chamber, was employed to capture the signal emitted by immobilized bacteria placed on top of DNT-containing sand targets. The imaging was performed with two separate exposure times, 2000 and 200 ms. A two-plasmid design, harboring plasmids G2 and pBR-C55-luxPleio and containing the same relevant genetic parts, served for comparison. As demonstrated in **Figure 7**, the increased light emission of the G2a one-plasmid design enabled the detection of all tested DNT concentrations, even at the short exposure time (200 ms). In contrast, in the case of the two-plasmid system, it was not possible with this short exposure to differentiate the signal emitted in the presence of the low DNT concentration (0.125 mg/kg) from that of the background.

Detection of Buried DNT by Variant G3b

To demonstrate the detection capabilities of the most advanced *yhaJ* generation, G3b, the bacteria were immobilized in small (ca. 4 mm diameter) alginate beads and spread over a sand-filled container with three DNT "hotspots" (**Figure 8A**). After several hours, a clear luminescent response was visible, even with the camera's modest imaging sensitivity parameters (**Figure 8B**). The images across 9 h of the experiment (**Supplementary Video S1**) were joined and analyzed by integrating the grey values across equal areas above the different hotspots. Interestingly, the luminescent signal across the entire target rose during the first 2 h of the experiment, then the background decreased, and the signal above the buried DNT could be clearly discerned (**Figure 8C**). The response time increased with decreasing DNT concentrations; a response ratio of two was observed after 105 min above 1 g of DNT, while 225 and 375 min were required to obtain the same response ratio for 0.3 and 0.1 g DNT, respectively (**Figure 8D**).

DISCUSSION

The microbial sensor strain at the core of the present study harbors a fusion of the *E. coli yqjF* gene promoter to bioluminescence reporter genes. In previous studies we have significantly enhanced the performance of this bioreporter by manipulating the sequence of the promoter region (Yagur-Kroll et al., 2015) and by introducing mutations into the host strain (Shemer et al., 2020), as well as by varying the origin of the reporter genes (Shemer et al., 2021). In the present study we have adopted a different approach: modifying YhaJ, the LysR-type transcriptional regulator of *yqjF* (Palevsky et al., 2016), by inserting into it potentially beneficial mutations by error-prone PCR. After three rounds of mutagenesis we have isolated a *yhaJ* variant (G3b) hosting point-mutations in both its promoter and its coding sequence, the activity of which was highly superior to that of the parent strain. Its maximal luminescent signal intensity was 69-fold higher (in the presence of 0.12 mg/L DNT), its DNT detection threshold 37-fold lower, and its response time (in the presence of 3.3 mg/L DNT) was reduced by ca. 50% (**Table 2**). Furthermore, we have

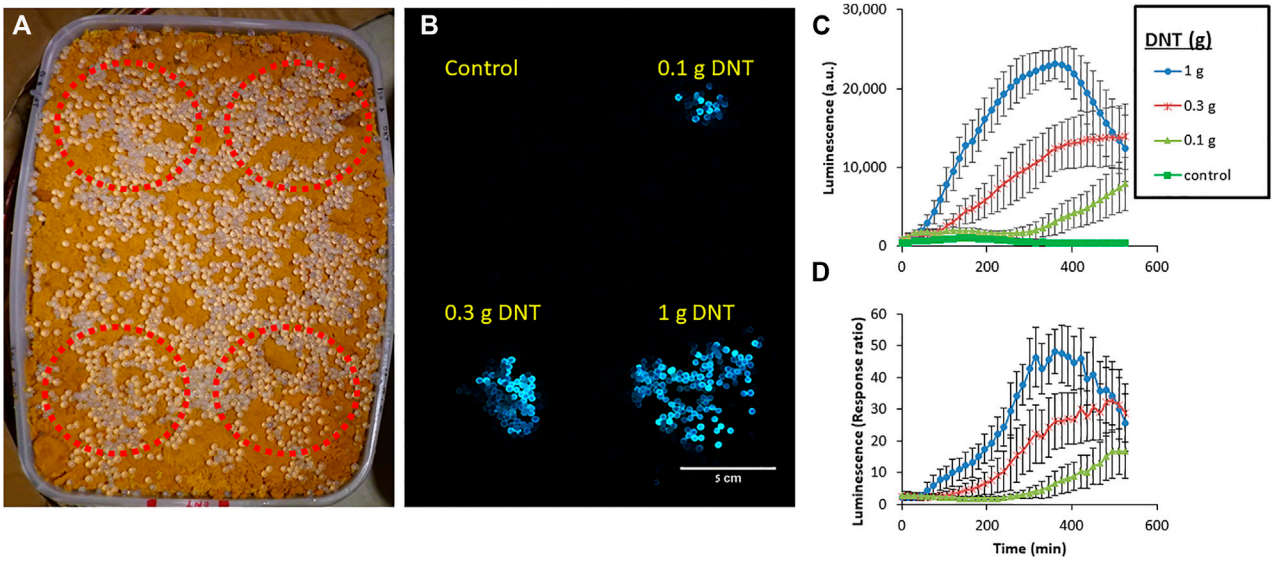

FIGURE 8 | Detection of DNT buried in sand by the G3b variant. Immobilized bioreporters were spread across a target containing three DNT "hotspots" (marked in red), buried in a sand-filled container **(A)**, incubated at room temperature, and imaged every 15 min. **(B)**—an image taken after 9 h of incubation. **(C)**—Average signal intensity across 10 beads located above each hotspot, calculated by grey value integration. **(D)**—Response ratio measured above each hotspot. Imaging was performed with a Sony a7s ii camera (4 s exposure time, ISO 400) in a dark chamber, from a distance of ca. 1 m. Error bars represent the standard deviation based on luminescence measurement of nine random beads located above each target.

demonstrated the capability of this enhanced luminescent bioreporter to detect DNT buried in soil with a relatively simple imaging device.

Putting the CDS mutations in a wider context reveals additional details about their unique locations in YhaJ's secondary and tertiary structures. The activity of a single point mutation clone carrying L31M was comparable to that of the wild type (data not shown), as was a substitution of serine for L26 in the LTTR MetR (Maxon et al., 1990). The M154T mutation by itself could also not account for the G0 to G1 improvement; only when combined, have these two mutations brought about the phenotype exhibited by G1 (data not shown). M154 and A274 are situated next to conserved or semi-conserved positions (I)150 and (I)271, respectively (**Figure 4**). In the LTTR DntR, which has been isolated from a *Burkholderia* species that is able to degrade 2,4-DNT, the amino acids in these positions (L151 and I273; **Figure 9**) were predicted to form direct hydrogen bonds with the carboxyl and hydroxyl groups of salicylate as an inducer (L151) and to stabilize its aromatic ring by hydrophobic interactions (I273; Smirnova et al., 2004). Therefore, M154 and A274 may directly interact with Yhaj's ligand, providing the protein with its specificity. Similar to M154 and A274, Q233 is located in a small flanking region of a conserved domain, which contains a part of the inducer-binding crevice predicted for the LTTR NodD (**Figure 4** and **Figure 9**; Schell 1993; Györgypal and Kondorosi 1991). Mutations in this region alter the responses of LTTRs to their inducers, highlighting its importance to the multiple functions of this protein family. For example, substitution mutations at positions 231 and 252 in NahR (Huang and Schell 1991) or position 234 of OxyR (Christman et al., 1989) caused an inducer-independent phenotype, resembling the increase in light intensity in the transition between strains G2a and G3a, where Q233R was added (**Figure 2C** and **Figure 9**). In contrast, substitutions at NahR's positions 227 or 253 resulted in activation-deficient mutants (Schell et al., 1990). These two different phenotypes emphasize the benefit of the random mutagenesis approach, given the high number of possible substitutions and the complexity in the *a priori* prediction of their effects.

From examination of the data in **Figure 2** and **Figure 3**, it appears that the main improvement in detection sensitivity occurred during the first two rounds of random mutagenesis, from G0 to G2, while the main enhancement of signal intensity was contributed by mutations in the promoter region, as well as by changes in the reporter element and plasmid design. It could be postulated that changes to the coding sequence resulted in increased binding of the YhaJ transcription factor to its ligand, therefore increasing its sensitivity. Alternatively, changes to the promoter region resulted in increased production of YhaJ, leading to an overall increase in response but not necessarily to an increased detection sensitivity.

In an approach different from the one presented here, successful performance enhancement of bacterial reporters, involving a ligand-binding transcriptional regulator, has previously been reported by molecular redesign of the sensor's response circuit, rather than by directed evolution. Small molecule-inducible gene expression was amplified by tuning intracellular receptor densities and the use of transcriptional amplifiers (Wang et al., 2014; Wang et al., 2015; Wan et al., 2019). Reducing the background signal while maintaining maximum output levels was achieved using protease-based post-translational degradation, which was put under the regulation of the cloned receptor, along with the reporter gene (Wan et al., 2019). Clearly, future optimal improvement of whole-cell sensor design should combine both approaches: a targeted redesign of specific

FIGURE 9 | Multiple sequence alignment of YhaJ and selected LTTRs, as generated using the Clustal Omega tool (Sievers et al., 2011). YhaJ (WT): *Escherichia coli*, NCBI Reference Sequence: NP_417576.1; MetR: *E. coli*, UniProtKB Entry Identifier: P0A9F9; DntR: *Burkholderia* sp, UniProtKB Entry Identifier: Q7WT50; NodD: *Rhizobium meliloti*, UniProtKB Entry Identifier: P03031; NahR: *Pseudomonas putida*, UniProtKB Entry Identifier: P10183; OxyR: *E. coli*, UniProtKB Entry Identifier: P0ACQ4. Positions that were altered in this study are marked in red. Other positions mentioned in the main text are marked in blue.

circuit components interfaced with random modifications yielding beneficial effects that are difficult to predict.

Over 20 years ago, Burlage et al. (1999) were the first to propose the identification of the location of buried explosives by bacterial bioreporters engineered to respond by an optical signal to explosives' vapors. For such a scheme to materialize, advances need to be made in two closely intertwined research directions–the development of the bacterial sensors on the one hand, and the engineering/optics involved in their imaging on the other hand. The present communication comprises another step towards the realization of the former objective. When contemplating such a field application for landmine detection employing luminescent bacterial sensor strains, a key factor would be the ability to perform rapid imaging, thus enabling the real-time scanning of large areas for the presence of buried explosives. A consequence of this need is for the bioreporters to produce high light intensities. In the final round of random mutagenesis, we have therefore focused on variants with a stronger luminescence, represented here by G3b, rather than on those exhibiting improved response ratios; the latter were characterized by low light emission under both induced and the non-induced conditions. Another significant factor that necessitates the field use of highly luminescent bioreporters is potential interference by ambient light. In a previous study (Shemer et al., 2021), imaging of the luminescent response of immobilized bioreporters spread on top of a buried antipersonnel landmine was possible only under complete darkness. One possible pathway towards a further reduction of the detection threshold involves the lowering of background luminescence; it is important that such an activity will also be accompanied with actions to increase signal intensity. An optimal balance between detection sensitivity and luminescence intensity will also depend upon the imaging apparatus employed, and its ability to separate the luminescent signal from ambient light.

DATA AVAILABILITY STATEMENT

The original contributions presented in the study are included in the article/**Supplementary Material**; further inquiries can be directed to the corresponding author.

AUTHOR CONTRIBUTIONS

The majority of clone design and construction and the experiments described in this publication were carried out by TE and BS under the supervision of SB. Cloning of single point mutations and inspection of their effects on the bioreporter were carried out by TE, ES, and SS. Controlled experiments with a CMOS camera, carried out in a specialized chamber simulating environmental conditions, were designed and performed by YK, AG, and YM, under the supervision of AJA. TE, BS, and SB wrote the paper with inputs and comments from all co-authors.

FUNDING

Research was sponsored by the Israel Ministry of Defense—Directorate of Defense Research and Development, and by the Army Research Office and the Defense Advanced Research Projects Agency (DARPA) Biological Technologies Office (BTO) and was accomplished under Cooperative Agreement Number W911NF-18-2-0002. The views and conclusion contained in this document are those of the authors and should not be interpreted as representing the official policies, either expressed or implied, of the Army Research Office and the Defense Advanced Research Projects Agency (DARPA) Biological Technologies Office (BTO) or the U.S. Government. The U.S. Government is authorized to reproduce and distribute reprints for Government purposes notwithstanding any copyright notation herein. Research by the Belkin group was also partially supported by the Minerva Center for Bio-Hybrid Complex Systems.

SUPPLEMENTARY MATERIAL

The Supplementary Material for this article can be found online at: https://www.frontiersin.org/articles/10.3389/fbioe.2022.821835/full#supplementary-material

REFERENCES

Agranat, A. J., Kabessa, Y., Shemer, B., Shpigel, E., Schwartsglass, O., Atamneh, L., et al. (2021). An Autonomous Bioluminescent Bacterial Biosensor Module for Outdoor Sensor Networks, and its Application for the Detection of Buried Explosives. *Biosens. Bioelectron.* 185, 113253. doi:10.1016/j.bios.2021.113253

Altamirano, M., Garcı´a-Villada, L., Agrelo, M., Sánchez-Martı´n, L., Martı´n-Otero, L., Flores-Moya, A., et al. (2004). A Novel Approach to Improve Specificity of Algal Biosensors Using Wild-type and Resistant Mutants: an Application to Detect TNT. *Biosens. Bioelectron.* 19, 1319–1323. doi:10.1016/j.bios.2003.11.001

Ashkenazy, H., Abadi, S., Martz, E., Chay, O., Mayrose, I., Pupko, T., et al. (2016). ConSurf 2016: an Improved Methodology to Estimate and Visualize Evolutionary Conservation in Macromolecules. *Nucleic Acids Res.* 44, W344–W350. doi:10.1093/nar/gkw408

Baba, T., Ara, T., Hasegawa, M., Takai, Y., Okumura, Y., Baba, M., et al. (2006). Construction of *Escherichia coli* K-12 In-frame, Single-gene Knockout Mutants: the Keio Collection. *Mol. Syst. Biol.* 2, 2006–0008. doi:10.1038/msb4100050

Bailey, T. L., Williams, N., Misleh, C., and Li, W. W. (2006). MEME: Discovering and Analyzing DNA and Protein Sequence Motifs. *Nucleic Acids Res.* 34, W369–W373. doi:10.1093/nar/gkl198

Ballard, D. H. (1981). Generalizing the Hough Transform to Detect Arbitrary Shapes. *Pattern Recognition* 13, 111–122. doi:10.1016/0031-3203(81)90009-1

Belkin, S., Smulski, D. R., Dadon, S., Vollmer, A. C., Van Dyk, T. K., and Larossa, R. A. (1997). A Panel of Stress-Responsive Luminous Bacteria for the Detection of Selected Classes of Toxicants. *Water Res.* 31, 3009–3016. doi:10.1016/S0043-1354(97)00169-3

Belkin, S., Yagur-Kroll, S., Kabessa, Y., Korouma, V., Septon, T., Anati, Y., et al. (2017). Remote Detection of Buried Landmines Using a Bacterial Sensor. *Nat. Biotechnol.* 35, 308–310. doi:10.1038/nbt.3791

Burlage, R. S., Everman, K. R., and Patek, D. R. (1999). "Method for Detection of Buried Explosives Using a Biosensor," in *U.S. Patent No 5* (Washington, DC: U.S. Patent and Trademark Office), 972,638.

Chang, A. C., and Cohen, S. N. (1978). Construction and Characterization of Amplifiable Multicopy DNA Cloning Vehicles Derived from the P15A Cryptic Miniplasmid. *J. Bacteriol.* 134, 1141–1156. doi:10.1128/jb.134.3.1141-1156.1978

Christman, M. F., Storz, G., and Ames, B. N. (1989). OxyR, a Positive Regulator of Hydrogen Peroxide-Inducible Genes in *Escherichia coli* and *Salmonella typhimurium*, Is Homologous to a Family of Bacterial Regulatory Proteins. *Proc. Natl. Acad. Sci.* 86, 3484–3488. doi:10.1073/pnas.86.10.3484

Connolly, J. P. R., O'Boyle, N., and Roe, A. J. (2020). Widespread Strain-specific Distinctions in Chromosomal Binding Dynamics of a Highly Conserved *Escherichia coli* Transcription Factor. *Mbio* 11, 3. doi:10.1128/mBio.01058-20

Connolly, J. P. R., O'Boyle, N., Turner, N. C. A., Browning, D. F., and Roe, A. J. (2019). Distinct Intraspecies Virulence Mechanisms Regulated by a Conserved Transcription Factor. *Proc. Natl. Acad. Sci. USA* 116, 19695–19704. doi:10.1073/pnas.1903461116

Davidson, M. E., Harbaugh, S. V., Chushak, Y. G., Stone, M. O., and Kelley-Loughnane, N. (2012). Development of a 2,4-Dinitrotoluene-Responsive Synthetic Riboswitch in *E. coli* Cells. *ACS Chem. Biol.* 8, 234–241. doi:10.1021/cb300274g

de las Heras, A., and de Lorenzo, V. (2011). *In Situ* detection of Aromatic Compounds with Biosensor *Pseudomonas Putida* Cells Preserved and Delivered to Soil in Water-Soluble Gelatin Capsules. *Anal. Bioanal. Chem.* 400, 1093–1104. doi:10.1007/s00216-010-4558-y

Elad, T., and Belkin, S. (2016). "Reporter Gene Assays in Ecotoxicology," *in VitroEnvironmental Toxicology-Concepts, Application and Assessment*. Editors G. Reifferscheid and S. Buchinger (Springer), 135–157. doi:10.1007/10_2016_47

Garmendia, J., De Las Heras, A., Galvão, T. C., and De Lorenzo, V. (2008). Tracing Explosives in Soil with Transcriptional Regulators of *Pseudomonas Putida* Evolved for Responding to Nitrotoluenes. *Microb. Biotechnol.* 1, 236–246. doi:10.1111/j.1751-7915.2008.00027.x

Györgypa, Z., and Kondorosi, A. (1991). Homology of the Ligand-Binding Regions of *Rhizobium* Symbiotic Regulatory Protein NodD and Vertebrate Nuclear Receptors. *Mol. Gen. Genet.* 226-226, 337–340. doi:10.1007/BF00273624

Habib, M. K. (2007). Controlled Biological and Biomimetic Systems for Landmine Detection. *Biosens. Bioelectron.* 23, 1–18. doi:10.1016/j.bios.2007.05.005

Henshke, Y., Shemer, B., and Belkin, S. (2021). The *Escherichia coli azoR* Gene Promoter: a New Sensing Element for Microbial Biodetection of Trace Explosives. *Curr. Res. Biotechnol.* 3, 21–28. doi:10.1016/j.crbiot.2021.01.003

Huang, J. Z., and Schell, M. A. (1991). *In Vivo* interactions of the NahR Transcriptional Activator with its Target Sequences. Inducer-Mediated Changes Resulting in Transcription Activation. *J. Biol. Chem.* 266, 10830–10838. doi:10.1016/S0021-9258(18)99094-0

Jenkins, T., Leggett, D. C., Miyares, P. H., Walsh, M. E., Ranney, T. A., Cragin, J. H., et al. (2001). Chemical Signatures of TNT-Filled Land Mines. *Talanta* 54, 501–513. doi:10.1016/S0039-9140(00)00547-6

Jin-Woo Kim, J.-W., Jeong-Hwan Kim, J.-H., and Steve Tung, S. (2008). "Nanoscale Flagellar-Motor Based MEMS Biosensor for Explosive Detection," in Proceeding of the 3rd IEEE International Conference on Nano/Micro Engineered and Molecular Systems, Sanya, 6-9 Jan. 2008 (IEEE), 630–632. doi:10.1109/NEMS.2008.4484411

Kagiya, G., Ogawa, R., Hatashita, M., Takagi, K., Kodaki, T., Hiroishi, S., et al. (2005). Generation of a strong Promoter for *Escherichia coli* from Eukaryotic Genome DNA. *J. Biotechnol.* 115, 239–248. doi:10.1016/j.jbiotec.2004.08.015

Lönneborg, R., Varga, E., and Brzezinski, P. (2012). Directed Evolution of the Transcriptional Regulator DntR: Isolation of Mutants with Improved DNT-Response. *PloS one* 7, e29994. doi:10.1371/journal.pone.0029994

Maddocks, S. E., and Oyston, P. C. F. (2008). Structure and Function of the LysR-type Transcriptional Regulator (LTTR) Family Proteins. *Microbiology* 154, 3609–3623. doi:10.1099/mic.0.2008/022772-0

Maxon, M. E., Wigboldus, J., Brot, N., and Weissbach, H. (1990). Structure-function Studies on *Escherichia coli* MetR Protein, a Putative Prokaryotic Leucine Zipper Protein. *Pnas* 87, 7076–7079. doi:10.1073/pnas.87.18.7076

Otsu, N. (1979). A Threshold Selection Method from Gray-Level Histograms. *IEEE Trans. Syst. Man. Cybern.* 9, 62–66. doi:10.1109/TSMC.1979.4310076

Palevsky, N., Shemer, B., Connolly, J. P. R., and Belkin, S. (2016). The Highly Conserved *Escherichia coli* Transcription Factor YhaJ Regulates Aromatic Compound Degradation. *Front. Microbiol.* 7, 1490. doi:10.3389/fmicb.2016.01490

Radhika, V., Proikas-Cezanne, T., Jayaraman, M., Onesime, D., Ha, J. H., and Dhanasekaran, D. N. (2007). Chemical Sensing of DNT by Engineered Olfactory Yeast Strain. *Nat. Chem. Biol.* 3, 325–330. doi:10.1038/nchembio882

Sainsbury, S., Lane, L. A., Ren, J., Gilbert, R. J., Saunders, N. J., Robinson, C. V., et al. (2009). The Structure of CrgA from *Neisseria Meningitidis* Reveals a New Octameric Assembly State for LysR Transcriptional Regulators. *Nucleic Acids Res.* 37, 4545–4558. doi:10.1093/nar/gkp445

Schell, M. A., Brown, P. H., and Raju, S. (1990). Use of Saturation Mutagenesis to Localize Probable Functional Domains in the NahR Protein, a LysR-type Transcription Activator. *J. Biol. Chem.* 265, 3844–3850. doi:10.1016/S0021-9258(19)39671-1

Schell, M. A. (1993). Molecular Biology of the LysR Family of Transcriptional Regulators. *Annu. Rev. Microbiol.* 47, 597–626. doi:10.1146/annurev.mi.47.100193.003121

Schindelin, J., Arganda-Carreras, I., Frise, E., Kaynig, V., Longair, M., Pietzsch, T., et al. (2012). Fiji: an Open-Source Platform for Biological-Image Analysis. *Nat. Methods* 9, 676–682. doi:10.1038/nmeth.2019

Shemer, B., Koshet, O., Yagur-Kroll, S., and Belkin, S. (2017). Microbial Bioreporters of Trace Explosives. *Curr. Opin. Biotechnol.* 45, 113–119. doi:10.1016/j.copbio.2017.03.003

Shemer, B., Palevsky, N., Yagur-Kroll, S., and Belkin, S. (2015). Genetically Engineered Microorganisms for the Detection of Explosives' Residues. *Front. Microbiol.* 6, 1175. doi:10.3389/fmicb.2015.01175

Shemer, B., Shpigel, E., Glozman, A., Yagur-Kroll, S., Kabessa, Y., Agranat, A. J., et al. (2020). Genome-wide Gene-Deletion Screening Identifies Mutations that Significantly Enhance Explosives Vapor Detection by a Microbial Sensor. *New Biotechnol.* 59, 65–73. doi:10.1016/j.nbt.2020.06.002

Shemer, B., Shpigel, E., Hazan, C., Kabessa, Y., Agranat, A. J., and Belkin, S. (2021). Detection of Buried Explosives with Immobilized Bacterial Bioreporters. *Microb. Biotechnol.* 14, 251–261. doi:10.1111/1751-7915.13683

Shemer, B., Yagur-Kroll, S., Hazan, C., and Belkin, S. (2018). Aerobic Transformation of 2,4-Dinitrotoluene by *Escherichia coli* and its Implications for the Detection of Trace Explosives. *Appl. Environ. Microbiol.* 84, e01729–17. doi:10.1128/AEM.01729-17

Shpigel, E., Shemer, B., Elad, T., Glozman, A., and Belkin, S. (2021). Bacterial Bioreporters for the Detection of Trace Explosives: Performance Enhancement by DNA Shuffling and Random Mutagenesis. *Appl. Microbiol. Biotechnol.* 105, 4329–4337. doi:10.1007/s00253-021-11290-2

Sievers, F., Wilm, A., Dineen, D., Gibson, T. J., Karplus, K., Li, W., et al. (2011). Fast, Scalable Generation of High-quality Protein Multiple Sequence Alignments Using Clustal Omega. *Mol. Syst. Biol.* 7, 539. doi:10.1038/msb.2011.75

Smirnova, I. A., Dian, C., Leonard, G. A., McSweeney, S., Birse, D., and Brzezinski, P. (2004). Development of a Bacterial Biosensor for Nitrotoluenes: the crystal Structure of the Transcriptional Regulator DntR. *J. Mol. Biol.* 340, 405–418. doi:10.1016/j.jmb.2004.04.071

Smith, R. G., D'Souza, N., and Nicklin, S. (2008). A Review of Biosensors and Biologically-Inspired Systems for Explosives Detection. *Analyst* 133, 571–584. doi:10.1039/B717933M

Sylvia, J. M., Janni, J. A., Klein, J. D., and Spencer, K. M. (2000). Surface-Enhanced Raman Detection of 2,4-Dinitrotoluene Impurity Vapor as a Marker to Locate Landmines. *Anal. Chem.* 72, 5834–5840. doi:10.1021/ac0006573

Tan, J., Kan, N., Wang, W., Ling, J., Qu, G., Jin, J., et al. (2015). Construction of 2,4,6-Trinitrotoluene Biosensors with Novel Sensing Elements from *Escherichia coli* K-12 MG1655. *Cell Biochem. Biophys.* 72, 417–428. doi:10.1007/s12013-014-0481-8

Van der Meer, J. R., and Belkin, S. (2010). Where Microbiology Meets Microengineering: Design and Applications of Reporter Bacteria. *Nat. Rev. Microbiol.* 8, 511–522. doi:10.1038/nrmicro2392

Wan, X., Volpetti, F., Petrova, E., French, C., Maerkl, S. J., and Wang, B. (2019). Cascaded Amplifying Circuits Enable Ultrasensitive Cellular Sensors for Toxic Metals. *Nat. Chem. Biol.* 15, 540–548. doi:10.1038/s41589-019-0244-3

Wang, B., Barahona, M., and Buck, M. (2015). Amplification of Small Molecule-Inducible Gene Expression via Tuning of Intracellular Receptor Densities. *Nucleic Acids Res.* 43, 1955–1964. doi:10.1093/nar/gku1388

Wang, B., Barahona, M., and Buck, M. (2014). Engineering Modular and Tunable Genetic Amplifiers for Scaling Transcriptional Signals in Cascaded Gene Networks. *Nucleic Acids Res.* 42, 9484–9492. doi:10.1093/nar/gku593

Wenshuo Gao, W., Xiaoguang Zhang, X., Lei Yang, L., and Huizhong Liu, H. (2010). "An Improved Sobel Edge Detection," in Proceeding of the 2010 3rd International Conference on Computer Science and Information Technology, Chengdu, 9-11 July 2010 (IEEE), 67–71. doi:10.1109/ICCSIT.2010.5563693

wwPDB consortium (2019). Protein Data Bank: the Single Global Archive for 3D Macromolecular Structure Data. *Nucleic Acids Res.* 47, D520–D528. doi:10.1093/nar/gky949

Yagur-Kroll, S., Amiel, E., Rosen, R., and Belkin, S. (2015). Detection of 2,4-dinitrotoluene and 2,4,6-trinitrotoluene by an *Escherichia coli* Bioreporter: Performance Enhancement by Directed Evolution. *Appl. Microbiol. Biotechnol.* 99, 7177–7188. doi:10.1007/s00253-015-6607-0

Yagur-Kroll, S., Lalush, C., Rosen, R., Bachar, N., Moskovitz, Y., and Belkin, S. (2014). *Escherichia coli* Bioreporters for the Detection of 2,4-dinitrotoluene and 2,4,6-trinitrotoluene. *Appl. Microbiol. Biotechnol.* 98, 885–895. doi:10.1007/s00253-013-4888-8

Conflict of Interest: The authors declare that the research was conducted in the absence of any commercial or financial relationships that could be construed as a potential conflict of interest.

Publisher's Note: All claims expressed in this article are solely those of the authors and do not necessarily represent those of their affiliated organizations, or those of the publisher, the editors and the reviewers. Any product that may be evaluated in this article, or claim that may be made by its manufacturer, is not guaranteed or endorsed by the publisher.

frontiers | Frontiers in Bioengineering and Biotechnology

ORIGINAL RESEARCH
published: 09 May 2022
doi: 10.3389/fbioe.2022.867164

Near-Infrared Bioluminescence Imaging of Macrophage Sensors for Cancer Detection *In Vivo*

Giorgia Zambito[1,2], *Gunja Mishra*[3], *Christopher Schliehe*[3] *and Laura Mezzanotte*[1,2]*

[1]Department of Radiology and Nuclear Medicine, Erasmus MC University Medical Center, Rotterdam, Netherlands, [2]Department of Molecular Genetics, Erasmus MC University Medical Center, Rotterdam, Netherlands, [3]Department of Immunology, Erasmus MC University Medical Center, Rotterdam, Netherlands,

Melanoma is an aggressive type of skin cancer with a poor prognosis after it gets metastasized. The early detection of malignant melanoma is critical for effective therapy. Because melanoma often resembles moles, routine skin check-up may help for timely identification of suspicious areas. Recently, it has been shown that the interplay of melanoma cells with the immune system can help develop efficient therapeutic strategies. Here, we leveraged engineered macrophages (BMC2) as cell-based sensors for metastatic melanoma. To perform dual-color bioluminescence imaging (BLI) *in vivo*, macrophages were engineered to express a green click beetle luciferase (CBG2) and a near-infrared fluorescent dye (DiR), and B16F10 melanoma cells were instead engineered to express a near-infrared click beetle luciferase (CBR2). Using real-time *in vivo* dual-color BLI and near-infrared fluorescence (FL) imaging, we could demonstrate that macrophages were able to sense and substantially accumulate in subcutaneous and metastatic melanoma tissues at 72 h after systemic injections. Together, we showed the potentiality to use optical imaging technologies to track circulating macrophages for the non-invasive detection of metastatic melanoma.

Keywords: near-infrared bioluminescence, macrophage, cancer diagnostic, optical imaging, biosensor

OPEN ACCESS

Edited by:
Vadim R. Viviani,
Federal University of São Carlos, Brazil

Reviewed by:
Nuria Vilaboa,
University Hospital La Paz, Spain
Honglin Jin,
Huazhong University of Science and Technology, China

***Correspondence:**
Laura Mezzanotte
l.mezzanotte@erasmusmc.nl

Specialty section:
This article was submitted to Biomaterials, a section of the journal Frontiers in Bioengineering and Biotechnology

Received: *31 January 2022*
Accepted: *23 March 2022*
Published: *09 May 2022*

Citation:
Zambito G, Mishra G, Schliehe C and Mezzanotte L (2022) Near-Infrared Bioluminescence Imaging of Macrophage Sensors for Cancer Detection In Vivo. Front. Bioeng. Biotechnol. 10:867164. doi: 10.3389/fbioe.2022.867164

INTRODUCTION

Detecting early-stage cancer is a promising avenue to enhance the effect of medical interventions and reduce cancer mortality (Etzion et al., 2003). Specifically, melanoma is an aggressive cutaneous type of cancer with an incidence that has been rapidly increasing in the past decade (Matthews et al., 2017). Nowadays, the identification of molecular markers together with histopathological assessment is more often used to guide prompt therapeutic decisions (Bianchini et al., 2007; Yang et al., 2020). These markers are melanoma mutations, gene polymorphisms, signaling receptors, and melanin pigment (Yang et al., 2020). In addition, melanoma is also one of the most immunologic malignancies associated with rapid infiltration of immune cells such as tumor-infiltrating T-lymphocytes and tumor-associated macrophages. The use of immunotherapies in the treatment of patients with metastatic melanoma has produced promising therapeutic advantages, increasing the overall survival of patients (Uhara 2019; Ralli et al., 2020). Thus, having early detection of metastatic tumor progression may significantly change the medical intervention in this type of tumor.

Here, we exploited monocytes as part of the innate immune system that are actively recruited into tumor tissues where they differentiate into tumor-associated macrophages (TAMs) and also

accumulate in hypoxic areas (Burke et al., 2003; Yang et al., 2018). The accumulation of TAMs has also been demonstrated in primary lesions of melanoma and pulmonary metastases (Gajewski et al., 2013; Elpek et al., 2014; Pieniazek et al., 2018). The relative abundance of TAMs in melanoma ranges from 0 to 30%, and their density increases proportionally to tumor thickness (Hussein 2006). As a consequence of these natural properties, we decided to leverage light-emitting macrophages as a cellular sensor for the detection of subcutaneous and metastatic melanomas using a murine melanoma model as a proof-of-principle experiment. Engineered macrophages have previously been exploited as cell-based delivery platforms for breast cancer chemotherapeutics and also to shuttle oncolytic viruses specific to treat prostate cancer and related metastases (Muthana et al., 2013; Huang et al., 2021). Another seminal work proposed a cell-based "immunodiagnostic" system by using macrophages as pan-cancer cell sensors due to their ability to accumulate in breast tumors. In this study, macrophage sensors expressing a secreted form of Gluc (Gaussia luciferase) driven by an M2-like promoter were able to detect small tumors as small as 25–50 mm^3 by real-time blood luciferase measurements (Aalipour et al., 2019).

However, the potential of macrophages as pan-cancer sensors has not been proved in other tumor models yet. Additionally, the description of macrophage dynamics and relative recruitment in the tumor site is still incomplete partly due to the scarcity of sensitive *in vivo* imaging detections (McCarthy et al., 2020; Su et al., 2020). In our previous work, we demonstrated that near-infrared dual-color bioluminescence imaging (BLI) is a sensitive method for the detection of two cell populations in deep tissues. However, the detection accuracy depends on the relative level of the expression of the two luciferases (Zambito et al., 2020; Zambito and Mezzanotte, 2021). Here, we exploited our previously developed method for the visualization of macrophage infiltration and for their accumulation in melanoma tissues *in vivo*. Therefore, we engineered BMC2 macrophages to express a near-infrared click beetle green luciferase mutant named CBG2 (λ = 680 nm) and B16F10 melanoma cells to express a near-infrared red click beetle luciferase mutant named CBR2 (λ = 740 nm) (Hall et al., 2018; Zambito et al., 2021). In addition to BL imaging, we also used a DiR (1,1′-dioctadecyl-3,3,3′,3′-tetramethylindotricarbocyanine iodide) near-infrared dye allowing non-invasive tracking of labeled macrophages after their systemic injection *in vivo* (Shan 2004; Eisenblatter et al., 2009; Liu and Wu 2016). Overall, this work provides a conceptual scenario for the use of engineered macrophages as a diagnostic sensor for cancer, and it provides proof-of-concept evidence for its successful application in clinically relevant murine melanoma models.

RESULTS

Macrophages and Melanoma Cells Engineered to Express Luciferase Reporter Genes *In Vitro*

CBG2 and CBR2 luciferase mutants were engineered to have superior stability and red and near-infrared color-shift capability when combined with the NH_2-NpLH2 luciferin substrate (Zambito et al., 2020). The macrophage cell line BMC2 was engineered to express the CBG2 luciferase mutant (BMC2-CBG2), and B16F10 melanoma cells were engineered to express CBR2 luciferase (B16-CBR2). To perform dual-color BLI and spectral unmixing *in vivo*, both BMC2-CBG2 and B16-CBR2 were seeded in a black 96-well plate, and living cells were spectrally imaged after the addition of NH_2-NpLH2 luciferin on an IVIS spectrum imager. First, specific bioluminescent spectra of BMC2-CBG2 and B16-CBR2 cells were measured and saved in distinct spectral libraries. These libraries are useful to discriminate each luciferase contribution when BMC2-CBG2 and B16-CBR2 cells result colocalized in the same area of interest (Zambito and Mezzanotte 2021). As expected, the emission spectra registered a consistent red peak for CBG2 (λ = 680 nm) and a near-infrared peak for CBR2 (λ = 740 nm) when using NH_2-NpLH2 luciferin (**Figure 1A**). Then, the spectral unmixing algorithm was applied for BMC2-CBG2 and pure B16-CBR2 cell mixture using selected pure libraries and setting bandpass filters ranging from 580 to 800 nm (**Figure 1B**). First, both cell types were cocultured at various ratios ranging from 100 to 0%, respectively, followed by spectral imaging in the presence of NH_2-NpLH2 luciferin and subsequent unmixing (**Figure 1B**). As expected, the accurate spectral unmixing algorithm correctly classified the B16-CBR2-containing wells (unmix B16-CBR2) placed in the left panel of **Figure 1B**. With decreasing amounts of B16-CBR2 cells (magenta color in the composite figure), the CBR2-specific signal also gradually decreased toward the bottom of the plate. At the same time, BMC2-CBG2 cells (unmix BMC2-CBG2) were accurately classified in the right panel of **Figure 1B**. Here, the signal for BMC2-CBG2 cells (green color in the composite image) gradually decreased toward the upper end of the plate, which was in line with the increasing proportions of B16-CBR2 cells. The specific libraries were also used to quantify the photon flux of mixed BMC2-CBG2 and B16-CBR2 cell populations at various percentages between 100 and 0%. Quantification of the unmixed photon flux signals was normalized to 100% cell ratio and plotted in a bar graph revealing the linear correlation between the percentage of cells plated and the photons recorded (**Figure 1C**). To monitor higher accuracy BMC2-CBG2 cells *in vivo*, we labeled macrophages with a near-infrared fluorescent dye (XenoLight DiR, Perkin Elmer) to perform dual-optical imaging by bioluminescence (BL) and fluorescence (FL) imaging. To check the *in vitro* labeling efficiency, BMC2-CBG2 cells were prelabeled with DiR near-infrared dye and plated in various cell ratios ranging from 100 to 0% of the total volume in a black 96-well plate. Fluorescence imaging was performed by selecting DiR filters at 710 nm for excitation and 760 nm for emission. The radiant efficiency was calculated by subtracting the FL signal registered from unlabeled macrophages used as control. The fluorescence detected was found linearly proportional to the number of plated cells (**Figure 1D**). Additionally, to confirm that BMC2-CBG2 macrophages were successfully labeled with the DiR fluorescence dye, images of macrophages were taken at 24, 48, and 72 h after DiR treatment (**Supplementary Figure S3A**).

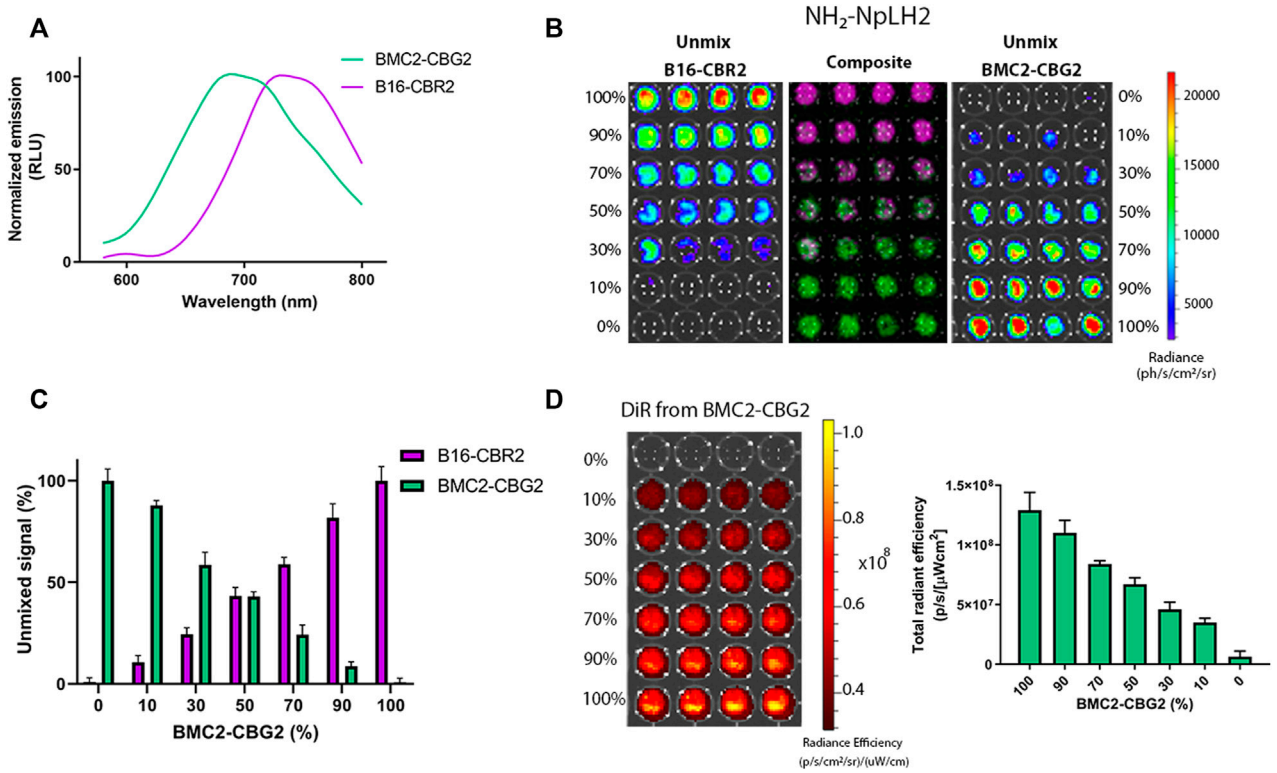

FIGURE 1 | *In vitro* characterization and spectral unmixing of BMC2-CBG2 and B16-CBR2 luciferase-expressing cells. **(A)** Normalized bioluminescence emission spectra for BMC2-CBG2 and B16-CBR2 cells treated with NH_2-NpLH2 luciferin as the luciferase substrate. Spectra were normalized to the peak emission for each click beetle mutants with the NH_2-NpLH2 substrate. Spectra were acquired using an IVIS spectrum imager with the following settings: FOV C, f/stop = 1, medium binning, 30 s exposure time, and a range of bandpass filters ranging from 580 to 800 nm.**(B)** Spectral unmixing of B16-CBR2 and BMC2-CBG2 cells (n = 4 samples). Cells were mixed in various proportions ranging from 100 to 0% cell number of the total population. Quantification of the BL unmixed outputs for B16-CBR2 (magenta color) and BMC2-CBG2 (green color) registered after NH_2-NpLH2 substrate administration. A black 96-well plate was spectrally imaged using a selected bandpass filter ranging from 580 to 800 nm by using an IVIS spectrum imager. **(C)** Quantification of the percentage of unmixed signals of B16-CBR2 and BMC2-CBG2 cells (n = 4 samples). Unmixed signals were normalized to 100% cell ratios with $p < 0.0001$ calculated by multiple comparisons and one-way ANOVA. Error bars represent ±SD. **(D)** Radiant efficiency was recorded for BMC2-CBG2 macrophages pre-labeled with the DiR near-infrared fluorescent dye. Cells were plated in a black 96-well plate in various proportions ranging from 0 to 100% of the total population. The bar graph shows the mean fluorescence intensity. Error bars represent ±SD (n = 4 samples). The plate was spectrally imaged using an IVIS imager system, and DiR filters were set at 710 nm for excitation and 760 nm for emission.

Together, the *in vitro* results collected from BL and FL outputs validated that BMC2-CBG2 and B16-CBR2 cells could be further used for *in vivo* dual-color bioluminescence and fluorescence imaging.

DiR-Labeled BMC2 Macrophages Detected in Subcutaneous Melanoma Tumors

To investigate the potential of BMC2 macrophage sensors as a tool for melanoma detection, C57BL/6 mice were subcutaneously engrafted with B16F10 melanoma cells expressing CBR2 luciferase (B16-CBR2). Tumor growth was spectrally imaged using the NH_2-NpLH2 luciferin substrate and monitored over time by BL imaging. To set up the optimal cell concentration and optimal time-point for the detection of DiR-labeled BMC2-CBG2 macrophages, we first injected DiR-labeled BMC2-CBG2 macrophages systemically at three cell amounts: 1×10^6, 5×10^6, and 10×10^6 and 2 weeks after subcutaneous melanoma implantation. Fluorescence values for DiR-labeled BMC2-CBG2 macrophages were collected after BLI detection of B16-CBR2 melanoma tumors, and fluorescence values are plotted in **Figure 2A**. The proportional correlation between the number of DiR-labeled BMC2-CBG2 cells injected and the radiant efficiency registered show that both five and 10 million DiR-labeled BMC2-CBG2 cells can be efficiently measured in subcutaneous tumors (**Figure 2A**). Interestingly, the accumulation of DiR-labeled BMC2-CBG2 macrophages adjacent to the non-tumor areas is probably due to the on-target recruitment of macrophages with poor tumor-infiltration capability (**Figure 2A**, right panel). To validate the feasibility to visualize the DiR-labeled BMC2-CBG2 macrophages in subcutaneous tumor models, we first measured the BL photon yields in mice bearing wildtype B16-CBR2 melanoma tumors, and later, we injected the DiR-labeled BMC2-CBG2 cells with three different cell numbers: 1×10^6, 5×10^6, and 10×10^6. BL outputs from the DiR-labeled BMC2-CBG2 macrophages were registered after NH_2-NpLH2 substrate administration and selecting appropriate bandpass filters ranging from 580 to

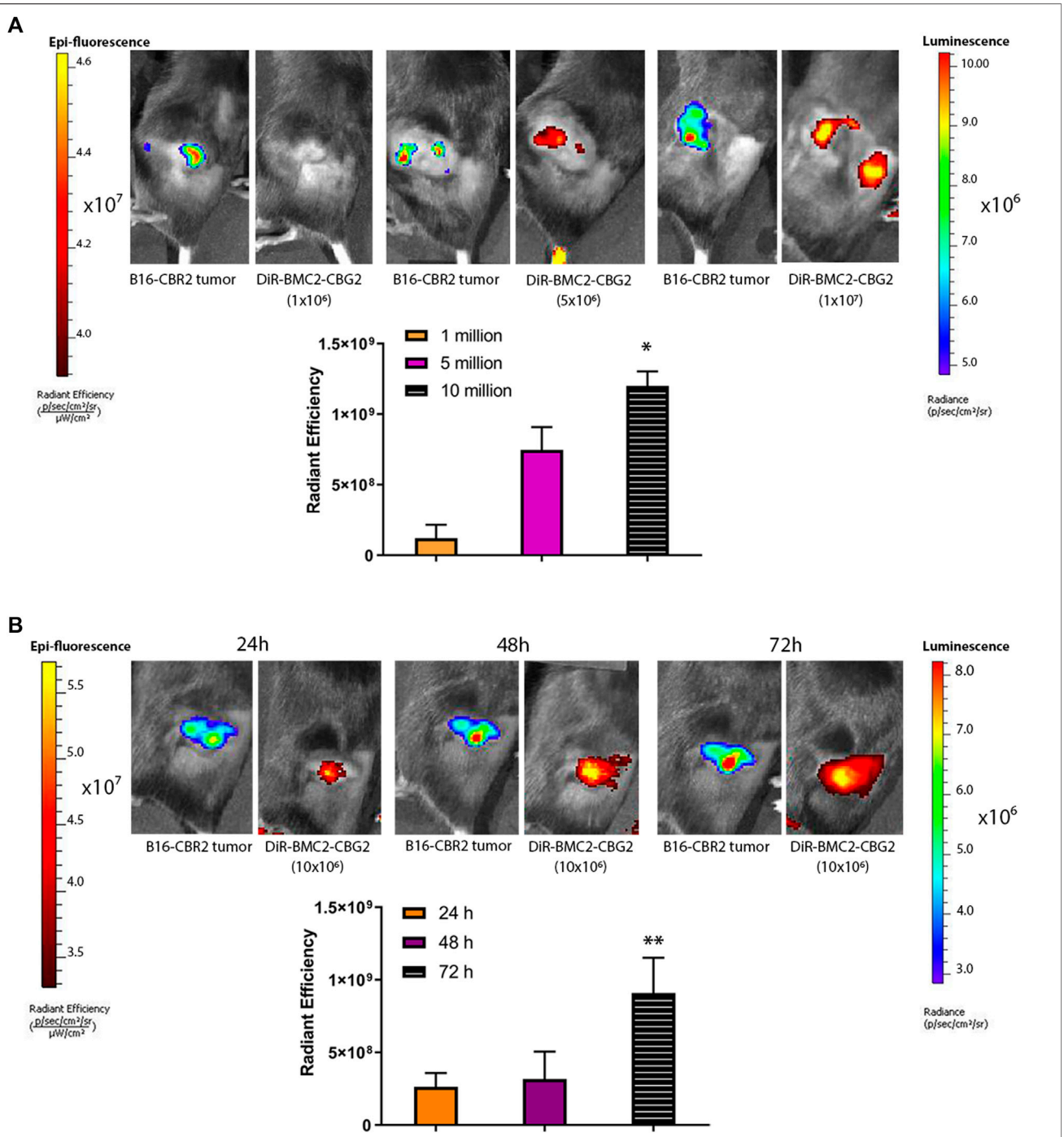

FIGURE 2 | BMC2-CBG2 macrophages for subcutaneous melanoma detection. **(A)** Mice were transplanted with a subcutaneous B16F10 melanoma tumor model engineered to express near-infrared CBR2 click beetle luciferase (B16-CBR2). Bioluminescence photon fluxes represent the light emission for B16-CBR2 melanoma before BMC2-CBG2 administration. BL images were acquired 15 min after NH_2-NpLH2 substrate injection. Before systemic injection, BMC2-CBG2 macrophages were pre-labeled with the DiR near-infrared dye (excitation 710 nm and emission 760 nm) at the amount of 1, 5, and 10 million per mouse ($n = 3$ mice). Respective radiant efficiencies were quantified and plotted. The bar graph shows the mean fluorescence intensity, and significance was registered for mean values of the 1-million group and mean values of the 10-million group. (*) p values ($p < 0.05$) were calculated by one-way ANOVA followed by Tukey's test for multiple comparisons. Error bars represent ±SD. **(B)** Fluorescence values of BMC2-CBG2 macrophages pre-labeled with the DiR near-infrared dye (filters selected for excitation at 710 nm and emission at 760 nm) injected systemically at a dose of 10 million cells per mouse. Fluorescence image acquisition was performed at 24, 48, and 72 h after BMC2-CBG2 macrophage administration. The respective radiant efficiencies were quantified and plotted. Bioluminescence photon fluxes represent the light emission for B16-CBR2 melanoma before BMC2-CBG2 macrophage administrations. BL images were acquired 15 min after NH_2-NpLH2 substrate injection. The bar graph shows the mean fluorescence intensity ($n = 3$ mice). Significance was registered for mean values of 24- and 48-h groups versus mean values of the 72-h group. (*) $p < 0.05$. Error bars represent ±SD.

800 nm. Dim photon fluxes (~4×10^4 photon/s) were registered for the wildtype B16-CBR2 melanoma-bearing mice after receiving 10 million BMC2-CBG2 cells (**Supplementary Figure S1A**). Additionally, BL outputs for BMC2-CBG2 cells resulted insufficient to register an accurate spectral library and to perform a spectral unmixing algorithm. On the contrary, near-infrared FL outputs of BMC2-CBG2 cells were accurately measured at the subcutaneous tumor area allowing more sensitive detection of the DiR-labeled BMC2-CBG2 macrophages compared to BL imaging. However, FL imaging of the DiR-labeled BMC2-CBG2 macrophages confirmed colocalization with the dim BL outputs found in the tumor region (**Supplementary Figure S1A**). Interestingly *ex vivo* data demonstrated that the highest value for DiR fluorescence from labeled BMC2-CBG2 macrophages was substantially detected in the lungs (1,6E+10 [ph/s/cm^2/sr]/[μW/cm^2]). The DiR fluorescence of subcutaneous melanoma registered instead radiant efficiency value that was ~7,3 fold lower compared to the DiR values registered in the lungs (**Supplementary Figure S1B** right panel). Once we assumed that 10 million BMC2-CBG2 cells gave the most accurate FL and BL signals *in vivo*, we further investigated the optimal time-point for imaging the DiR-labeled BMC2 cells in subcutaneous melanoma models. B16-CBR2 tumor-bearing mice were routinely imaged to monitor melanoma cancer growth by BLI (**Figure 2B**). Two weeks after tumor implantation, 10 million DiR-labeled BMC2-CBG2 cells were injected systemically, and FL measurements were performed at 24, 48, and 72 h post BMC2-CBG2 administration on the IVIS spectrum imager (**Figure 2B**). Control mice received B16-CBR2 melanoma cells only (data not shown). Radiance values at 72 h after DiR-labeled BMC-CBG2 injection were ~3 fold higher than the radiance values registered at 24 and 48 h at the melanoma tumor site. (**Figure 2B**). *Ex vivo* near-infrared FL imaging confirmed the localization of DiR-BMC2 macrophages at the subcutaneous tumor area at 72 h after DiR-labeled BMC2-CBG2 injection (**Supplementary Figure S2A**, right panel). Control mice were inoculated with B16-CBR2 melanoma tumors only. Together, the data suggest that the optimal time-point to localize 10 million DiR-labeled BMC2-CBG2 macrophages at the subcutaneous melanoma tumor site is 72 h after DiR-labeled BMC2-CBG2 macrophage administration.

Engineered BMC2 Macrophages Enable *In Vivo* Visualization of Melanoma Lung Metastasis by Bioluminescence and Fluorescence Imaging

We further explored whether BMC2-CBG2 macrophages may be used as a diagnostic cell sensor in metastatic cancer models. Thus, orthotopic metastatic C57BL/6 mouse models were established with systemic injections of B16-CBR2 cells. Tumor growth was monitored over time by BL imaging of CBR2 luciferase after administration of the NH_2-NpLH2 luciferin substrate. Once the tumor growth could be visualized by BLI and showed spreading in the chest (usually on day 10), DiR-labeled BMC2-CBG2 macrophages were injected systemically (1×10^7 cells per mouse). Fluorescence outputs for DiR-labeled BMC2-CBG2 macrophages were calculated by drawing the region of interest (ROI) at the metastatic tumor region (yellow circle). DiR radiance values were collected at 24, 48, and 72 h after BMC2-CBG2 macrophage injection (**Figure 3A**), considering that BMC2-CBG2 macrophages could retain the DiR *in vitro* at least 72 h (**Supplementary Figure S3A**). A substantial localization of DiR-labeled BMC2-CBG2 macrophages was registered in the metastatic lungs at 72 h post macrophage injection (**Figure 3A**). Interestingly, FL imaging measured a strong localization of DiR-labeled BMC2-CBG2 cells also in the cervical lymph node at 24 and 48 h post injection of macrophages. Radiant efficiencies of the DiR dye measured in the metastases at the three different time points are depicted in **Figure 3A** (right panel). In addition, we successfully applied the spectral unmixing algorithm to separate the colocalized bioluminescent signals of BMC2-CBG2 and B16-CBR2 in the lungs (**Figure 3B**). To perform that, specific bioluminescent spectral libraries for pure BMC2-CBG2 and B16-CBR2 outputs were built. Of note, BL outputs emitted by either BMC2-CBG2 (green color) or B16-CBR2 (magenta color) were accurately extracted from the melanoma area 48 h post BMC2-CBG2 administration (**Figure 3B**). The spectral properties of BMC2-CBG2 and B16-CBR2 were measured and depicted in **Figure 3B** (right panel). The spectral unmixing algorithm was also conducted for *ex vivo* harvested lungs 72 h post BMC2-CBG2 administration. The representative images of BL spectral unmixing are shown in **Figure 3C**. Radiant efficiency values for DiR pre-labeled BMC2-CBG2 macrophages were measured in the lungs, livers, and spleens. FL outputs were plotted highlighting that the values for the DiR registered in the lungs were 2-3 fold greater than the values in the liver.

To confirm the localization of the activated BMC2-CBG2 macrophages to the tumor site, 15-micron thick tumor sections from mice inoculated with DiR-labeled BMC2-CBG2 cells were stained for CD68 to detect macrophages, as shown in red color in **Supplementary Figure S3B**.

Furthermore, confirmation of injected macrophages labeled with the DiR dye was conducted by imaging scan of cryosections of the lungs infused with DiR-labeled BMC2-CBG2 macrophages using the Odyssey CLx device. Filters at 700 and 800 nm were selected for the imaging. A channel at 700 nm was used to distinguish CD68+ macrophages, and a channel at 800 nm was used to distinguish macrophages labeled with the DiR dye. A substantial difference was detected between B16 tumors treated with DiR-labeled BMC2-CBG2 macrophages localized at the tumor site (green color, top panels) compared to the B16 tumor controls not treated with DiR-labeled BMC2-CBG2 macrophages (bottom panels) (**Supplementary Figure S3C**).

Together, these data suggest the feasibility to visualize and localize DiR-labeled BMC2-CBG2 macrophages in the lungs affected by metastatic melanoma tumors.

DISCUSSION

The timely detection of cancer growth, cancer recurrence, and monitoring therapies will increase the chances of prompt

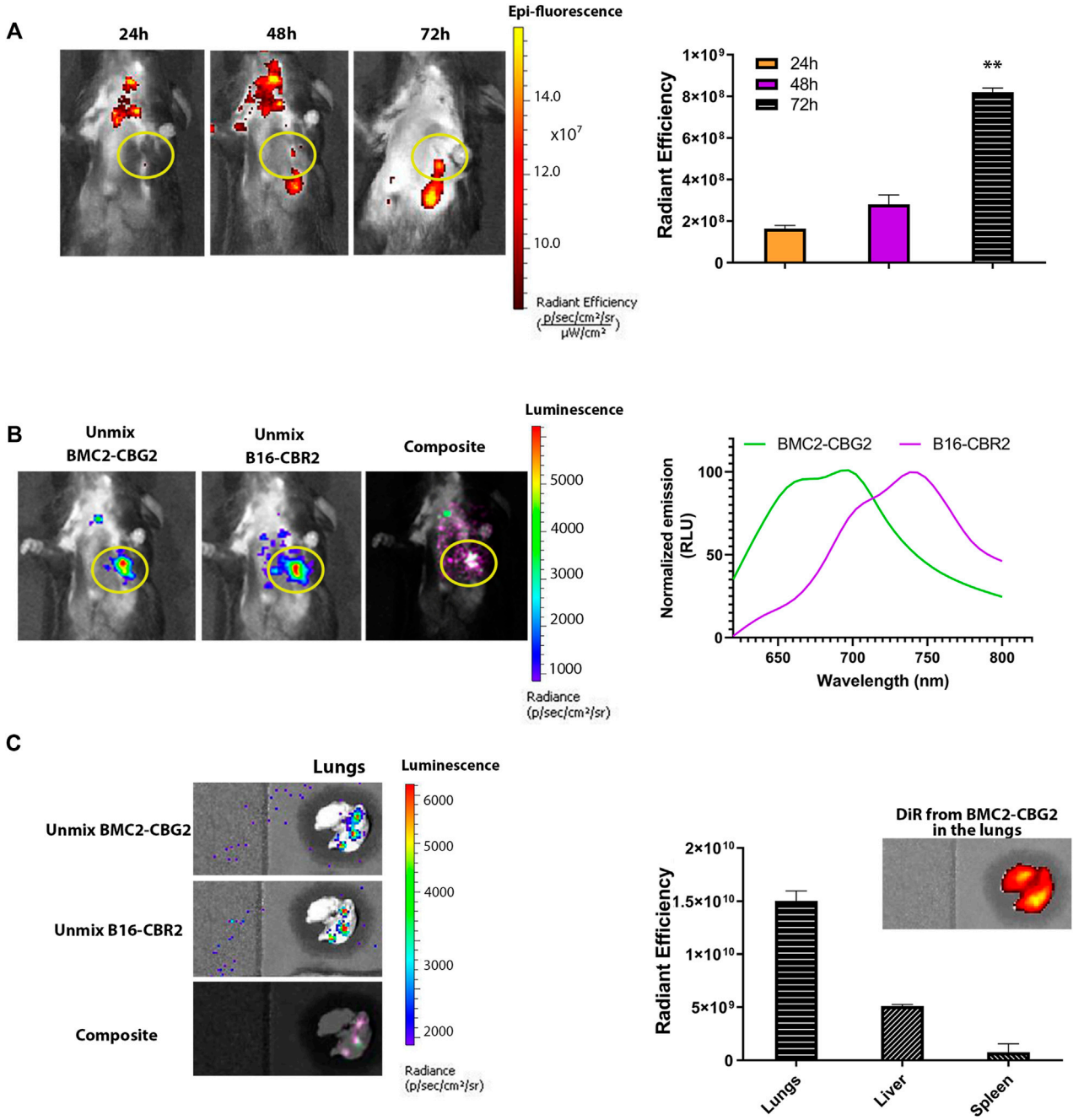

FIGURE 3 | Engineered macrophages enable *in vivo* visualization of the metastatic tumor model by BLI. **(A)** Fluorescence imaging of mice bearing B16-CBR2 metastatic cancer cells ($n = 3$ mice). After metastatic tumor establishment, C57BL/6 mice were injected with 10 million BMC2-CBG2 macrophages pre-labeled with the DiR near-infrared dye. Fluorescence imaging was performed at 24, 48, and 72 h post BMC2-CBG2 administration (left panel). Fluorescent outputs registered from the lungs were recorded and plotted in the right panel, demonstrating that BMC2-CBG2 macrophages accumulate at the tumor site mainly at 72 h after BMC2-CBG2 macrophage administration. The ROI region for the tumor site is marked in the yellow circle. The bar graph shows mean fluorescence intensity ($n = 3$ mice). Significance was registered for mean values of 24- and 48-h groups versus mean values of the 72-h group. (*) $p < 0.05$ was calculated by one-way ANOVA followed by Tukey's test. Error bars represent ±SD. **(B)** Representative BL spectral unmixing of a mouse engrafted with metastatic B16-CBR2 melanoma ($n = 3$) (left panel). Mice ($n = 3$) were imaged 48 h after the injection of 10 million BMC2-CBG2 macrophages pre-labeled with the DiR near-infrared dye. Images were acquired 15 min after NH_2-NpLH2 substrate injection. The filter selected for the green spectral unmixing (BMC2-CBG2) was set at 700 nm, and for the magenta spectral unmixing (B16-CBR2), the filter was set at 740 nm. Spectral properties of BMC2-CBG2 macrophages and B16-CBR2 melanoma with the NH_2-NpLH2 substrate are depicted in the right panel. The ROI region for the tumor site is marked in the yellow circle. **(C)** Representative images of *ex vivo* spectral unmixing of the lungs. The green color was used for unmixed BMC2-CBG2 macrophages and magenta color for unmixed B16-CBR2 melanoma tumors. Colocalized bioluminescent signals for BMC2-CBG2 and B16-CBR2 cells in the lungs resulted in overlapped colors (light pink), as shown in the composite image (left panel). Radiant efficiency values for DiR-labeled BMC2-CBG2 macrophages were measured in the lungs, livers, and spleens and are depicted in the right panel. FL emissions for the DiR fluorescent dye were recorded from the lungs, liver, and spleen, selecting the DiR filters for excitation at 710 nm and emission at 760 nm. The bar graph shows the mean fluorescence intensity. Error bars represent ±SD.

response to medical intervention. The success of blood-based biomarkers for early tumor lesions is often limited by short circulation times, blood dilutions, and demonstrating suboptimal sensitivity for cancer diagnostics (Mamdani et al., 2017). Encouraging the use of engineered immune cells as an emerging class of cellular sensors for inflammation and disease will foster new technologies for cellular immunotherapies. A clear advantage of using immune cells such as macrophages as diagnostic vehicles is based on their homing and infiltrating capabilities at the cancer sites (Muthana et al., 2013). Recently, Aalipour A. and coworkers in a seminal work, exploited macrophages engineered to express the Gluc luciferase gene activated when switching their phenotype in tumor-associated macrophages (TAMs) in the tumor area. The BL measurement of the Gluc activity was conducted by a simple blood test for sensitive detection of modest breast cancer tumor volume (25–30 mm^3) (Aalipour et al., 2019).

Melanoma tumor is intrinsically linked to an inflammation reaction and therefore stimulates the recruitment of "tumor-homing" cells such as macrophages. Thus, we leveraged the natural property of macrophages to infiltrate subcutaneous and metastatic melanoma tumors and image them by dual-color BLI and by near-infrared FL *in vivo*. In our case, *in vivo* and *ex vivo* data showed that we could visualize macrophages homing small metastatic melanoma tumors in the lungs (size ranging between 30 and 100 mm^3) 15 days after tumor inoculation. To perform sensitive real-time dual-color bioluminescence imaging in deep tissues, we engineered BMC2 macrophages to express the CBG2 luciferase mutant (λ = 680 nm) and B16F10 melanoma cells to express the CBR2 click beetle luciferase mutant (λ = 740 nm) (Hall et al., 2018; Zambito et al., 2020). We applied this technology using NH_2-NpLH2 luciferin as a single substrate to monitor immune cell dynamics and tumor growth qualitatively. The administration of a unique substrate makes the BLI sessions highly specific compared to other systems where multiple injections of substrates are required (Hall et al., 2018; Ji et al., 2020; Zambito et al., 2020). However, we expect the performance of dual-color BLI using orthogonal luciferase/substrate couples such as AkaBLI (Iwano et al., 2018) and NanoLuc/hydrofurimazine systems (Su et al., 2020) would be similar. Moreover, our approach can also be exploited to genetically engineer various tumors and immune cells such as T cells, natural killer cells, and dendritic cells.

In the murine orthotopic melanoma model presented here, BMC2-CBG2 macrophages exhibited a visible accumulation in the primary tumors at 72 h after systemic administration. However, substantial off-target cell sequestration was also observed in the liver and the spleen. These findings were supported by the work of Combes F. and others, where viable DiR-labeled macrophages were first partly sequestered in the lungs and then redistributed to other off-target sites such as the liver and the spleen and also to on-target tumor sites up to 96 h after systemic administration (Combes et al., 2018).

The cell kinetics observed in this study are also supported by seminal imaging studies on the migratory properties of radio-labeled macrophages homing tumors by PET imaging modality. The biodistribution of engineering macrophages pre-labeled with an ^{18}F-FDG probe (half-life = 109.7 min) proved that macrophage-activated killer (MAK) cells are first sequestered in the liver and lungs and to a minor degree in the spleen after i.v. injection of patients. Then, cell redistribution occurs from the pulmonary vasculature to other tissues including peritoneal metastases in human patients at 4 h after ^{18}F-FDG-labeled macrophage-activated killer (MAK) cell administration. However, the short-life of ^{18}F-FDG and "leakage" of the probe out of the cells should be considered when performing cell biodistribution studies (Ritchie et al., 2007). In another study, also SPECT tracking of i.v. injected indium-oxine (half-life = 2.8 days)–labeled murine macrophages reveals the initial margination of macrophages in the lungs and then eventual migration to the liver, spleen, and kidneys before accumulating within sites of the tumor (Chokri et al., 1992). An improved alternative to future clinical application would be employing the ^{89}Zr-oxine probe that has a longer half-life (3.3 days), and it has been largely used to track infused T cells homing breast cancer and imaged for several days by PET imaging modalities in small animals (Man et al., 2019; Kurebayashi et al., 2021). However, to the best of our knowledge, ^{89}Zr-oxine has not been used to track macrophages *in vivo* yet. Additionally, the accumulation of macrophages in off-target organs should not be discounted when considering the use of macrophages as a cell-based platform for tumor diagnostic or the delivery of drugs into tumors and will be part of a follow-up study.

In our study, an adequate accumulation of macrophages was measured and visualized in subcutaneous and metastatic tumor models together with the longitudinal tracking of immune cells by bioluminescence. The fact that we could image macrophages by *in vivo* bioluminescence also suggests the accumulation of living cells at the tumor site and, therefore, excludes labeling artifacts attributed to the fluorescence observed.

Overall, we envisioned that engineered macrophages should be considered for their innate ability to sense and reach small tumors and metastasis in the body. Moreover, the advancement of optical imaging technologies and the design of novel near-infrared I and II probes will encourage to shed light on the mechanisms underlying macrophage recruitment and behavior in animal models, especially in genetically-engineered mouse models with spontaneous tumor formation.

DATA AVAILABILITY STATEMENT

The raw data supporting the conclusions of this article will be made available by the authors, without undue reservation.

ETHICS STATEMENT

The animal study was reviewed and approved by Erasmus MC Animal Experiments Committee (Animal work protocol number 17-867-81).

AUTHOR CONTRIBUTIONS

GZ, LM, CS, and GM contributed to the conception and design of the study. GM contributed to the lentiviral production of engineered cell lines. GZ wrote the first draft of the manuscript and performed *in vitro* and *in vivo* experiments. All authors contributed to manuscript revision, read, and approved the submitted version.

FUNDING

We acknowledge the funding for this project by the European Union's Horizon 2020 research and innovation program under the Marie Sklodowska-Curie grant agreement No 777682. GM was supported by the LEaDing Postdoc Fellowship Program, a Horizon 2020 Marie Sklodowska-Curie COFUND. This work was supported by the Applied Molecular Imaging Erasmus MC (AMIE) facility. We thank Mary Hall, Lance Encell, Thomas Kirkland, and Ce Shi from Promega for the fruitful discussion and synthesis of naphthyl luciferin.

SUPPLEMENTARY MATERIAL

The Supplementary Material for this article can be found online at: https://www.frontiersin.org/articles/10.3389/fbioe.2022.867164/full#supplementary-material

REFERENCES

Aalipour, A., Chuang, H.-Y., Murty, S., D'Souza, A. L., Park, S.-m., Gulati, G. S., et al. (2019). Engineered Immune Cells as Highly Sensitive Cancer Diagnostics. *Nat. Biotechnol.* 37 (5), 531–539. doi:10.1038/s41587-019-0064-8

Bianchini, F., Massi, D., Marconi, C., Franchi, A., Baroni, G., Santucci, M., et al. (2007). Expression of Cyclo-Oxygenase-2 in Macrophages Associated with Cutaneous Melanoma at Different Stages of Progression. *Prostaglandins & Other Lipid Mediators* 83 (4), 320–328. doi:10.1016/j.prostaglandins.2007.03.003

Burke, B., Giannoudis, A., Corke, K. P., Gill, D., Wells, M., Ziegler-Heitbrock, L., et al. (2003). Hypoxia-Induced Gene Expression in Human Macrophages. *Am. J. Pathol.* 163, 1233–1243. doi:10.1016/S0002-9440(10)63483-9

Chokri, M., Lopez, M., Oleron, C., Girard, A., Martinache, C., Siffert, J. C., et al. (1992). Production of Macrophages with Potent Antitumoral Properties (MAK) by Culture of Monocytes in the Presence of GM-CSF and 1,25 (OH)2 vitD3. *Anticancer Res.* 12, 2257–2260.

Combes, F., Mc Cafferty, S., Meyer, E., and Sanders, N. N. (2018). Off-Target and Tumor-specific Accumulation of Monocytes, Macrophages and Myeloid-Derived Suppressor Cells after Systemic Injection. *Neoplasia* 20 (8), 848–856. doi:10.1016/j.neo.2018.06.005

Eisenblätter, M., Ehrchen, J., Varga, G., Sunderkötter, C., Heindel, W., Roth, J., et al. (2009). *In Vivo* optical Imaging of Cellular Inflammatory Response in Granuloma Formation Using Fluorescence-Labeled Macrophages. *J. Nucl. Med.* 50 (10), 1676–1682. doi:10.2967/jnumed.108.060707

Elpek, K. G., Cremasco, V., Shen, H., Harvey, C. J., Wucherpfennig, K. W., Goldstein, D. R., et al. (2014). The Tumor Microenvironment Shapes Lineage, Transcriptional, and Functional Diversity of Infiltrating Myeloid Cells. *Cancer Immunol. Res.* 2 (7), 655–667. doi:10.1158/2326-6066.CIR-13-0209

Etzioni, R., Urban, N., Ramsey, S., McIntosh, M., Schwartz, S., Reid, B., et al. (2003). The Case for Early Detection. *Nat. Rev. Cancer* 3 (4), 243–252. doi:10.1038/nrc1041

Gajewski, T. F., Schreiber, H., and Fu, Y.-X. (2013). Innate and Adaptive Immune Cells in the Tumor Microenvironment. *Nat. Immunol.* 14 (10), 1014–1022. doi:10.1038/ni.2703

Hall, M. P., Woodroofe, C. C., Wood, M. G., Que, I., van't Root, M., Ridwan, Y., et al. (2018). Click Beetle Luciferase Mutant and Near Infrared Naphthyl-Luciferins for Improved Bioluminescence Imaging. *Nat. Commun.* 9, 132. doi:10.1038/s41467-017-02542-9

Huang, Y., Guan, Z., Dai, X., Shen, Y., Wei, Q., Ren, L., et al. (2021). Engineered Macrophages as Near-Infrared Light Activated Drug Vectors for Chemo-Photodynamic Therapy of Primary and Bone Metastatic Breast Cancer. *Nat. Commun.* 12, 4310. doi:10.1038/s41467-021-24564-0

Hussein, M. R. (2006). Tumour-associated Macrophages and Melanoma Tumourigenesis: Integrating the Complexity. *Int. J. Exp. Pathol.* 87 (3), 163–176. doi:10.1111/j.1365-2613.2006.00478.x

Iwano, S., Sugiyama, M., Hama, H., Watakabe, A., Hasegawa, N., Kuchimaru, T., et al. (2018). Single-cell Bioluminescence Imaging of Deep Tissue in Freely Moving Animals. *Science* 359, 935. doi:10.1126/science.aaq1067

Ji, X., Spencer, T., and Stephen, C. (2020). Bioluminescence Imaging in Mice with Synthetic Luciferin Analogues. *Science* 640, 165–183. doi:10.1016/bs.mie.2020.04.033

Kurebayashi, Y., Choyke, P. L., and Sato, N. (2021). Imaging of Cell-Based Therapy Using 89Zr-Oxine *Ex Vivo* Cell Labeling for Positron Emission Tomography. *Nanotheranostics* 5 (1), 27–35. doi:10.7150/ntno.51391

Liu, H., and Wu, D. (2016). *In Vivo* near-infrared Fluorescence Tumor Imaging Using DiR-Loaded Nanocarriers. *Curr Drug Deliv.* 13 (1), 40–48. doi:10.2174/1567201812666150703114908

Mamdani, H., Ahmed, S., Armstrong, S., Mok, T., and Jalal, S. I. (2017). Blood-based Tumor Biomarkers in Lung Cancer for Detection and Treatment. *Transl. Lung Cancer Res.* 6 (6), 648–660. doi:10.21037/tlcr.2017.09.03

Man, F., Lim, L., Volpe, A., Gabizon, A., Shmeeda, H., Draper, B., et al. (2019). *In Vivo* PET Tracking of 89Zr-Labeled Vγ9Vδ2 T Cells to Mouse Xenograft Breast Tumors Activated with Liposomal Alendronate. *Mol. Ther.* 27, 219–229. doi:10.1016/j.ymthe.2018.10.006

Matthews, N. H., Li, W. Q., Qureshi, A. A., Weinstock, M. A., and Cho, E. (2017). *Epidemiology of Melanoma Etiology and Therapy*. Editor Ward, W. H., and Farma, J. M. Brisbane (AU): Codon Publications. doi:10.15586/codon.cutaneousmelanoma.2017.ch1

McCarthy, C. E., White, J. M., Viola, N. T., and Gibson, H. M. (2020). *In Vivo* Imaging Technologies to Monitor the Immune System. *Front. Immunol.* 11, 1067. doi:10.3389/fimmu.2020.01067

Muthana, M., Rodrigues, S., Chen, Y.-Y., Welford, A., Hughes, R., Tazzyman, S., et al. (2013). Macrophage Delivery of an Oncolytic Virus Abolishes Tumor Regrowth and Metastasis after Chemotherapy or Irradiation. *Cancer Res.* 73 (732), 490–495. doi:10.1158/0008-5472.CAN-12-3056

Pieniazek, M., Matkowski, R., and Donizy, P. (2018). Macrophages in Skin Melanoma-The Key Element in Melanomagenesis (Review). *Oncol. Lett.* 15 (4), 5399–5404. doi:10.3892/ol.2018.8021

Ralli, M., Botticelli, A., Visconti, I. C., Angeletti, D., Fiore, M., Marchetti, P., et al. (2020). Immunotherapy in the Treatment of Metastatic Melanoma: Current Knowledge and Future Directions. *J. Immunol. Res.* 2020, 1–12. doi:10.1155/2020/9235638

Ritchie, D., Mileshkin, L., Wall, D., Bartholeyns, J., Thompson, M., Coverdale, J., et al. (2007). *In Vivo* tracking of Macrophage Activated Killer Cells to Sites of Metastatic Ovarian Carcinoma. *Cancer Immunol. Immunother.* 56, 155–163. doi:10.1007/s00262-006-0181-3

Shan, L. (2004). *Near-infrared Fluorescence 1,1-Dioctadecyl-3,3,3,3-Tetramethylindotricarbocyanine Iodide (DiR)-Labeled Macrophages for Cell Imaging. Molecular Imaging and Contrast Agent Database (MICAD). (US).* Bethesda (MD): National Center for Biotechnology Information.

Su, Y., Walker, J. R., Park, Y., Smith, T. P., Liu, L. X., Hall, M. P., et al. (2020). Novel NanoLuc Substrates Enable Bright Two-Population Bioluminescence Imaging in Animals. *Nat. Methods* 17, 852–860. doi:10.1038/s41592-020-0889-6

Uhara, H. (2019). Recent Advances in Therapeutic Strategies for Unresectable or Metastatic Melanoma and Real-World Data in Japan. *Int. J. Clin. Oncol.* 24 (12), 1508–1514. doi:10.1007/s10147-018-1246-y

Yang, K., Oak, A. S. W., Slominski, R. M., Brożyna, A. A., and Slominski, A. T. (2020). Current Molecular Markers of Melanoma and Treatment Targets. *Int. J. Mol. Sci.* 21 (10), 3535. doi:10.3390/ijms21103535

Yang, M., McKay, D., Pollard, J. W., and Lewis, C. E. (2018). Diverse Functions of Macrophages in Different Tumor Microenvironments. *Cancer Res.* 78 (19), 5492–5503. doi:10.1158/0008-5472.CAN-18-1367

Zambito, G., Chawda, C., and Mezzanotte, L. (2021). Emerging Tools for Bioluminescence Imaging. *Curr. Opin. Chem. Biol.* 63, 86–94. doi:10.1016/j.cbpa.2021.02.005

Zambito, G., Hall, M. P., Wood, M. G., Gaspar, N., Ridwan, Y., Stellari, F. F., et al. (2021). Red-shifted Click Beetle Luciferase Mutant Expands the Multicolor Bioluminescent Palette for Deep Tissue Imaging. *iScience* 24 (1), 101986. doi:10.1016/j.isci.2020.101986

Zambito, G., and Mezzanotte, L. (2021). Near-infrared Bioluminescence Imaging of Two Cell Populations in Living Mice. *STAR Protoc.* 2 (3), 100662. doi:10.1016/j.xpro.2021.100662

Conflict of Interest: The authors declare that the research was conducted in the absence of any commercial or financial relationships that could be construed as a potential conflict of interest.

Publisher's Note: All claims expressed in this article are solely those of the authors and do not necessarily represent those of their affiliated organizations, or those of the publisher, the editors and the reviewers. Any product that may be evaluated in this article, or claim that may be made by its manufacturer, is not guaranteed or endorsed by the publisher.

frontiers | Frontiers in Bioengineering and Biotechnology

TYPE Original Research
PUBLISHED 26 August 2022
DOI 10.3389/fbioe.2022.897272

OPEN ACCESS

EDITED BY
Vadim R. Viviani,
Federal University of São Carlos, Brazil

REVIEWED BY
Kiryl Piatkevich,
Westlake University, China
Dhermendra K. Tiwari,
Goa University, India

*CORRESPONDENCE
James A. H. Murray,
MurrayJAH@Cardiff.ac.uk,
ajathoul@bioflares.com

SPECIALTY SECTION
This article was submitted to Biomaterials, a section of the journal Frontiers in Bioengineering and Biotechnology

RECEIVED 15 March 2022
ACCEPTED 30 June 2022
PUBLISHED 26 August 2022

CITATION
Jathoul AP, Branchini BR, Anderson JC and Murray JAH (2022), A higher spectral range of beetle bioluminescence with infraluciferin. *Front. Bioeng. Biotechnol.* 10:897272. doi: 10.3389/fbioe.2022.897272

A higher spectral range of beetle bioluminescence with infraluciferin

Amit P. Jathoul[1,2], Bruce R. Branchini[3], James C. Anderson[4] and James A. H. Murray[1]*

[1]School of Biosciences, University of Cardiff, Cardiff, United Kingdom, [2]Bioflares Ltd., Trowbridge, Wiltshire, United Kingdom, [3]Hale Laboratory, Connecticut College, New London, CT, United States, [4]Department of Chemistry, University College London, London, United Kingdom

Coleopteran bioluminescence is unique in that beetle luciferases emit colors ranging between green (ca.550 nm) and red (ca.600 nm), including intermediate colors such as yellow and orange, allowing up to 3 simultaneous parameters to be resolved *in vitro* with natural luciferin (*D*-LH_2). Here, we report a more than doubling of the maximum bioluminescence wavelength range using a single synthetic substrate, infraluciferin (iLH_2). We report that different luciferases can emit colors ranging from visible green to near-infrared (nIR) with iLH_2, including in human cells. iLH_2 was designed for dual color far-red to nIR bioluminescence imaging (BLI) in small animals and has been utilized in different mouse models of cancer (including a metastatic hepatic model showing detailed hepatic morphology) and for robust dual parameter imaging *in vivo* (including in systemic hematological models). Here, we report the properties of different enzymes with iLH_2: Lampyrid wild-type (WT) *Photinus pyralis* (*Ppy*) firefly luciferase, *Ppy*-based derivatives previously engineered to be thermostable with *D*-LH_2, and also color-shifted Elaterid-based enzymes: blue-shifted *Pyrearinus termitilluminans* derivative Eluc (reported D-LH_2 λmax = 538 nm) and red-shifted *Pyrophorus plagiopthalamus* derivative click beetle red (CBR) luciferase (*D*-LH_2 λmax = 618 nm). As purified enzyme, in bacteria or in human cells, Eluc emitted green light (λmax = 536 nm) with *DL*-iLH_2 whereas *Ppy* Fluc (λmax = 689 nm), x2 Fluc (λmax = 704 nm), x5 Fluc (λmax = 694 nm), x11 Fluc (λmax = 694 nm) and CBR (λmax = 721 nm) produced far-red to nIR peak wavelengths. Therefore, with iLH_2, enzyme λmaxes can be separated by ca.185nm, giving almost non-overlapping spectra. This is the first report of single-substrate bioluminescence color emission ranging from visible green to nIR in cells and may help shed light on the color tuning mechanism of beetle luciferases. We also report on the reason for the improvement in activity of x11 Fluc with iLH_2 and engineer an improved infraluciferase (iluc) based on this mutant.

KEYWORDS

bioluminescence, green, near-infrared, multicolor, infraluciferin, luciferase, spectral range

1 Introduction

Beetle luciferases catalyze a reaction of beetle *D*-luciferin (*D*-LH_2), adenosine triphosphate (ATP), and oxygen to produce bright genetically encodable light of colors ranging from green to red (Viviani and Ohmiya, 2000; Nakajima et al., 2005). This widely studied reaction has numerous applications, including being used for molecular diagnostics (Kiddle et al., 2012) and BLI in biomedicine (Badr and Tannous, 2011), helping unravel mammalian molecular and cellular mechanisms or responses to therapies. However, applications in mammalian tissues are limited by the presence of oxy- and deoxy-hemoglobin (HbO_2 and Hb), which absorb light at <600 nm wavelengths (Liang et al., 2012)· (Li et al., 2009), complicating signal rendering and quantification of BLI and dual parameter BLI *in vivo* (Rice et al., 2001; Zhao et al., 2005; Rice and Contag, 2009). As mammalian tissues are relatively transparent to wavelengths of 650–1350 nm (the bio-optical window), to overcome these challenges, we previously described infraluciferin (iLH_2), a red-shifted analog of *D*-LH_2 (Figure 1) that can produce different far-red to nIR colors with different luciferases in the bio-optical window of mammalian tissues (Jathoul et al., 2014; Anderson et al., 2017; Stowe et al., 2019). In other words, wavelength shifts that were normally only observed with *D*-LH_2 were observed at longer wavelengths with iLH_2, demonstrating color tuning with a red-shifted analog. BLI in mice using *D*-iLH_2 methyl (Me) ester (or even *DL*-iLH_2 Me ester) with wild-type (WT) *Photinus pyralis* (*Ppy*) firefly luciferase (Fluc) and its thermostable/color derivatives previously allowed nIR BLI of detailed disease morphologies in small animal models of cancer (Jathoul et al., 2014) and allowed robust dual color imaging of T-cell effectors and cancer targets in a Chimeric Antigen Receptor (CAR) T-cell cancer therapy model *in vivo* (Stowe et al., 2019), showing its advantages for BLI compared to *D*-LH_2. However, pure WT *Ppy* Fluc enzyme produced much lower specific activity with *DL*-iLH_2 than with *D*-LH_2, by over 3-orders of magnitude at pH 7.8 (Anderson et al., 2019). x11 Fluc (Jathoul et al., 2012a) was found to be our most active mutant, approximately 7-fold brighter, and contained subsets of mutations previously engineered in Murray Lab (Figure 1). As there is a significant reduction of *in vivo* attenuation by Hb/HbO_2 using iLH_2, x11 Fluc and x11 Fluc color derivatives (Jathoul et al., 2012b) have proven efficient, and the single-substrate dual-parameter *in vivo* BLI approach made possible by iLH_2 is attractive owing to homogeneous *in vivo* pharmacokinetics and dynamics of the single substrate in simultaneous or consecutive acquisitions.

Here, we report some basic properties of beetle luciferases with *DL*-iLH_2, such as specific activities, kinetics, and pH dependence of activities and colors. We established some foundational aspects of *Ppy*-based Fluc activities and developed brighter infraluciferases (ilucs) based on the x11 Fluc scaffold. To better understand color shifting potential with *DL*-iLH_2, we also examined two of the most extremely color-shifted luciferases: Eluc, derived from *Pyrearinus termitiluminans* luciferase, is one of the most blue-shifted enzymes reported with *D*-LH_2 (λmax = 538 nm) (Neto et al., 2009)· (Nakajima et al., 2010) and click beetle red (CBR) luciferase, from *Pyrophorus plagiopthalamus* luciferase, one of the most red-shifted (*D*-LH_2 λmax = 618) (Miloud et al., 2007), close to the most red-shifted enzyme with *D*-LH_2 from *Phrixotrix hirtus* (PxRE, *D*-LH_2 λmax = 623) (Bevilaqua et al., 2019).

2 Results and discussion

2.1 Bioluminescence of beetle luciferase enzymes with luciferin and infraluciferin

2.1.1 Basic bioluminescence properties of beetle luciferases with infraluciferin

To test conditions in human cells appropriately, WT Fluc, x2 Fluc, x5 Fluc, x11 Fluc, Eluc, and CBR enzymes were purified to measure their basic properties with substrates. We utilized *DL*-iLH_2

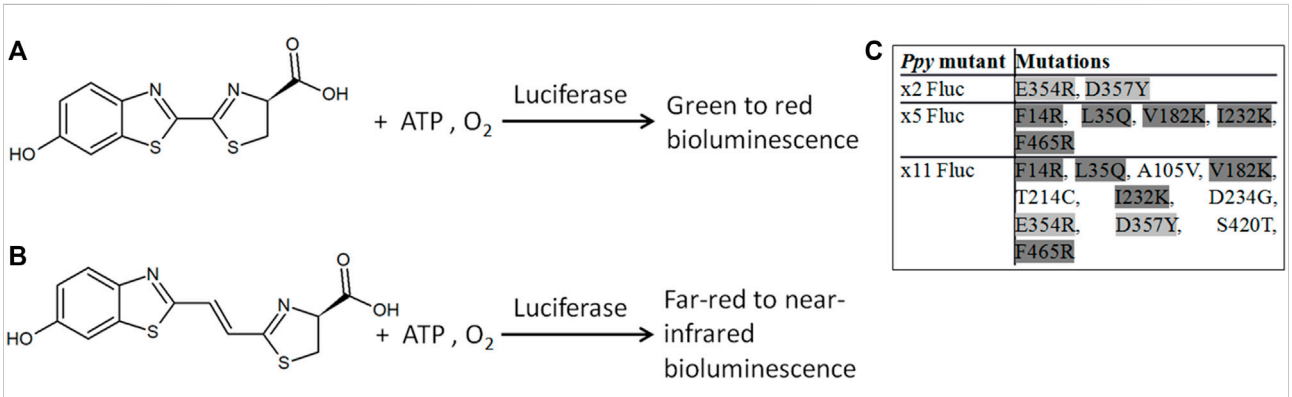

C

Ppy mutant	Mutations
x2 Fluc	E354R, D357Y
x5 Fluc	F14R, L35Q, V182K, I232K, F465R
x11 Fluc	F14R, L35Q, A105V, V182K, T214C, I232K, D234G, E354R, D357Y, S420T, F465R

FIGURE 1
Bioluminescence reactions of beetle luciferases. Bioluminescence with *D*-LH_2 **(A)** and *D*-iLH_2 **(B)** (4S)-2-[(E)-2-(6-hydroxy-1,3-benzothiazol-2-yl)ethenyl]-4,5-dihydro-1,3-thiazole-4-carboxylic acid; ATP: adenosine triphosphate. **(C)** Inset table of different subsets of mutations in thermostable mutants of *Ppy* Fluc: x2 Fluc (Willey et al., 2001), x5 Fluc (Law et al., 2006), and x11 Fluc (Jathoul et al., 2012a).

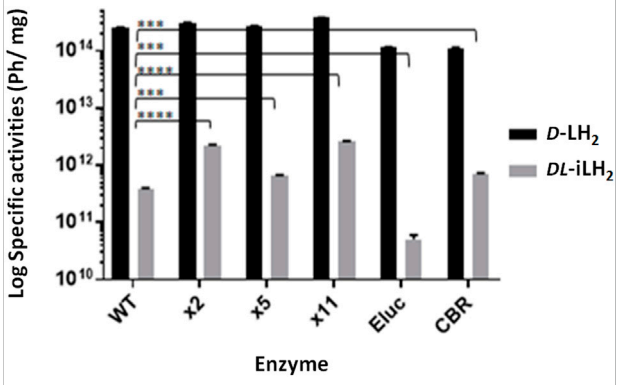

FIGURE 2
Specific activities of WT *Ppy* Fluc, thermostable *Ppy*-based Fluc mutants, Eluc, and CBR with *DL*-iLH$_2$. Specific activity of 0.16 µM enzymes at pH 7.3 in PEM buffer, 200 µM *D*-LH$_2$ or *DL*-iLH$_2$ and 2 mM ATP, and emission was captured for 3 min through the open filter in the PIO. *p*-values for *t*-test of activity with *DL*-iLH$_2$ between WT Fluc and x2 (>0.0001), x5 (0.0003), x11 (>0.0001), Eluc (0.0001), and CBR (0.0002).

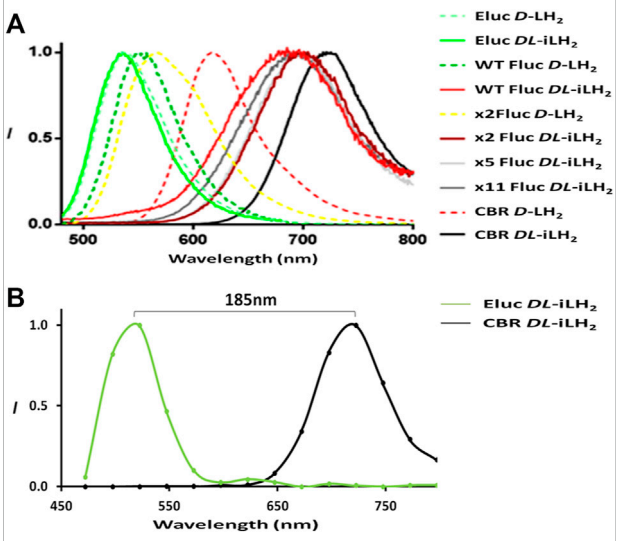

FIGURE 3
Expanded bioluminescence spectral range with infraluciferin. **(A)** Bioluminescence spectra of different luciferases with *D*-LH$_2$ and *DL*-iLH$_2$: 5 µM enzymes were assayed with 200 µM luciferins and 2 mM ATP, and light was captured using the Clariostar instrument. For ease of visualization, x5 and x11 Fluc spectra with *D*-LH$_2$ are omitted but are near identical to WT Fluc (Reference, Table 1). **(B)** Illustration of spectral separation between Eluc and CBR with *DL*-iLH$_2$ measured in the PIO with 0.5 µM enzymes (details as in Supplementary Figure S5).

free acid for enzyme work and its carboxy-methyl ester for cell work. The use of the racemic mix was for ease of synthesis, as reported for the development of other red-shifted luciferin analogs (Miura et al., 2013). Similar to that case, we expected that light yields could be in the order of 2–3-times lower than with an enantiopure *D*-iLH$_2$. Flash kinetics of enzymes were similar with both *D*-LH$_2$ and *DL*-iLH$_2$ (Supplementary Figure S1A–C), suggesting that adenylation of *DL*-iLH$_2$ proceeds effectively, but oxidation is less efficient. We could not measure Km for *DL*-iLH$_2$ due to the presence of the inhibitory *L*-form. Kms for ATP in the presence of *DL*-iLH$_2$ (ATP$_{(iLH2)}$) are significant to imaging in cells (Branchini et al., 2015) and were found to be in the range of 200–300 µM for all enzymes (Supplementary Table S1). pH dependence of activity measurements with *DL*-iLH$_2$ showed that Eluc, WT *Ppy*, x2, and x5 Flucs had optimal activity in the region of pH 6.6, while x11 Fluc was at pH 7.8, and CBR had a lower pH optimum of pH 5.6 (Supplementary Figure S2).

2.1.2 Activity of beetle luciferases and thermostable mutants with luciferin and infraluciferin

2.1.2.1 Enzyme-specific activities at physiological pH, effect of substrate concentration, coenzyme A and hemoglobin attenuation on specific activity

Since *DL*-iLH$_2$ is for use in cells and animals, we compared the specific activities of pure enzymes at close to physiological pH (7.3) (Figure 2). With 200 µM *DL*-iLH$_2$ at pH 7.3, Eluc, WT Fluc, x5 Fluc, and CBR produced 0.02, 0.15, 0.26, and 0.28% of the specific activity of WT Fluc with *D*-LH$_2$. In comparison, x2 and x11 Flucs produced 6–7-fold enhanced activity of 0.88 and 1.04%, indicating mutations E354R and/or D357Y are responsible for enhancement. Overall, x11 Fluc was the most active enzyme with *DL*-iLH$_2$, maintaining linear emission kinetics and also 5-times higher activity when expressed in *E. coli* (Supplementary Figure S3). Reactions of x2, x5 Flucs, and Eluc were inhibited by increasing concentrations of substrate, possibly due to *L*-iLH$_2$ (da Silva and da Silva, 2011). At lower concentrations of *DL*-iLH$_2$ (1.5–15 µM), the activity of Eluc was markedly increased to the level of x11 Fluc (Supplementary Figure S4A). Coenzyme A (CoA) improves the activity of Fluc with *D*-LH$_2$ (Fraga et al., 2005) and, in an analogous fashion, CoA increased the maximum level of emission 2–5-fold and reduced signal decay of enzymes with *DL*-iLH$_2$, with the exception of Eluc, with which CoA reduced activity (Supplementary Figure S4A and B). To account for signal augmentation *in vivo*, we simulated the effect of Hb attenuation with a 1 cm thick agarose phantom containing 50% whole equine blood (Hb concentration estimated by spectrometry to be 0.55 mM) (Supplementary Figure S4C). Through blood, the integrated light emission from WT, x2, x5, or x11 Flucs was attenuated more than 100-fold with *D*-LH$_2$ but less than 10-fold with *DL*-iLH$_2$.

2.1.2 An expanded spectral range of beetle bioluminescence with infraluciferin

To examine the emission colors of enzymes with *DL*-iLH$_2$, bioluminescence spectra (Figure 3A) were acquired using a Clariostar multimeter (Clariostar, BMG Labtech, Ortenburg,

TABLE 1 Bioluminescence spectral λmax and full-width half maxima. Data were acquired using the Clariostar instrument. Experimental details are as shown in Figure 3A.

Enzyme	Substrate			
	D-LH_2		*DL*-iLH_2	
	λmax (nm)	FWHM (nm)	λmax (nm)	FWHM (nm)
Eluc	536	71	536	67
WT Fluc	554	68	685	121
x2 Fluc	566	92	704	107
x5 Fluc	557	75	694	104
x11 Fluc	557	75	694	115
CBR	618	74	721	88

Germany) fitted with a detector module with improved sensitivity to nIR wavelengths and in the PhotonIMAGER Optima (PIO, Biospace Labs, Paris, France) small animal imager (Supplementary Figure S5). Bioluminescence spectra λmax values for WT, x2, x5, and x11 Flucs with *DL*-iLH_2 were 685, 704, 694, and 694 nm, respectively (Table 1), which 131, 138, 137 and 137 nm shifted compared to their λmaxes with *D*-LH_2. Full width half maximum (FWHM) values of most enzymes were larger with *DL*-iLH_2 than with *D*-LH_2, indicating room for improvement for spectral specificities. Remarkably the emission color of Eluc with *DL*-iLH_2 was green (from *E. coli* or as purified protein, λmax = 536 nm), and CBR was nIR (λmax = 721 nm), with similar or narrower spectra than with *D*-LH_2. These click beetle enzymes are extremely blue- and red-shifted and pH-independent in terms of color with *D*-LH_2 (Viviani, 2002). However, with *DL*-iLH_2, they produced almost mutually exclusively spectra with a 185 nm peak separation between them (Figure 3B). Therefore, bioluminescence with *DL*-iLH_2 can range in emission color from the visible to the nIR. This effect has the potential to benefit academia in the future and to multicolor BLI in the absence of Hb. Eluc produced a much smaller secondary nIR peak (ca.700 nm), giving an overall 7.5% overlap between normalized spectra of Eluc and CBR with *DL*-iLH_2 measured in the PIO, as opposed to 28% with *D*-LH_2, which was previously one of the largest spectral separations achievable with *D*-LH_2. Green emission was recently reported from enzymes CBG99 and CBG99opt (λmax = 545 nm) with near-infrared emitting naphthyl amino-luciferin (NH2-NpLH2) (Zambito et al., 2020); however, the supplementary supporting bioluminescence spectra provided for that study show that these enzymes are red for CBG99 (λmax = ca.600 nm) and far-red for CBG99opt (λmax = ca.650 nm) with NH2-NpLH2 (Zambito et al., 2020) in human embryonic kidney (HEK) cells. pH dependence of bioluminescence spectra of *Ppy*-based Flucs with *DL*-iLH_2 mirrored the classical effects typically obtained with Flucs and *D*-LH_2 (Supplementary Figure S6, S7): WT Fluc displayed a classic bathochromic shift (Tisi et al., 2002) at lower pH values with *DL*-iLH_2; Eluc had pH-independent color with *DL*-iLH_2; CBR displayed a small reciprocal hypsochromic shift at low pH.

Despite Eluc having a low activity with *DL*-iLH_2, we were confident that this was due to a low rate of oxidation and that the effect was not due to the chemiluminescence of free infraluciferyl adenylate initiated by Eluc. The spectral shape of the green emission was very similar to the narrow spectrum of Eluc with *D*-LH_2. The activity of Eluc with *DL*-iLH_2 was dependent on enzyme concentration, though the green spectrum did not vary with enzyme concentration (Figure 3). Chemiluminescence of *DL*-iLH_2 Me ester initiated using 1M potassium tert-butoxide (t-BuOK) (Miura et al., 2013) was seen to emit broadly in the visible between green and red depending on the buffer, and its shape differed entirely from that of Eluc (Supplementary Figure S8). This result has ramifications for the color tuning mechanism of beetle luciferases (Branchini et al., 2017) (Supplementary Figure S9).

2.2 Engineering brighter enzymes with infraluciferin

2.2.1 WT *Ppy* Fluc mutation E354R improves activity with *DL*-iLH_2 and D357Y red-shifts emission

To examine the reasons for the relatively higher activities of x2 and x11 Flucs with *DL*-iLH_2 over WT *Ppy* Fluc, the mutations E354R and D357Y, located in a solvent-exposed omega-loop (Ω-loop) (Halliwell et al., 2018), (Conti et al., 1996) were individually constructed in WT Fluc. Mutations (Willey et al., 2001), insertions (Tafreshi et al., 2007), and deletions (Halliwell et al., 2018) in the Ω-loop affect properties such as thermostability and color with *D*-LH_2 by altering H-bond

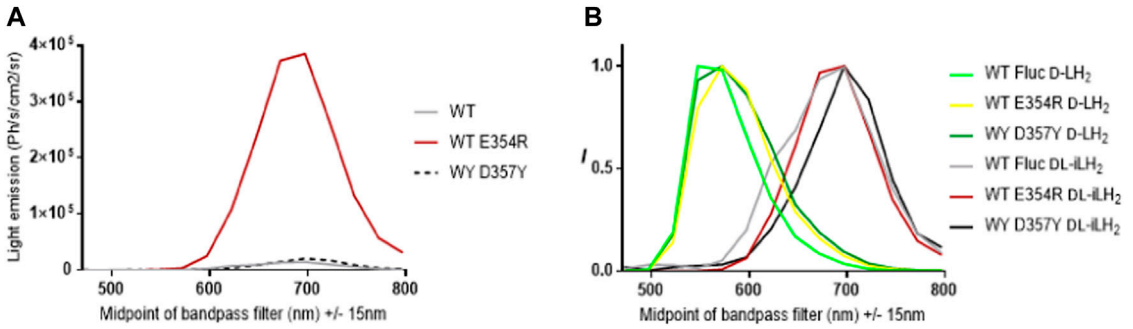

FIGURE 4
Effect of Fluc mutations E354R and D357Y on activity and color with *DL*-iLH$_2$. **(A)** Quantitative bioluminescence spectra showing that E354R leads to significant improvement in activity with *DL*-iLH$_2$. **(B)** Normalized bioluminescence spectra of WT *Ppy* Fluc, E354R, and D357Y with *D*-LH$_2$ and *DL*-iLH$_2$.

networks which link adjacent surface loops to enclose the active site in the region that coordinates the 6-hydroxyl of *D*-LH$_2$. Deletions in the Ω-loop can also affect substrate specificity with *DL*-iLH$_2$ (Halliwell et al., 2018). In the *Ppy* Fluc structure with 5′-O-[N-(dehydroluciferyl)-sulfamoyl] adenosine (DLSA) bound (4G36.pdb) (Sundlov et al., 2012), E354 H-bonds to H310, and E311 H-bonds to nearby loop residue R337. This network has been implicated in the stabilization of the hydrophobic active site and providing a counterion for LO phenolate (Viviani et al., 2016). We found that E354R alone in WT Fluc was sufficient to cause an average 3.3-fold improvement in activity with *DL*-iLH$_2$ through an open filter on the PIO (Figure 4). Mutation D357Y did not affect activity but red-shifted emission color and double mutant x2 Fluc displayed both effects of improved activity and red-shift. No further improvement was found by screening random mutations at both positions in WT Fluc, and the addition of E354R/D357Y to x5 Fluc only marginally improved activity. Some hints to a mechanism were gained by *in silico* docking (Goodsell and Olson, 1990), suggesting that improved iLH$_2$ coordination enhances the light yield of WT Fluc E354R (Berraud-Pache and Naviet, 2016) (Reference Supplementary Figure S10 and S11).

2.2.2 x11 Fluc R354H/Y357A displays enhanced activity specifically with *DL*-iLH$_2$

Since the activity of x11 Fluc with *DL*-iLH$_2$ was affected by the conformation of the Ω-loop, we randomly mutated both positions singly and together in x11 Fluc and improvements in activity were observed in double mutant screens (Figure 5). Basic and polar residues enhanced activity at position 354, but this depended on the identity of residue 357, at which less polarity appeared favorable. We isolated significantly brighter x11 Fluc mutants, E354H/D357A, E354Q/D357S, and E354S/D357P, with 3-, 2-, and 2.5-fold higher activities than x11 Fluc, respectively. The improved activity of mutant x11 Fluc R354H/Y357A was confirmed separately in the laboratory of the second co-author. However, it was less active than x11 Fluc with *D*-LH$_2$, so we termed this mutant infraluciferase 1 (iluc1). Pure iluc1 proved to be up to 17-fold brighter than WT Fluc with *DL*-iLH$_2$ and with a small blue-shift in emission compared to WT Fluc and x11 Fluc (Supplementary Figure S12A–C). The pH dependence of specific activity showed that iluc1 had optimum pH at 7.4, compared to 7.8 for x11 Fluc, but the pH affected the emission color of iluc1 more than x11 Fluc, and it displayed a slightly larger bathochromic shift at low pH and reciprocal hypsochromic shift at higher pH with diminution of activity at pH 9.8 (Supplementary Figure S12D–F). The kinetics of iluc1 showed a slightly higher decay than x11 Fluc (Supplementary Figure S12G). Iluc1 proved to be 20-fold brighter than WT Fluc with *DL*-iLH$_2$ in *E. coli* BL21 cells (Supplementary Figure S12H).

2.3 Properties of iluc1 and color-shifted iluc1 derivatives in human embryonic kidney 293 cells

Human codon-optimized Eluc, WT Fluc, x11 Fluc, iluc1, and CBR were purchased as gblocks (IDT DNA, IA, United States) and cloned using AfeI/XbaI into a lentiviral vector pCCL (Dull et al., 1998) co-expressing EGFP downstream of an internal ribosome entry site (IRES). Vectors encoding different mutants were transfected into human embryonic kidney (HEK) cells and, after 48 h, were imaged for EGFP, followed by BLI by addition of either 1 mM *D*-LH$_2$ potassium salt (Regis Tech, IL, United States) or 1 mM *DL*-iLH$_2$ Me ester both in phosphate-buffered saline (PBS) onto whole cells with culture medium (containing phenol red) removed. BLI signals were EGFP normalized to account for transfection efficiencies, and no bioluminescence was detected from any non-transfected

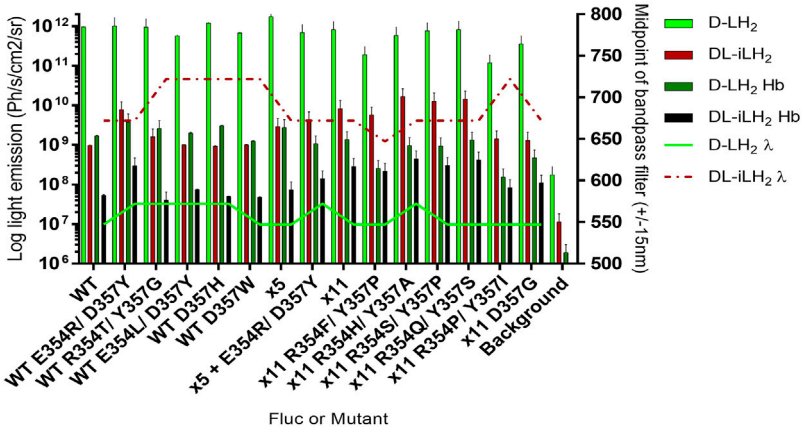

FIGURE 5
Activity of purified Flucs and mutants with both substrates. Specific activity and emission peak wavelengths of selected R354 and/or D357 mutants of WT, x5, and x11 Flucs. 150μM *D*-LH_2 or 15 μM *DL*-iLH_2 and 2 mM ATP were used to saturate 0.167 and 0.0167 μM Flucs, respectively, and light emission was captured using the PIO. The assay was then repeated with the blood phantom.

control cells with either substrate. Eluc and WT *Ppy* Fluc gave 0.17 and 0.2% total integrated light emission with *DL*-iLH_2 compared to WT Fluc with *D*-LH_2, whereas with x11 Fluc and iluc1 gave 1.8 and 3.1%, respectively (Figure 6A and Supplementary Figure S13). Eluc activity was weak and did not improve at lower concentrations (100 μM) of *DL*-iLH_2 ester. Though the green peak was stable in HEK cells, the secondary unstable nIR peak (peaking in the 697 nm +/− 15 nm filter) was observed in some measurements. Iluc1 dual color mutants were constructed by the introduction of mutations V241I, G246A, and F250S to blue-shift and S284T to red-shift spectra (Branchini et al., 2007). x11 Fluc is relatively refractory to classic red-shifting mutation S284T, requiring the additional substitution R354I ("x11 red2", or "FLuc_red") (Jathoul et al., 2012b; Stowe et al., 2019) to stabilize red-shift (Willey et al., 2001) for dual imaging with V245I/G246S/F250S ("x11 green", or "FLuc_green"). In iluc1, however, the addition of S284T alone produced a stable red-shifted variant (ilucR) almost identical in spectrum to x11 red2 (Supplementary Figure S14). The addition of S284T to a bright x11 Fluc Ω-loop deletion mutant (ΔP359) (Halliwell et al., 2018) also produced a bright red-shifted mutant, x11 S284T/ΔP359, and these gave 2.3 and 2.4% of activity with *DL*-iLH_2 compared to WT Fluc with *D*-LH_2, respectively. To blue-shift iluc1, double mutant V2451/G246S (ilucG1), single mutant F250S (ilucG2) and triple mutant V2451/G246S/F250S (ilucG3) were constructed, giving 1, 3.6, and 1.7% of activity with *DL*-iLH_2 compared to WT Fluc with *D*-LH_2, respectively. All these produced blue-shifted spectra compared to iluc1. CBR was the most red-shifted variant tested (peaking in the 722 nm filter) (Supplementary Figure S15) but was relatively dim compared to red-shifted ilucs with *DL*-iLH_2 (0.2%) and, thus, not further examined.

2.4 Dual-cell type unmixing with infraluciferin in human embryonic kidney 293 cells

To test the ability to simultaneously image and resolve HEK 293 cells *in vitro* expressing the different colored iluc mutants from each other with *DL*-iLH_2, potential dual color pairings ilucG2/x11 S284T ΔP359 and ilucG3/ilucR were compared in HEK cell unmixing experiments. 1.5×10^6 HEK 293 cells were plated in a 48-well format and transfected after 24 h with mixes (0, 25, 50, 75, and 100%) lentiviral vectors, encoding either of the dual far-red to nIR pairs and after 24 h were imaged by the addition of either *D*-LH_2 or *DL*-iLH_2. The brightest pairing, ilucG2 and x11 S284T ΔP359, was not found to be separable due to variation in an unstable spectrum of ilucG2; however, ilucG3 and ilucR spectra were stable and increasing amounts of cells (ca.7800-31,250) in mixes could be imaged in separate far-red to nIR band-pass filters in the PIO with *DL*-iLH_2 (Figures 7A and B).

3 Concluding remarks

We report an unexpected finding that the bioluminescence of Eluc with *DL*-iLH_2 is in the visible region (green) and that pairing it with other enzymes produces unprecedentedly large single-substrate bioluminescence wavelength separations. Thus, synthetic bioluminescence using *DL*-iLH_2 has more than double the possible spectral range of natural firefly bioluminescence without the requirement for resonance energy transfer acceptors. This basic discovery could have ramifications in academia in terms of the color tuning

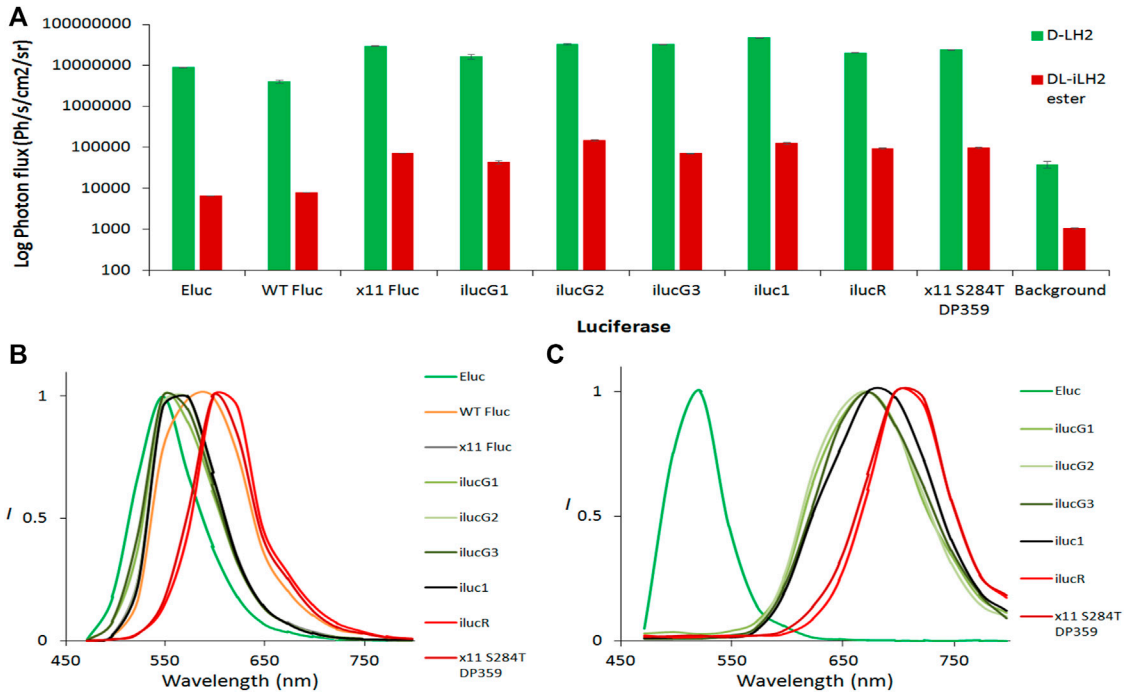

FIGURE 6
Bioluminescence yields and spectra from transfected HEK 293 cells. **(A)** EGFP normalized light yields from whole HEK cells. 1mM *D*-LH_2 K^+ salt or *DL*-iLH_2 Me ester was added to initiate luminescence, and emission was captured over 5 min at 30°C in the PIO (Biospace Labs, Paris, France). Emission with both substrates was observed to take approximately 1 min to reach a plateau, and light yields given were from 1 min after addition of substrates. Background signals were obtained from triplicate ROIs placed in areas of images containing no wells. **(B)** Normalized bioluminescence spectra obtained from whole transfected HEK cells expressing different variants with **(B)** *D*-LH_2 and **(C)** *DL*-iLH_2 Me ester imaged in the PIO.

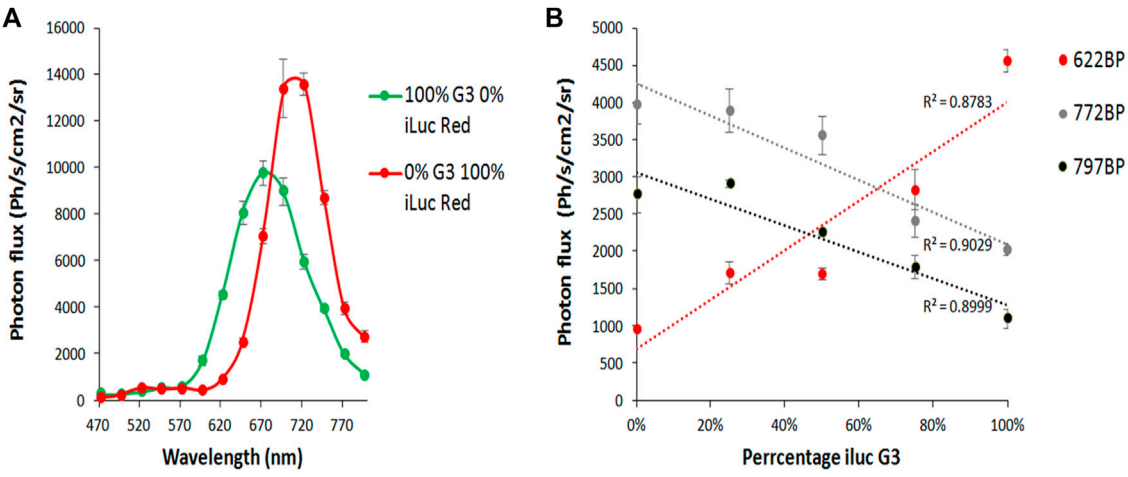

FIGURE 7
Imaging and unmixing HEK 293 cells expressing dual mixes of iLucG3 and iLucR. Substrates were dispensed with a multiwell pipette and, after 5 min, were imaged in successive filters on the PIO (622, 722, and 797 nm band-passes (BP)). Regions of interest were analyzed for photon flux at different wavelengths using the M3 Vision software. **(A)** Quantitative bioluminescence spectra from variants. **(B)** Increasing percentage of iLucG3 imaged through 622, 722 and 797BP filters.

mechanism of beetle luciferases and in bioimaging with the engineering of enzymes that are brighter at visible wavelengths, and enzymes with emission colors intermediate between green and far-red. We have identified enzymes with improved activity, good color stability, and emission kinetics with *DL*-iLH$_2$, which could be useful as first-generation infraluciferases (ilucs) for use in dual *in vivo* imaging and continue to test and engineer new generation ilucs for potential application to simultaneous single-substrate multiparametric BLI in the future.

3.1 Contribution to the field statement

Synthetic bioluminescence with infraluciferin has advantageous properties over naturally evolved bioluminescence for applications in bioimaging. With an extended spectral range, in the future, enzymes may be engineered with high activity emissions ranging from the green to the nIR and improve the amount of biological information that can be imaged simultaneously from living systems.

4 Materials and methods

4.1 Synthesis of luciferins and luciferin source

D-luciferin potassium salt was purchased from Regis Technologies (CA, United States). The free acid and methyl ester of *DL*-infraluciferin were synthesized as described within the literature (Anderson et al., 2017) and prepared by first dissolving them to 10 mg/ml in DMSO and then further in a relevant buffer.

4.2 Vectors, cloning, over-expression, and purification of enzymes

Vectors encoding WT, x2, x5, and x11 Flucs in pET16b were prepared in previous work. 10X-N-terminal His-tagged Eluc and CBR were amplified from pLR6-Eluc (GenBank KU756582.1), provided kindly by Mikhail Koksharov (Brown University, United States), or pGex-CBR plasmids, respectively, and cloned into the pET16b with NcoI and BamHI. These were transformed into *E. coli* BL21 (DE3) pLysS cells (Agilent Technologies, CA, United States) and over-expressed and purified by nickel-NTA affinity chromatography as described previously (Law et al., 2006; Jathoul et al., 2012a). The pCCL vector 305 was kindly provided by Prof. Riccardo Brambilla (Cardiff University, Cardiff, United Kingdom) under MTA.

4.3 Construction of random mutants at positions E354 and D357 by overlap extension mutagenesis

Overlap extension was used to introduce mutations into Flucs by site-directed random mutagenesis since this method gives added versatility when introducing simultaneous mutations at different sites. To construct random mutations at E354 and D357, first, a fragment of ca.1070 bp was amplified from pET16b x2 Fluc using outer primer pETPpyFor (AGGTCGTCATATGGAAGACGCCAAAA) and overlap primer RYrRev (GACCGCGCCCGGTTTNNNATCCCCNNNGGGTGTAATCAGAATAG). Another ca.580 bp fragment was amplified separately amplified using overlap primer RYrFor (CTATTCTGATTACACCCNNNGGGGATNNNAAACCGGGCGCGGTC) and outer primer pETPpyRev (GCAGCCGGATCCAGTTACATTTTACA). Each fragment was gel purified, and they were fused together by PCR using outer primers pETPpyFor and Rev to produce a single band of ca.1500bp, which was further extracted and digested with NdeI and BamHI before subcloning into pET16b. Luminescent colonies were identified by spraying with 60 μM DL-iLH$_2$ in 0.1M citrate buffer (pH 5) and being imaged for 1 min in the PIO and were verified by sequencing.

4.4 Measurement of specific activity, coenzyme A assays, and flash kinetics

For specific activity, each enzyme was prepared in chilled PEM (1x PBS, 2 mM ethylenediaminetetraacetic acid (EDTA) and 10 mM magnesium sulphate ($MgSO_4$), pH 7.3) or TEM buffer (100 mM Tris-acetate, 2 mM ethylenediaminetetraacetic acid (EDTA) and 10 mM magnesium sulphate ($MgSO_4$), pH 7.8) and 200 μM *D*-LH$_2$ or 60 μM *DL*-iLH$_2$ and 2 mM ATP at pH 7.8 were used to saturate reactions. Measurements were captured with or without band-pass filters in the PIO 1 min after addition of substrates, for periods of up to 1 h at 28–30°C. Flash kinetics were measured with both substrates by dispensing 2 mM ATP onto 0.167 μM enzymes with 200 μM *D*-LH$_2$ or 60 mM iLH$_2$ and adjusting PMT gain values to 1,500 v for *D*-LH$_2$ and 4,095 v for *DL*-iLH$_2$. To test the effect of coenzyme A (CoA), 200 μM was also supplemented into experiments. To construct the Hb phantom, 50% whole equine blood in 1% agarose was allowed to set in a 150 mm square Petri dish, and 96-well plates containing samples were overlaid with this to test the effect of filtering of emission by blood.

4.5 pH dependence of bioluminescence spectra

Bioluminescent spectra were captured using both the PIO and Clariostar multimeter (BMG Labtech, Ortenburg, Germany).

For measurements at differing pH values, TEM buffer was adjusted to different pH values using acetic acid or sodium hydroxide, and these were used to prepare both substrates and enzymes.

4.6 Kinetics assays: measurement of K_m for ATP

For ATP K_m measurements, light emission was measured when substrate concentrations of ATP were varied between 1 μM and 2 mM in the presence of either saturating *D*-LH_2 or *DL*-iLH_2, respectively. Data were plotted using the Hanes–Woolf plot to derive K_m and k_{cat} values (obtained with a BMG Fluostar PMT gain of 4,095 v).

4.7 Chemiluminescence of infraluciferin Me ester

To initiate chemiluminescence, 50 μl of 10 mg/ml iLH_2 Me ester was added to 200 μl 2M t-BuOK in TEM buffer or 5 μl of ester was added to 50 μl 1M t-BuOK in DMSO and light emission was integrated over 1 min using different band pass filters in the PIO.

4.8 HEK cell transfection, transduction, and imaging

HEK cells were plated at the density of 1.5×10^6 cells per plate in a 6-well dish. The following day, wells were transfected with 500 ng pCCL vectors encoding Flucs using 3 μl of GeneJuice transfection reagent (Novagen, WI, United States) and imaged after 48h for EGFP expression using an excitation wavelength of 487 nm and acquisition with a 547 nm (+/−15 nm) filter, and subtraction of the subsequent image taken with an excitation value of 412 nm. BLI was then acquired for 5 min after dispensing substrates on cells using a multiwell pipette.

Data availability statement

The original contributions presented in the study are included in the article/Supplementary Material; further inquiries can be directed to the corresponding author. Data and materials will be made available in line with UKRI policies.

Author contributions

APJ/BB carried out experiments planned with other authors.

Funding

BB was funded by the Air Force Office of Scientific Research, Grant number FA9550-18-1-0017, United States. This work was partly funded by BBSRC grant BB/L022346/1 to JM. APJ was funded by the Welsh Government for a Ser Cymru II Award (80762-CU-063) and JCA was funded by the University College London.

Acknowledgments

The authors acknowledge Mikhail Koksharov (Brown University, United States) for providing Eluc pDNA and helpful discussions. The authors also acknowledge George Roberts (a graduate of Cardiff University) for carrying out mutagenesis of Eluc at position F243. APJ and JCA are inventors of infra-luciferin, listed on patent EP2981527 A1.

Conflict of interest

APJ was employed by Bioflares Ltd.

The remaining authors declare that the research was conducted in the absence of any commercial or financial relationships that could be construed as a potential conflict of interest.

Publisher's note

Supplementary material

The Supplementary Material for this article can be found online at: https://www.frontiersin.org/articles/10.3389/fbioe.2022.897272/full#supplementary-material

References

Anderson, J. C., Chang, C. H., Jathoul, A. P., and Syed, A. J. (2019). Synthesis and bioluminescence of electronically modified and rotationally restricted colour-shifting infraluciferin analogues. *Tetrahedron* 75, 347–356. doi:10.1016/j.tet.2018.11.061

Anderson, J. C., Grounds, H., Jathoul, A. P., Murray, J. A. H., Pacman, S. J., and Tisi, L. C. (2017). Convergent synthesis and optical properties of near-infrared emitting bioluminescent infra-luciferins. *RSC Adv.* 7, 3975–3982. doi:10.1039/c6ra19541e

Badr, C. E., and Tannous, B. A. (2011). Bioluminescence imaging: progress and applications. *Trends Biotechnol.* 29, 624–633. doi:10.1016/j.tibtech.2011.06.010

Berraud-Pache, R., and Naviet, I. (2016). QM/MM calculations on a newly synthesised oxyluciferin substrate: new insights into the conformational effect. *Phys. Chem. Chem. Phys.* 18, 27460–27467. doi:10.1039/c6cp02585d

Bevilaqua, V. R., Matsuhashi, T., Oliveira, G., Oliveira, P. S. L., Hirano, T., and Viviani, V. R. (2019). Phrixotrix luciferase and 6'-aminoluciferins reveal a larger luciferin phenolate binding site and provide novel far-red combinations for bioimaging purposes. *Sci. Rep.* 9, 8998. doi:10.1038/s41598-019-44534-3

Branchini, B. R., Ablamsky, D. M., Murtiashaw, M. H., Uzasci, L., Fraga, H., and Southworth, T. L. (2007). Thermostable red and green light-producing firefly luciferase mutants for bioluminescent reporter applications. *Anal. Biochem.* 361, 253–262. doi:10.1016/j.ab.2006.10.043

Branchini, B. R., Southworth, T. L., Fontaine, D. M., Murtiashaw, M. H., McGurk, A., Talukder, M. H., et al. (2017). Cloning of the orange light-producing luciferase from *Photinus scintillans* - a new proposal on how bioluminescence color is determined. *Photochem. Photobiol.* 93, 479–485. doi:10.1111/php.12671

Branchini, B. R., Southworth, T. L., Fontaine, D. M., Kohrt, D., Talukder, M., Michelini, E., et al. (2015). An enhanced chimeric firefly luciferase-inspired enzyme for ATP detection and bioluminescence reporter and imaging applications. *Anal. Biochem.* 484, 148–153. doi:10.1016/j.ab.2015.05.020

Conti, E., Franks, N. P., and Brick, P. (1996). Crystal structure of firefly luciferase throws light on a superfamily of adenylate-forming enzymes. *Structure* 4, 287–298. doi:10.1016/s0969-2126(96)00033-0

da Silva, L. P., and da Silva, J. C. (2011). Kinetics of inhibition of firefly luciferase by dehydroluciferyl-coenzyme A, dehydroluciferin and L-luciferin. *Photochem. Photobiol. Sci.* 10, 1039–1045. doi:10.1039/c0pp00379d

Dull, T., Zufferey, R., Kelly, M., Mandel, R. J., Nguyen, M., Trono, D., et al. (1998). A third-generation lentivirus vector with a conditional packaging system. *J. Virol.* 72, 8463–8471. doi:10.1128/jvi.72.11.8463-8471.1998

Fraga, H., Fernandes, D., Fontes, R., and da Silva, J. C. (2005). Coenzyme A affects firefly luciferase luminescence because it acts as a substrate and not as an allosteric effector. *FEBS J.* 272, 5206–5216. doi:10.1111/j.1742-4658.2005.04895.x

Goodsell, D. S., and Olson, A. J. (1990). Automated docking of substrates to proteins by simulated annealing. *Proteins.* 8, 195–202. doi:10.1002/prot.340080302

Halliwell, L. M., Jathoul, A. P., Bate, J. P., Worthy, H. L., Anderson, J. C., Jones, D. D., et al. (2018). ΔFlucs: brighter *Photinus pyralis* firefly luciferases identified by surveying consecutive single amino acid substitutions in a thermostable variant. *Biotechnol. Bioeng.* 115, 50–59. doi:10.1002/bit.26451

Jathoul, A., Law, E., Gandelman, O., Pule, M., Tisi, L., and Murray, J. (2012). "Development of a pH-tolerant thermostable *photinus pyralis* luciferase for brighter *in vivo* imaging," in *Bioluminescence - recent advances in oceanic measurements and laboratory applications*. Editor D. Lapota (London: IntechOpen).

Jathoul, A. P., Grounds, H., Anderson, J. C., and Pule, M. A. (2014). A dual-color far-red to near-infrared firefly luciferin analogue designed for multiparametric bioluminescence imaging. *Angew. Chem. Int. Ed. Engl.* 53, 13275–13279. doi:10.1002/ange.201405955

Jathoul, A. P., Thomas, S., Philip, B., and Pule, M. A. (2012). "Characteisation of a bright and thermostable rainbow of firefly luciferases: enhanced tools for *in vivo* bioluminescence imaging," in *World molecular imaging conference poster session* (Dublin, Ireland, UK. https://wmis.org/abstracts/2012/data/papers/P297.html.

Kiddle, G., Hardinge, P., Buttigieg, N., Gandelman, O., Pereira, C., McElgunn, C. J., et al. (2012). GMO detection using a bioluminescent real time reporter (BART) of loop mediated isothermal amplification (LAMP) suitable for field use. *BMC Biotechnol.* 12, 15. doi:10.1186/1472-6750-12-15

Law, G. H. E., Gandelman, O. A., Tisi, L. C., Lowe, C. R., and Murray, J. A. H. (2006). Mutagenesis of solvent exposed amino acids in Photinus pyralis luciferase improves thermostability and pH-tolerance. *Biochem. J.* 397, 305–312. doi:10.1042/bj20051847

Li, X., Nakajima, Y., Niwa, K., Viviani, V. R., and Ohmiya, Y. (2009). Enhanced red-emitting railroad worm luciferase for bioassays and bioimaging. *Protein Sci.* 19, 26–33. doi:10.1002/pro.279

Liang, Y., Walczak, P., and Bulte, J. W. (2012). Comparison of red-shifted firefly luciferase *Ppy* RE9 and conventional Luc2 as bioluminescence imaging reporter genes for *in vivo* imaging of stem cells. *J. Biomed. Opt.* 17, 016004. doi:10.1117/1.jbo.17.1.016004

Miloud, T., Henrich, C., and Hammerling, G. J. (2007). Quantitative comparison of click beetle and firefly luciferases for *in vivo* bioluminescence imaging. *J. Biomed. Opt.* 12, 054018. doi:10.1117/1.2800386

Miura, C., Kiyama, M., Iwano, S., Ito, K., Obata, R., Hirano, T., et al. (2013). Synthesis and luminescence properties of biphenyl-type firefly luciferin analogs with a new, near-infrared light-emitting bioluminophore. *Tetrahedron* 69, 9726–9734. doi:10.1016/j.tet.2013.09.018

Nakajima, Y., Kimura, T., Sugata, K., Enomoto, T., Asakawa, A., Kubota, H., et al. (2005). Multicolor luciferase assay system: one-step monitoring of multiple gene expressions with a single substrate. *BioTechniques* 38, 891–894. doi:10.2144/05386st03

Nakajima, Y., Yamazaki, T., Nishii, S., Noguchi, T., Hoshino, H., Niwa, K., et al. (2010). Enhanced beetle luciferase for high-resolution bioluminescence imaging. *PLoS ONE* 5, e10011. doi:10.1371/journal.pone.0010011

Neto, A. J., Scorsato, V., Arnoldi, F. G. C., and Viviani, V. R. (2009). *Pyrearinus termitilluminans* larval click beetle luciferase: active site properties, structure and function relationships and comparison with other beetle luciferases. *Photochem. Photobiol. Sci.* 8, 1748–1754. doi:10.1039/b9pp00053d

Rice, B. W., Cable, M. D., and Nelson, M. B. (2001). *In vivo* imaging of light-emitting probes. *J. Biomed. Opt.* 6, 432–440. doi:10.1117/1.1413210

Rice, B. W., and Contag, C. H. (2009). The importance of being red. *Nat. Biotechnol.* 27, 624–625. doi:10.1038/nbt0709-624

Stowe, C., Burley, T. A., Allan, H., Vinci, M., Kramer-Marek, G., Ciobota, D. M., et al. (2019). Near-infrared dual bioluminescence imaging in mouse models of cancer using infraluciferin. *Elife* 8, e45801. doi:10.7554/elife.45801

Sundlov, J. A., Fontaine, D. M., Southworth, T. L., Branchini, B. R., and Gulick, A. M. (2012). Crystal structure of firefly luciferase in a second catalytic conformation supports a domain alternation mechanism. *Biochemistry* 51, 6493–6495. doi:10.1021/bi300934s

Tafreshi, N. K., Hosseinkhani, S., Sadeghizadeh, M., Sadeghi, M., Ranjbar, B., and Naderi-Manesh, H. (2007). The influence of insertion of a critical residue (Arg356) in structure and bioluminescence spectra of firefly luciferase. *J. Biol. Chem.* 282, 8641–8647. doi:10.1074/jbc.m609271200

Tisi, L. C., Law, E. L., Gandelman, O., Lowe, C. R., and Murray, J. A. H. (2002). "The basis of the bathochromic shift in the luciferase from," in *Bioluminescence and chemiluminescence: Progress and current applications edited by stanley PE and kricka LJ* (Singapore: World Scientific).*Photinus pyralis*

Viviani, V. R., and Ohmiya, Y. (2000). Bioluminescence color determinants of phrixothrix railroad-worm luciferases: Chimeric luciferases, site-directed mutagenesis of arg 215 and guanidine effect. *Photochem. Photobiol.* 72, 267–271. doi:10.1562/0031-8655(2000)0720267bcdopr2.0.co2

Viviani, V. R., Simões, A., Bevilaqua, V. R., Gabriel, G. V., Arnoldi, F. G., and Hirano, T. (2016). Glu311 and Arg337 stabilize a closed active-site conformation and provide a critical catalytic base and countercation for green bioluminescence in beetle luciferases. *Biochemistry* 55, 4764–4776. doi:10.1021/acs.biochem.6b00260

Viviani, V. R. (2002). The origin, diversity, and structure function relationships of insect luciferases. *Cell. Mol. Life Sci.* 59, 1833–1850. doi:10.1007/pl00012509

Willey, T. L., Squirrell, D. J., and White, P. J. (2001). "Design and selection of firefly luciferases with novel *in vivo* and *in vitro* properties," in Proc. 11th int. Symp. Biolum. Chemilum. Editors J. F. Case, P. J. Herring, B. H. Robinson, S. H. D. Haddock, L. J. Kricka, and P. E. Stanley (Singapore: World Scientific), 201–204. Pgs.

Zambito, G., Hall, M. P., Wood, M. G., Gaspar, N., Ridwan, Y., Stellari, F. F., et al. (2020). Red-shifted click beetle luciferase mutant expands the multicolorbioluminescent palette for deep tissue imaging. *iScience* 24, 101986.

Zhao, H., Doyle, T. C., Coquoz, O., Kalish, F., Rice, B. W., and Contag, C. H. (2005). Emission spectra of bioluminescent reporters and interaction with mammalian tissue determine the sensitivity of detection *in vivo*. *J. Biomed. Opt.* 10, 041210. doi:10.1117/1.2032388

frontiers | Frontiers in Microbiology

TYPE Original Research
PUBLISHED 26 October 2022
DOI 10.3389/fmicb.2022.970233

OPEN ACCESS

EDITED BY
Axel Cloeckaert,
Institut National de recherche pour l'agriculture, l'alimentation et l'environnement (INRAE), France

REVIEWED BY
Helmut Fickenscher,
University of Kiel, Germany
Uriel Urquiza-Garcia,
Heinrich Heine University of Düsseldorf, Germany

*CORRESPONDENCE
Melanie L. Dart
melanie.dart@promega.com

†These authors have contributed equally to this work

SPECIALTY SECTION
This article was submitted to Infectious Agents and Disease, a section of the journal Frontiers in Microbiology

RECEIVED 27 June 2022
ACCEPTED 06 October 2022
PUBLISHED 26 October 2022

CITATION
Torio EA, Ressler VT, Kincaid VA, Hurst R, Hall MP, Encell LP, Zimmerman K, Forsyth SK, Rehrauer WM, Accola MA, Hsu C-C, Machleidt T and Dart ML (2022) Development of a rapid, simple, and sensitive point-of-care technology platform utilizing ternary NanoLuc. *Front. Microbiol.* 13:970233. doi: 10.3389/fmicb.2022.970233

Development of a rapid, simple, and sensitive point-of-care technology platform utilizing ternary NanoLuc

Emily A. Torio[1†], Valerie T. Ressler[1†], Virginia A. Kincaid[1], Robin Hurst[1], Mary P. Hall[1], Lance P. Encell[1], Kristopher Zimmerman[1], Stuart K. Forsyth[1], William M. Rehrauer[2,3], Molly A. Accola[3], Chia-Chang Hsu[1], Thomas Machleidt[1] and Melanie L. Dart[1*]

[1]Promega Corporation, Madison, WI, United States, [2]Department of Pathology and Laboratory Medicine, School of Medicine and Public Health, University of Wisconsin-Madison, Madison, WI, United States, [3]University of Wisconsin Hospital and Clinics, Clinical Laboratories, Madison, WI, United States

Point-of-care tests are highly valuable in providing fast results for medical decisions for greater flexibility in patient care. Many diagnostic tests, such as ELISAs, that are commonly used within clinical laboratory settings require trained technicians, laborious workflows, and complex instrumentation hindering their translation into point-of-care applications. Herein, we demonstrate the use of a homogeneous, bioluminescent-based, split reporter platform that enables a simple, sensitive, and rapid method for analyte detection in clinical samples. We developed this point-of-care application using an optimized ternary, split-NanoLuc luciferase reporter system that consists of two small reporter peptides added as appendages to analyte-specific affinity reagents. A bright, stable bioluminescent signal is generated as the affinity reagents bind to the analyte, allowing for proximity-induced complementation between the two reporter peptides and the polypeptide protein, in addition to the furimazine substrate. Through lyophilization of the stabilized reporter system with the formulated substrate, we demonstrate a shelf-stable, all-in-one, add-and-read analyte-detection system for use in complex sample matrices at the point-of-care. We highlight the modularity of this platform using two distinct SARS-CoV-2 model systems: SARS-CoV-2 N-antigen detection for active infections and anti-SARS-CoV-2 antibodies for immunity status detection using chemically conjugated or genetically fused affinity reagents, respectively. This technology provides a simple and standardized method to develop rapid, robust, and sensitive analyte-detection assays with flexible assay formatting making this an ideal platform for research, clinical laboratory, as well as point-of-care applications utilizing a simple handheld luminometer.

KEYWORDS

point-of-care, bioluminescence, NanoLuc complementation, SARS-CoV-2 antigen, rapid testing

Introduction

Point-of-care testing (POCT) is an essential tool for the rapid detection of analytes at the site of the patient enabling quick, actionable, informed medical decisions for improved disease management. This form of decentralized diagnostic analysis allows for testing at the bedside, outpatient clinics, and even over the counter as direct-to-consumer tests (Luppa et al., 2011; Tolan, 2017). There is a continuous and growing need for POCTs as they offer rapid turnaround times and streamlined workflows, thereby reducing the need for multiple patient visits, improving medication adherence and antibiotic stewardship, and aiding in the containment of infectious diseases (Patzer et al., 2018; Cooke et al., 2020; HealthEuropa, 2021).

The COVID-19 pandemic, caused by the SARS-CoV-2 virus, has exacerbated the need for POCTs while highlighting their utility both in the clinic and in the hands of a patient. This demand is evidenced by the widespread use of COVID-19 rapid antigen tests (RATs) which have been employed as a useful screening tool for telemedicine visits and drive-thru clinics in addition to their utility in contact tracing (Allen et al., 2020; Chau et al., 2020; Ngo et al., 2020). While the ongoing COVID-19 global pandemic has emphasized the importance of POCTs, these technologies serve an essential role in addressing a variety of public health and safety issues. For example, POCTs are proven tools for the detection of potential contaminants, pathogens, and biothreats in agricultural water sources, food production facilities, and public health settings (Louie et al., 2009; Malcata et al., 2020; Hu et al., 2021).

Analyte tests are used for the detection of biomolecules from a wide array of sample types and matrices. Heterogeneous immunoassays, such as ELISAs, remain the gold standard for analyte quantitation and are widely used in clinical laboratory settings due to their sensitivity, specificity, and modularity. Unfortunately, these assays have workflow limitations, requiring skilled technicians, multiple wash steps, long incubation times, and specialized equipment, which makes it difficult to transition the technology from lab-based to point-of-care formats which require speed, simplicity, and reagent stability (Kozel and Burnham-Marusich, 2017). The dominant format for POCT is lateral flow immunoassay (LFIA) that is configured to mimic a heterogeneous ELISA-like workflow by use of capillary action to separate bound from unbound material to capture the analyte-specific detection signal without the need for multiple wash steps (Koczula and Gallotta, 2016). The majority of LFIAs rely on either colorimetric reporter systems that can be read with the naked eye or fluorescence-based systems that require instrumentation for detection (Di Nardo et al., 2021). Despite the extensive use of POCTs, they continue to be plagued by widespread issues including low sensitivity, sample-matrix interferences, rigid analyses time frames, manufacturing difficulties, format inflexibility, and multiple reagent and material components (St John and Price, 2014; Shaw, 2016; Dalton, 2021). Many of these limitations are inherently linked to the colorimetric and fluorescence-based reporters that dominate the point-of-care space indicating that new chemistries must be developed to overcome these challenges (Koczula and Gallotta, 2016; Roy et al., 2022).

Bioluminescence-based reporter assays have shown distinct advantages over other reporter chemistries including low intrinsic background and broad dynamic range (Allard, 2008). This makes bioluminescence potentially well suited for use with complex sample matrices, like blood and serum, as the background is not affected by autofluorescence as seen with fluorescent detection methods, thus improving sensitivity (Fan and Wood, 2007; Suzuki and Nagai, 2017). Additionally, bioluminescence-based reporters do not require complex instrumentation for analyses since the readout is simply capturing the total light emission which negates the need for filters, mirrors, and external excitation light sources (Tung et al., 2016). These attributes make bioluminescence a promising readout modality for POCT formats that have historically suffered from poor sensitivity when compared to clinical lab-based assays (Hwang et al., 2020; Shaw, 2021).

NanoLuc (Nluc) is a small engineered 19 kDa luciferase. Its brightness and compact thermodynamically stable 10-strand β-barrel structure make Nluc an ideal candidate to meet the challenges faced during POCT development (Hall et al., 2012). Recently reported POCT biosensors such as luciferase-based indicators of drugs (LUCIDS) and luminescent antibody sensors have been developed for bioluminescent resonance energy transfer (BRET) based detection of analytes. The ratiometric nature of BRET measurements allows for robust quantification of analytes independent of bioluminescent signal intensity and sample volume.

However, these BRET-based platforms tend to be complex and require extensive re-design and optimization of biosensors for each analyte of interest which makes rapid prototyping and development challenging (Arts et al., 2017; Xue et al., 2017; Tenda et al., 2018; Ni et al., 2019; Tomimuro et al., 2020; Ni et al., 2021). Additionally, poor environmental stability of principal assay components, including coelenterazine-based luciferase substrates restrict the use of these platforms to cold storage-dependent designs which significantly restricts the range of potential POCT applications (Hawkins et al., 2002).

Split versions of Nluc have been used as binary or ternary complementation reporters for the sensitive detection of analytes using several configurations (Dixon et al., 2016, 2017; Schwinn et al., 2018; Elledge et al., 2020; Hwang et al., 2020; Hall et al., 2021; Kainulainen et al., 2021; Ni et al., 2021; Yao et al., 2021; Kincaid et al., 2022). These examples highlighted the benefits of using bioluminescence for analyte detection providing sensitive assays with simplified workflows. However, to meet the requirements needed for the POCT setting, the assay must be able to maintain performance paired with thermal and chemical stability for extended shelf-life in various environments. Previously reported assays that were based on the binary Nluc system or earlier versions of the ternary Nluc system were shown to carry liabilities in reporter stability as well as the inability to create the high concentration of reagents and substrate needed for

a one-pot lyophilized cake (Dixon et al., 2017; Ohmuro-Matsuyama and Ueda, 2018).

The ternary Nluc technology combined with formulated substrate enabled the generation of shelf-stable lyophilized single-reagent homogeneous immunoassays for the sensitive detection analytes in clinical samples (Hall et al., 2021). The ternary Nluc cleaved an additional peptide piece from the binary LgBiT piece to form a new 17 kDa, 8-strand polypeptide piece (LgTrip) and two reporter peptides (β9 and β10). Since the three pieces have low affinities toward one another, complementation of the functional luciferase is driven quantitatively by analyte-induced interactions bringing these three pieces within a close enough proximity to interact, thus increasing simplicity and reducing the need for wash steps without affecting sensitivity as the background remains low (Hall et al., 2021). This system has the additional advantage over the binary system in that the peptide-tagged affinity reagent concentrations are independent from the light generation allowing to work under saturating conditions of the LgTrip reagent thus maximizing assay performance (Dixon et al., 2016; Hwang et al., 2020; Hall et al., 2021).

The benefits of the ternary Nluc reporter system make it well suited to address current limitations with POCTs. In this study, we utilized a further evolved version of the ternary Nluc system with improved strand 9 peptide solubility and enhanced LgTrip stability to design assays specifically formatted for rapid add-and-read POCT. Using COVID-19 as a model system, we utilize the modularity of this platform for development of sensitive and specific assays to detect either SARS-CoV-2 antigen proteins or anti-SARS-CoV-2 antibodies in clinical samples with POC-compatible formats. These assays provide a large dynamic range, exceeding three orders of magnitude, with a rapid 15-min readout. We showcase the flexibility of the reporter peptides by attaching them to the recognition elements *via* either chemical conjugation or as genetic fusion. We also demonstrate that these assays are highly adaptable and scalable to different assay formats as demonstrated here using both, a moderate-high-throughput plate-based format as well as nasal swab POCT without the need for changing the reagent components. In summary, this platform allows for the fast development of simple, add-and-read analyte-detection assays in a variety of formats relevant for point-of-care applications across a broad range of clinically relevant analytes.

Materials and methods

Antibody labeling

The following antibody pairs were used for the SARS-CoV-2 receptor binding domain (RBD) and nucleocapsid model systems: (1) Chimeric anti-human SARS-CoV/SARS-CoV-2 Spike monoclonal antibodies (mAbs) Cat: 40150-D002 and Cat: 40150-D003 (Sino Biological) and (2) Mouse anti-human SARS-CoV-2 Nucleocapsid mAbs Cat: 9547 and 9,548 (Meridian Bioscience). Labeling of the antibodies with the HaloTag-peptide fusions was performed as previously described (Hall et al., 2021). Antibodies were buffer exchanged 3X into 10 mM sodium bicarbonate buffer (pH 8.5) using Zeba spin desalting columns (Thermo Fisher). Antibodies were then incubated with 200 μM amine-reactive HaloTag Succinimidyl Ester (04) Ligand (Promega) for 2 h with orbital shaking (1,000 rpm) at 22°C. Unreacted ligand was removed with two passes through Zeba spin columns in Phosphate Buffered Saline (PBS). Antibodies were then incubated with 30 μM of the HaloTag-peptide 840 or HaloTag-*VS*-HiBiT fusion protein overnight with shaking at 4°C. HaloLink Resin (Promega) was used to remove excess HaloTag fusions from the reactions and characterization of antibody labeling was carried out using SDS-PAGE.

Solution-based SARS-CoV-2 RBD or N immunoassay on GloMax

A 2X master mix stock solution containing 60 ng/ml β9-labeled anti-SARS-CoV-2 spike RBD antibody D003, 120 ng/ml β10-labeled anti- SARS-CoV-2 spike RBD antibody D002, and 2 μM LgTrip protein was prepared in assay buffer consisting of 0.01% Blocker BSA (Thermo Fisher) in PBS (PBSB), and 50 μl/well was dispensed in solid, white, nonbinding surface (NBS) 96-well plates (Costar). Either a 2× solution containing recombinant SARS-CoV-2 Spike or heat-inactivated virus for dose-response curve generation was prepared, and 50 μl/ well was added to the wells containing the master mix. Plates were incubated for 90 min at ambient temperature prior to the addition of 100 μl/well of a 30-fold dilution of Fz (Nano-Glo Live Cell Substrate; Promega N205) in PBSB. Assays were read on a GloMax Discover Multimode Microplate Reader (Promega) collecting total luminescence using kinetic or endpoint reads, depending on the experimental design. Variations on this methodology, including shorter incubation times, were examined as part of the optimization process. The same method was carried out for the nucleocapsid model system by using 60 ng/ml β9-labeled anti-SARS-CoV-2 N mAb Cat. 9,547, 120 ng/ml β10-labeled anti-SARS-CoV-2 N mAb Cat. 9,548, and 2 μM LgTrip and creating 2× titrations of recombinant CoV N-proteins or heat-inactivated SARS-CoV-2 variants (a comprehensive list can be found in the Supplementary material).

Complete SARS-CoV-2 RBD or N immunoassay lyophilization in swab jackets and characterization

A 4× stock solution containing β10-labeled anti- SARS-CoV-2 RBD mAb (D002), β9-labeled anti- SARS-CoV-2 RBD mAb (D003), LgTrip, Fz, and excipients was prepared for the RBD model system. The same 4× stock was made for the N model systems but instead, with β10-labeled anti- SARS-CoV-2 N mAb 9,548 and β9-labeled anti- SARS-CoV-2 N mAb 9,547. We define

the buffer (i.e., everything except antibody, LgTrip, and Fz) used to make this solution as "complete complex buffer." Aliquots (400 µl) were prepared in disposable swab jackets for lyophilization. The swab jackets were loaded into the lyophilizer (Virtis Genesis 12EL) with shelves pre-set to 4°C. Product then underwent a freezing step with a shelf temperature of −50°C for 2 h. Upon evacuation of the system, the lyophilization process was performed between shelf temperatures of −25°C and 25°C and pressures of 75 and 200 mTorr. The ice sublimation phase lasted 5 h and the bound water desorption phase lasted 16 h. At the end of the lyophilization process, the swab jackets were covered with a temporary stopper under atmospheric conditions.

Immediately prior to use, the jackets were reconstituted with 400 µl of sample (100 µl) + PBSB mixture, shaken manually, and read on the handheld prototype luminometer every 15 min.

Data analysis

Immunoassay dose response titrations were fitted to a 4-parameter logistic regression equation with $1/Y^2$ weighting function (GraphPad Prism 8). Limit of detection (LOD) was calculated as $RLU_{blank} + 3 \times SD_{blank}$. Signal over background (S/B) was calculated by dividing the raw Relative Light Unit signal for a given sample by the average of the background with buffer alone ($n = 3$). To quantify protein concentrations in samples, RLU values were interpolated on the standard curve.

Results

Solution-based homogeneous SARS-CoV-2 antigen immunoassay development

Prior to development of the proof-of-concept POCT, we first established solution-based, homogeneous assays targeting the SARS-CoV-2 nucleocapsid protein (N-antigen) or the SARS-CoV-2 RBD protein (RBD antigen). Both viral proteins are highly immunogenic with the nucleocapsid protein playing an essential role in replication and virion assembly while the RBD protein mediates viral binding of the host cell Angiotensin-converting enzyme 2 (ACE2) receptor (Lutomski et al., 2021). We have previously engineered the ternary Nluc reporter peptides by splitting Nluc, a 10-strand β-barrel luciferase, at the C-terminus at strands 9 and 10 resulting in two small peptides and a larger polypeptide, LgTrip (Hall et al., 2021). HiBiT, a high-affinity strand 10 peptide, has been identified as the preferred strand 10 peptide (β10) based on luminescent signal output in the ternary system and was carried through for these experiments. We further evolved the strand 9 (β9) derived peptide as well as LgTrip to overcome poor aqueous solubility and improve protein stability (Hall et al., 2021; Kincaid et al., 2022; Supplementary Figure 1). To create the chemical conjugation reporter tags, we relied on HaloTag-mediated chemical labeling of a pair of complementary antibodies that recognized non-overlapping epitopes of the target analyte (Nath et al., 2017).

Commercially available complementary antibody pairs specific to each target protein from the Wuhan-Hu 1 strain were chemically conjugated with either HaloTag- β9 or HaloTag- β10 proteins. Binding to the target analyte brings both antibodies into proximity and allows the complementation of the active ternary Nluc complex with the addition of LgTrip and a bioluminescent signal can be measured in the presence of the Nluc substrate, Fz, as shown in the schematic in Figure 1. The design of the system required 4 antibody conjugates (antibody 1-HT-β9, antibody 1-HT-β10, antibody 2-HT-β9, and antibody 2-HT-β10) that were paired for matrix experiments (Supplementary Figure 2) for complete evaluation. Both combinations performed well with a protein standard; therefore, we selected the orientation that provided the highest signal-to-background (S/B) ratio. Next, we determined the optimal concentrations of the labeled antibodies for each target analyte immunoassay by conducting a matrix experiment using serial dilutions of each antibody under saturating conditions of the LgTrip and Fz substrate in the presence or absence of analyte (Supplementary Figure 2A). The S/B was calculated to identify the concentration of each antibody that produced the maximal sensitivity and dynamic range (Supplementary Figures 2B–E). Results for the N-antigen assay returned optimal concentrations of 30 ng/ml HT- β9-labeled anti-SARS-CoV-2 N mAb Cat. 9,547 and 60 ng/ml HT- β10 labeled anti-SARS-CoV-2 N mAb Cat. 9,548. The RBD assay final affinity reagent concentrations were 60 ng/ml HT- β9-labeled anti-SARS-CoV-2 spike RBD antibody D003 and 120 ng/ml HT-β10-labeled anti- SARS-CoV-2 spike RBD antibody D002 (Supplementary Figures 2B–G).

To establish assay performance, dose-response curves were generated using a simple, homogeneous workflow with viral proteins added directly to the plate, followed by a master mix including all assay reagents. This plate-based format has advantages of being fast, sensitive, and high-throughput, thereby potentially alleviating key issues routinely encountered with ELISAs in central laboratory settings (Supplementary Figure 3; Kozel and Burnham-Marusich, 2017; Sakamoto et al., 2018). Assay performance was established for both the N-antigen as well as the RBD antigen using recombinant proteins from various SARS-CoV-2 variants. The N-antigen assay displayed great sensitivity across all tested recombinant SARS N-protein samples from different SARS-CoV-2 variants, including Wuhan-Hu-1 (LOD = 0.108 ng/ml), Alpha (LOD = 0.019 ng/ml), Beta (LOD = 0.066 ng/ml), Lambda (LOD = 0.089 ng/ml), Delta (LOD = 0.050 ng/ml), and Omicron (LOD = 0.522 ng/ml) with a dynamic range spanning about four orders of magnitude (Figure 2A).

Similarly, the RBD antigen assay demonstrated great sensitivity across the majority of SARS-CoV recombinant RBD proteins resulting in LODs for Wuhan-Hu-1 (0.007 ng/ml), Alpha (0.009 ng/ml), Beta (0.004 ng/ml), Delta (0.006 ng/ml), and

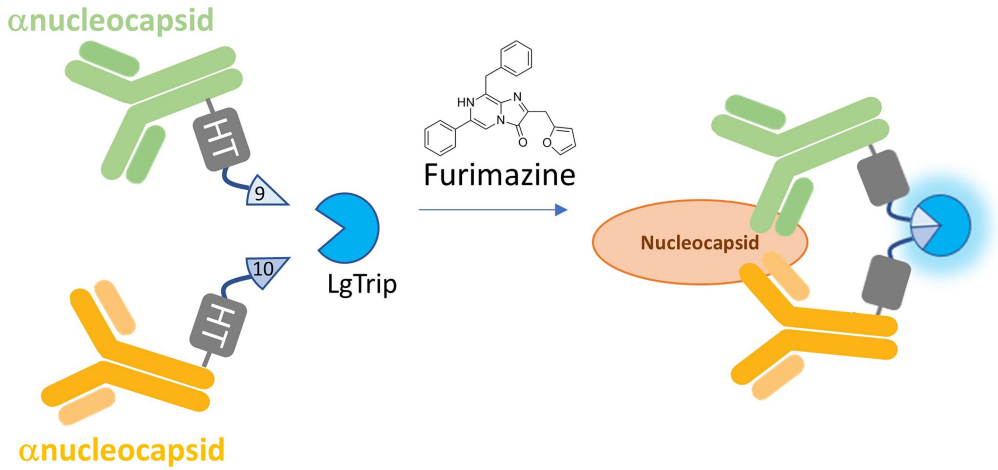

FIGURE 1
Schematic of the ternary Nluc reporter immunoassay. β9 and β10 peptides are chemically conjugated *via* HaloTag (HT) to a pair of antibodies that recognize separate epitopes on the target analyte. Binding to the analyte brings the antibodies and their respective peptide subunits into close proximity. With the addition of LgTrip and the furimazine substrate, complementation of the active ternary Nluc complex occurs, producing bioluminescence.

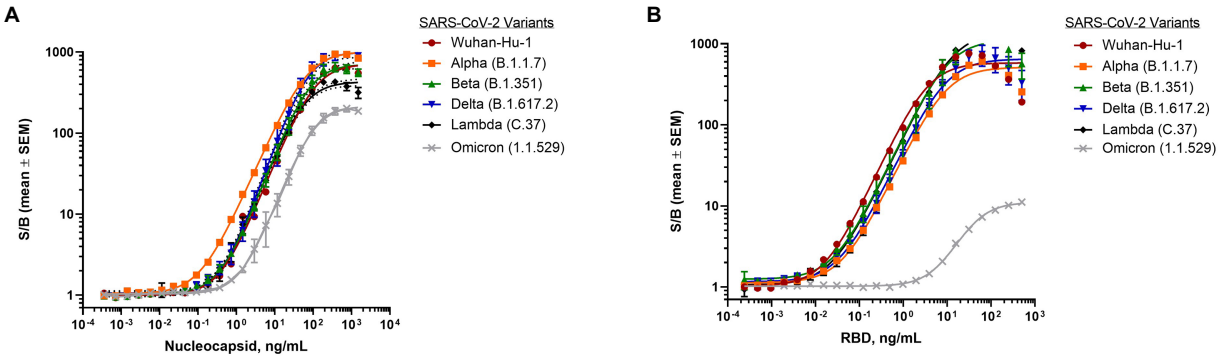

FIGURE 2
Detection of SARS-CoV-2 purified proteins from different variants. **(A)** Dose-response curve of purified nucleocapsid proteins from variants using nucleocapsid antigen assay. Final antibody concentrations were 30ng/ml β9-labeled anti-SARS-CoV-2N mAb Cat. 9,547 and 60ng/ml β10-labeled anti-SARS-CoV-2N mAb Cat. 9,548. **(B)** Dose-response curve of purified RBD proteins from variants using RBD antigen assay. Final antibody concentrations were 30ng/ml β9-labeled anti-SARS-CoV-2 spike RBD antibody D003 and 60ng/ml β10-labeled anti- SARS-CoV-2 spike RBD antibody D002. 1μM LgTrip was used in all experiments. Reagents were incubated for 90min prior to the addition of Fz substrate. Luminescence was measured and the signal over background (S/B) was calculated for each concentration of purified viral protein. Shown are means ± SEM (*n*=3 independent experiments).

Lambda (0.002 ng/ml) with a dynamic range spanning three orders of magnitude (Figure 2B). Interestingly, the assay sensitivity was found to be significantly lower for the Omicron variant RBD protein (2.2 ng/ml) (Figure 2B), which carries 15 mutations known to impact antibody binding (Wu et al., 2022).

In addition, recombinant N and RBD antigens from different coronaviruses including SARS-CoV, Middle East Respiratory Syndrome coronavirus (MERS-CoV), and a variety of low pathogenicity human coronaviruses, were tested to determine assay cross-reactivity. Both antigens from SARS-CoV were recognized in this format with high sensitivity which is not surprising considering the high degree of homology found between SARS-CoV and the Wuhan-Hu-1 strain of SARS CoV-2 (Grifoni et al., 2020). Importantly, the N-antigen assay did not cross-react with any of the recombinant proteins from low pathogenicity coronaviruses or MERS-CoV demonstrating excellent specificity (Supplementary Figure 4A) across pathogenic coronaviruses. Surprisingly, we found substantial cross-reactivity in the RBD antigen assay for coronavirus strain HCoV-NL63 spike protein that might be attributed to epitope sequence homology (Supplementary Figure 4B; Simula et al., 2020). This finding in combination with lower observed sensitivity against the Omicron variant suggests potential liabilities with utilizing the RBD antigen for specific detection of SARS-CoV-2 in a POCT.

Taking into consideration that speed is a key requirement for POCT to accommodate rapid sample-to-answer workflows, we next

examined the kinetics of the signal formation for both antigen assays. Signal intensity and kinetics are driven by the complementation and maturation of the ternary Nluc components into a functional luciferase complex, affinity and avidity of the antibodies, and the concentration of the analyte. When all the assay components were added at $t = 0$, we observed that the development of the luminescence signal was both time- and analyte concentration-dependent as expected (Supplementary Figures 5A–D). Both assays exhibited greater sensitivity over time but did not vary in terms of signal amplitude. Importantly, kinetic analysis revealed that the analyte-specific signal is sustained for an extended period of time without a rise in background signal and concomitant loss of sensitivity. Analysis of assay performance over time indicates stability for at least 90 min without discernible loss in sensitivity (Supplementary Figures 6A,B). This signal stability highlights the technology's robustness which permits reliable sample analyses across a broad time window without increased occurrence of false results. This marks a significant improvement over many current standard ELISA and point-of-care assay formats which often require narrow time windows for obtaining reliable results.

Assay performance using heat-inactivated virus and clinical nasopharyngeal samples

To establish assay performance against clinically relevant viral samples, we next analyzed the ability of the assay to detect heat-inactivated virus. Surprisingly, when tested with heat-inactivated viral SARS-CoV-2 variants Wuhan-Hu 1, Alpha (B.1.1.7), and Beta (B.1.351), the RBD antigen assay failed to produce a signal despite increasing amounts of virus (Supplementary Figure 7A). To determine if the poor performance could be attributed to heat-induced damage of the target epitope, the RBD antigen assay was also tested using non-heat treated residual clinical nasopharyngeal (NP) samples obtained from our clinical collaborator at the University of Wisconsin Hospital and Clinics. Individual NP samples that had previously been identified by PCR as negative ($n = 10$) or positive ($n = 10$) were tested in the RBD antigen assay and no significant difference in signal generation was found ($p = 0.17$; Supplementary Figure 7B) between positive and negative samples. Due to these results, the SARS-CoV-2 RBD antigen assay was abandoned for further assay development.

In contrast, the SARS-CoV-2 N-antigen assay displayed a dose-dependent response across all heat-inactivated SARS-CoV-2 variants tested (Figure 3). Interestingly, the assay demonstrated a decrease in sensitivity for the Alpha (B.1.1.7) variant (LOD = 242 genome copies/µl) and an increase in sensitivity for the Beta (B.1.351) variant (LOD = 26 genome copies/µl) relative to the Wuhan-Hu-1 variant (LOD = 74 genome copies/µl), which was used to generate N-antigen specific antibodies. These results differ from what was previously observed when using purified recombinant N-antigen (Figure 2A) and could indicate differences in the epitope presentation in the naturally occurring virus versus recombinantly expressed viral proteins. The results found for the Wuhan-Hu-1 variant were expected given that the α-nucleocapsid antibodies for the assay were developed against this variant during the original wave of the pandemic. It was previously shown that post-translational modifications of RBD varied significantly between different SARS-CoV-2 variants. We hypothesized that the poor performance could be attributed to a variety of factors, including lack of accessibility due to glycosylation of the spike protein or low abundance of the target epitope in samples with a whole virus (Ke et al., 2020; Shajahan et al., 2020). The nucleocapsid protein of the Alpha (B.1.1.7) variant has been shown to be heavily phosphorylated relative to the original Wuhan-Hu-1 strain, while the Beta (B.1.351) has fewer post-translational modifications (PTMs; Supekar et al., 2020; Mohammad et al., 2021). We speculate that differences in PTM composition and abundance could lead to altered epitope presentation and therefore impact the binding of antibodies to the viral nucleocapsid protein which would explain the observed differences in sensitivity.

To demonstrate the clinical utility of the N-antigen assay, residual clinical NP samples that were previously PCR-confirmed negative ($n = 21$) or positive ($n = 89$) were analyzed using the plate-based format of the assay to allow for a high-throughput approach given the large number of samples being tested (Supplementary Figure 3). The N-antigen assay showed great specificity with all negatives grouping tightly at low RLU values (Figure 4A). The positive cohort had a dynamic range covering four log orders of signal magnitude, highlighting the benefit of using a bioluminescence-based reporter, which minimizes the need to dilute samples with high analyte concentrations while preserving

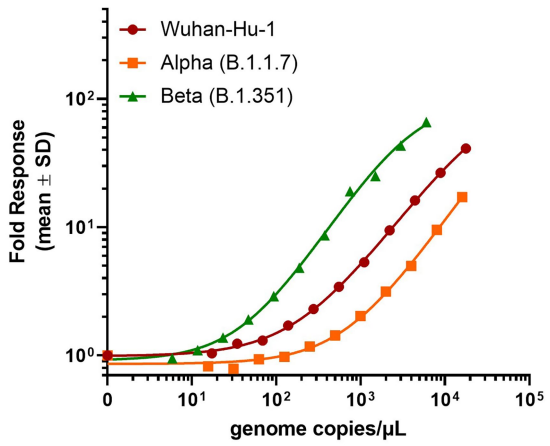

FIGURE 3
Detection of SARS-CoV-2 heat-inactivated viruses with N-antigen assay. 30ng/ml β9-labeled anti-SARS-CoV-2N mAb Cat. 9,547, 60ng/ml β10-labeled anti-SARS-CoV-2N mAb Cat. 9,548, and 1µM LgTrip were incubated in the presence of sample for 90min prior to the addition of Fz substrate and the measurement of luminescence. Signal over background (S/B) was calculated for each concentration of heat-inactivated virus. Shown mean±SD of a representative experiment.

sensitivity due to its inherently low background (Figure 4A). The results demonstrated a clear and significant delineation between samples ($p < 0.0001$; Figure 4A). In a further effort to categorize samples as positive or negative in the immunoassay in a standardized fashion, we established a cut-off value using the mean + 3 × SD of RLU values obtained from all PCR negative samples. Based on this cut-off, there was some discordance in outcome between the PCR results and the N-antigen assay resulting in 19/89 samples considered as false-negatives (Table 1). As these samples were residual clinical samples, we acknowledge the liabilities with the sample set including poor antigen stability due to prolonged and improper sample storage, variety of viral transport media (VTM) that could affect protein stability, as well as samples containing very low viral loads which could all contribute to the false-negatives reported here.

In order to determine if low viral load could explain the discordance between PCR and antigen assay, we investigated the relationship between reported PCR cycle threshold (Ct) values and signal in the antigen assay. We compared the RLU values obtained with the developed immunoassay to the reported Ct values to determine if the false-negatives contained a low viral load. Sample viral load is inversely related to the Ct value and an increase of 3.3 in Ct value corresponds to a 10-fold reduction in viral RNA molecules (Al Bayat et al., 2021). We found good correlation between Ct values and RLU values produced by the N-antigen assay in samples with high viral load (Figure 4B). Previously, a Ct value ≤30 has been identified as a cut-off for viral infectivity with a markedly lower risk of secondary transmission to close contacts (Al Bayat et al., 2021). These false-positives have delayed hospitals in discharging non-infectious patients and have emphasized the need for reliable, accurate antigen tests to combat the pandemic (Braunstein et al., 2021). Samples with a Ct value ≤30 were detected with 69/79 concordance while samples with a Ct ≤ 25 had an improved concordance finding 64/65 in agreement. One factor that might have impacted N-antigen detection in PCR positive samples is the use of VTM for collection and storage of most tested clinical samples. VTM reagents include chemical additives typically optimized for downstream molecular testing and have been shown to denature proteins thus affecting performance in antigen detection assays. To illustrate the potential impact of VTM on the N-antigen assay performance, we tested the compatibility of a number of commonly used commercially available VTMs with the N-antigen assay. The experiment was conducted using a fixed concentration of purified SARS-CoV-2 nucleocapsid protein from the Wuhan-Hu-1 strain in the presence of a serial dilution of each VTM (Supplementary Figure 8). The data indicate that the choice of VTM has a significant impact on assay performance and should be therefore considered as a critical reagent. Certain VTMs, including PrimeStore® MTM and Hologic Aptima® were found to be completely incompatible with the assay even at high dilutions of the VTM. Other commercial VTMs were found to lead to various degrees of signal loss compared to PBS and saline in a concentration-dependent manner. This experiment

TABLE 1 Overall assay performance.

		RT-PCR results		
		+	–	
N-antigen test results	+	70	0	70
	–	19	21	38
		89	21	108

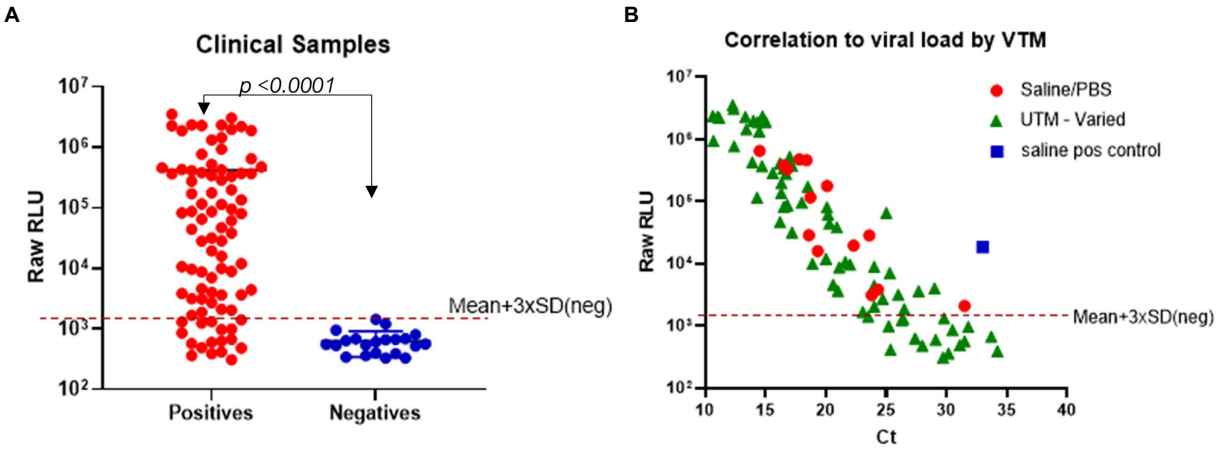

FIGURE 4
Detection of SARS-CoV-2N-antigen in clinical samples. **(A)** Clinical samples that had previously been identified by PCR as negative (n=21) or positive (n=89) were individually tested in the N-antigen assay. **(B)** N-antigen assay raw RLU results were correlated to viral load (Ct) by VTM for all PCR positive samples (n=89). In both panels a and b, 30ng/ml β9-labeled anti-SARS-CoV-2N mAb Cat. 9,547, 60ng/ml β10-labeled anti-SARS-CoV-2N mAb Cat. 9,548, and 1μM LgTrip were incubated in the presence of sample for 90min prior to the addition of Fz substrate and the measurement of luminescence. A red, dotted line has been added to each panel to represent a cut-off based on Mean+3 × SD (neg). Statistical analyses determined by using an unpaired, non-parametric Mann–Whitney t-test.

demonstrates that the choice of sample medium is a critical factor for assay performance.

Point-of-care assay development

We have previously demonstrated that through formulation and lyophilization, we can develop assays using a stable, all-in-one reagent that can be reconstituted in aqueous buffers and added directly to sample in standard microtiter plates (Hall et al., 2021). To further explore the potential use of this technology in a POCT format, we utilized the same formulation and lyophilization approach to create a prototype POCT with the assay reagent directly placed into a swab jacket as outlined in the schematic depicted in Figure 5. In this format individually collected samples are added directly to a swab jacket containing the all-in-one lyophilized N-antigen assay reagent and reconstitution buffer, briefly incubated, and then analyzed using a basic handheld luminometer. Using this approach, we generated a titration of recombinant N-antigen to establish a standard curve on the handheld device which showed a good correlation ($R^2 = 0.9676$) with standard curve values measured on a plate reader (Supplementary Figure 9). Following this proof-of-concept experiment, we next examined the performance of the N-antigen immunoassay in a true POCT format. To this end, all components of the N-antigen immunoassay (peptide-labeled antibodies, LgTrip, and furimazine substrate) were directly lyophilized into a nasal swab jacket to mimic a homogeneous, rapid POCT format for the detection of SARS-CoV-2 antigen in clinical samples. Samples previously determined as positive ($n = 20$) or negative ($n = 13$) by both PCR and standard immunoassay were added directly to the swab jacket along with PBS reconstitution buffer (in a 100 µl:300 µl ratio) and analyzed using the handheld luminometer following a 15-min incubation period. The results demonstrated a clear and significant delineation between PCR-confirmed positive and negative samples ($p < 0.0001$; Figure 6A). For analysis, we utilized a cut-off value set at the mean + 3 × SD of all negative samples which returned a 100% specificity for the samples tested (Figure 6A). The positive samples displayed results spanning two orders of magnitude in dynamic range and showed a good correlation between the handheld and GloMax plate reader (Supplementary Figure 10). Assay development time is a critical parameter to be considered in POCT development. To understand the kinetics of the signal generation, a subset of samples was measured repeatedly in 15 min intervals over the course of 1 h (Figure 6B). The results of the kinetic read demonstrate the beneficial effects provided by the sustained bioluminescence glow reaction. The negative samples showed no increase in signal which minimizes the danger of false-positives due to overdevelopment over time (Figure 6B) which is a common problem in colorimetric formats (Terato et al., 2014; Mouliou and Gourgoulianis, 2021). Of equal importance is signal stability for preventing positive samples returning false-negative results over time due to loss of signal. We observed that positive samples provided a high RLU value that increases over time. The improved signal separation seen with a longer reading window could potentially improve assay sensitivity, if needed. Flexible assay incubation times allow users to batch analyze samples and streamline workflows in a point-of-care environment without compromising on assay accuracy. We also

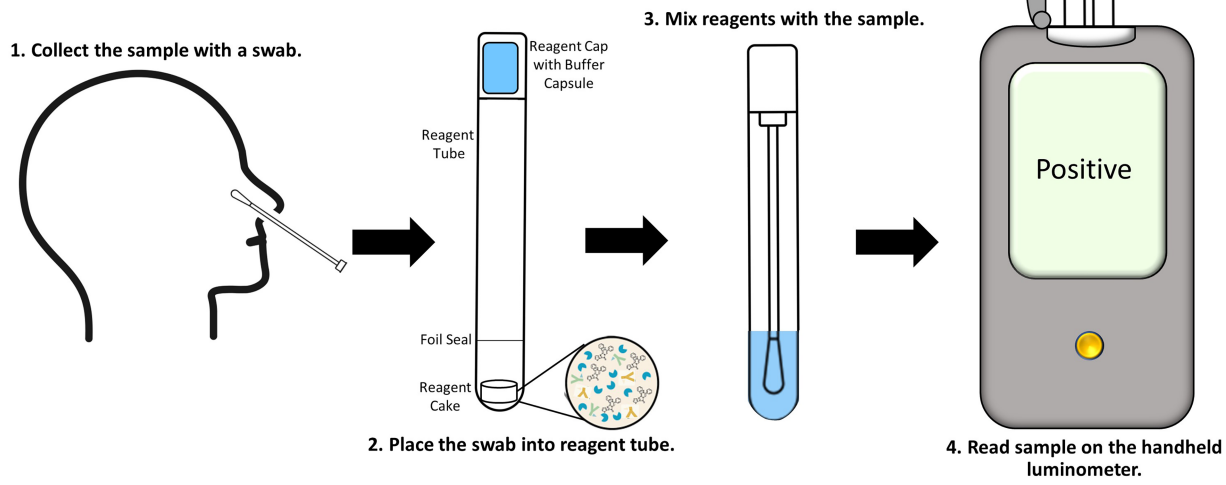

FIGURE 5
Proposed workflow for the point-of-care SARS-CoV-2 antigen immunoassay utilizing the ternary Nluc reporter system. Nasal swabs are collected (1) and placed into the reagent tube, breaking through the foil seal to expose the reagent cake (2). The cap is placed and locked onto the tube containing the sample. The buffer capsule in the cap is then cracked and the tube is shaken to reconstitute the cake and mix the assay reagents with the sample (3). The tube is then inserted into the handheld luminometer and read (4).

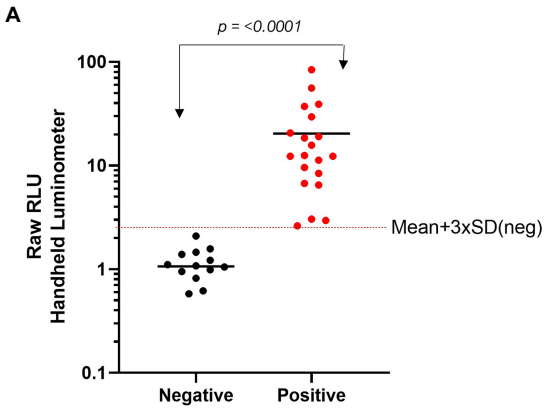

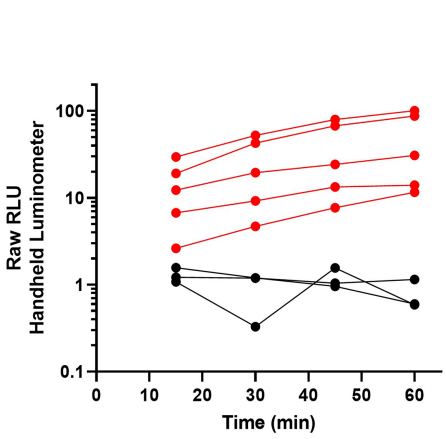

FIGURE 6
Characterization of a single-reagent SARS-CoV-2 antigen assay for point-of –care testing with nasal clinical samples. **(A)** Clinical samples that had previously been identified by PCR as negative (n=13) or positive (n=20) were added directly to the lyophilized N-antigen assay then read with a handheld luminometer after 15min. **(B)** A subset of clinical samples were added to the lyophilized N-antigen assay and measured at 15min intervals over a 1h time period. Statistical analyses performed by using unpaired, non-parametric Mann–Whitney t-test.

used the kinetic workflow to highlight the potential for sample quantitation by calculating the concentration of nucleocapsid protein in each positive sample at 30 or 60 min based on the Wuhan-Hu-1 standard curve generated with the handheld device (Supplementary Figure 11). The sample quantitation covered a broad range at both time points but showed improved separation between samples after 60 min.

To further showcase the flexibility and performance of the ternary Nluc technology POCT platform, we developed an assay to detect SARS-CoV-2 antibodies in human plasma and serum samples using RBD-Trip peptide genetic fusions. Serological tests can provide information about serostatus from previous infections as well as post-vaccination and are frequently used for public health decision-making (West et al., 2021). For this model, we generated RBD- β9 and RBD- β10 genetic fusions which negates the need for chemical labeling. A combination of these fusions was used to detect anti-SARS-CoV-2 antibodies present in serum or plasma. Because of the bivalent nature of antibodies incubating positive serum with an equimolar mixture of both RBD genetic fusions will result in half of the RBD-specific antibodies binding simultaneous to one molecule of RBD- β9 and RBD- β10 each, thus bringing the β9 and β10 into close proximity. Upon addition of the detection reagent containing the LgTrip and furimazine substrate, reconstitution of an active enzyme complex will result in a luminescent signal that is proportional to the level of the anti-SARS-CoV-2 antibody present in the sample. A schematic of this assay can be found in Supplementary Figure 12. The ability to use this same chemistry in combination with genetic fusions offers yet another aspect of flexibility to the ternary Nluc assay design. Genetic fusions add a single tag to the detection proteins at a defined position, which simplifies manufacturing by removing the need for a chemical purification and decreases lot-to-lot variability. To create a POCT prototype for SARS-CoV-2 serology analyses, all components including furimazine substrate were lyophilized directly into swab jackets for an add-sample-and-read assay format. Clinical samples were collected from convalescent patients (n = 13) who had experienced a natural SARS-CoV-2 infection prior to the administration of vaccination or negative samples commercially sourced pre-pandemic (n = 12). The reagent cake was resuspended in PBS buffer and added directly to samples in a swab tube. Luminescence was read in the handheld device at 15, 30, 45, 60, and 90 min (Figure 7). Within this limited study, the assay showed great specificity using a cut-off derived from the mean + 3 × SD of all negative samples. The positive samples showed excellent sensitivity with a dynamic range spanning two orders of magnitude with no apparent interference from the serum sample-matrix. The assay also displayed sustained signal kinetics over time allowing for flexible read times but importantly preventing false-negatives or false-positives that can be associated with changes in signal over time as frequently observed with standard colorimetric or fluorescent reporter systems used for POCT (Mouliou and Gourgoulianis, 2021).

Discussion

There is a continued need to expand the ability to detect clinically relevant analytes at the site of the patient using POCT. This need is particularly relevant for monitoring and controlling emerging infectious diseases such as the ongoing SARS-CoV-2 pandemic. We have previously introduced the ternary split-Nluc platform as a bioluminescence-based homogeneous immunoassay that can be readily adapted for a range of model systems and herein adapt this technology for POCT (Hall et al., 2021). The platform is highly flexible since two of the three reporter fragments are small peptides and can be used to chemically label any amenable molecules. The other

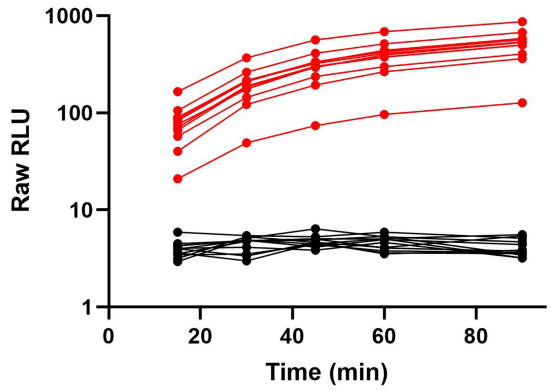

FIGURE 7
Ternary Nluc-based assay for SARS-CoV-2 antibody response in serological samples. Serum samples from convalescent SARS-CoV-2 patients (*n*=13) in red or pre-pandemic patients (*n*=12) in black were individually tested with the lyophilized, all-in-one ternary Nluc serology assay. Samples were measured at 15, 30, 45, 60, and 90-min intervals with a handheld luminometer.

components, LgTrip and formulated furimazine, have been optimized to allow for all-in-one lyophilized assays suitable for ambient temperature storage in resource-limited settings. The ternary system offers major advantages over other systems in that the affinity reagent concentrations are separate from the assay signal generation, broadening the dynamic range of the assay at the upper end of analyte concentrations. During assay development, the concentration of peptide-labeled antibodies can be independently adjusted with saturating concentrations of the LgTrip detection reagent and furimazine substrate to obtain the optimal assay performance.

In this study, we introduce a proof-of-concept for POCT by adapting a flexible, all-in-one technology for a SARS-CoV-2 model system. Initially, we pursued two potential SARS-CoV-2 antigens, the nucleocapsid protein (N) and the RBD protein with the ternary Nluc platform. Each immunoassay was initially optimized in a homogeneous plate-based format with purified recombinant proteins prior to transitioning to a point-of-care format. While the dynamic range for the assays spanned multiple orders of magnitude, the assay signal for both antigens decreased at extremely high concentrations of proteins, a phenomenon common to all homogeneous immunoassays known as the "Hook effect"(Ross et al., 2020). Although the loss in signal never resulted in a false-negative reading, absolute quantitation of the analyte once outside of the linear range would not be possible. This effect could be addressed by using a higher concentration of antibodies to capture the higher end of analyte concentrations if quantitation was needed.

Surprisingly, while the RBD assay performed well with purified proteins, it failed to detect antigen in either the heat-inactivated virus or clinical NP samples. Currently, all commercially available antigen assays use nucleocapsid protein as the target analyte, indicating others have noted limitations with using RBD as a target analyte (Liu et al., 2021). Given the poor performance with clinical samples, we abandoned RBD as a target and advanced with the N-antigen assay.

Overall, the plate-based N-antigen immunoassay was two orders of magnitude more sensitive than reported values for all commercially available high-throughput and RATs (Scohy et al., 2020; Eshghifar et al., 2021). Currently available RATs have been plagued by low sensitivity in clinical practice with LODs well below manufacturer-reported values, especially in asymptomatic cases (Kahn et al., 2021). Such a drastic improvement in sensitivity could be crucial for combating the rise of new variants and further spread of SARS-CoV-2, especially with the growing reliance on direct-to-consumer RATs by the public.

Given the superior performance of the N-antigen assay with the model systems, we moved forward with a small set of residual patient samples in an add-and-read approach. We recognize development of this prototype would require a much larger sample cohort in order to establish a reliable threshold value for distinguishing positive from negative samples. However, using the limited number of clinical samples available allowed us to demonstrate a prototype test that showed overall good discrimination between positive and negative samples.

Several PCR-confirmed positive samples (19/89) returned a potential negative with the N-antigen assay, indicating some discrepancy between the two assays. We hypothesized that there were liabilities with the limited sample set including storage conditions such as multiple freeze/thaw cycles, temperature, and VTM. Potential VTM interference with RAT performance has been well documented, specifically in causing false results (Cubas-Atienzar et al., 2021; Patriquin et al., 2021; Zhou et al., 2021). We obtained commercial VTMs and verified their compatibility with the N-antigen assay. Based on this work, we moved forward with PBS for the assay media, allowing for direct sample addition to the assay without additional handling or dilution of the target analyte. This add-and-read approach streamlined the overall workflow and pushed the assay further into the POCT space.

We have previously shown that the ternary Nluc bulk reagents can be reformulated from a solution-based format to a lyophilized, all-in-one format to address different sample types and application needs (Hall et al., 2021). Taking the next step, the N-antigen assay (including Fz substrate) was converted into a POCT prototype format, with all the assay components from the solution-based work lyophilized into a cake within a nasal swab tube. To demonstrate utility of this format in a realistic POCT setup we used a handheld luminometer for data collection. Within 15 min, our N-antigen POCT was able to distinguish between SARS-CoV-2 positive and negative samples with a high degree of confidence. This underscores the potential of this technology for use in POCT applications.

Using the same format, we measured clinical samples over the course of a 1 h period to demonstrate that the assay results were stable over extended periods of time. In this way, the ternary Nluc system provides a major benefit over other reporter technologies that suffer from overdevelopment of the reporter or waning signal over time, thereby potentially impacting validity of assay results

over time. The extended read window for the assay could allow assay users and technicians to test samples more efficiently in large batches without having to worry about false results.

Given the broad dynamic signal range observed with positive clinical samples, we also attempted to quantify the amount of nucleocapsid protein, or the amount of virus based on our previously established standard curve (Supplementary Figure 9). The sheer number of SARS-CoV-2 variants and the numerous mutations within those variants confounds antigen quantitation, especially in clinical samples. The rapid evolution of SARS-CoV-2 represents a rather unique situation, which implies that quantifying other clinically relevant analytes (e.g., troponin, CRP, etc.) with the Nluc technology would likely be more straightforward and could offer major benefits at the point-of-care.

Though PCR-based techniques have served as the primary diagnostic for SARS-CoV-2 infections, global testing capacities have been strained, which emphasizes an urgent need for antigen tests that meet the set of criteria published by the World Health Organization for POC diagnostics known by the acronym ASSURED (affordable, sensitive, specific, user-friendly, rapid/robust, equipment-free/minimal equipment, and deliverable to end-users) for better disease control (Land et al., 2019). The modular nature of the ternary Nluc technology allowed us to rapidly design and develop a serological assay detecting immune responses against SARS-CoV-2. Using this model system, we showcased another accommodating assay feature of the ternary, split-Nluc platform, namely the ability to append β9 and β10 peptides as genetic fusions rather than the chemical labeling approach used in the antigen assay. This and a recently published study have focused on transitioning the ternary Nluc technology from HaloTag-based labeling approach to direct peptide labeling and genetic fusions to enable flexible labeling options for different targets and model systems(Kincaid et al., 2022). The direct labeling and genetic fusion methods use smaller peptide tags that are bioinert and can be easily appended anywhere on targets of interest. Genetic fusions add an additional benefit in being able to control the number of labels added to the target. All labeling options rely on the same chemistry to generate bioluminescence thereby allowing the same flexibility across all assay formats including solution-based and lyophilized all-in-one.

The same chemistries used in the ternary Nluc solution-based assays translate directly into lyophilized formats while maintaining performance, which offers unique assay flexibility compared to other available technologies. Herein, we were able to lyophilize the reporter system and formulated substrate into a shelf-stable, homogeneous, add-and-read analyte detection reagent cake for point-of-care applications using a simple handheld luminometer. POCT is valuable in providing rapid results outside of a typical clinical laboratory setting with simplified workflows, but often can suffer in sensitivity, sample-matrix interference, and is often limited to qualitative results. As demonstrated in this work, the ternary Nluc technology overcomes current limitations in the point-of-care space, enabling a rapid, sensitive, robust platform for a variety of targets and model systems.

Data availability statement

The original contributions presented in the study are included in the article/Supplementary material, further inquiries can be directed to the corresponding author.

Author contributions

ET and VR purified proteins, performed all immunoassays and calibrations, conducted data analysis, and wrote the manuscript. WR and MA provided nasopharyngeal swab samples and associated clinical data. VK, MH, and LE designed and evolved the stabilized version of the ternary Nluc system. KZ constructed plasmids for all protein components. RH and C-CH expressed, purified, and characterized proteins described in the manuscript including LgTrip and genetic fusion proteins. SF conducted all lyophilization runs and optimized lyophilization conditions for all assays described in the manuscript. TM and MD performed data analysis, conceptualized the work, and designed the overall project scope. All authors contributed to the article and approved the submitted version.

Acknowledgments

We thank GayeLyn LaFleur and Luke Van Herwynen for their help in preparing buffers, culture media, and other reagents.

Conflict of interest

ET, VR, VK, RH, MH, LE, KZ, SF, C-CH, TM, and MD were employed by the company Promega Corporation.

The remaining authors declare that the research was conducted in the absence of any commercial or financial relationships that could be construed as a potential conflict of interest.

Publisher's note

Supplementary material

The Supplementary material for this article can be found online at: https://www.frontiersin.org/articles/10.3389/fmicb.2022.970233/full#supplementary-material

References

Al Bayat, S., Mundodan, J., Hasnain, S., Sallam, M., Khogali, H., Ali, D., et al. (2021). Can the cycle threshold (CT) value of RT-PCR test for SARS-CoV-2 predict infectivity among close contacts? *J. Infect. Public Health* 14, 1201–1205. doi: 10.1016/j.jiph.2021.08.013

Allard, S. T. M. (2008). Bioluminescent reporter genes. *Postepy Biochem.* 54, 350–353.

Allen, D., Block, S., Cohen, J., Eckersley, P., Eifler, M., Gostin, L., et al. (2020). *Roadmap to Pandemic Resilience—Massive Scale Testing, Tracing, and Supported Isolation (TTSI) as the Path to Pandemic Resilience for a Free Society*. Cambridge, MA: Edmond J. Safra Center for Ethics: Harvard University.

Arts, R., Ludwig, S. K. J., Van Gerven, B. C. B., Estirado, E. M., Milroy, L. G., and Merkx, M. (2017). Semisynthetic bioluminescent sensor proteins for direct detection of antibodies and small molecules in solution. *ACS Sens.* 2, 1730–1736. doi: 10.1021/acssensors.7b00695

Braunstein, G. D., Schwartz, L., Hymel, P., and Fielding, J. (2021). False positive results with SARS-Cov-2 RT-PCR tests and how to evaluate a RT-PCR-positive test for the possibility of a false positive result. *J. Occup. Environ. Med.* 63, e159–e162. doi: 10.1097/JOM.0000000000002138

Chau, C. H., Strope, J. D., and Figg, W. D. (2020). COVID-19 clinical diagnostics and testing technology. *Pharmacotherapy* 40, 857–868. doi: 10.1002/phar.2439

Cooke, J., Llor, C., Hopstaken, R., Dryden, M., and Butler, C. (2020). Respiratory tract infections (RTIS) in primary care: narrative review of c reactive protein (CRP) point-of-care testing (POCT) and antibacterial use in patients who present with symptoms of RTI. *BMJ Open Respir. Res.* 7:7. doi: 10.1136/bmjresp-2020-000624

Cubas-Atienzar, A. I., Kontogianni, K., Edwards, T., Wooding, D., Buist, K., Thompson, C. R., et al. (2021). Limit of detection in different matrices of 19 commercially available rapid antigen tests for the detection of SARS-CoV-2. *Sci. Rep.* 11:18313. doi: 10.1038/s41598-021-97489-9

Dalton, J. (2021). Communications with lab and POCT users. *Pract. Lab Med.* 25:e00223. doi: 10.1016/j.plabm.2021.e00223

Di Nardo, F., Chiarello, M., Cavalera, S., Baggiani, C., and Anfossi, L. (2021). Ten years of lateral flow immunoassay technique applications: trends, challenges and future perspectives. *Sensors* 21:5185. doi: 10.3390/s21155185

Dixon, A. S., Kim, S. J., Baumgartner, B. K., Krippner, S., and Owen, S. C. (2017). A tri-part protein complementation system using antibody-small peptide fusions enables homogeneous immunoassays. *Sci. Rep.* 7:8186. doi: 10.1038/s41598-017-07569-y

Dixon, A. S., Schwinn, M. K., Hall, M. P., Zimmerman, K., Otto, P., Lubben, T. H., et al. (2016). Nanoluc complementation reporter optimized for accurate measurement of protein interactions in cells. *ACS Chem. Biol.* 11, 400–408. doi: 10.1021/acschembio.5b00753

Elledge, S. K., Zhou, X. X., Byrnes, J. R., Martinko, A. J., Lui, I., Pance, K., et al. (2020). Engineering luminescent biosensors for point-of-care SARS-CoV-2 antibody detection. *Nat. Biotechnol.* 39, 928–935. doi: 10.1038/s41587-021-00878-8

Eshghifar, N., Busheri, A., Shrestha, R., and Beqaj, S. (2021). Evaluation of analytical performance of seven rapid antigen detection kits for detection of SARS-CoV-2 virus. *Int. J. Gen. Med.* 14, 435–440. doi: 10.2147/IJGM.S297762

Fan, F., and Wood, K. V. (2007). Bioluminescent assays for high-throughput screening. *Assay Drug Dev. Technol.* 5, 127–136. doi: 10.1089/adt.2006.053

Grifoni, A., Sidney, J., Zhang, Y., Scheuermann, R. H., Peters, B., and Sette, A. (2020). A sequence homology and bioinformatic approach can predict candidate targets for immune responses to SARS-CoV-2. *Cell Host Microbe* 27, 671.e2–680.e2. doi: 10.1016/j.chom.2020.03.002

Hall, M. P., Kincaid, V. A., Jost, E. A., Smith, T. P., Hurst, R., Forsyth, S. K., et al. (2021). Toward a point-of-need bioluminescence-based immunoassay utilizing a complete shelf-stable reagent. *Anal. Chem.* 93, 5177–5184. doi: 10.1021/acs.analchem.0c05074

Hall, M. P., Unch, J., Binkowski, B. F., Valley, M. P., Butler, B. L., Wood, M. G., et al. (2012). Engineered luciferase reporter from a deep sea shrimp utilizing a novel imidazopyrazinone substrate. *ACS Chem. Biol.* 7, 1848–1857. doi: 10.1021/cb3002478

Hawkins, E. M., Ogrady, M., Klaubert, D., Scurria, M., Good, T., Stratford, C., et al. (2002). Coelenterazine derivatives for improved solution solubility. *J. Biolumin. Chemilumin.* 149–152. doi: 10.1142/9789812776624_0033

Healtheuropa (2021). *Point-of-Care Medicine: The Future of Rapid Diagnostics in Healthcare*. Cheshire, United Kingdom: Healtheuropa.

Hu, X., Zhang, P., Wang, D., Jiang, J., Chen, X., Liu, Y., et al. (2021). Aiegens enabled ultrasensitive point-of-care test for multiple targets of food safety: aflatoxin b. *Biosens. Bioelectron.* 182:113188. doi: 10.1016/j.bios.2021.113188

Hwang, B., Engel, L., Goueli, S. A., and Zegzouti, H. (2020). A homogeneous bioluminescent immunoassay to probe cellular signaling pathway regulation. *Commun. Biol.* 3:8. doi: 10.1038/s42003-019-0723-9

Kahn, M., Schuierer, L., Bartenschlager, C., Zellmer, S., Frey, R., Freitag, M., et al. (2021). Performance of antigen testing for diagnosis of covid-19: a direct comparison of a lateral flow device to nucleic acid amplification based tests. *BMC Infect. Dis.* 21:798. doi: 10.1186/s12879-021-06524-7

Kainulainen, M. H., Bergeron, E., Chatterjee, P., Chapman, A. P., Lee, J., Chida, A., et al. (2021). High-throughput quantitation of SARS-CoV-2 antibodies in a single-dilution homogeneous assay. *Sci. Rep.* 11:12330. doi: 10.1038/s41598-021-91300-5

Ke, Z., Oton, J., Qu, K., Cortese, M., Zila, V., Mckeane, L., et al. (2020). Structures and distributions of SARS-CoV-2 spike proteins on intact virions. *Nature* 588, 498–502. doi: 10.1038/s41586-020-2665-2

Kincaid, V. A., Wang, H., Sondgeroth, C. A., Torio, E. A., Ressler, V. T., Fitzgerald, C., et al. (2022). Simple, rapid chemical labeling and screening of antibodies with luminescent peptides. *ACS Chem. Biol.* 17, 2179–2187. doi: 10.1021/acschembio.2c00306

Koczula, K. M., and Gallotta, A. (2016). Lateral flow assays. *Essays Biochem.* 60, 111–120. doi: 10.1042/EBC20150012

Kozel, T. R., and Burnham-Marusich, A. R. (2017). Point of care testing for infectious diseases- past, present, and future. *J. Clin. Microbiol.* 55, 2313–2320. doi: 10.1128/JCM.00476-17

Land, K. J., Boeras, D. I., Chen, X.-S., Ramsay, A. R., and Peeling, R. W. (2019). Reassured diagnostics to inform disease control strategies, strengthen health systems and improve patient outcomes. *Nat. Microbiol.* 4, 46–54. doi: 10.1038/s41564-018-0295-3

Liu, D., Wu, F., Cen, Y., Ye, L., Shi, X., Huang, Y., et al. (2021). Comparative research on nucleocapsid and spike glycoprotein as the rapid immunodetection targets of COVID-19 and establishment of immunoassay strips. *Mol. Immunol.* 131, 6–12. doi: 10.1016/j.molimm.2021.01.005

Louie, R. F., Kitano, T., Brock, T. K., Derlet, R., and Kost, G. J. (2009). Point-of-care testing for pandemic influenza and biothreats. *Disaster Med. Public Health Prep.* 3, S193–S202. doi: 10.1097/DMP.0b013e3181be6dc4

Luppa, P. B., Muller, C., Schlichtiger, A., and Schlebusch, H. (2011). Point-of-care testing (POCT): current techniques and future perspectives. *Trends Anal. Chem.* 30, 887–898. doi: 10.1016/j.trac.2011.01.019

Lutomski, C. A., El-Baba, T. J., Bolla, J. R., and Robinson, C. V. (2021). Multiple roles of SARS-CoV-2 N protein facilitated by proteoform-specific interactions with RNA, host proteins, and convalescent antibodies. *JACS Au* 1, 1147–1157. doi: 10.1021/jacsau.1c00139

Malcata, F. B., Pepler, P. T., O'reilly, E. L., Brady, N., Eckersall, P. D., Zadoks, R. N., et al. (2020). Point-of-care tests for bovine clinical mastitis: what do we have and what do we need? *J. Dairy Res.* 87, 60–66. doi: 10.1017/S002202992000062X

Mohammad, T., Choudhury, A., Habib, I., Asrani, P., Mathur, Y., Umair, M., et al. (2021). Genomic variations in the structural proteins of SARS-CoV-2 and their deleterious impact on pathogenesis: a comparative genomics approach. *Front. Cell Infect. Microbiol.* 11:765039.

Mouliou, D. S., and Gourgoulianis, K. I. (2021). False-positive and false-negative covid-19 cases: respiratory prevention and management strategies, vaccination, and further perspectives. *Expert Rev. Respir. Med.* 15, 993–1002. doi: 10.1080/17476348.2021.1917389

Nath, N., Flemming, R., Godat, B., and Urh, M. (2017). Development of nanoluc bridging immunoassay for detection of anti-drug antibodies. *J. Immunol. Methods* 450, 17–26. doi: 10.1016/j.jim.2017.07.006

Ngo, J., Ravi, S., Kim, N., and Boukhman, M. (2020). Drive-through medicine for covid-19 and future pandemics. *West. J. Emerg. Med.* 22, 252–256. doi: 10.5811/westjem.2020.9.48799

Ni, Y., Arts, R., and Merkx, M. (2019). Ratiometric bioluminescent sensor proteins based on intramolecular split luciferase complementation. *ACS Sens.* 4, 20–25. doi: 10.1021/acssensors.8b01381

Ni, Y., Rosier, B., Van Aalen, E. A., Hanckmann, E. T. L., Biewenga, L., Pistikou, A. M., et al. (2021). A plug-and-play platform of ratiometric bioluminescent sensors for homogeneous immunoassays. *Nat. Commun.* 12:4586. doi: 10.1038/s41467-021-24874-3

Ohmuro-Matsuyama, Y., and Ueda, H. (2018). Homogeneous noncompetitive luminescent immunodetection of small molecules by ternary protein fragment complementation. *Anal. Chem.* 90, 3001–3004. doi: 10.1021/acs.analchem.7b05140

Patriquin, G., Davidson, R. J., Hatchette, T. F., Head, B. M., Mejia, E., Becker, M. G., et al. (2021). Generation of false-positive SARS-CoV-2 antigen results with testing conditions outside manufacturer recommendations: a scientific approach to pandemic misinformation. *Microbiol. Spectr.* 9:e0068321. doi: 10.1128/Spectrum.00683-21

Patzer, K.-H., Ardjomand, P., Göhring, K., Klempt, G., Patzelt, A., Redzich, M., et al. (2018). Implementation of hba1c point of care testing in 3 German medical

practices: impact on workflow and physician, staff, and patient satisfaction. *J. Diabetes Sci. Technol.* 12, 687–694. doi: 10.1177/1932296818759690

Ross, G. M. S., Filippini, D., Nielen, M. W. F., and Salentijn, G. I. J. (2020). Unraveling the hook effect: a comprehensive study of high antigen concentration effects in sandwich lateral flow immunoassays. *Anal. Chem.* 92, 15587–15595. doi: 10.1021/acs.analchem.0c03740

Roy, L., Buragohain, P., and Borse, V. (2022). Strategies for sensitivity enhancement of point-of-care devices. *Biosens. Bioelectron. X* 10:100098. doi: 10.1016/j.biosx.2021.100098

Sakamoto, S., Putalun, W., Vimolmangkang, S., Phoolcharoen, W., Shoyama, Y., Tanaka, H., et al. (2018). Enzyme-linked immunosorbent assay for the quantitative/qualitative analysis of plant secondary metabolites. *J. Nat. Med.* 72, 32–42. doi: 10.1007/s11418-017-1144-z

Schwinn, M. K., Machleidt, T., Zimmerman, K., Eggers, C. T., Dixon, A. S., Hurst, R., et al. (2018). CRISPR-mediated tagging of endogenous proteins with a luminescent peptide. *ACS Chem. Biol.* 13, 467–474. doi: 10.1021/acschembio.7b00549

Scohy, A., Anantharajah, A., Bodéus, M., Kabamba-Mukadi, B., Verroken, A., and Rodriguez-Villalobos, H. (2020). Low performance of rapid antigen detection test as frontline testing for COVID-19 diagnosis. *J. Clin. Virol.* 129:104455. doi: 10.1016/j.jcv.2020.104455

Shajahan, A., Supekar, N. T., Gleinich, A. S., and Azadi, P. (2020). Deducing the N- and O-glycosylation profile of the spike protein of novel coronavirus SARS-CoV-2. *Glycobiology* 30, 981–988. doi: 10.1093/glycob/cwaa042

Shaw, J. L. V. (2016). Practical challenges related to point of care testing. *Pract. Lab Med.* 4, 22–29. doi: 10.1016/j.plabm.2015.12.002

Shaw, J. L. V. (2021). Point-of-care testing: the good, the bad, and the laboratory oversight. *JALM* 6, 1090–1093. doi: 10.1093/jalm/jfaa200

Simula, E. R., Manca, M. A., Jasemi, S., Uzzau, S., Rubino, S., Manchia, P., et al. (2020). HCoV-NL63 and SARS-CoV-2 share recognized epitopes by the humoral response in sera of people collected pre-and during COV-2 pandemic. *Microorganisms* 8:1993. doi: 10.3390/microorganisms8121993

St John, A., and Price, C. P. (2014). Existing and emerging technologies for point-of-care testing. *Clin. Biochem. Rev.* 35, 155–167.

Supekar, N. T., Shajahan, A., Gleinich, A. S., Rouhani, D., Heiss, C., and Azadi, P. (2020). SARS-CoV-2 nucleocapsid protein is decorated with multiple N- and O-glycans. bioRxiv the preprint server for biology [Preprint]. doi: 10.1101/2020.08.26.269043

Suzuki, K., and Nagai, T. (2017). Recent progress in expanding the chemiluminescent toolbox for bioimaging. *Curr. Opin. Biotechnol.* 48, 135–141. doi: 10.1016/j.copbio.2017.04.001

Tenda, K., Van Gerven, B., Arts, R., Hiruta, Y., Merkx, M., and Citterio, D. (2018). Paper-based antibody detection devices using bioluminescent BRET-switching sensor proteins. *Angew. Chem. Int. Ed.* 130, 15595–15599. doi: 10.1002/ange.201808070

Terato, K., Do, C. T., Cutler, D., Waritani, T., and Shionoya, H. (2014). Preventing intense false positive and negative reactions attributed to the principle of ELISA to re-investigate antibody studies in autoimmune diseases. *J. Immunol. Methods* 407, 15–25. doi: 10.1016/j.jim.2014.03.013

Tolan, N. (2017). Direct-to-consumer testing: a new paradigm for point-of-care testing. *Point of Care J. Near-Patient Test. Technol.* 16, 108–111. doi: 10.1097/POC.0000000000000137

Tomimuro, K., Tenda, K., Ni, Y., Hiruta, Y., Merkx, M., and Citterio, D. (2020). Thread-based bioluminescent sensor for detecting multiple antibodies in a single drop of whole blood. *ACS Sens.* 5, 1786–1794. doi: 10.1021/acssensors.0c00564

Tung, J. K., Berglund, K., Gutekunst, C. A., Hochgeschwender, U., and Gross, R. E. (2016). Bioluminescence imaging in live cells and animals. *Neurophotonics* 3:025001. doi: 10.1117/1.NPh.3.2.025001

West, R., Kobokovich, A., Connell, N., and Gronvall, G. K. (2021). COVID-19 antibody tests: a valuable public health tool with limited relevance to individuals. *Trends Microbiol.* 29, 214–223. doi: 10.1016/j.tim.2020.11.002

Wu, L., Zhou, L., Mo, M., Liu, T., Wu, C., Gong, C., et al. (2022). SARS-CoV-2 omicron RBD shows weaker binding affinity than the currently dominant delta variant to human ACE2. *Signal Transduct. Target. Ther.* 7:8. doi: 10.1038/s41392-021-00863-2

Xue, L., Yu, Q., Griss, R., Schena, A., and Johnsson, K. (2017). Bioluminescent antibodies for point-of-care diagnostics. *Angew. Chem. Int. Ed.* 56, 7112–7116. doi: 10.1002/anie.201702403

Yao, Z., Drecun, L., Aboualizadeh, F., Kim, S. J., Li, Z., Wood, H., et al. (2021). A homogeneous split-luciferase assay for rapid and sensitive detection of anti-SARS CoV-2 antibodies. *Nat. Commun.* 12:1806. doi: 10.1038/s41467-021-22102-6

Zhou, H., Wang, C., Rao, J., Chen, L., Ma, T., Liu, D., et al. (2021). The impact of sample processing on the rapid antigen detection test for SARS-CoV-2: virus inactivation, VTM selection, and sample preservation. *Biosaf. Health* 3, 238–243. doi: 10.1016/j.bsheal.2021.09.001

Frontiers in
Bioengineering and Biotechnology

Accelerates the development of therapies, devices, and technologies to improve our lives

A multidisciplinary journal that accelerates the development of biological therapies, devices, processes and technologies to improve our lives by bridging the gap between discoveries and their application.

Discover the latest Research Topics

See more →

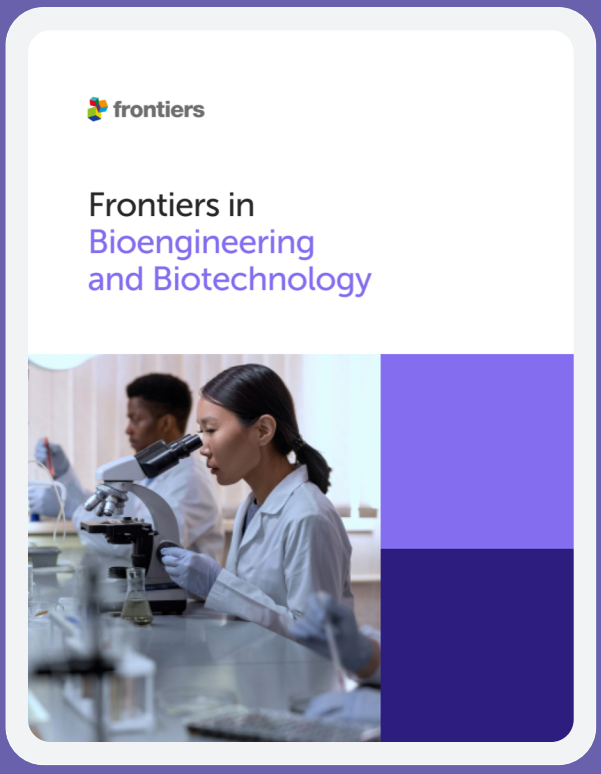

Frontiers

Avenue du Tribunal-Fédéral 34
1005 Lausanne, Swizerland
frontiersin.org

Contact us

+41 (0)21 510 17 00
frontiersin.org/about/contact